Titre: Title:	Passive Millimeter-Wave Imaging Based on Subharmonic Self-Oscillating Mixing
Auteur: Author:	Simone Angela Winkler
Date:	2011
Type:	Mémoire ou thèse / Dissertation or Thesis
Référence: Citation:	Winkler, S. A. (2011). Passive Millimeter-Wave Imaging Based on Subharmonic Self-Oscillating Mixing [Thèse de doctorat, École Polytechnique de Montréal]. PolyPublie. https://publications.polymtl.ca/508/

UNIVERSITÉ DE MONTRÉAL

PASSIVE MILLIMETER-WAVE IMAGING BASED ON SUBHARMONIC SELF-OSCILLATING MIXING

SIMONE ANGELA WINKLER
DÉPARTEMENT DE GÉNIE ÉLECTRIQUE
ÉCOLE POLYTECHNIQUE DE MONTRÉAL

THÈSE PRÉSENTÉE EN VUE DE L'OBTENTION
DU DIPLÔME DE PHILOSOPHIAE DOCTOR (Ph.D.)
(GÉNIE ÉLECTRIQUE)
JANVIER 2011

UNIVERSITÉ DE MONTRÉAL

ÉCOLE POLYTECHNIQUE DE MONTRÉAL

Cette thèse intitulée:

PASSIVE MILLIMETER-WAVE IMAGING BASED ON SUBHARMONIC SELF-OSCILLATING MIXING

présentée par: WINKLER Simone Angela
en vue de l'obtention du diplôme de: Philosophiae Doctor
a été dûment acceptée par le jury d'examen constitué de:

M. KASHYAP Raman, Ph.D., président
M. WU Ke, Ph.D., membre et directeur de recherche
M. AKYEL Cevdet, D.Sc.A., membre
Mme. POPOVICH Milica, Ph.D., membre

Dédicace :

Because life is wonderful.
To all those who cannot see it yet.

REMERCIEMENTS

I would like to express my gratitude to the many people who have been guiding me on my path toward the completion of my PhD. project and thesis during all these years.

First of all I would like to honour my professor and supervisor Prof. Ke Wu, who has offered me the incredible possibility to work with the Poly-Grames Research Center, and who has always been supportive during this thesis work.

My thanks go to Dr. Stephen Maas, Nonlintec Inc., Long Beach, CA, who throughout the years grew into a great technical help and friend, a person whom I will never forget.

I would like to mention the financial support provided to me by the Austrian Academy of Science, the Fonds Québécois sur la Recherche de la Nature et les Technologies, both for scholarships financing my PhD. work, the Oesterreichische Forschungsgemeinschaft and the European Microwave Association supporting me in the travel expenses for various conferences, the IEEE Microwave Theory and Techniques Society for their awarding of a graduate scholarship, and various other organizations supporting me with awards and prizes.

My thanks go to the École Polytechnique Montréal and their staff for making these PhD. studies possible.

My gratitude goes to Prof. Wei Hong at the Southeast University in Nanjing, China, where I had the great possibility to spend a research period.

I would like to thank our technicians, especially M. Jules Gauthier, who was more than only supportive throughout my thesis work and always managed to improve my experiments with his year-long experience. My thanks go to my office colleague and invaluable friend Liang Han, who helped me with numerous technical problems and sparking my interest with lots of fruitful discussions throughout the years.

I would like to thank my parents, because sometimes they are the only ones who will never stop thinking positive about you. My huge thanks go to Dr. Dieter Weber, without whom I would not be where, who, and how I am now. I'd like to thank my great, great friends who have made my time here unforgettable and who have not ceased to support me during the downsides of the thesis work.

RÉSUMÉ

Le sujet général de la thèse de doctorat présentée réside dans la recherche sur des nouvelles méthodes dans le domaine de l'imagerie aux micro-ondes, en particulier l'imagerie passive aux ondes millimétriques, qui est aussi connue sous le nom d'imagerie radiométrique. Cette dernière technique est utilisée pour former une image d'une scène particulière en capturant la radiation électromagnétique émise naturellement par chaque objet à la bande de fréquence des micro-ondes / ondes millimétriques, similaire à la façon dont une photographie est prise en capturant la radiation aux fréquences optiques. De cette façon, une image d'ondes millimétriques peut être formée et utilisée pour tracer différentes caractéristiques de la scène ou de l'objet, qui sont implicites à la bande de fréquences des micro-ondes / ondes millimétriques.

L'imagerie à ondes millimétriques représente un des sujets d'actualité des plus prometteurs dans le domaine de la conception des capteurs à haute fréquence. L'utilité de cette technique réside surtout dans les particularités des phénomènes de l'atténuation atmosphérique permettant aux ondes millimétriques de pénétrer à travers une grande variété de conditions de mauvaise visibilité, comme par exemple la brume, le brouillard, les nuages, la fumée et les tempêtes de sable, ainsi que la capacité de se propager à travers des vêtements et certains autres matériaux. Outre ces avantages par rapport aux systèmes infrarouges ou optiques, les systèmes à ondes millimétriques surpassent les systèmes micro-ondes à plus basse fréquence par leurs longueurs d'ondes plus petites permettant d'atteindre une plus haute résolution. Pour leur mise en application, des fenêtres de propagation à 35, 77, 94, 140 et 220 GHz ont été assignées.

Les domaines d'application présents et futurs sont principalement associés aux infrastructures militaires et commerciales. Ceux-ci englobent la surveillance, la navigation et la technologie automobile, ainsi que l'atterrissage des avions et le suivi de la circulation dans le brouillard sur les autoroutes. De plus, la demande de plus en plus grande en systèmes de détection de sécurité aux aéroports et d'autres lieux publics crée une demande toujours plus grande en scanners automatisés en temps réel dotés des caractéristiques suivantes : ne présenter aucun risque pour la santé, générer un nombre

réduit de fausses alertes et permettre la détection des armes cachées ou des objets dangereux à travers les vêtements. Cette dernière caractéristique recherchée désigne l'imagerie aux ondes millimétriques comme choix approprié. En outre, les ondes millimétriques sont appliquées à l'imagerie biomédicale comme dans la localisation des points chauds, des tumeurs ou d'autres anomalies dans le corps humain. Des applications supplémentaires consistent dans l'essai non-destructif des matériaux et des examens géologiques comme l'observation de l'atmosphère de la Terre, la détection des marées noires, la recherche sur l'activité des volcans ou la météorologie.

Le développement de tels systèmes à ondes millimétriques à haute performance présente un grand défi technologique, et un certain nombre de systèmes récents ont été réalisés. L'acquisition d'une image millimétrique peut être effectuée de plusieurs façons différentes, avec la méthode la plus simple, mais aussi la plus lente, qui consiste en un scan mécanique *x-y* de la région d'intérêt en utilisant un récepteur simple, contrairement à un réseau à plan focal avec un grand nombre d'éléments de détection entièrement indépendants dans le plan focal d'une lentille ou d'un réflecteur d'imagerie opérant en parallèle et par conséquent à une vitesse d'acquisition plus élevée et souvent à temps réel. Quelques systèmes utilisent aussi une combinaison plus coûteuse des deux méthodes, et l'approche moins utilisée présentement et plus complexe basée sur les réseaux de phase représente une autre possibilité pour l'acquisition d'une image à ondes millimétriques.

Toutefois, les présents systèmes de pointe nécessitent presque toujours un compromis entre un système de réseau à plan focal coûteux et un système de scan mécanique moins coûteux, plus encombrant et plus lent. Présentement, un nombre important de limitations technologiques est rencontré dans la conception des récepteurs opérant aux fréquences millimétriques. Les amplificateurs à faible bruit aux fréquences millimétriques sont coûteux et sujet à une consommation d'énergie très élevée à cause de leur faible efficacité, ce qui entraîne un problème de dissipation de chaleur surtout pour des réseaux à plan focal à taille compacte et haute densité avec un grand nombre de canaux de récepteurs en parallèle. En évitant ce problème au moyen d'un récepteur hétérodyne, l'utilisation des oscillateurs externes avec une puissance adéquate devient nécessaire, ce qui, encore une fois, introduit une conception difficile et coûteuse à haute fréquence et augmente en plus

les dimensions des circuits, puisqu'un oscillateur externe doit être intégré avec chaque élément de récepteur.

Par conséquent, les directions possibles de recherche future sont dans le développement des systèmes de réseau à plan focal à haute fréquence et temps réel, qui sont efficaces en termes de coût et compacts au niveau des dimensions. Une approche novatrice réside dans l'utilisation des ainsi nommés mélangeurs auto-oscillants dans les récepteurs hétérodynes d'imagerie de haute fréquence. Les mélangeurs auto-oscillants représentent un choix excellent pour un tel concept car la source oscillante et le mélangeur sont tous deux combinés dans un seul composant. Outre la réduction du nombre de composants, ils offrent plusieurs avantages comme leur consommation d'énergie plus basse et la possibilité d'une intégration simple et directe dans des circuits micro-ondes monolithiques intégrés.

Une extension à la technique standard du mélangeur auto-oscillant est l'opération subharmonique : au lieu de mélanger l'énergie incidente millimétrique radiofréquence avec la fondamentale de la fréquence d'oscillation, une harmonique de la fréquence d'oscillation est utilisée.

De cette façon, les limitations des présents systèmes de réseaux à plan focal peuvent être surmontées, car d'une part un récepteur hétérodyne plus efficace peut être utilisé avec l'oscillateur intégré dans le mélangeur, qui d'un seul coup résout le problème mentionné ci-haut de la dissipation de chaleur et des dimensions du circuit. D'autre part une puissance d'oscillation suffisante peut être atteinte en se servant de l'opération subharmonique parce que la génération du signal d'oscillation à une fraction de fréquence de celle du signal radiofréquence est beaucoup moins problématique.

Dans ce projet, un système d'imagerie passif complet à 35 GHz basé sur la technique des mélangeurs auto-oscillations subharmoniques mentionnés ci-haut est proposé. Le travail de recherche dans cette thèse de doctorat se concentre en particulier sur la conception, la mise en opération, et le test expérimental des mélangeurs auto-oscillants subharmoniques. Le circuit final de mélangeur auto-oscillant à 35 GHz est finalement intégré dans un simple système d'imagerie basé sur le scan mécanique avec un récepteur simple afin de prouver la fonctionnalité de la technique des mélangeurs auto-oscillants dans le cadre des systèmes d'imagerie millimétrique. Ce premier environnement de test d'imagerie millimétrique sert

de base pour la recherche future dans le domaine. Les travaux futurs incluent la parallélisation de ces récepteurs dans un réseau à plan focal, et aussi l'adaptation du concept à des fréquences plus élevées, en particulier à 94 GHz, afin d'atteindre une résolution plus précise et des systèmes plus compacts.

Le présent travail a été effectué en trois étapes majeures de conception avec, en premier lieu, la recherche profonde sur les mélangeurs auto-oscillants et leur mise en opération en mode subharmonique. Cette étape a été réalisée en réalisant un prototype à basse fréquence, soit à 5.8 GHz, afin de bien pouvoir analyser et optimiser le design et a ensuite été transféré à une fréquence de 35 GHz. En deuxième lieu le travail présenté consiste du développement d'un récepteur basé sur le concept de mélangeur auto-oscillant, et, en troisième lieu, l'intégration de ce récepteur dans un système complet d'imagerie de scan mécanique à 35 GHz est effectuée.

ABSTRACT

The broad topic of the presented Ph.D. thesis consists in the research on novel methods in the field of microwave imaging, in particular the so-called passive millimetre-wave imaging, which is also referred to as radiometric imaging. This latter technique is used to form an image of a particular scene by means of sensing the natural electromagnetic radiation emitted by any object at microwave / millimetre-wave wavelengths, similar to the way in which a photograph is captured by sensing the radiation occurring at optical wavelengths. In this way, different characteristics of the observed scene or object, which are inherent to the microwave / millimetre-wave frequency range, can be mapped in the form of an image.

Millimetre-wave imaging represents one of today's most promising research topics in the field of high frequency sensor design. The usefulness of this technique lies in particular in the peculiarities of atmospheric attenuation phenomenologies allowing millimetre-waves to penetrate through a variety of low-visibility conditions such as haze, fog, clouds, smoke, and sandstorms and furthermore in the ability to propagate through clothing and a number of other materials. Together with these advantages over infrared and optical systems, moreover, millimetre-wave systems outperform imagers at the lower microwave frequency range due to their smaller wavelengths and the thus achievable higher resolution. For their implementation, propagation windows at 35, 77, 94, 140, and 220 GHz are generally allocated.

Present and future applications consist in both military and commercial infrastructure fields such as in surveillance, navigation, and automotive technology, as well as aircraft landing or highway traffic monitoring in fog. Moreover, the ever increasing demand for security screening systems at airports and other public environments creates a growing need for health-hazardless automated real-time scanners with minimized false alarms, and millimetre-wave imaging offering the ability to detect concealed weapons or hazardous objects through clothing material represents an excellent choice for this purpose. Furthermore, millimetre-wave imaging is applied to biomedical imaging such as the location of hot spots, tumours, or other anomalies in the body. Additional applications

consist in non-destructive material testing and geological examinations such as the sensing of the Earth's atmosphere, oil spill detection, research on volcano activity, or meteorology.

The development of such high-performance millimetre-wave imaging systems presents a great technological challenge and a number of recent systems have been demonstrated. The acquisition of a millimetre-wave image can be performed in several ways, with the simplest but also slowest method being a mechanical *x*-*y* raster scan of the area of interest using a single receiver as opposed to a focal plane array (FPA) system employing an array of many entirely independent detector elements in the focal surface of an imaging lens or reflector working in parallel and therefore at higher and often real-time acquisition speed. Some systems also employ a more cost-effective combination of both methods, and the currently less employed and more complex phased-array approach represents another possibility for the acquisition of a millimetre-wave image.

However, present state-of-the-art systems almost always require a trade-off between a cost-intensive real-time FPA imager and lower-cost bulkier and slower mechanical scanning systems. Currently, a number of technological limitations are encountered in the design of receivers operating at millimetre frequencies. Low-noise amplifiers (LNA) at millimetre-wave frequencies are cost-intensive and subject to high power consumption due to their low efficiency, which results in a heat dissipation problem especially for compact-size high-density FPAs with a large number of parallel receiver channels. Avoiding this problem by using a heterodyne receiver requires the use of external local oscillators (LO) with adequate power, which, once again, introduces a difficult and cost-intensive design at high frequencies and moreover increases circuit size as an external LO has to be implemented on each receiver element.

Consequently, future research aims for the development of cost-effective, compact size high-frequency real-time FPA systems overcoming these limitations. A novel approach consists in the use of so-called self-oscillating mixers (SOMs) in high-frequency heterodyne millimetre-wave imaging receivers. SOMs are excellent choices for such a design as both the oscillating source and the mixer are combined in one single device. In addition to the reduction in component number, they offer numerous advantages such as their lower power consumption and the possibility of simple and straight-forward integration into microwave monolithic integrated circuits (MMICs).

An extension to the standard SOM technique is given by subharmonic operation: instead of mixing the incoming millimetre-wave radio frequency (RF) signal with the fundamental LO frequency, a harmonic of the LO frequency is used.

In this way, the limitations of current FPA systems may be overcome, as on one hand, a more efficient heterodyne receiver can be used with the external LO being integrated in the mixer, which simultaneously solves the previously mentioned heat dissipation and circuit size problem. On the other hand, adequate LO power can be generated by employing subharmonic operation, thus generating the LO signal at a frequency of only a fraction of the RF input, where its generation is much less problematic.

In this project, a complete passive millimetre-wave imager at 35 GHz based on the previously described subharmonic SOM technique is proposed. The research work in this Ph.D. thesis focuses in particular on the design, implementation, and experimental testing of subharmonic SOMs. The final 35 GHz SOM circuit is eventually implemented into a straight-forward mechanical raster scanning imaging system based on a single-element receiver in order to prove functionality of the SOM technique in the framework of millimetre-wave imaging systems. This first millimetre-wave imaging test-bed serves as the base for future research in the field. Future work includes the parallelization of these receivers in the form of an FPA system, and also the task of pushing the design toward higher frequencies, in particular 94 GHz, for achieving higher image resolutions and more compact-sized imagers.

The presented work has been carried out in three major design steps with 1) the extensive research on SOMs and their subharmonic implementation using a low-frequency prototype at 5.8 GHz as a means of design optimization and verification and its subsequent scaling to the final design frequency of 35 GHz, 2) the development of a single-element receiver based on the successfully implemented subharmonic SOM design, and 3) the integration of the receiver into a complete mechanical scanning imaging system at 35 GHz.

CONDENSÉ EN FRANÇAIS

Le sujet général de la thèse de doctorat présentée réside dans la recherche sur des nouvelles méthodes dans le domaine de l'imagerie aux micro-ondes, en particulier l'imagerie passive aux ondes millimétriques, qui est aussi connue sous le nom d'imagerie radiométrique. Cette dernière technique est utilisée pour former une image d'une scène particulière en capturant la radiation électromagnétique émise naturellement par chaque objet à la bande de fréquence des micro-ondes / ondes millimétriques, similaire à la façon dont une photographie est prise en capturant la radiation aux fréquences optiques. De cette façon, une image d'ondes millimétriques peut être formée et utilisée pour tracer différentes caractéristiques de la scène ou de l'objet, qui sont implicites à la bande de fréquences des micro-ondes / ondes millimétriques.

L'imagerie à ondes millimétriques représente un des sujets d'actualité des plus prometteurs dans le domaine de la conception des capteurs à haute fréquence. L'utilité de cette technique réside surtout dans les particularités des phénomènes de l'atténuation atmosphérique permettant aux ondes millimétriques de pénétrer à travers une grande variété de conditions de mauvaise visibilité, comme par exemple la brume, le brouillard, les nuages, la fumée et les tempêtes de sable, ainsi que la capacité de se propager à travers des vêtements et certains autres matériaux. Outre ces avantages par rapport aux systèmes infrarouges ou optiques, les systèmes à ondes millimétriques surpassent les systèmes micro-ondes à plus basse fréquence par leurs longueurs d'ondes plus petites permettant d'atteindre une plus haute résolution. Pour leur mise en application, des fenêtres de propagation à 35, 77, 94, 140 et 220 GHz ont été assignées.

Les domaines d'application présents et futurs sont principalement associés aux infrastructures militaires et commerciales. Ceux-ci englobent la surveillance, la navigation et la technologie automobile, ainsi que l'atterrissage des avions et le suivi de la circulation dans le brouillard sur les autoroutes. De plus, la demande de plus en plus grande en systèmes de détection de sécurité aux aéroports et d'autres lieux publics crée une demande toujours plus grande en scanners automatisés en temps réel dotés des caractéristiques suivantes : ne présenter aucun risque pour la santé, générer un nombre

réduit de fausses alertes et permettre la détection des armes cachées ou des objets dangereux à travers les vêtements. Cette dernière caractéristique recherchée désigne l'imagerie aux ondes millimétriques comme choix approprié. En outre, les ondes millimétriques sont appliquées à l'imagerie biomédicale comme dans la localisation des points chauds, des tumeurs ou d'autres anomalies dans le corps humain. Des applications supplémentaires consistent dans l'essai non-destructif des matériaux et des examens géologiques comme l'observation de l'atmosphère de la Terre, la détection des marées noires, la recherche sur l'activité des volcans ou la météorologie.

Le développement de tels systèmes à ondes millimétriques à haute performance présente un grand défi technologique, et un certain nombre de systèmes récents ont été réalisés. L'acquisition d'une image millimétrique peut être effectuée de plusieurs façons différentes, avec la méthode la plus simple, mais aussi la plus lente, qui consiste en un scan mécanique *x-y* de la région d'intérêt en utilisant un récepteur simple, contrairement à un réseau à plan focal avec un grand nombre d'éléments de détection entièrement indépendants dans le plan focal d'une lentille ou d'un réflecteur d'imagerie opérant en parallèle et par conséquent à une vitesse d'acquisition plus élevée et souvent à temps réel. Quelques systèmes utilisent aussi une combinaison plus coûteuse des deux méthodes, et l'approche moins utilisée présentement et plus complexe basée sur les réseaux de phase représente une autre possibilité pour l'acquisition d'une image à ondes millimétriques.

Toutefois, les présents systèmes de pointe nécessitent presque toujours un compromis entre un système de réseau à plan focal coûteux et un système de scan mécanique moins coûteux, plus encombrant et plus lent. Présentement, un nombre important de limitations technologiques est rencontré dans la conception des récepteurs opérant aux fréquences millimétriques. Les amplificateurs à faible bruit aux fréquences millimétriques sont coûteux et sujet à une consommation d'énergie très élevée à cause de leur faible efficacité, ce qui entraîne un problème de dissipation de chaleur surtout pour des réseaux à plan focal à taille compacte et haute densité avec un grand nombre de canaux de récepteurs en parallèle. En évitant ce problème au moyen d'un récepteur hétérodyne, l'utilisation des oscillateurs externes avec une puissance adéquate devient nécessaire, ce qui, encore une fois, introduit une conception difficile et coûteuse à haute fréquence et augmente en plus

les dimensions des circuits, puisqu'un oscillateur externe doit être intégré avec chaque élément de récepteur.

Par conséquent, les directions possibles de recherche future sont dans le développement des systèmes de réseau à plan focal à haute fréquence et temps réel, qui sont efficaces en termes de coût et compacts au niveau des dimensions. Une approche novatrice réside dans l'utilisation des ainsi nommés mélangeurs auto-oscillants dans les récepteurs hétérodynes d'imagerie de haute fréquence. Les mélangeurs auto-oscillants représentent un choix excellent pour un tel concept car la source oscillante et le mélangeur sont tous deux combinés dans un seul composant. Outre la réduction du nombre de composants, ils offrent plusieurs avantages comme leur consommation d'énergie plus basse et la possibilité d'une intégration simple et directe dans des circuits micro-ondes monolithiques intégrés.

Une extension à la technique standard du mélangeur auto-oscillant est l'opération subharmonique : au lieu de mélanger l'énergie incidente millimétrique radiofréquence avec la fondamentale de la fréquence d'oscillation, une harmonique de la fréquence d'oscillation est utilisée.

De cette façon, les limitations des présents systèmes de réseaux à plan focal peuvent être surmontées, car d'une part un récepteur hétérodyne plus efficace peut être utilisé avec l'oscillateur intégré dans le mélangeur, qui d'un seul coup résout le problème mentionné ci-haut de la dissipation de chaleur et des dimensions du circuit. D'autre part une puissance d'oscillation suffisante peut être atteinte en se servant de l'opération subharmonique parce que la génération du signal d'oscillation à une fraction de fréquence de celle du signal radiofréquence est beaucoup moins problématique.

Dans ce projet, un système d'imagerie passif complet à 35 GHz basé sur la technique des mélangeurs auto-oscillations subharmoniques mentionnés ci-haut est proposé. Le travail de recherche dans cette thèse de doctorat se concentre en particulier sur la conception, la mise en opération, et le test expérimental des mélangeurs auto-oscillants subharmoniques. Le circuit final de mélangeur auto-oscillant à 35 GHz est finalement intégré dans un simple système d'imagerie basé sur le scan mécanique avec un récepteur simple afin de prouver la fonctionnalité de la technique des mélangeurs auto-oscillants dans le cadre des systèmes d'imagerie millimétrique. Ce premier environnement de test d'imagerie millimétrique sert

de base pour la recherche future dans le domaine. Les travaux futurs incluent la parallélisation de ces récepteurs dans un réseau à plan focal, et aussi l'adaptation du concept à des fréquences plus élevées, en particulier à 94 GHz, afin d'atteindre une résolution plus précise et des systèmes plus compacts (Figure 0.1).

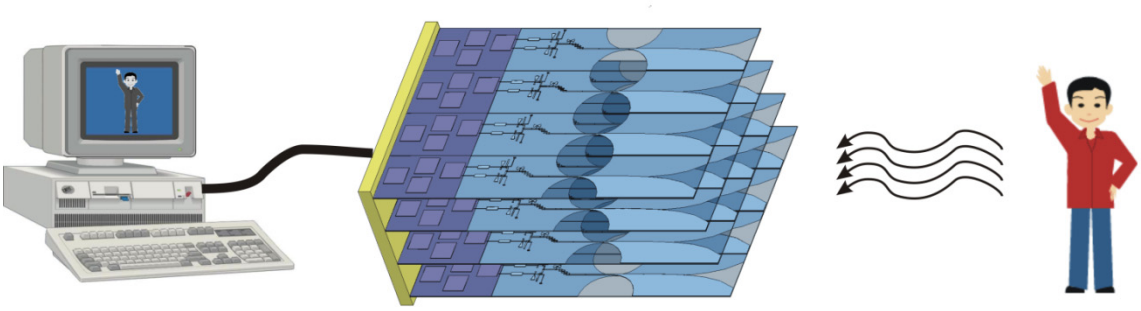

Figure 0.1 Système d'imagerie à réseau focal: La radiation électromagnétique émise naturellement par un objet est reçue par un capteur à haute sensibilité à réseau focal. Ensuite, les signaux sont convertis à une bande de fréquence intermédiaire et évalués par un système d'ordinateur ou de processeur digital.

Le présent travail a été effectué en trois étapes majeures de conception avec, en premier lieu, la recherche profonde sur les mélangeurs auto-oscillants et leur mise en opération en mode subharmonique, en deuxième lieu le développement d'un récepteur basé sur le concept de mélangeur auto-oscillant, et, en troisième lieu, l'intégration de ce récepteur dans un système complet d'imagerie de scan mécanique à 35 GHz.

CONCEPTION D'UN MÉLANGEUR AUTO-OSCILLANT

Le travail principal de la thèse de doctorat présentée se situe au niveau de la première étape, soit la recherche détaillée sur les mélangeurs auto-oscillants à ondes millimétriques et leurs équivalents subharmoniques. Une analyse détaillée de leur conception, des techniques spécifiques pour leur simulation, des techniques appropriées pour leurs mesures afin de pouvoir qualifier leur performance, et leur applicabilité pratique dans une variété d'applications est effectuée, gardant toujours à l'esprit leur utilisation finale dans

un système d'imagerie passive aux ondes millimétriques, guidant l'optimisation en performance et les paramètres de conception en fonction de cette application.

Comme nous l'avons déjà mentionné, les mélangeurs auto-oscillants représentent un choix excellent pour le développement des architectures de récepteurs de radiomètre compacts à faible coût, étant donné que la source oscillante et le mélangeur sont combinés dans un seul dispositif, tel que démontré dans l'exemple d'un radiomètre à puissance totale dans la Figure 0.2. Ceci résulte en un nombre de composants réduit, une consommation d'énergie plus basse, et la possibilité d'une intégration simple dans des circuits monolithiques intégrés à micro-ondes. Dans des travaux réalisés pendant les dernières décennies, les mélangeurs auto-oscillants ont été réalisés en utilisant des diodes et des transistors. Par contre, la capacité d'atteindre un gain de conversion en utilisant des transistors comme dispositifs actifs et leur développement technologique récent dans la bande de fréquence des ondes millimétriques a favorisé leur adoption, au point où ils sont devenus les dispositifs les plus fréquemment utilisés.

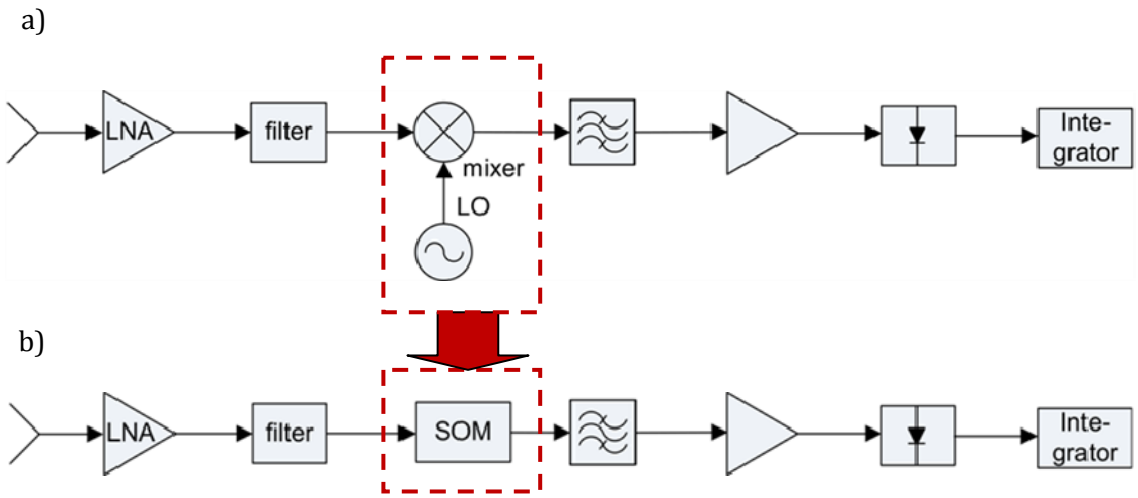

Figure 0.2 a) Structure d'un récepteur de radiomètre à puissance totale, b) substitution du mélangeur conventionnel par un mélangeur auto-oscillant.

Comme nous l'avons décrit précédemment, une extension à la technique standard des mélangeurs auto-oscillants est l'opération subharmonique, laquelle s'avère particulièrement bien adaptée pour les applications dans la bande des ondes

millimétriques. En utilisant cette technique, le transistor doit avoir un gain seulement à la fréquence fondamentale de l'oscillateur local, ce qui réduit dramatiquement les exigences à la fréquence maximale du transistor et représente ainsi un choix excellent pour la conception des systèmes à ondes millimétriques, tel qu'expliqué précédemment.

L'opération subharmonique peut être réalisée à l'aide d'une structure balancée. De cette façon, d'une part soit les produits de mélange pairs ou impairs peuvent être augmentés, et d'autre part certains produits de mélange pas désirés peuvent être éliminés de la sortie. De plus, les structures balancés offrent une isolation RF-LO inhérente ainsi que plusieurs autres avantages importants tel qu'un bruit AM plus faible, l'élimination des harmoniques non-désirées, etc. En outre, l'entrée ne doit pas être adaptée à la fois à la fréquence de RF et LO, ce qui simplifie les exigences d'adaptation d'entrée.

Pour le succès dans la conception d'un tel mélangeur auto-oscillant subharmonique, de multiples considérations importantes doivent être prises en compte afin d'atteindre une architecture de circuit à haute performance qui est applicable dans des systèmes réels.

Premièrement, la sélection de la technologie du transistor est un point important dans la conception : les composants qui ont été utilisés dans le circuit de mélangeur auto-oscillant présenté ici sont des transistors GaAs pHEMT offrant des caractéristiques de faible bruit et une capacité d'opération aux ondes millimétriques.

Une autre considération très importante est l'utilisation des outils appropriés pour la simulation et l'analyse afin de pouvoir prédire correctement la performance des mélangeurs auto-oscillants proposés. En utilisant des méthodes « Harmonic Balance », il n'est pas directement possible d'analyser les circuits des mélangeurs auto-oscillants à cause de leur opération autonome. En général, les simulateurs de circuits RF standards doivent être adaptés afin de pouvoir simuler ces structures. De plus, des algorithmes spécifiques pourraient devenir nécessaires afin de bien s'adapter aux caractéristiques spéciales des circuits des mélangeurs auto-oscillants. Dans la thèse de doctorat présentée, ces aspects de simulation ont été considérés et inclus dans la procédure de conception, et un nouvel algorithme a été développé.

Pour une analyse et une procédure de conception précise, il est également important d'utiliser un modèle de transistor approprié qui représente le composant utilisé dans le design du mélangeur auto-oscillant. Comme ceci est un point faible pour beaucoup de

dispositifs commerciaux, la modélisation des transistors devient une partie importante du circuit de mélangeur auto-oscillant proposé.

La performance des circuits mélangeurs auto-oscillants peut être analysée en considérant les paramètres combinés des mélangeurs et les oscillateurs. En détail, une attention particulière doit être portée au gain de conversion, la largeur de bande, et la figure de bruit, mais aussi la dérive de fréquence d'oscillation et le bruit de phase. Le travail présenté inclut une analyse détaillée des mélangeurs auto-oscillants subharmoniques.

De plus, afin de réduire le temps et le coût de conception de tels circuits, nous proposons de prouver le concept proposé à l'aide d'un prototype à basse fréquence. Un transfert à haute fréquence vers la bande des ondes millimétriques est plus facile à ce point et peut être basé sur les nombreux résultats tirés des expériences à basse fréquence. Ceci est d'une grande importance, car le coût et la durée prohibitifs de fabrication des circuits fonctionnant aux fréquences des ondes millimétriques requièrent des méthodes de prédiction pour l'analyse du comportement du circuit très précises. Ceci permet d'éviter que les erreurs soient détectées seulement après la fabrication. De plus, les prototypes à basse fréquence offrent une meilleure reconfigurabilité comme ils utilisent des composants discrets qui peuvent être échangés facilement et conséquemment permettent une analyse paramétrique expérimentale plus simple par rapport aux éléments imprimés distribués fixés géométriquement utilisés dans les structures à ondes millimétriques à plus haute fréquence. Pour cette raison, la conception des mélangeurs auto-oscillants dans la thèse présentée a été divisée en deux étapes majeures. La première étape consiste dans le développement d'un prototype à basse fréquence comme et est ensuite transformé dans la bande des ondes millimétriques, spécifiquement à 35 GHz pour cette thèse, comme la deuxième étape.

LE DÉVELOPPEMENT D'UN RÉCEPTEUR DE RADIOMÈTRE À BASE DE MÉLANGEUR AUTO-OSCILLANT

Dans cette étape, un prototype de récepteur à la base du mélangeur auto-oscillant développé dans l'étape précédente est réalisé à une fréquence de 35 GHz.

Un récepteur radiométrique mesure la radiation passive incidente émise par un objet en utilisant une antenne, qui peut recevoir la radiation respective à travers une certaine largeur de bande. La tâche principale d'un récepteur radiométrique est de mesurer la puissance de cette radiation, ce qui, dans la plupart des cas, est effectué à l'aide d'une diode détecteur qui convertit la puissance reçue à une tension DC. La puissance de la radiation incidente peut être soit mesurée directement à la fréquence RF, ce qui est connu sous le nom d'un récepteur à conversion directe, ou bien peut être préalablement convertie à une fréquence intermédiaire, ce qui permet de rendre l'amplification et la détection plus faciles et moins chers à réaliser, comme il est le cas dans un récepteur hétérodyne. Dans le projet proposé, cette dernière technique est appliquée, utilisant le mélangeur auto-oscillant subharmonique qui a été développé dans l'étape précédente pour la conversion.

Dans la radiométrie, des nombreux types de récepteurs ont été proposés. Le type le plus élémentaire se nomme radiomètre à puissance totale. Il est utilisé pour capter la puissance totale de la radiation incidente, tel que démontré dans la Figure 0.3, en amplifiant tout simplement la radiation incidente jusqu'à un niveau adéquat, en convertissant ensuite le signal à une fréquence intermédiaire, puis en détectant la puissance du signal avec une diode de détecteur. L'intégration à travers le temps offre une moyenne de la puissance mesurée et améliore ainsi la sensibilité. Certains types de récepteurs plus complexes incluent le radiomètre de Dicke, qui est utilisé à calibrer automatiquement le récepteur et à éliminer l'influence des fluctuations de gain et de température, ainsi que des nombreux autres récepteurs plus évolués.

Le but de cette thèse de doctorat étant la preuve de concept d'un système d'imagerie basé sur les mélangeurs auto-oscillants, le type de récepteur le plus élémentaire est réalisé: le radiomètre à puissance totale.

Dans le développement des récepteurs de radiométrie, il est très important de considérer différents facteurs qui influencent la performance. Un radiomètre mesure sa radiation incidente dans la forme de puissance de bruit, qui s'ajoute au bruit interne du système du récepteur. En considérant cet aspect, il devient clair qu'un des paramètres clés dans un récepteur de radiomètre est sa sensibilité, qui est défini comme le signal incident égal à la valeur effective des fluctuations de la sortie causé par le bruit interne du système. Cette valeur est habituellement donnée en Kelvin. La sensibilité augmente 1) avec une largeur de

bande plus grande à cause de la quantité de bruit plus grande accumulée; 2) avec une figure de bruit de récepteur plus basse car il réduit le bruit interne du système; 3) avec le gain du système car la radiation incidente est plus fortement amplifiée; 4) le temps d'intégration car le calcul de la moyenne de la puissance de bruit accumulé élimine le bruit du système encore plus. La sensibilité théorique représente seulement des limites de base. Celle-ci est dégradée encore par des fluctuations de gain, l'efficacité des antennes, et d'autres pertes dans le système. Ainsi, pour la conception de notre système entier, il n'est pas seulement important d'atteindre un niveau de bruit faible, un gain élevé et une large bande, mais il est aussi essentiel de minimiser les pertes autant que possible.

La procédure de conception pour cette thèse de doctorat a été réalisée en développant une antenne appropriée, suivie par la conception d'une escale d'amplificateur à faible bruit, et leur intégration avec le mélangeur auto-oscillant et les éléments à fréquence intermédiaire.

LA RÉALISATION D'UN SYSTÈME MÉCANIQUE D'IMAGERIE COMPLET

Cette étape inclut l'intégration du module d'un simple récepteur présenté dans un système d'imagerie à ondes millimétriques à 35 GHz.

Différents techniques permettent d'obtenir une image passive radiométrique d'une scène. Premièrement, un récepteur simple peut être scanné à travers une scène afin de former l'image (Figure 0.3). Dans ce type de récepteur, la radiation est focalisée sur le récepteur avec soit des réflecteurs paraboliques ou des lentilles diélectriques, et l'image est formée par soit un mouvement du détecteur dans son plan focal ou en balayant mécaniquement ou électriquement la direction du faisceau du système.

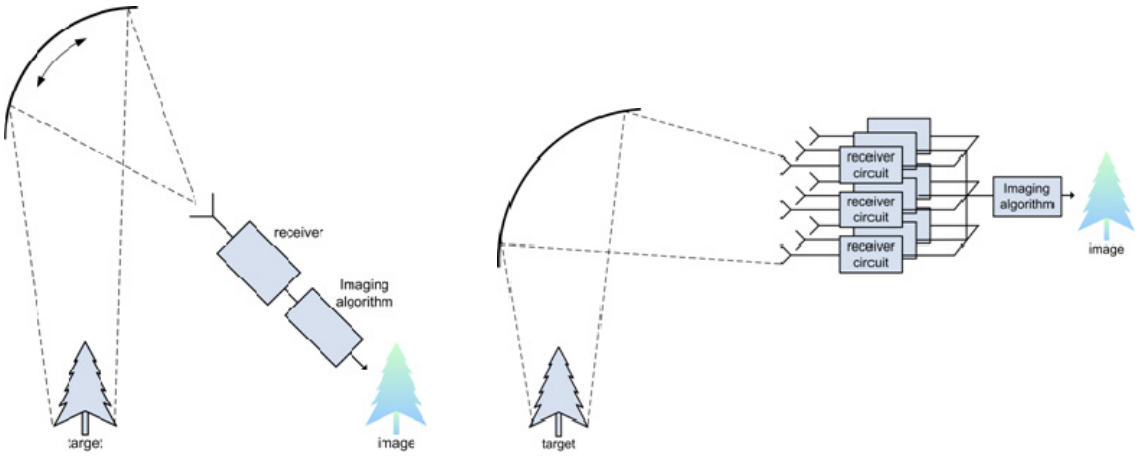

(a) (b)

Figure 0.3 Comparaison des techniques d'acquisition d'image: a) imagerie en utilisant un seul récepteur à balayage mécanique; b) réseau à plan focal utilisé pour l'imagerie à faisceaux multiples.

Une autre manière d'acquérir une image à ondes millimétriques est la réalisation d'un réseau à plan focal, qui utilise un réseau d'éléments de détection indépendants dans la surface d'une lentille ou d'un réflecteur d'imagerie (Figure 0.3). Finalement, des systèmes de réseau de phase peuvent être utilisés pour l'imagerie à ondes millimétriques qui effectuent un scan électronique de la scène d'intérêt, mais un faible niveau de succès a été atteint pour ceux-ci à cause de leur conception difficile et complexe.

L'utilité des systèmes mécaniques a été prouvée pour un grand nombre d'applications d'imagerie, mais ceux-ci souffrent de leur grand taille et de leur vitesse d'acquisition de données lente, compliquant ainsi leur déploiement dans des applications en temps réel. La solution équivalente plus sophistiquée qui utilise un mécanisme à balayage électronique a jusqu'à présent été une solution complexe surtout aux fréquences des ondes millimétriques. Les récepteurs à réseau à plan focal représentent l'architecture de choix du futur pour des systèmes d'imagerie commerciaux mais souffrent encore d'inconvénients en termes de coût et complexité dans des systèmes utilisant un large nombre de pixels ainsi qu'une large consommation d'énergie et le problème de la dissipation de chaleur associé

qui ont été décrits précédemment. Ainsi, récemment, plusieurs essais ont été réalisés afin de combiner des petits réseaux à plan focal avec une procédure de balayage afin de former un système à faible coût qui permet tout-de-même une acquisition de données en temps réel.

Le but de cette thèse est le développement d'un premier système à balayage mécanique basé sur la technique des mélangeurs auto-oscillants étant utilisés pour développer de l'expérience expérimentale dans les mesures radiométriques, faisant partie intégrante d'un système d'imagerie à ondes millimétriques basé sur un réseau à plan focal.

Un autre aspect très intéressant de cette thèse est le développement d'un système d'imagerie à plusieurs polarisations. L'utilisation de polarimétrie ajoute une dimension supplémentaire à l'acquisition des données d'imagerie.

Essentiellement, la radiation naturelle radiométrique n'est pas polarisée, mais la réfraction et la réflexion des médias et des objets introduit la polarisation, qui peut être exploité afin de pouvoir distinguer entre les objets qui émettent de la radiation électromagnétique naturellement par eux-mêmes et les objets qui réfléchissent la radiation qui émerge d'autres sources de la scène, comme c'est souvent le cas avec des réflexions du ciel radiométriquement froid. Les paramètres Stokes représentent une technique permettant de caractériser ces effets de polarisation. Certainement, le système d'imagerie envisagé doit être adapté afin de fonctionner comme un système à plusieurs polarisations. Les antennes Vivaldi croisées avec une architecture antipodale miroir permettent de réaliser un tel système afin d'étendre le réseau à plan focal à polarisation linéaire versus un système multi-polarisations. L'antenne Vivaldi et son extension à un réseau à deux dimensions est illustré par la Figure 0.4. Une autre possibilité est l'utilisation d'une surface sélective aux fréquences, comme il peut séparer la radiation incidente dans une onde à polarisation horizontale et une onde à polarisation verticale pour les signaux réfléchis et transmis.

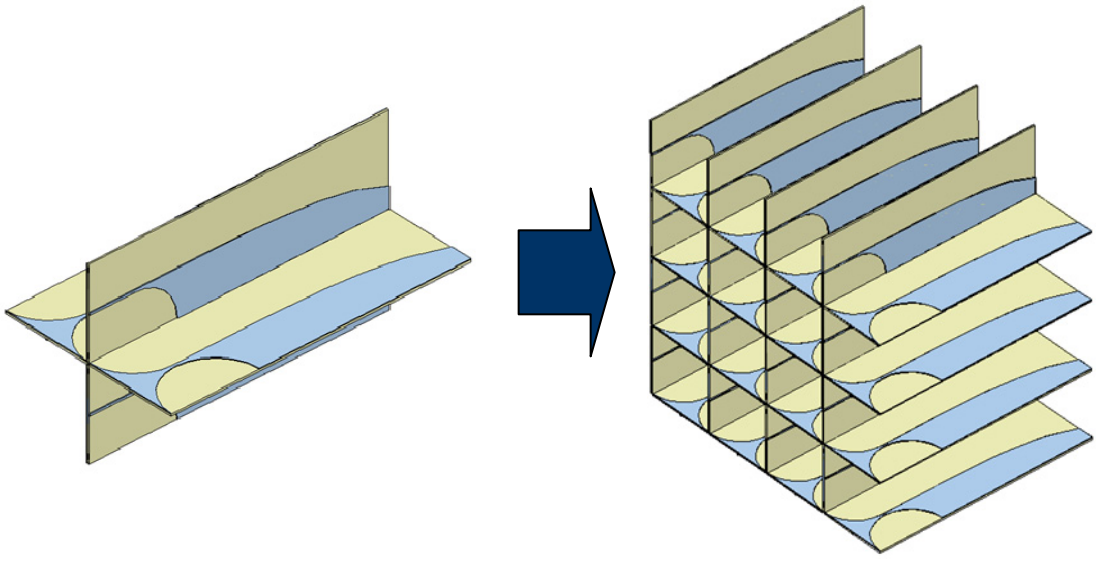

(a) (b)

Figure 0.4 Concept of dual-polarization Vivaldi antenna: a) 4-element Vivaldi antenna employing dual polarization; b) integration into a multibeam array.

Dans la thèse présentée, une telle surface sélective aux fréquences est construite et testée, et sert comme un test de futur pour la polarisation de deux orientations du système d'imagerie proposé.

TABLE DES MATIÈRES

LISTE DE TABLEAUX

LISTE DE FIGURES

LISTE DES SIGLES ET ABRÉVIATIONS

ABBREVIATION	DENOTATION
ADC	Analog Digital Converter
ADS	Advanced Design System
AM	Amplitude Modulation
BI-RME	Boundary Integral Resonant Mode Expansion
CAD	Computer Aided Design
CPW	Coplanar Waveguide
DC	Direct Current
DSP	Digital Signal Processor
EM	Electromagnetics
IF	Intermediate Frequency
FDTD	Frequency Domain Time Domain
FEM	Finite Element Method
FET	Field-Effect Transistor
FPA	Focal Plane Array
FSS	Frequency Selective Surface
GaAs	Gallium Arsenide
HB	Harmonic Balance
HFSS	High Frequency Structural Simulator
HPBW	Half-Power Beamwidth
IMD	Intermodulation Distortion
IR	Infrared
LNA	Low Noise Amplifier
LO	Local Oscillator
MHMIC	Miniature Hybrid Microwave Integrated Circuit
MoM	Method of Moments
MMIC	Monolithic Microwave Integrated Circuit
NETD	Noise Equivalent Temperature Difference
pHEMT	Pseudomorphic High Electron Mobility Transistor
PC	Personal Computer
PCB	Printed Circuit Board
RF	Radio Frequency
SGH	Standard Gain Horn
SIW	Substrate Integrated Waveguide
SOM	Self-Oscillating Mixer
SoS	System on Substrate
TE	Transverse Electric
TM	Transverse Magnetic
TOI	Third-Order Intercept Point
TSA	Tapered Slot Array

Chapter 1

INTRODUCTION

The broad topic of the presented Ph.D. thesis consists in the research on novel methods in the field of microwave imaging, in particular the so-called passive millimetre-wave imaging, which is also referred to as radiometric imaging. This latter technique is used to form an image of a particular scene by means of sensing the natural electromagnetic radiation emitted by any object at microwave / millimetre-wave wavelengths, similar to the way in which a photograph is captured by sensing the radiation occurring at optical wavelengths. In this way, different characteristics of the observed scene or object, which are inherent to the microwave / millimetre-wave frequency range, can be mapped in the form of an image.

Millimetre-wave imaging represents one of today's most promising research topics in the field of high frequency sensor design. The usefulness of this technique lies in particular in the peculiarities of atmospheric attenuation phenomenologies allowing millimetre-waves to penetrate through a variety of low-visibility conditions such as haze, fog, clouds, smoke, and sandstorms and furthermore in the ability to propagate through clothing and a number of other materials. Together with these advantages over infrared (IR) and optical systems, moreover, millimetre-wave systems outperform imagers at the lower microwave frequency range due to their smaller wavelengths and the thus achievable higher resolution. For their implementation, propagation windows at 35, 77, 94, 140, and 220 GHz are generally allocated [1]–[4].

Present and future applications consist in both military and commercial infrastructure fields such as in surveillance, navigation, automotive technology, and precision targeting, as well as aircraft landing or highway traffic monitoring in fog. Moreover, the ever increasing demand for security screening systems at airports and other public environments creates a growing need for health-hazardless automated real-time scanners with minimized false alarms, and millimetre-wave imaging offering the ability to detect concealed weapons or hazardous objects through clothing material represents an excellent

choice for this purpose. Furthermore, millimetre-wave imaging is applied to biomedical imaging such as the location of hot spots, tumours, or other anomalies in the body. Additional applications consist in non-destructive material testing and geological examinations such as the sensing of the Earth's atmosphere, oil spill detection, research on volcano activity, or meteorology.

The development of such high-performance millimetre-wave imaging systems presents a great technological challenge and a number of recent systems have been demonstrated. The acquisition of a millimetre-wave image can be performed in several ways, with the simplest but also slowest method being a mechanical *x*-*y* raster scan of the area of interest using a single receiver [5]–[9] as opposed to a focal plane array (FPA) system employing an array of many entirely independent detector elements in the focal surface of an imaging lens or reflector working in parallel and therefore at higher and often real-time acquisition speed [10]–[13]. Some systems also employ a more cost-effective combination of both methods [14]–[16], and the currently less employed and more complex phased-array approach [17] represents another possibility for the acquisition of a millimetre-wave image.

However, present state-of-the-art systems almost always require a trade-off between cost-intensive real-time FPA imagers and lower-cost bulkier and slower mechanical scanning systems. Currently, a number of technological limitations are encountered in the design of receivers operating at millimetre frequencies. LNAs at millimetre-wave frequencies are cost-intensive and subject to high power consumption due to their low efficiency, which results in a heat dissipation problem especially for compact-size high-density FPAs with a large number of parallel receiver channels. Avoiding this problem by using a heterodyne receiver requires the use of external local oscillators (LO) with adequate power, which, once again, introduces a difficult and cost-intensive design at high frequencies [18] and moreover increases circuit size as an external LO has to be implemented on each receiver element.

Consequently, future research aims for the development of cost-effective, compact size high-frequency real-time FPA systems overcoming these limitations. A novel approach consists in the use of so-called self-oscillating mixers (SOMs) [19] in high-frequency heterodyne millimetre-wave imaging receivers. SOMs are excellent choices for such a

design as both the oscillating source and the mixer are combined in one single device. In addition to the reduction in component number, they offer numerous advantages such as their lower power consumption and the possibility of simple and straight-forward integration into MMICs.

An extension to the standard SOM technique is given by subharmonic operation [20]–[24]: instead of mixing the incoming millimetre-wave radio frequency (RF) signal with the fundamental LO frequency, a harmonic of the LO frequency is used.

In this way, the limitations of current FPA systems may be overcome, as on one hand, a more efficient heterodyne receiver can be used with the external LO being integrated in the mixer, which simultaneously solves the previously mentioned heat dissipation and circuit size problem. On the other hand, adequate LO power can be generated by employing subharmonic operation, thus generating the LO signal at a frequency of only a fraction of the RF input, where its generation is much more unproblematic.

In this project, a complete passive millimetre-wave imager at 35 GHz based on the previously described subharmonic SOM technique is proposed. The research work in this Ph.D. thesis focuses in particular on the design, implementation, and experimental testing of subharmonic SOMs. The final 35 GHz SOM circuit is eventually implemented into a straight-forward mechanical raster scanning imaging system based on a single-element receiver in order to prove functionality of the SOM technique in the framework of millimetre-wave imaging systems. This first millimetre-wave imaging test-bed serves as the base for future research in the field. Future work includes the parallelization of these receivers in the form of an FPA system such as shown in Figure 1.1, and also the task of pushing the design toward higher frequencies, in particular 94 GHz, for achieving higher image resolutions and more compact-sized imagers.

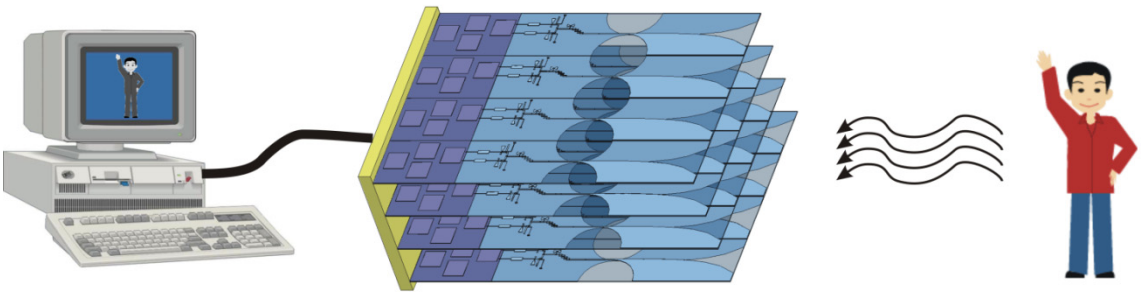

Figure 1.1 Proposed FPA multibeam imaging system: The naturally emitted electromagnetic radiation of an object is received by a high-sensitive FPA receiver. Subsequently, the baseband IF signals are evaluated in a PC or DSP based system.

The presented work has been carried out in three major design steps with 1) the extensive research on SOMs and their subharmonic implementation, 2) the development of a single-element receiver based on the successfully implemented subharmonic SOM design, and 3) the integration of the receiver into a complete mechanical scanning imaging system at 35 GHz.

1.1 SUBHARMONIC SELF-OSCILLATING MIXER DESIGN

The first design step and at the same time the main focus of the presented Ph.D. thesis is concerned with the extensive research on millimetre-wave SOMs and their subharmonic counterparts in theory and experiment. A detailed investigation on their design, on specific techniques for their simulation and analysis, appropriate measurement techniques for assessing their performance, and their practical applicability in a variety of application scenarios is carried out, always keeping in mind their eventual implementation into a passive millimetre-wave system and optimizing performance and design parameters toward this final application.

As previously mentioned, SOMs represent excellent choices for the development of low-cost and compact imaging radiometer receiver architectures due to the combination of both the oscillating source and the mixer into one single device as shown for the example of a total power radiometer receiver in Figure 1.2, resulting in a reduced component

number, lower power consumption, and the possibility of easy integration into microwave monolithic integrated circuits (MMICs). In previous works throughout the past decades, SOMs have been implemented using both diodes and transistors. However, the capability of obtaining conversion gain using transistors as the active devices and their recent technological development well into the millimetre-wave region has promoted them to the mainly used devices for SOM design. The first FET SOM was presented in [19].

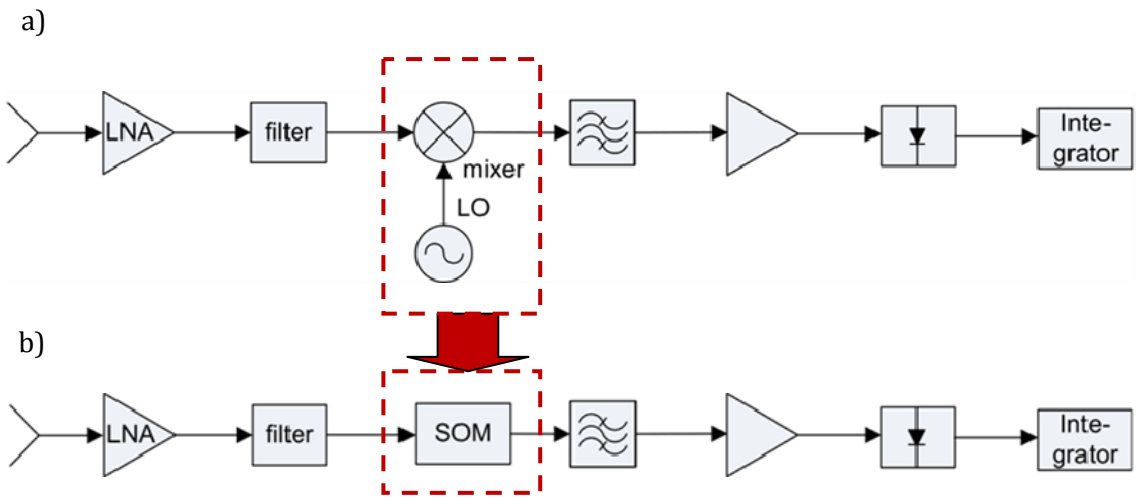

Figure 1.2 a) Total power radiometer receiver structure, b) substitution of conventional mixer by an SOM.

As outlined earlier, an extension to the standard SOM technique is given by subharmonic operation [20]–[24] being especially convenient for applications in the range of millimetre-waves. Using this technique, transistor gain has to occur only until the fundamental LO frequency, which drastically lowers the transistor maximum frequency (f_{max}) requirements [22] and thus represents an excellent choice for the design of millimetre-wave systems as explained previously.

Subharmonic operation can be easily implemented with the help of a balanced structure [23]–[27], as in this way on the one hand either even- or odd-order mixing products can be easily enhanced and on the other hand certain other unwanted mixing products can be eliminated from the IF output. In addition, balanced structures offer inherent RF-LO isolation as well as a number of other important advantages such as lower AM noise,

suppression of unwanted harmonics, etc. Furthermore, the input does not have to be matched both at LO and RF frequencies, which simplifies the input matching requirements.
For the successful design of such a subharmonic SOM structure, a number of important considerations have to be taken into account in order to achieve a high-performance system-implementable circuit architecture.
First of all, the selection of transistor technology is an important design point: the devices that have been used in the presented SOM design are GaAs pHEMT transistors offering low noise characteristics and millimetre-wave frequency operation capability.
Another very important consideration is the use of adequate simulation and analysis tools for correctly predicting the performance of the proposed SOMs. Using standard Harmonic Balance (HB) methods, it is not straight-forward to analyze SOM circuits because of their autonomous operation nature. In general, standard RF circuit simulators must be adapted in certain ways in order to be able to simulate these structures [54], [55]. Moreover, specific simulation algorithms may have to be worked out that adapt well to the special characteristics of SOM circuits. In the presented Ph.D. thesis, these simulation aspects have been considered and included in the design procedure, and a new simulation algorithm has been established in addition.
For the purpose of an accurate analysis and design procedure it is also important to use an appropriate transistor model of the device employed in the SOM design. As this is a weak point for many commercially available devices, transistor modeling becomes an important part of the optimization and development of the proposed SOM circuit.
The performance of SOM circuits can be assessed in the form of the combined performance parameters of mixers and oscillators. In detail, special attention needs to be paid to conversion gain, bandwidth, and noise figure, but also toward oscillation frequency drift and phase noise. The work presented here includes a detailed investigation about performance modeling of subharmonic SOMs.
Moreover, in order to save time and cost in the course of the circuit design, it is advisable to proof the proposed concept with the help of a low-frequency prototype beforehand. A subsequent scaling into the millimetre-wave frequencies is then easier and may be based on the many results obtained from the low-frequency experiments. This is especially important, as at millimetre-wave frequencies it is necessary to provide good prediction

methods for analyzing circuit behaviour and performance due to the mostly very expensive and time-consuming fabrication procedures. Moreover, low-frequency prototypes offer an easy reconfigurability as they employ discrete components that can be easily exchanged and hence an easier experimental parametric analysis as opposed to fixed geometrically determined distributed printed elements being employed in higher-frequency millimetre-wave structures. For this reason, the SOM design in the presented thesis has been divided into two major steps based on the development of a low-frequency microwave prototype as a first step that is subsequently scaled into the millimetre-wave region, i.e. to 35 GHz for this thesis, as the second and final design step.

1.2 Development of a Self-Oscillating Mixing radiometry receiver

In this design step, a receiver prototype on the basis of the previously developed subharmonic SOM has been fabricated at a frequency of 35 GHz.

A radiometric receiver measures the incoming passive radiometric radiation emitted from an object by using an antenna, which can receive the respective radiation over a certain bandwidth. The main task of a radiometric receiver is to measure the power of this radiation, which in most cases is carried out by a square-law detector diode converting the received RF power to a DC voltage. The power of the incoming radiation can be either measured directly at the RF frequency, which is referred to as a direct-conversion receiver, or it can be downconverted to an IF frequency beforehand, where amplification and detection becomes easier and less costly to realize, such as in a heterodyne receiver. In the proposed project, the latter technique is used, employing the previously described subharmonic SOM as a downconverting element.

In radiometry, various types of receivers have been proposed, with the most basic type being the so-called total power radiometer. It is used to sense the total power of the incoming radiation as shown in Figure 1.2 by simply amplifying the incoming radiation to an adequate level, downconverting it to IF frequency and then detecting the signal power with a square-law detector. Integration over time provides averaging of the measured

power and thus enhances sensitivity. Enhanced receiver types include the Dicke radiometer, which is used to automatically calibrate the receiver and eliminate the influence of gain and temperature fluctuations, as well as numerous other, more complex types of radiometer receivers [30].

The purpose of this Ph.D. thesis being the proof of concept of an SOM-based radiometric imaging system, the most straight-forward receiver type, i.e. the total power radiometer receiver, is selected and implemented.

In the development of radiometer receivers, it is very important to consider different factors that affect performance. A radiometer measures its incident radiation in the form of noise power, which adds up to the internal system noise of the receiver. Considering this aspect, it becomes clear that one of the key parameters in a radiometer receiver is its sensitivity, which is defined as the incident signal that is just equal to the effective value of the output fluctuations due to the internal system noise. This value is usually given in Kelvin. Sensitivity increases 1) with larger bandwidth due to the higher noise quantity collected; 2) with a lower receiver noise figure as it reduces the internal system noise; 3) with the system gain as the incident radiation is amplified more; and 4) the integration time as averaging over the collected noise power eliminates the system noise further. The theoretical sensitivity [30] only represents lower limits, which are further degraded by gain fluctuations, antenna efficiency, and other system losses. Thus, for our overall system design it is not only important to achieve a low noise, high gain, and broadband design but it is also essential to minimize losses as far as possible.

The practical design considerations for this design step include the antenna requirements, which are mostly determined by the specified imaging performance such as spatial resolution, as well as the characteristics of the LNA employed in the design. The antenna simulations were carried out with commercial simulators such as Ansoft HFSS and a prototype was fabricated and measured in an anechoic chamber environment fully available at the Poly-Grames Research center. Furthermore, the IF circuitry consisting of the IF amplifier stage, power detector, and integrator was realized by commercially available components. The entire receiver stage can be simulated on a block diagram level and its functionality will be verified by performance measurements.

The design procedure for this Ph.D. thesis has been carried out developing an appropriate antenna, followed by the design of a high-quality LNA stage, and its subsequent integration with the SOM and the IF circuitry elements.

1.3 COMPLETE MECHANICAL IMAGING SYSTEM IMPLEMENTATION

This design step involves the integration of the presented single receiver module into a complete millimetre-wave imaging system at 35 GHz.

There are a number different ways to obtain a passive radiometric image from a scene. First, a single focused receiver can be raster scanned across the scene to form the image (Figure 1.3a). In this type of receiver, the radiation is focused onto the receiver with either parabolic reflectors or dielectric lenses, and the image is formed by either moving a detector in its focal plane or by mechanically or electrically scanning the beam direction of the system [5]–[9].

Another way of acquiring a millimetre-wave image is the implementation of an FPA, which uses an array of independent detector elements in the focal surface of an imaging lens or reflector (Figure 1.3b). Finally, phased array systems can be employed for millimetre-wave imaging [17] performing an electronic scan of the area of interest, but have been limited in their success due to the very complex and difficult design.

Mechanical systems have been proven useful for a number of millimetre-wave imaging applications but usually suffer from bulky size and a low data rate complicating real-time requirements. The more sophisticated equivalent solution employing an electrical scanning mechanism has up to date been complex solution especially at millimetre-wave frequencies [31], [32]. FPA receivers represent the future architecture of choice for commercial millimetre-wave imaging systems but still suffer from significant drawbacks in terms of cost and complexity inherent in systems employing large number of pixels as well as high power consumption and associated heat dissipation problem that were described earlier. Thus, recently, a number of attempts have been made to combine small FPAs with a scanning procedure in order to form a low-cost system that still allows for real-time processing [14]–[16].

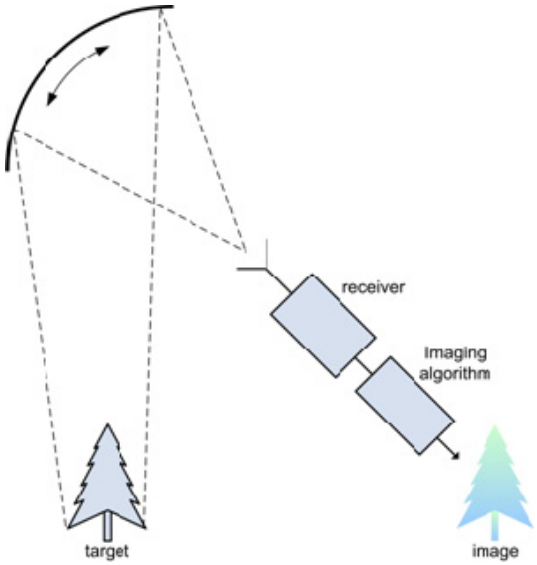

(a)

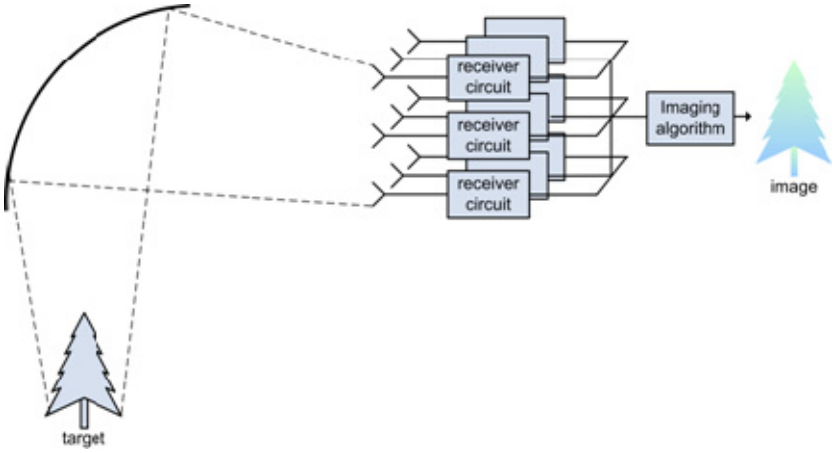

(b)

Figure 1.3 Comparison of image acquisition techniques: a) single-receiver imaging with mechanical scanning; b) FPA multibeam based imaging.

The purpose of this thesis is to develop a first basic mechanically scanning imaging system test-bed based on the SOM technique being used for assessing feasibility and developing

experimental experience in radiometric measurement, which can then be extended in the future to an FPA based millimetre-wave system.

A further very interesting innovative aspect lies in the development of a multi-polarization millimetre-wave imaging system [43], [44]. The use of polarimetry adds an extra dimension to the acquisition of imaging data.

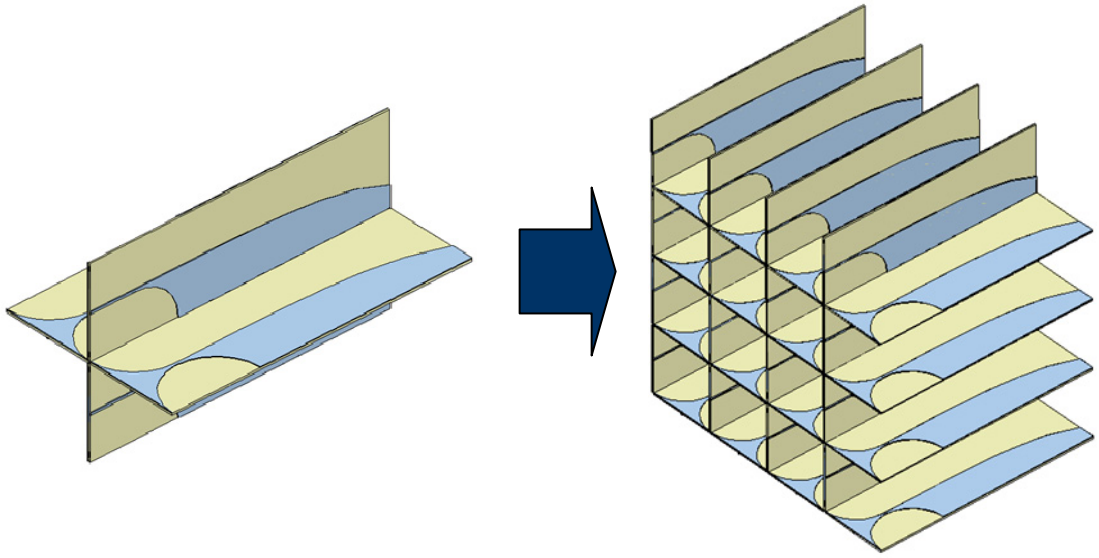

(a) (b)

Figure 1.4 Concept of dual-polarization Vivaldi antenna: a) 4-element Vivaldi antenna employing dual polarization; b) integration into a multibeam array.

Essentially, natural background millimetre-wave radiation is unpolarized, but refraction and reflection from media and objects introduces polarization, which can be exploited in order to distinguish between objects naturally emitting electromagnetic radiation by themselves and objects reflecting the radiation emerging from other sources of the scene such as it happens very often with reflections from the radiometrically cold sky. A means to characterize these polarization effects is given by the Stokes parameters [30]. Certainly, the envisioned imaging system needs to be adapted in order to function as a multi-polarization system. One way to realize such a system is to use a crossed Vivaldi structure

[41] with mirrored antipodal architecture [42] in order to extend our linearly-polarized FPA millimetre-wave imager towards a multi-polarization system. The dual-polarized Vivaldi antenna and its extension to a 2-D array are shown in Figure 1.4. Another possibility is the use of a polarizing frequency selective surface (FSS), as it may separate the incoming radiation into a horizontally and vertically polarized wave for reflected and transmitted energy.
In the presented thesis, such a polarization rotating FSS is built and tested, and serves for a future dual-polarization test of the proposed imaging system.

1.4 NOVEL CONTRIBUTIONS PROVIDED IN THIS PH.D. THESIS

Summarizing the previous sections, the main novel contributions realized in this thesis work are outlined in the following sections.

1.4.1 Development of a high-order self-oscillating mixing technique

The authors present for the first time a high-order SOM concept using FETs. It pushes the state-of-the-art beyond second order mixing, and mixing orders of 3rd and 4th order are presented in theory, simulation, and experiment.

1.4.2 Ultra-high order self-oscillating mixing technique

An ultra-high order SOM technique is presented being able to realize arbitrary mixing orders by combining several lower-order SOMs. The theory is presented mathematically, and a prototype is built to validate the idea.

1.4.3 Simulation techniques specific to self-oscillating mixing

Observing the lack of straightforward methods applicable to the case of the nonlinear phenomena in SOMs, a new technique is presented, which combines Volterra series and conversion matrix approaches in order to form a new method for simulation of SOMs and their subharmonic counterparts.

1.4.4 Self-oscillating mixing based imaging system

The presented Ph.D. thesis pushes towards the realization of an SOM based imaging system. Using an SOM for imaging array systems allows for drastic reduction in power consumption, heat generation, cost, and size restrictions.

1.4.5 Frequency selective surface

For the first time, an FSS, which is capable of rotating the polarization of an incident wave is presented in SIW technology. The structure finds suitable application in the proposed imaging system for multi-polarization purposes.

Chapter 2

RADIOMETRY AND MILLIMETRE-WAVE IMAGING

This chapter introduces the general concept of radiometry and its physical background. It describes the peculiarities of atmospheric attenuation and how they can be exploited in passive millimetre-wave imaging. The chapter concludes with a set of application scenarios, in which passive millimetre-wave imaging can be used.

2.1 INTRODUCTION

A radiometer is a device measuring the microwave/millimetre-wave portion of black-body radiation. Any object in nature emits this type of radiation, and its spectral frequency response depends primarily on the temperature of the object and its surface characteristics. Based on this physical phenomenon, it is possible to develop a radiometer receiver that is able to measure the temperature, to distinguish between different materials, etc. Figure 2.1 shows the concept of a radiometer: the radiation emitted by an object/target is collected by a receiver circuit that extracts the desired radiation information of the received energy and measures its power.

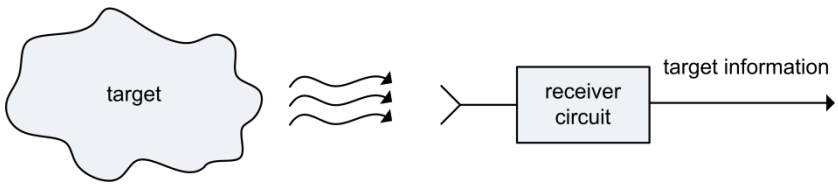

Figure 2.1 Concept of a radiometer system.

Radiometric radiation as being related to black-body radiation occurs in the form of noise, whose intensity depends on the temperature of the radiating object. In the millimetre-wave regime, the available spectral noise power density of an object differs from its noise temperature T only by a proportional constant:

$$S(f) = kT \tag{2.1}$$

Therefore the temperature fully defines the available noise spectral power. In this way it is not necessary to know the source of the noise, but only its spectrum:

$$P = kTB \tag{2.2}$$

with k as the Boltzmann's constant (k = 1.38 x 10^{-23}), T as the noise temperature and B as the bandwidth of observation.

2.2 MILLIMETRE-WAVE RADIOMETRY

The presented thesis concentrates on the detection of radiometric radiation in the frequency range of millimetre-waves. The usefulness of millimetre waves lies in the peculiarities of atmospheric attenuation phenomenologies over the prescribed frequency range. Figure 2.2 shows the attenuation of electromagnetic signals in decibels per kilometre of propagation path length from the microwave to the visible regime. Propagation of the electromagnetic waves over this frequency range is subject to continuum and resonant absorption by various atmospheric constituents, including water, oxygen, nitrogen, carbon dioxide, ozone, etc.

Atmospheric water content in the form of fog, clouds, and rain causes significant absorption and scattering. In the far IR and submillimetre-wave regime significant attenuation occurs from water vapour, while in the millimetre-wave regime there are propagation windows at 35, 94, 140, and 220 GHz, where the attenuation is relatively modest in both clear air and fog.

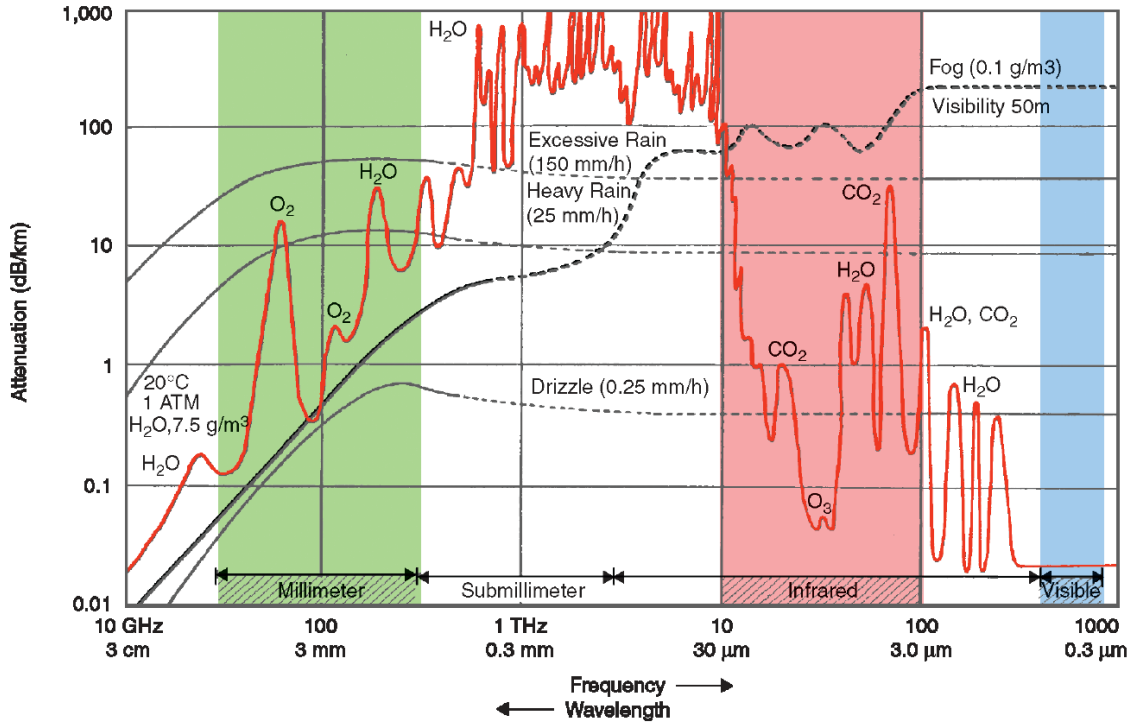

Figure 2.2 Atmospheric attenuation and attenuation of propagation for different weather conditions over the electromagnetic spectrum [48], [49].

Even taking into account the much higher blackbody radiation at IR and visible frequencies (Figure 2.3), millimetre-wave radiation is attenuated millions of times less in clouds, fog, smoke, snow, and sandstorms than visual or IR radiation (Figure 2.2). Moreover, millimetre-wave imagery is minimally affected by sun or artificial illumination.

Objects reflect and emit radiation in the millimetre-wave range, just as they do in the IR and visible range. The degree to which an object reflects or emits is characterized by the emissivity ε of the object. The blackbody is the perfect radiator and has ε = 1. A perfect reflector has ε = 0.

The emissivity of an object is a function of the dielectric properties of its constituents, its surface roughness, the angle of observation and it is polarization dependency. Emissivities for different materials at various frequencies, at normal incidence, and measured at one polarization are given in Table 2.1.

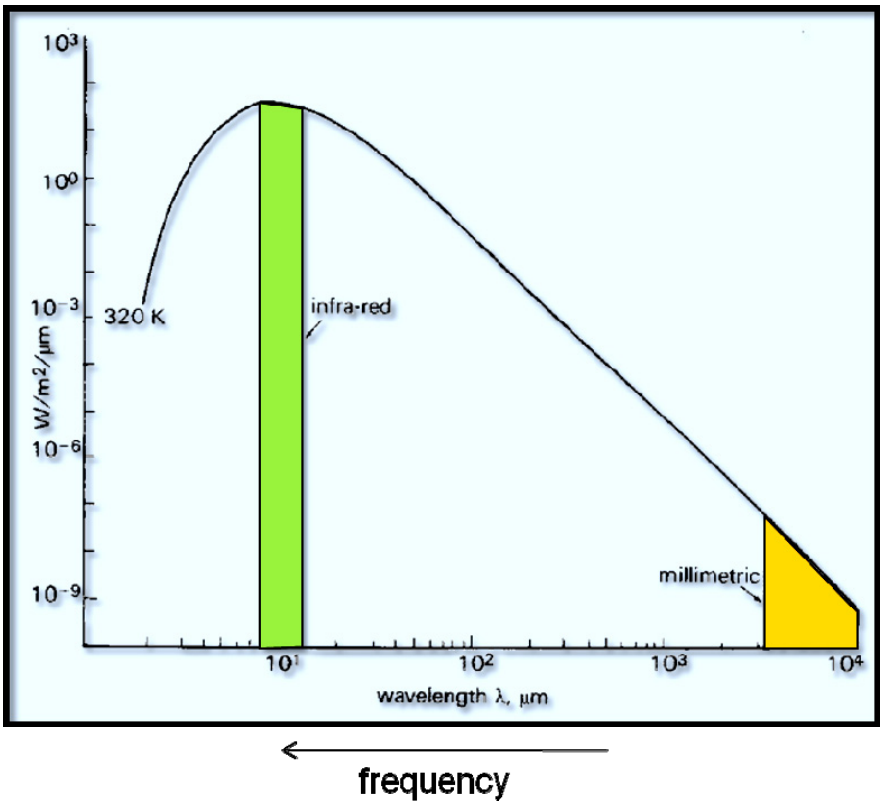

Figure 2.3 Intensity of black body radiation at a temperature of 320 K.

	Effective Emissivity		
Surface	**44 GHz**	**94 GHz**	**140 GHz**
Bare metal	0.01	0.04	0.06
Painted metal	0.03	0.10	0.12
Painted metal under canvas	0.18	0.24	0.30
Painted metal under camouflage	0.22	0.39	0.46
Dry gravel	0.88	0.92	0.96
Dry asphalt	0.89	0.91	0.94
Dry concrete	0.86	0.91	0.95
Smooth water	0.47	0.59	0.66
Rough or hard-packed dirt	1.00	1.00	1.00

Table 2.1 Effective emissivity for different materials [49].

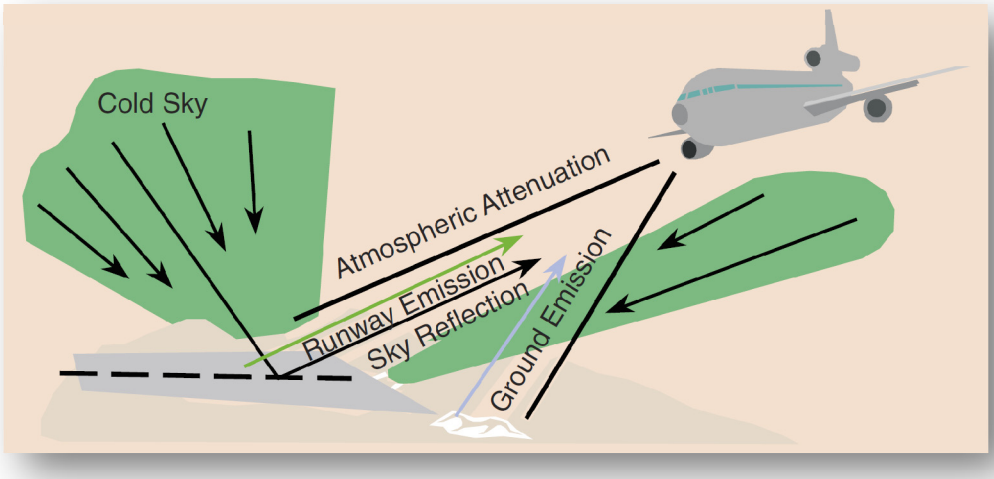

Figure 2.4 Measured radiated power consisting of different components of emitted and reflected radiation [49].

The variation in emissivity is an important factor in the generation of scene images by causing variations in the power radiated from different parts of the scene. In fact the radiation emitted by a non-ideal object in nature differs from an ideal black body. The radiometric temperature or surface brightness T_S of a non-ideal object is obtained multiplying its physical thermodynamic temperature T by its emissivity ε:

$$T_S = \varepsilon T \tag{2.3}$$

However, radiometric temperature is not the only factor involved: the way the scene is illuminated is critical in determining the way the scene actually looks. It is sufficient to observe that a perfect reflector ($T_S = 0$) will appear to have the radiometric temperature of whatever it is reflecting. This effect is taken into account by the surface scattered radiometric temperature T_{SC} defined as the product of the object reflectivity ρ and the radiometric temperature T_{ILL} of whatever happens to be illuminating it:

$$T_{SC} = \rho T_{illum} \tag{2.4}$$

Combining the terms T_S and T_{SC} gives the effective radiometric temperature T of the object:

$$T = T_S + T_{SC} \tag{2.5}$$

So, the power measured by the radiometer is that related with T_E:

$$P = kTB \tag{2.6}$$

The observed image is the result of the image contrast provided by differences in material, temperature, and sky illumination of the scene. The principal factors that affect the observed radiometric temperature of a scene are: emissions from scene constituents, reflections of the down-welling sky radiation by the scene, up-welling atmospheric emissions between the scene and the observer, and propagation of electromagnetic energy from the scene to the observer. This becomes clear when considering the situation in Figure 2.4, where different sources of radiation are emitted/reflected and sum up to the total measured radiated power.

2.3 IMAGING RADIOMETRY

A single-element radiometer receiver can be extended to form an imaging radiometer. As outlined in Chapter 1, there are various ways for acquiring a millimetre-wave image of a defined scene. As an example, Figure 2.5 depicts a block diagram of an FPA with a number of parallel receiver elements, each of them sensing one pixel of the scene of interest and hence forming an entire millimetre-wave image.

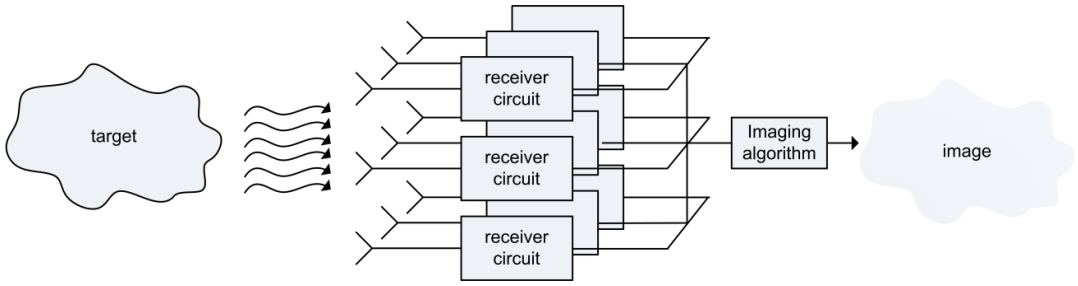

Figure 2.5 Concept of an imaging radiometer.

This thesis project aims for the development of an imaging system at a frequency of 35 GHz. As mentioned previously, the advantage of a design within this frequency range is that electromagnetic waves at this frequency can propagate through a variety of materials and under various problematic conditions, such as snow, fog, ice, and even some solid materials such as concrete or textiles. The higher the selected millimetre-wave imaging frequency, the higher the resolution of the produced image will be.

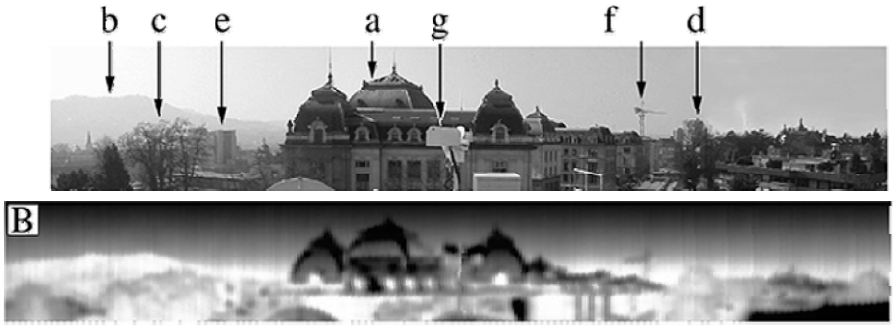

Figure 2.6 Example of a millimetre-wave 94 GHz radiometer image [8].

Figure 2.6 shows an image that has been taken by a radiometer at 94 GHz. Objects at higher temperature appear white, such as vegetation (trees, mountains, etc.), whereas cold objects are dark in the image. The concept of reflected radiation is very well visible in this example, as the metallic rooftops of the buildings in the image reflect the cold temperature of the sky. The formation of such millimetre-wave images add an extra dimension to the

information we can obtain from optical images. Using this technique, areas with different temperatures can be differentiated, such as the cold and warm regions in the photograph above, but also different materials can be identified and traced due to their different emissivities and hence different radiated power levels. This leads to a large number of possible application scenarios, as it is described in the next section.

2.4 APPLICATIONS

Present and future applications of passive millimetre-wave imaging consist in both military and commercial infrastructure fields and are widely gaining in popularity, especially with the development of real-time video-capable imagers. In the following, a selection of commercial and industrial applications are presented and documented along with image examples [49].

2.4.1 Aircraft landing and guidance

Figure 2.7 shows radiometric images compared with visible images acquired in both clear and foggy weather conditions. Darker shades in the radiometric images denote increasingly colder radiometric temperatures. The asphalt runway is brighter than the contour due to the fact that it reflects the sky at the horizon, which is warmer than the overhead sky.

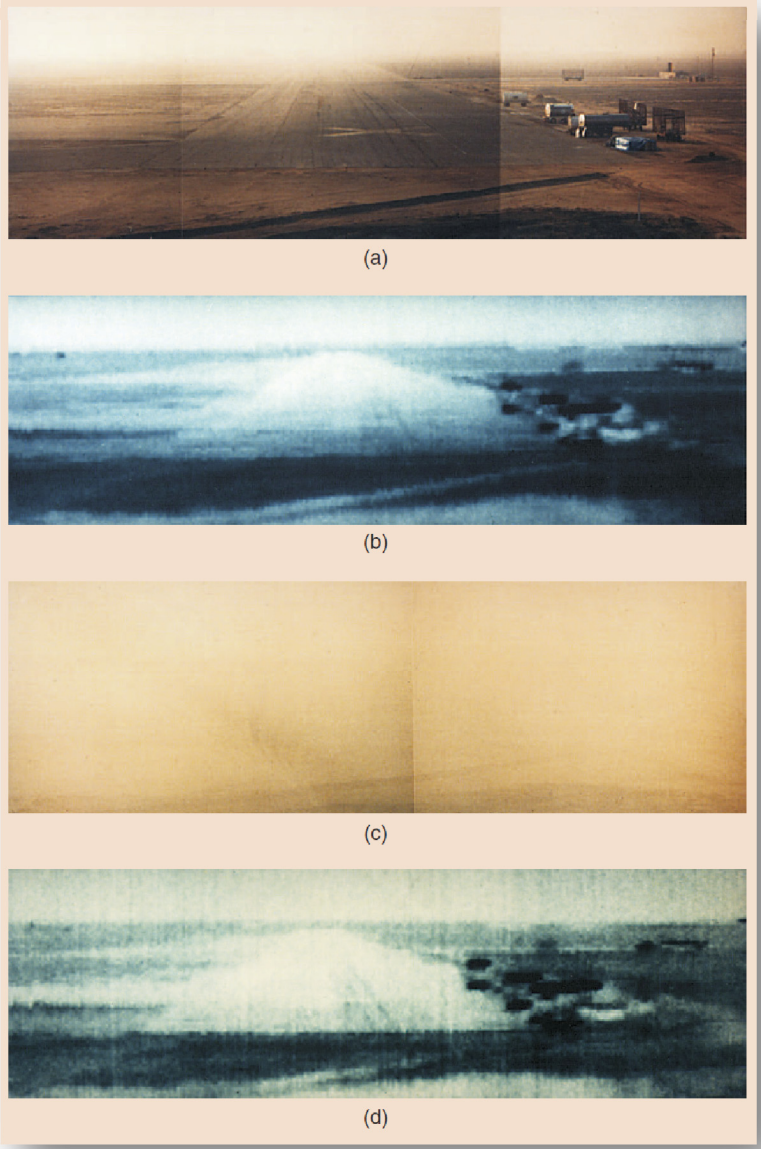

Figure 2.7 94 GHz image of a runway: a) and d) show optical images without and with fog, whereas b) and c) show millimetre-wave images without and with fog [49].

Comparing the images through fog it can be seen that the visual images are totally obscured, while the millimetre-wave image are nearly unaffected by the fog.

2.4.2 Navigation and transportation

An imaging system can be employed on patrol boats or ground vehicles to provide covert, near-all weather visibility for navigation, target location, and other enhanced vision needs, especially in fog and through marine cloud layers.

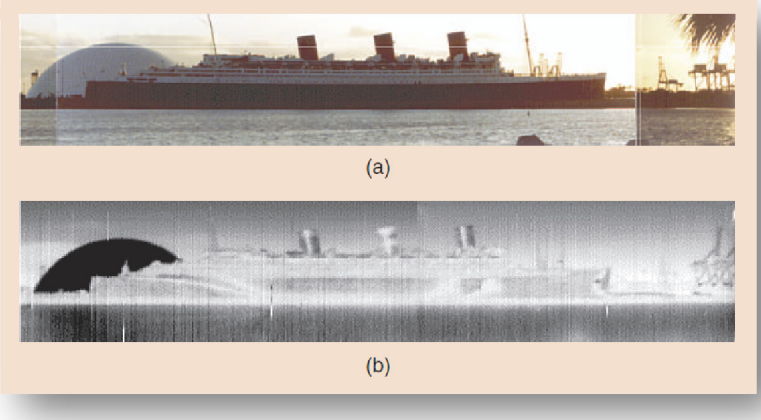

Figure 2.8 Near all-weather visibility for navigation at 94 GHz [49].

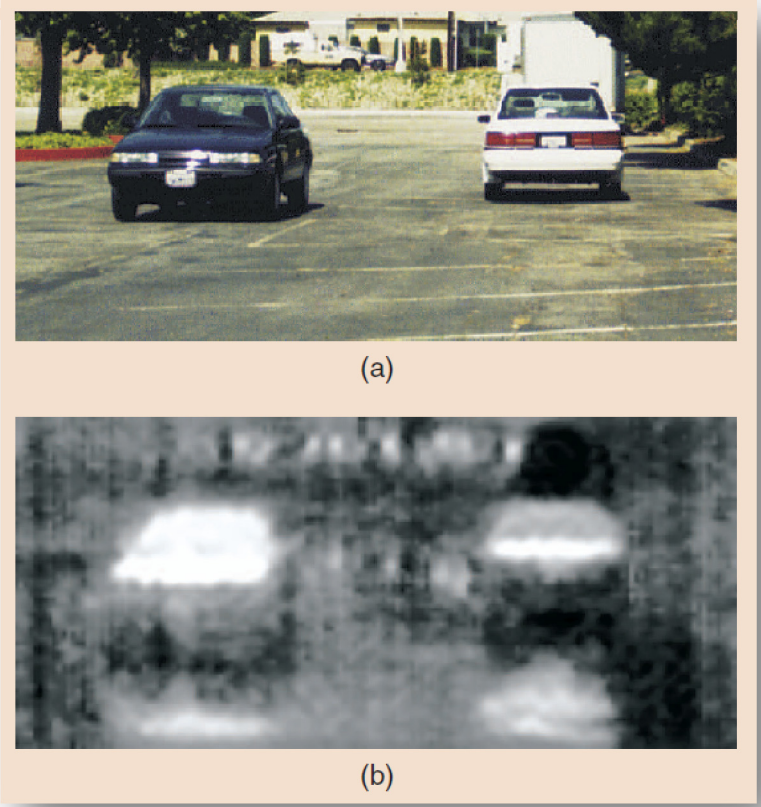

Figure 2.9 Millimeter-wave imaging applied to automotive tracking [49].

2.4.3 Medical applications

Passive millimetre-wave imaging is also applied to biomedical imaging such as for locating hot spots, tumours, or other anomalies in the body. As it is a non-invasive and passive method not requiring the use of any actively transmitted radiation, it represents a highly secure and health-hazardless method for the use in medical applications where strict standards for maximum radiation levels are required.

2.4.4 Surveillance, search, and rescue

View capability under low visibility conditions can be used for search and rescue or reconnaissance purposes. Detection of ship wakes, low radar cross-section boats, or other

vehicles are only a part of all the targets that can be identified for surveillance, searching or rescuing aims.

2.4.5 Geological applications

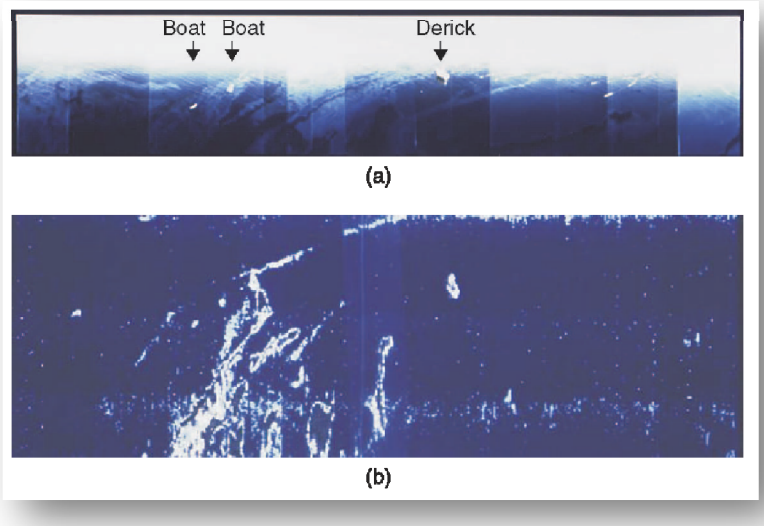

Figure 2.10 Oil-Spill detection [49].

Oil on water will produce a detectable change in the observed radiometric temperature in the milimeter-wave regime. In this frequency range the oil layer can increase or reduce the radiometric temperature of the areas where the oil patches are by varying the effective emissivity of those areas through change in thickness. The observed temperature can, in fact, be used to infer the thickness of the oil.

2.4.6 Security applications

Millimeter-waves can easily penetrate clothing and hair. The detected millimetre-wave radiation is a combination of the natural emissions from the body and reflections from the surroundings due to skin reflectivity. If an object is placed under the clothing that has a dielectric constant different than skin, the millimetre-wave image will reveal a radiometric temperature change caused by the object. Metallic or non metallic objects, such as plastics and ceramics can be seen.

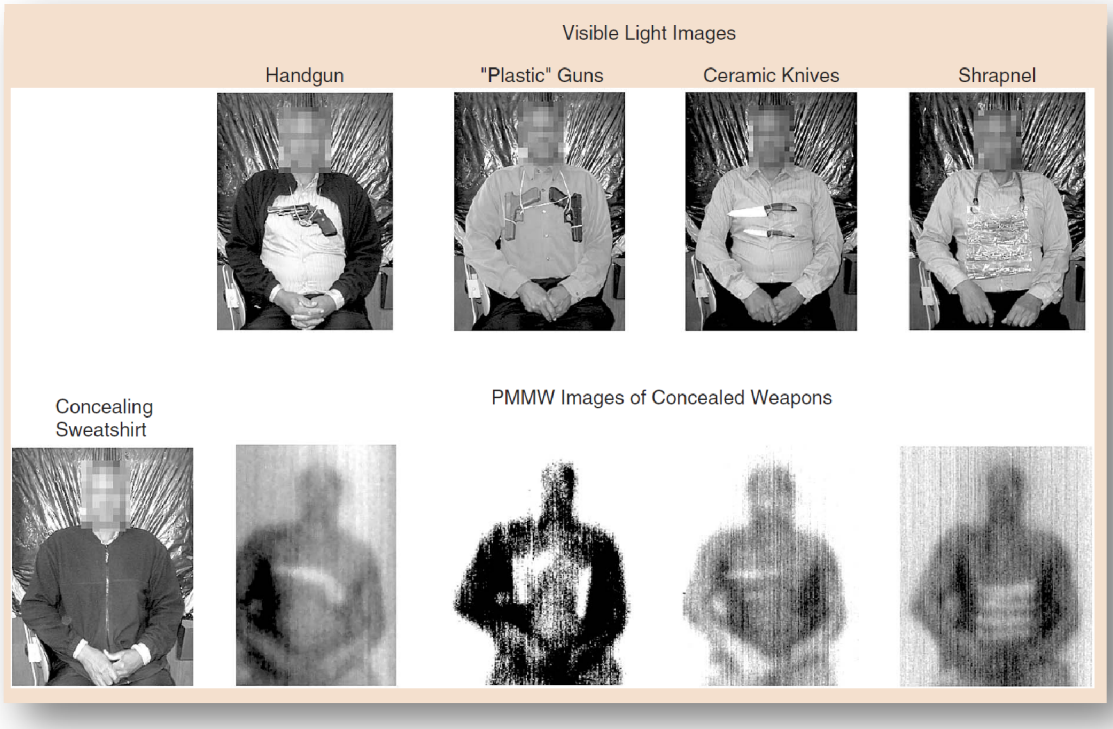

Figure 2.11 Concealed weapon detection [49].

2.4.7 Military applications

For ethical reasons, the author decides to exclude any description of military applications from the presented project.

2.5 Conclusions

This chapter has reviewed the physical background of radiometry, the peculiarities of millimetre-wave radiation and its propagation in atmosphere, as well as its usefulness for imaging systems. The chapter concludes with an outline of various possible application scenarios of high industrial and commercial importance.

Chapter 3

SELF-OSCILLATING MIXING TECHNIQUE

This chapter describes the first design step and at the same time the main focus of the presented Ph.D. thesis, which is concerned with the extensive research on millimetre-wave SOMs and their subharmonic counterparts. A detailed investigation on their design, on specific techniques for their simulation and analysis, appropriate measurement techniques for assessing their performance, and their practical applicability in a variety of application scenarios is carried out.

3.1 INTRODUCTION

Innovative millimetre-wave receiver designs in general and radiometer receivers in particular, demand for a variety of performance- and cost-related requirements including low power consumption and compact size.

In the structure of Figure 3.1a, a conventional total power radiometer receiver is shown using a mixer with a separate oscillating source, the LO. Combining the LO source with the mixer into a single device, an SOM-based receiver architecture can be established as depicted in Figure 3.1b.

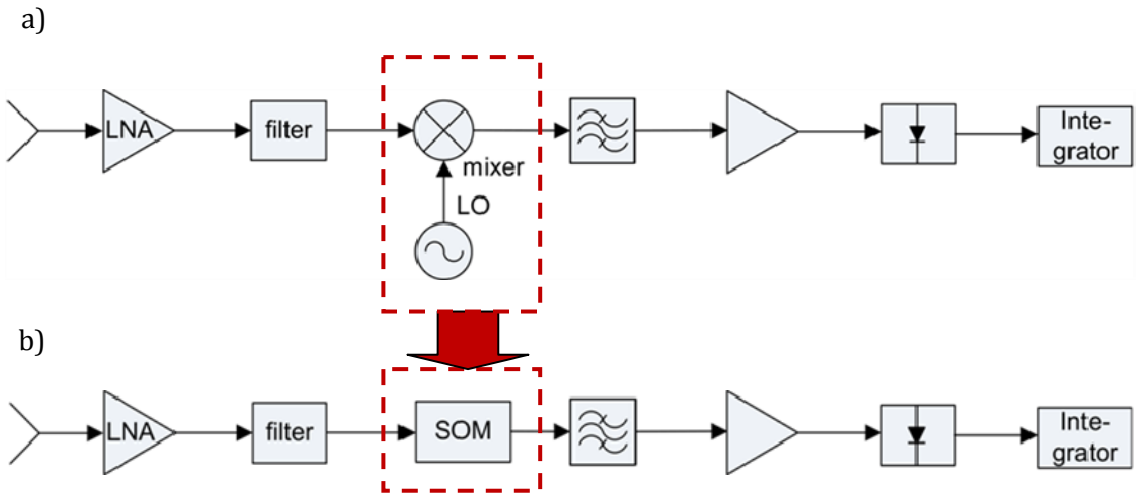

Figure 3.1 a) Total power radiometer receiver structure, b) substitution of conventional mixer by an SOM.

As previously mentioned, SOMs represent excellent choices for the development of low-cost and compact imaging radiometer receiver architectures, as they offer a reduced component number, lower power consumption, and the possibility of easy integration into MMICs.

3.1.1 Subharmonic operation

As outlined earlier, an extension to the standard SOM technique is given by subharmonic operation [20]–[24] being especially convenient for applications in the range of millimetre-waves. As shown in Figure 3.2, instead of mixing the RF signal with the fundamental LO frequency, a harmonic of the LO frequency is used. With the help of this technique, transistor gain has to occur only until the fundamental LO frequency, which drastically lowers the transistor maximum frequency (f_{max}) requirements [22] and thus represents an excellent choice for the design of millimetre-wave systems.

The particular problems encountered in the design of heterodyne millimetre-wave imaging radiometer receivers are given by the difficult generation of sufficient LO power at high frequencies, and the heat dissipation issues together with compact size requirements

emerging in the case of a dense FPA system. Subharmonic SOMs offer a good solution for both of these issues, as on the one hand, a more efficient low-power structure can be used with the external LO being integrated in the mixer, thus simultaneously solving the heat dissipation and circuit size problem. On the other hand, sufficient LO power can be generated by employing subharmonic operation, as the LO signal is generated at a frequency of only a fraction of the RF input, where its generation is much more unproblematic.

One of the important novelties presented in this Ph.D. thesis is amongst others the generation of especially high-order harmonics for SOM purposes, which will be presented within the following sections. Very high-order SOMs have not been studied very extensively up to now due to their difficult design, simulation, and low performance output when not understood properly. Their importance becomes especially visible in the case of millimetre-wave applications, because LO power can be generated at a fraction of the RF frequency, where it is less problematic to generate.

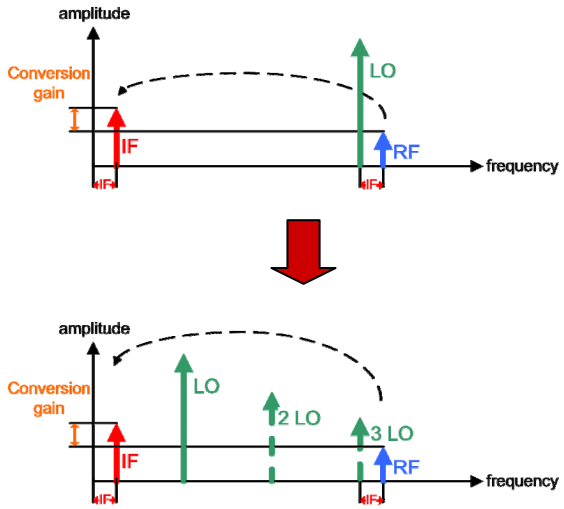

Figure 3.2 Concept of subharmonic self-oscillating mixing.

3.1.2 Balanced Architecture

One very efficient implementation method of subharmonic SOM operation is given by using a balanced circuit structure [23]–[27]. The major idea behind the performance advantages

of balanced mixer structures is related to the exploitation of the phase relations between the RF and LO signals at the two active device inputs as shown in Figure 3.3. For example, if the RF signals are provided in phase and the LO signals out of phase, either even- or odd-order mixing products can be easily enhanced depending on the output combination that is used. On the other hand, the respective non-enhanced mixing products are ideally suppressed in such a structure [28]. Moreover, conversion gain is enhanced, as the IF output is ideally a combination of the power of two single-ended mixers. Balanced structures also offer inherent RF-LO isolation as well as a number of additional important advantages such as lower AM noise, suppression of unwanted harmonics, etc.

Based on this concept, it is possible to establish a balanced subharmonic SOM from the depicted structure in Figure 3.3. A balanced mixer is built up from two single-ended gate mixers, and a balanced oscillation can be introduced using a resonance between the two gates. This oscillation is occurring out of phase at the two gates and hence represents the required out-of-phase LO condition for proper balanced mixing. Looking at this concept a little more in detail, a further advantage of this balanced SOM structure over conventional balanced mixers is revealed. In the presented case, the oscillation occurs internally and inherently, and no external balun/hybrid is needed to create the required out-of-phase LO condition at the gates as it is the case in conventional mixers where the LO must be applied externally. This allows for a compact size structure and moreover a possible cost-effective MMIC integration as baluns/hybrids always require a large amount of circuit area. The proposed concept thus seems highly interesting for commercial applications and will be implemented and outlined in detail in the following section.

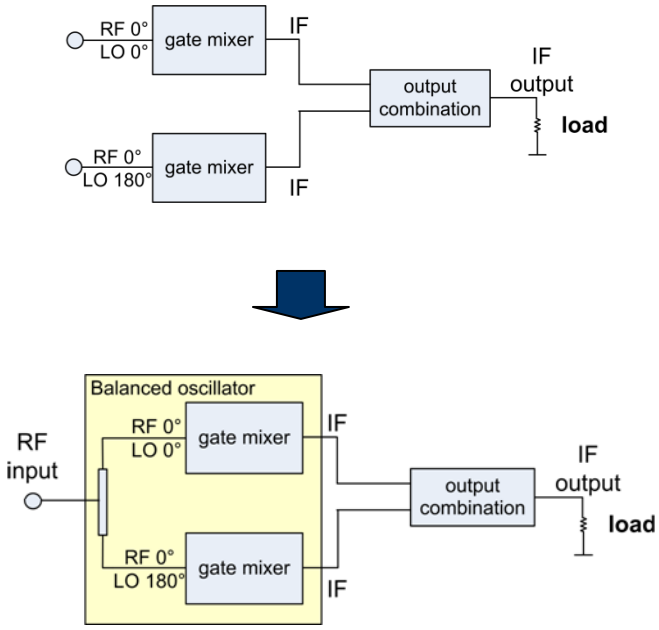

Figure 3.3 Balanced SOM concept: the gates of a single balanced gate mixer are connected by a resonating line to form a balanced oscillator. Applying RF power at the center of the structure allows for self-oscillating mixing.

3.2 LOW-FREQUENCY PROTOTYPE OF A SUBHARMONIC SELF-OSCILLATING MIXER

The circuit concept in Figure 3.3 has been implemented at low frequency, i.e. 5.8 GHz, in order to properly prove its functionality. This specific design frequency is chosen as a large number of commercial and industrial applications operate at this range and components are easily available, which makes testing and fabrication straight-forward and cost-efficient. In particular, it uses for the first time high-order harmonics of the oscillation signal, i.e. in the presented circuit the third and fourth order harmonic [23], [51]. A more detailed diagram of the proposed concept is shown in Figure 3.4.

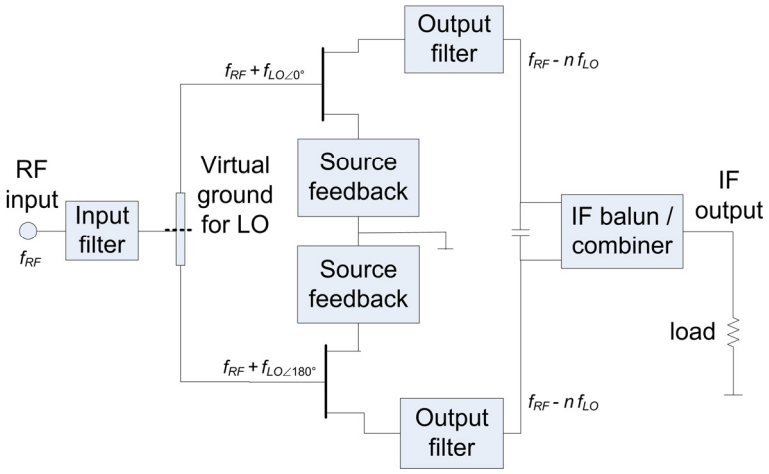

Figure 3.4 Concept of the third (n = 3) and fourth (n = 4) harmonic SOMs.

3.2.1 Circuit structure

3.2.1.1 Mixer configuration

The mixing function in the proposed circuit is introduced by a straightforward active transconductance gate mixer design. The RF signal is injected from the center of the structure and reaches the transistors in phase, where it is mixed with an out-of-phase LO signal. This allows for the generation of even-order mixing products in the case of an in-phase combination of the outputs and odd-order mixing products for out-of phase combination, respectively.

For proper mixer performance it is important to short-circuit the drains at LO frequency, so that during the entire LO cycle the transistor does not drop into the linear region.

Furthermore, undesired mixing products, RF leakage, and other spurious responses need to be eliminated from the output. These two requirements are fulfilled by a broadband stepped impedance output filter. In addition, short circuit stubs at the sources prevent instability at the gate at RF frequency, so that no possible oscillation may build up at this frequency and the circuit can be matched properly at the input.

The design is then balanced using two identical gate mixers with their outputs connected by an IF balun/combiner and their inputs connected by a transmission line. The RF power is injected via an input filter at the center of the transmission line. This causes the RF to be

in phase at the gates, while the LO is out of phase. The input filter serves both as input matching and as a means to improve RF-LO isolation.

3.2.1.2 Oscillator design

The oscillating part of the SOM follows a straightforward negative resistance oscillator design and capacitive feedback at the sources introduces negative resistance at the gates. To make the design balanced, the balanced oscillator theory based on the extended resonance technique [25] is used: A simple transmission line between the gates converts the reactance of one transistor to its negative value and therefore the two FETs can resonate with each other building up a stable oscillation signal.

3.2.1.3 SOM concept

If the LO signals at the gates of the transistors are provided out of phase and the RF signals are in phase, at the output, either a balun rejects the in-phase even-order mixing products or a power combiner rejects the out-of-phase odd order products. Thus, for a third harmonic SOM, a balun is used, while the fourth order harmonic SOM uses an output power combiner. The final SOM circuit is shown in detail in Figure 3.5.

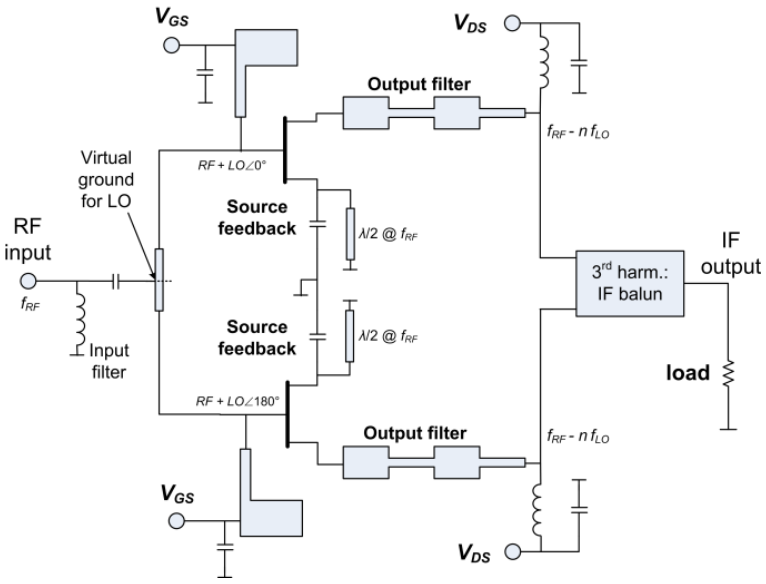

Figure 3.5 Circuit structure of the third-order SOM.

3.2.2 Simulation results

To prove its functionality, the proposed concept has been designed at low frequency (5.8 GHz). Simulations have been performed with Agilent ADS using the Harmonic Balance (HB) method. Simulation and measurement results are shown in Figure 3.6 to Figure 3.8: Figure 3.6 shows the output spectrum of the third harmonic SOM. A comparison between the balanced and the single-ended output indicates that a large number of undesired harmonics can be effectively eliminated, whereas the desired IF signal power resulting from mixing with the third harmonic LO component is successfully enhanced.

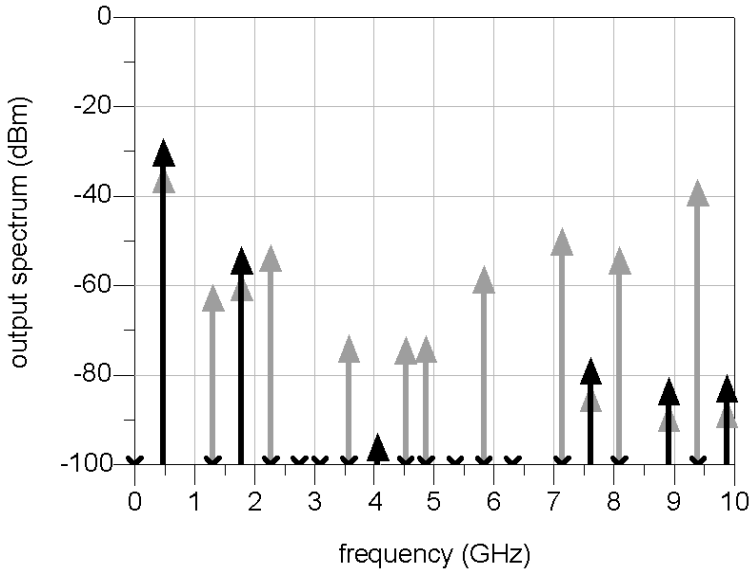

Figure 3.6 Output spectrum of the third harmonic SOM simulation (RF = 5.83 GHz at –30 dBm, LO = 1.78 GHz). grey = single ended output, black = balanced output.

Simulation of the fourth harmonic SOM in Figure 3.7 shows similar behavior for the suppression using a balanced structure. Moreover, since the LO signal is out of phase at the drains, LO leakage is inherently removed.

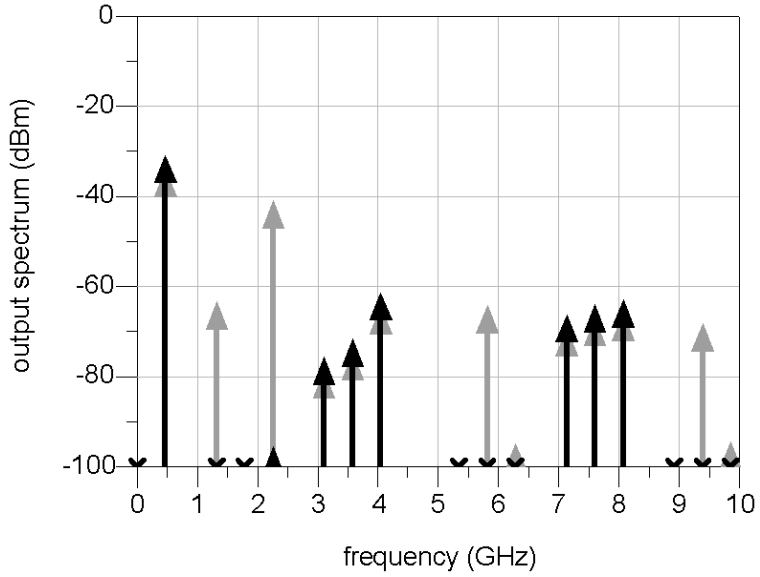

Figure 3.7 Output spectrum of the fourth harmonic SOM simulation (RF = 7.65 GHz at –30 dBm, LO = 1.78 GHz). grey = single ended output, black = balanced output.

3.2.3 Experimental results

For verification purposes of the proposed circuit concept, the third harmonic structure was selected and fabricated in microstrip technology on a Rogers RT5880 substrate with a relative dielectric permittivity of ε_r = 2.2. A photograph of the circuit is shown in Figure 3.9. The active devices employed in the design are NE34018 FETs biased at V_{gs} = -0.6 V and V_{ds} = 2 V. Figure 3.8 shows the measured output spectrum of the third harmonic SOM with an input RF input signal of 5.83 GHz and –30 dBm exhibiting a measured conversion gain of +11.1 dB. The oscillation of the circuit stabilizes to 1.783 GHz, hence yielding an IF frequency of approximately 480 MHz. It is further visible that the LO level at the output is as low as –39 dBm representing a very good result in terms of IF-LO isolation performance. The power consumption of the presented balanced SOM is 32 mW (16 mW per transistor) at a drain bias voltage of 2 V. This value agrees both in measurement and simulation and moreover emphasizes the low power consumption of the device.

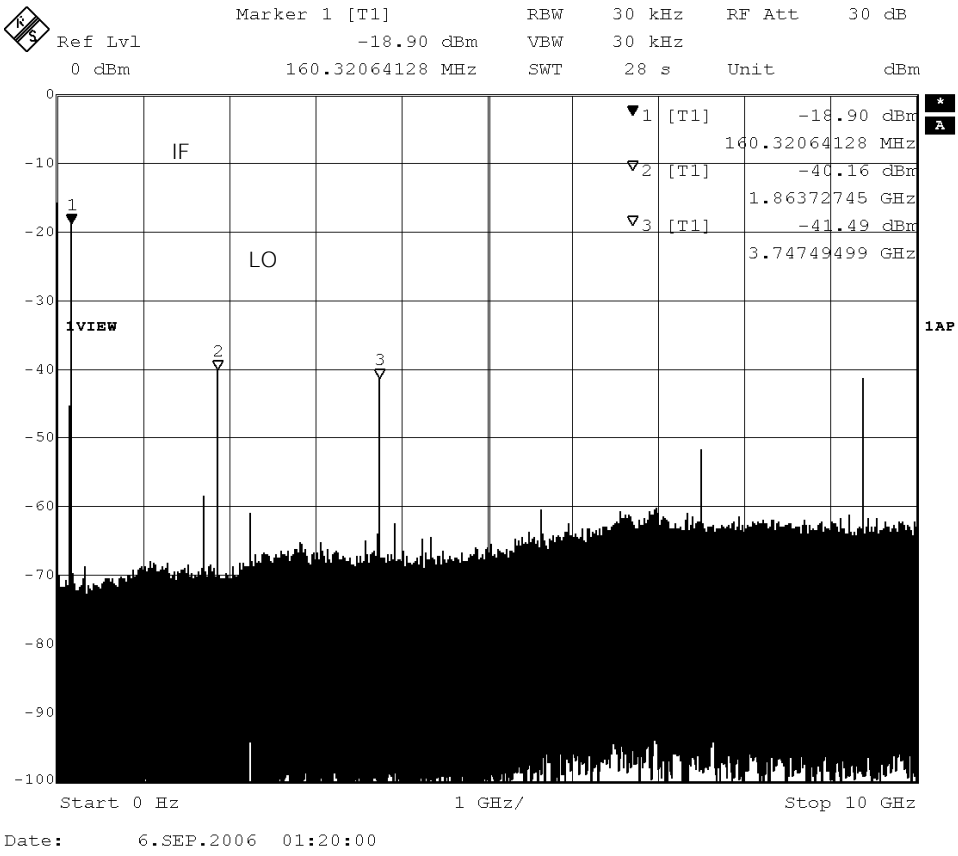

Figure 3.8 Output spectrum of the third-harmonic SOM at an RF input of 5.8 GHz and –30 dBm. The oscillation built up to 1.863 GHz, which yields an IF frequency of 160 MHz.

Conversion gain for the third and fourth harmonics vs. RF input power is illustrated together with measurement results in Figure 3.10. The simulated results show a slight deviation from the measured results, which is attributed to the use of the low-quality nonlinear transistor model coming along with the device employed in the presented design. Furthermore, at high RF input levels, HB simulation becomes inaccurate and experiences convergence failure.

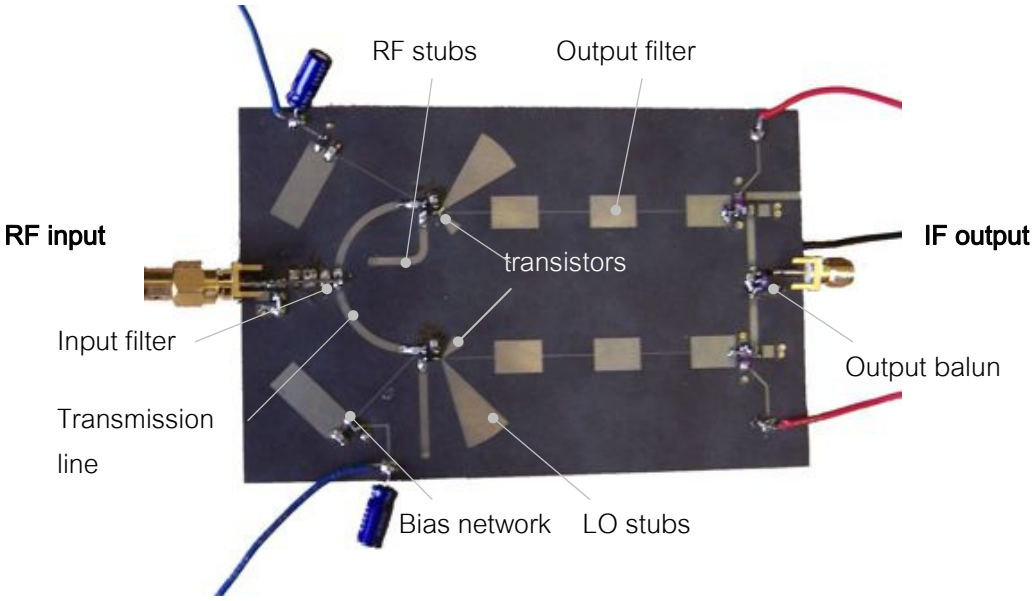

Figure 3.9 Photograph of the SOM circuit prototype (fabricated in microstrip technology, substrate RT5880 with $\varepsilon_r = 2.2$).

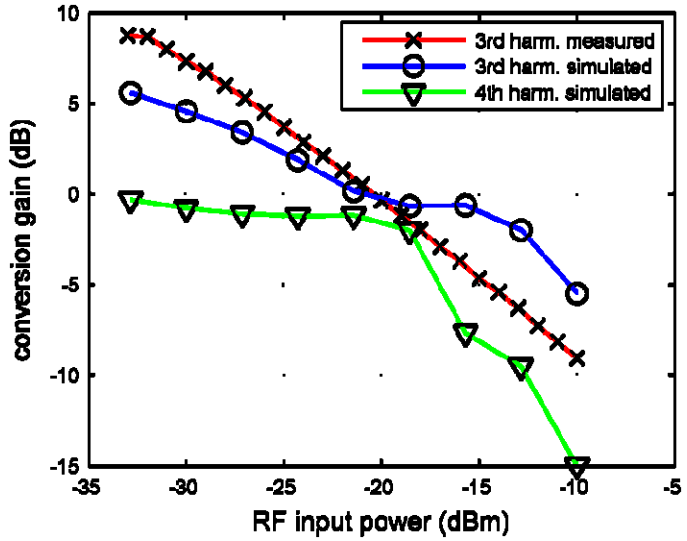

Figure 3.10 Conversion gain vs. input power for an RF frequency of 5.83 GHz and an LO frequency of 1.78 GHz.

3.3 PERFORMANCE MODEL OF SELF-OSCILLATING MIXERS

In order to assess the practical applicability of the proposed architecture, in this section a detailed performance investigation of the developed subharmonic SOM receiver is carried out. In a SOM, the main performance goals are given by its conversion gain, its IF frequency, noise figure, LO leakage, and its intermodulation distortion.

In the structure that has been described in the previous section, the primary design parameters that influence these performance goals are the gate and drain bias voltages of the transistor, the choice of the source feedback, the output terminations at the drain (also realized by the output filter), and the applied input power. For illustration, these parameters are indicated in Figure 3.5.

3.3.1 Harmonic output

In harmonic mixers, the gate voltage V_{gs} can be selected in order to maximize the desired harmonic output: a Fourier analysis of the transconductance waveform shows that maximizing the desired harmonic component by properly selecting the gate voltage enhances the desired harmonic mixing order. Thus, in the proposed design the third harmonic component needs to be maximized.

In Figure 3.11 a comparison of the third harmonic transconductance waveform component with the simulated and measured conversion gain is shown. It becomes clear that there is a direct relationship between these two parameters. The maximum conversion gain visible in the plot at V_{gs} = –0.6 V does not coincide with the maximum of the third order transconductance component, however, this additional peak is occurring due to a conjugate matching of the circuit at this bias point.

3.3.2 Conversion gain

In a mixer, a variety of mixing products at frequencies corresponding to

$$f_{out} = n\, f_{RF} + m\, f_{LO} \tag{3.1}$$

are created with f_{RF} as the RF input frequency, f_{LO} as the LO frequency, and n = 1, 2, 3,... and m = 1, 2, 3,.... Mixer performance is determined by the termination presented to the circuit at each of these frequency components. In general, the mixing products that are desired should be terminated with a conjugately matched load, whereas the undesired components are ideally terminated in a short circuit. This design rule must be held in mind when designing mixer circuits.

Moreover, conversion gain for harmonic mixers is mainly influenced by maximizing the desired harmonic component of the transconductance waveform as it has been shown in Figure 3.11. This is at first ensured by the proper choice of the gate voltage. It is also very important to provide a drain short-circuit at LO frequency and its harmonics in order to maintain the transistor from dropping into the linear region and therefore maximizing transconductance variation. Furthermore, conversion gain is improved by increased drain bias and by the power combination due to the balancing of the design as it is shown in Figure 3.12.

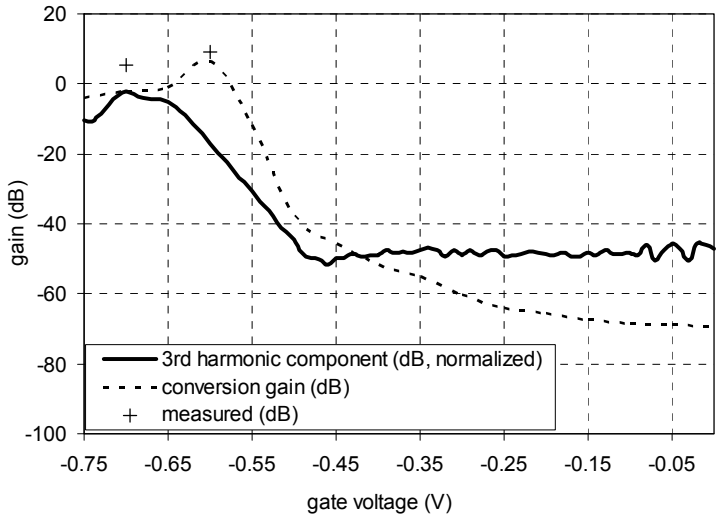

Figure 3.11 Fourier analysis of the transconductance waveform: the maximum of the third harmonic component lies at around –0.7 V, which complies with our gain performance results and the experimental results (gain maximum is at a different location due to matching).

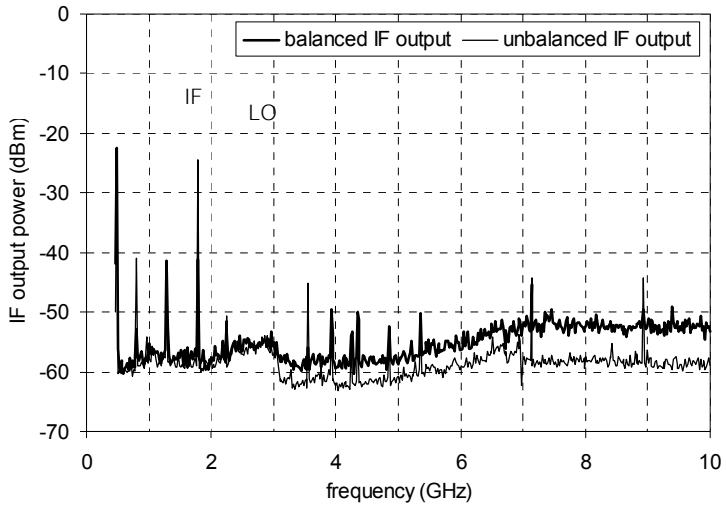

Figure 3.12 Comparison between the measured single-ended and balanced IF output power. Many undesired spurious responses, harmonics, and the LO leakage can be suppressed, whereas the conversion gain is increased.

3.3.3 Oscillation frequency tuning

In some applications it might be of interest to provide oscillation frequency tunability in order to downconvert different RF frequencies to the same IF frequency.

Oscillation frequency is determined by the source feedback capacitance, choice of gate bias voltage, and the output termination of the transistors.

Figure 3.13 shows the tunability of the oscillation frequency vs. drain bias voltage providing a relative tuning bandwidth of 2.3%. It is to be noted that in spite of the operation as a mixing and oscillating device at the same time, a linear tuning behaviour can be obtained. Tuning is also possible by varying the source capacitance.

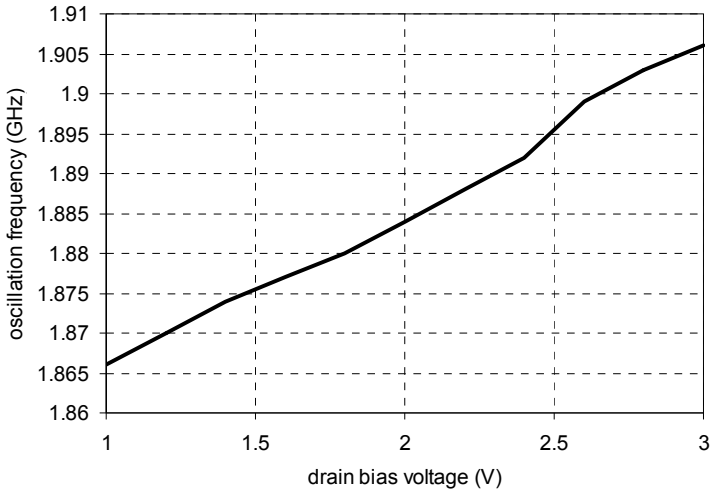

Figure 3.13 Measured oscillation frequency vs. drain bias voltage: oscillation frequency can be tuned linearly in a relative bandwidth of 2.3%.

3.3.4 Noise figure

In an active FET mixer, the main contribution to noise is given by the high-field diffusion noise at the drain. Therefore, unlike in an amplifier design, mismatch does not significantly improve noise behaviour, since thermal noise at the input and output is not high and the device shows lower gain due to a smaller value of transconductance variation. Noise figure optimization in our design is therefore given by short-circuit termination of gates and drains at LO frequency and its harmonics. Moreover, the gate should be short-circuited at IF frequency and the drain at RF frequency to prevent amplifier-mode gain. At the same time both ports are conjugately matched to maximize conversion gain. Furthermore, inherent improvement of the noise figure is given by a balanced design as it is presented in this circuit concept.

Figure 3.14 shows the measured noise figure of the circuit over the entire IF bandwidth. The measurement has been performed with an Agilent Noise Figure Analyzer that allows for simultaneous gain measurement, which is shown in Figure 3.14 as well. A minimum noise figure of 6.9 dB for an IF frequency of 140 MHz is measured. Considering the high gain of +11.1 dB, this value is very low and practical for almost any application. It is to be noted that the measured conversion gain is slightly lower compared to the results shown

in the above paragraphs due to the insertion loss of an additional output filter that is required for the band selection in the noise measurement.

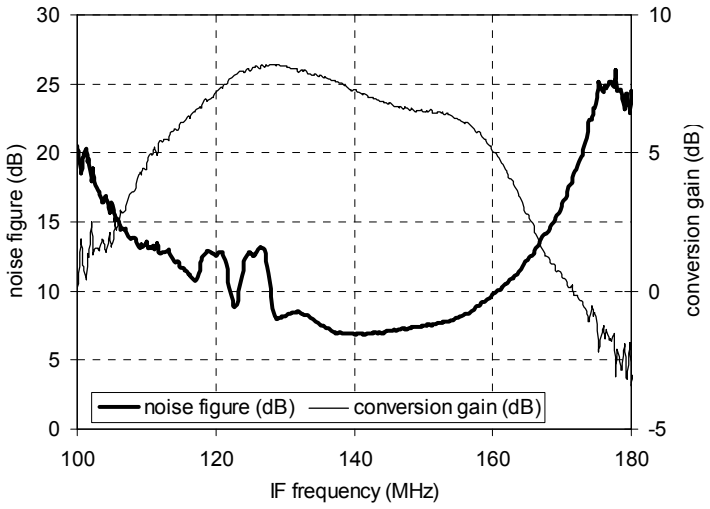

Figure 3.14 Noise figure compared to conversion gain over the IF bandwidth. A minimum noise figure of 6.9 dB is measured.

3.3.5 Frequency pulling

As opposed to conventional mixer circuits, the presented receiver involves an autonomous oscillation circuit, which makes the LO frequency a variable parameter whose changes can affect circuit performance. Especially the effect of applying external RF input power needs to be considered as it pulls the oscillation frequency and therefore can affect the dynamic range of the designed receiver circuit. The measurement in Figure 3.15 shows a constant LO frequency for low input powers (< –30 dBm) and a very low pulling effect of max. 2.8 MHz or 0.15% relative bandwidth for an RF power of –10 dBm, which proves the functionality of the presented circuit for practical applications.

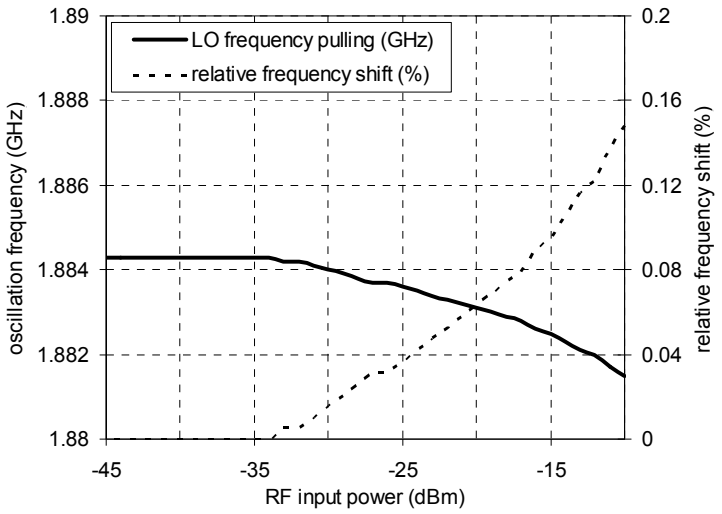

Figure 3.15 Pulling of the oscillation frequency by the RF input signal and the relative frequency shift.

3.3.6 Intermodulation distortion

Intermodulation distortion (IMD) has become increasingly important in microwave mixer design in terms of dynamic range performance. Unlike harmonic and second order distortion products, third order IMD products result very close to the IF signal and cannot be easily eliminated by filtering. Usually in receivers the mixer constitutes the greatest contributor to intermodulation distortion. In subharmonic mixers, the various performance advantages are outweighed by a generally lower third order IMD. For the designed third order SOM we measured an output-referred third order intercept point (TOI) of 4.5 dB.

3.3.7 LO leakage

LO leakage is mainly reduced by proper output filtering and the LO short-circuit terminations at the drain as described above. However, to further improve LO leakage, a capacity between the two outputs is introduced, which forms a lowpass filter that suppresses the LO signal but leaves the IF output and therefore the conversion gain

unaffected. In addition, this technique allows for a more effective suppression of any higher-order unwanted mixing products.

Figure 3.16 shows the influence of the drain capacitor: at low values, it reduces LO leakage but leaves the conversion gain unaffected. For optimum values, it can even enhance the gain due to the more effective LO short circuit at the drain.

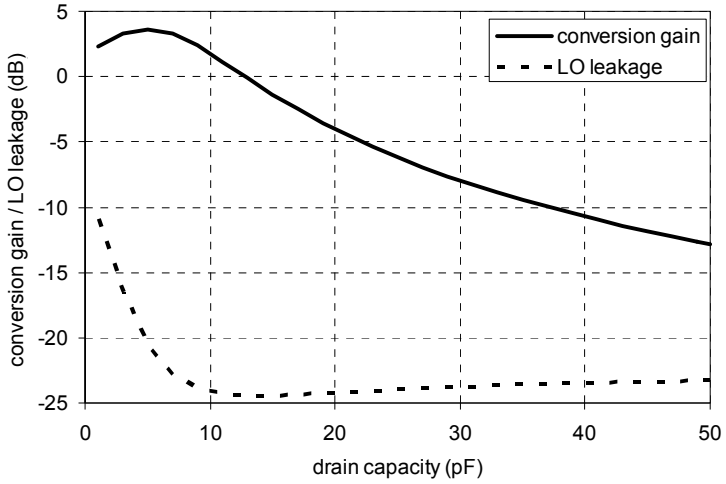

Figure 3.16 Conversion gain and LO leakage vs. drain capacity: Up to around 10 pF the LO leakage can be effectively reduced without affecting conversion gain.

In Figure 3.17 the LO leakage vs. RF power is shown, and simulation and measurement results agree well. The deviation can be explained by the difference in conversion gain in simulation and measurement.

LO leakage for this third harmonic SOM is also drastically decreased by balancing the design as it can be seen from Figure 3.12. Combining all these aspects, we can achieve an LO reduction by the drain capacitance of 31 dB and a suppression of 18 dB by balancing the design, which yields a total suppression of 39 dB.

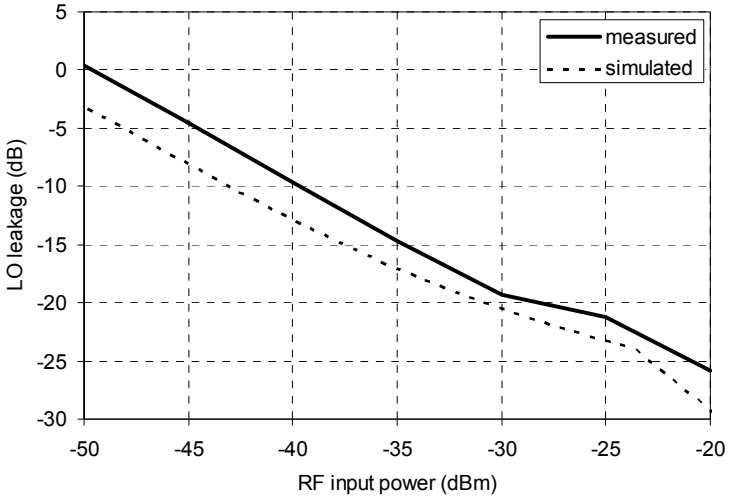

Figure 3.17 LO leakage vs. RF input power for simulation and fabricated circuit.

3.4 ULTRA HIGH-ORDER SUBHARMONIC SELF-OSCILLATING MIXING

Considering all their previously outlined advantages, in recent years, subharmonic mixers have received considerable attention as they represent excellent choices for high-end millimetre-wave applications. However, subharmonic mixing beyond the 2nd or 4th order becomes difficult due to the high number of necessary idler circuits in order to suppress unwanted mixing harmonics. Recently, an 8th-order mixer based on two pairs of anti-parallel diodes has been proposed using phased local oscillators [68].

In this section, the suggested subharmonic SOM technique is for the first time extended to ultra high orders. The advantage of this design over previously proposed solutions such as high-order subharmonic mixers based on antiparallel diode pairs [28] are in the first place its SOM structure, but also its ability to provide conversion gain due to the use of FETs as nonlinear devices instead of diodes. The presented high-order subharmonic operation drastically lowers the transistor maximum frequency (f_{max}) requirements and therefore this circuit architecture represents an excellent choice for future millimetre-wave receivers.

The technique presented here introduces a general approach for the design of such SOM architectures by providing different phase shifts to the nonlinear devices' inputs. A basic design procedure is developed in theory that can be applied to any desired arbitrary mixing order. Finally, the theoretically suggested results are experimentally verified with the design of a 6th-order subharmonic SOM.

3.4.1 Circuit concept

The circuit concept of the SOM presented in this paper is shown in Figure 3.18. K single balanced self-oscillating mixer blocks [23] are designed and connected by a phase-shifting input network locking the oscillators to phases φ_i of $i*\pi/K$ rad (i = 0,1,...,K–1). The outputs are combined by an appropriate output network in order to enhance either multiples of even-order ($N = 2l*K$, with l as an integer) or odd-order mixing products ($N = (2l–1)*K$),

respectively. RF power is injected at the center of the input network. This causes the RF to be in phase at the gates, while the LO is phase-shifted.

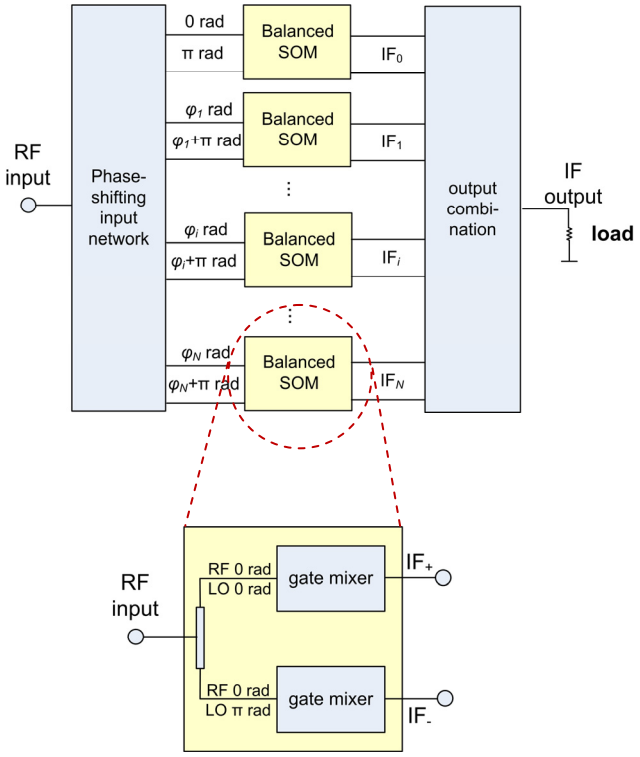

Figure 3.18 a) Multiple-element SOM concept: *K* SOM elements are connected by a phase-shifting input network and combined by an output network; b) each SOM block consists of a single balanced transconductance mixer that provides at the same time a balanced oscillation function by connecting the gates through a transmission line.

Each single block is built up as proposed in [23] by two transconductance gate mixers (Figure 3.18b). The two gates of the transistors are connected by a transmission line, which acts as a resonating element in order to create a balanced oscillator [29].

For each block, the balanced oscillator design employed for this circuit architecture yields oscillation signals at the gates with phases of 0 and π rad, respectively. Thus, between each pair of blocks, a phase shift of $i*\pi/K$ rad must be introduced in order to obtain the full

phase range of $2\pi/K$ rad. In our design, these phase relations is realized by introducing transmission lines between the blocks locking the relative phases of the transistors to the desired values (Figure 3.19). The lines between the gates of the single transistors in each SOM block have a length determined by the balanced oscillator theory [29].

Figure 3.19 shows the output network for the case of a circuit enhancing odd-order mixing products. It is implemented by in-phase combinations (+) that are realized in practice by power combiners, whereas out-of-phase combinations (–) require a balun.

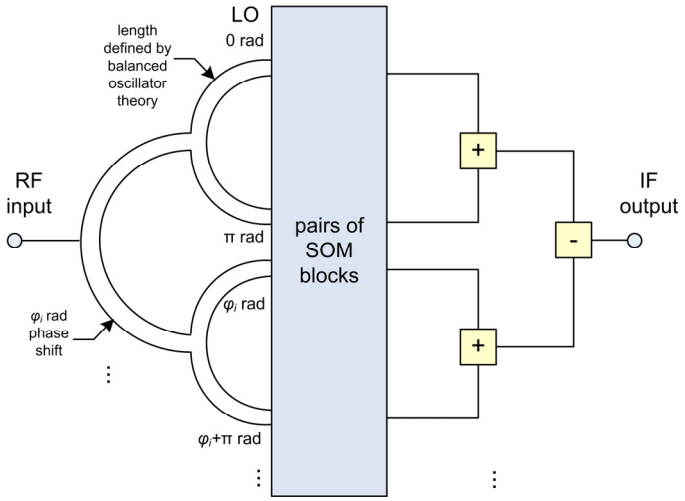

Figure 3.19 Structure of the input network providing the required phase shifts to the gates of the transistors together with the output network for the case of an out-of-phase connection.

It should be mentioned, that any of these combinations can be realized with only one single balun for meeting possible circuit space limitations. Section 3.4.2 theoretically proves the requirement of these specific output networks for the proposed application.

3.4.2 Theory

This section expands the theory presented in [28] to the case of high-order subharmonic SOMs using FET transistor pairs with arbitrary output phase connections.

In the case of in-phase connected outputs, the total IF current can be written as

$$I_{IF}^{total} = \sum_{i=0}^{K-1} I_0^i \tag{3.2}$$

where I_0^i represents the IF current for the i^{th} SOM block. For out-of-phase connections the total IF current becomes

$$I_{IF}^{total} = \sum_{i=0}^{K-1} (-1)^i I_0^i \tag{3.3}$$

Based on the conversion matrix approach [1], [9] for K blocks of balanced SOMs the total IF current can be written as

$$I_{IF}^{total} = \sum_{n=-\infty}^{\infty} Y_{0,n} V_n \sum_{i=0}^{K-1} \exp\left(jn\varphi_i\right) \tag{3.4}$$

in the case of in-phase connected outputs (3.2) and

$$I_{IF}^{total} = \sum_{n=-\infty}^{\infty} Y_{0,n} V_n \sum_{i=0}^{K-1} \exp\left(ji\pi\right) \exp\left(jn\varphi_i\right) \tag{3.5}$$

for the case of an out-of-phase combination (3.3). n stands for the voltage sideband index at the mixer input, V_n is the small-signal input voltage at sideband n, and $Y_{0,n}$ represents the mixer conversion admittance matrix [28].

Developing the exponential sums in (3.4) with the use of equally distributed phase shifts $\varphi_i = i*\pi/K$ we obtain in the case of in-phase combined outputs

$$\exp\left(j\frac{n(K-1)\pi}{2K}\right)\frac{\sin\left(\frac{n\pi}{2}\right)}{\sin\left(\frac{n\pi}{2K}\right)} = \begin{cases} 0, & \text{if } n \neq 2lK \\ \pm K, & \text{otherwise} \end{cases} \tag{3.6}$$

For the case of out-of-phase connections we can develop (3.5) into two cases for an even number K of SOM blocks

$$-j\exp\left(j\frac{n(K-1)\pi}{2K}\right)\frac{\sin\left(\frac{n\pi}{2}\right)}{\cos\left(\frac{n\pi}{2K}\right)}=\begin{cases}0, & \text{if } n\neq(2l-1)K\\ \pm jK, & \text{otherwise}\end{cases} \tag{3.7}$$

and

$$\exp\left(j\frac{n(K-1)\pi}{2K}\right)\frac{\cos\left(\frac{n\pi}{2}\right)}{\cos\left(\frac{n\pi}{2K}\right)}=\begin{cases}0, & \text{if } n\neq(2l-1)K\\ \pm K, & \text{otherwise}\end{cases} \tag{3.8}$$

for an odd number K of SOM blocks.

In (3.6) all sideband terms except $n = 2l*K$ are zero. This shows that mixers employing in-phase combined nonlinear devices result in mixing orders of $N = 2l*K$. In (3.8) only sidebands with index $n = (2l–1)*K$ yield nonzero IF currents. Thus, a mixer built up by an output network with out-of-phase combinations enhances $N = (2l–1)*K^{\text{th}}$-order mixing. This proves the assumptions taken for the output network in section II. Furthermore, it is important to note that the integer (l–1) in these expressions describes the number of necessary idler circuits required for enhancing the desired mixing order as a fundamental response.

3.4.3 Experimental Results

A subharmonic SOM based on the described novel approach has been designed and tested in order to verify the presented technique. A mixing order of $N = 6$ is selected as it represents a sufficiently high order to prove the novel concept, but also shows possible implementations of orders other than multiples of $2K$ that are enhanced by in-phase connected networks such as antiparallel diode pairs. Considering the observations made in

section III, a mixing order of N = 6 can either be realized by three in-phase SOM blocks (l =1) or two out-of-phase SOM blocks (l = 2). In order to reduce component number and power consumption we select the latter option. In this way, only an idler circuit for the third harmonic becomes necessary.

To realize this circuit architecture, two SOM blocks [23] as described in section II were implemented each of them providing phase shifts of 0 and π rad, respectively, at the gates. Connecting their inputs with a transmission line of length π/2 at LO frequency, phases of 0, π/2, π, and 3π/2 can be obtained. The outputs of each block are connected in phase and the two blocks are combined out-of phase by means of a balun.

The circuit was fabricated on Taconics TLY-5 substrate with a relative dielectric permittivity ε_r of 2.2 and a thickness of 20 mil. The nonlinear devices used in this work are NE34018 FETs. A picture of the final circuit is shown in Figure 3.20.

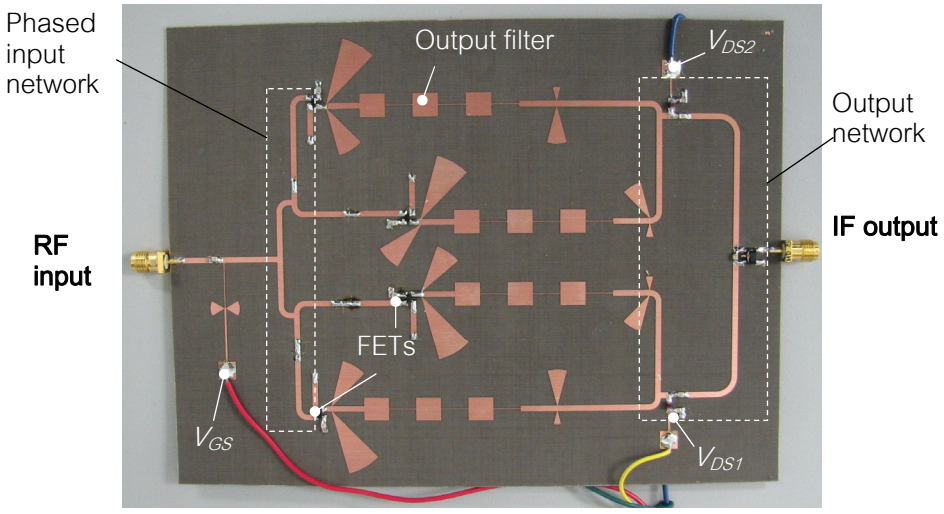

Figure 3.20 Photograph of the designed 6th-order subharmonic SOM using Taconics TLY-5 substrate with a relative dielectric permittivity of ε_r = 2.2 and a thickness of 20 mil.

The first step of the experimental setup required a careful investigation of the oscillation signals of each SOM block. To ensure proper functionality, the LO frequencies of both oscillators had to be synchronized to the same frequencies in order to enable the required

phase locking of the SOM blocks with each other. For this reason, separate bias connections for each SOM block were mounted in order to be able to tune the oscillation frequencies independently. Following this procedure, the oscillation output settled to an oscillation frequency of f_{LO} = 1.32 GHz. Thus, with an input frequency f_{RF} = 7.38 GHz an IF frequency of f_{IF} = 552 MHz has been achieved. A maximum conversion gain of +2.8 dB was measured at an input power of –30 dBm, which represents an excellent result considering the high mixing order.

The spectral behavior of the designed circuit is shown in Figure 3.21. The number of spurious responses of the balanced structure is as expected clearly reduced compared to single-ended mixers. A jitter has been observed around the oscillation frequency and that originates from the slightly different oscillation frequencies between the two SOM blocks and their fluctuations as described above.

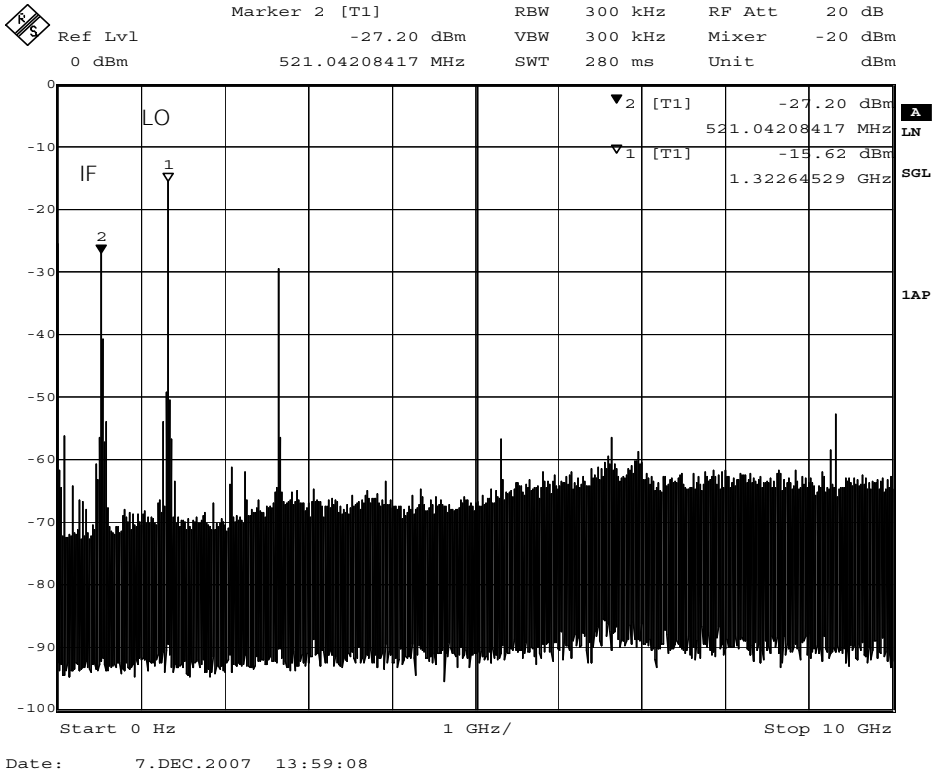

Figure 3.21 Output spectrum for the proposed 6th-order SOM at an oscillation frequency f_{LO} = 1.32 GHz, an RF input frequency f_{RF} = 7.38 GHz and an input power of –30 dBm, yielding an IF frequency f_{IF} = 552 MHz.

Figure 3.22 shows the conversion gain of the proposed structure vs. RF input power outlining the circuit compression behavior. A stable gain is observed below input powers of −30 dBm.

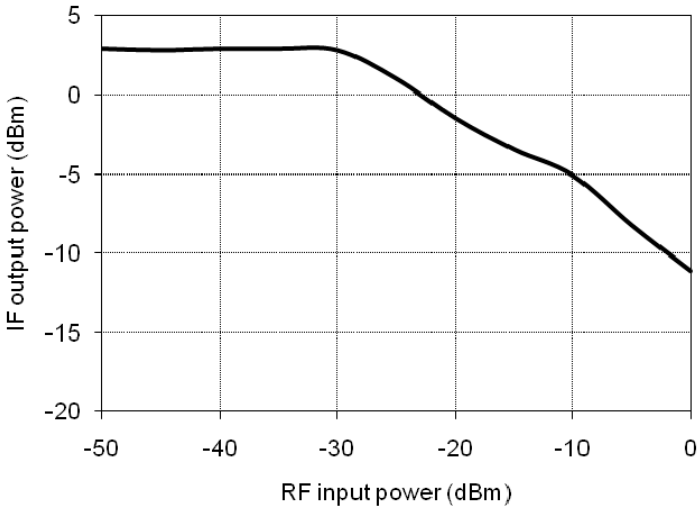

Figure 3.22 Measured compression behavior for the proposed 6th-order subharmonic SOM at an input frequency of f_{RF} = 7.38 GHz.

3.5 TRANSISTOR SELECTION AND MODELING

The analysis of millimetre-wave SOM architectures requires considerable design effort. Especially at millimetre-wave frequencies it is very important to provide good prediction methods for analyzing circuit behaviour and performance, since fabrication failures mostly become very expensive and time-consuming. Therefore, high-quality simulation analysis becomes essential and hence good modeling of the employed active devices must be used.

Especially for millimetre-wave transistor devices, there are mostly no nonlinear models readily available from the manufacturer. Many times a device is characterized up to a certain frequency, but the model does not cover the entire frequency range. For the requirements specified in this project, it was not possible to find a nonlinear transistor model, which made it necessary to develop our own set of data.

1.4.1 Transistor selection

The selection of the active device is critical for the proposed application. First of all, dealing with a radiometry receiver, a low noise figure is important, restricting our selection to low-noise devices. Second, a device is needed that operates at 35 GHz, which leads us to the selection of an unpackaged device in order to avoid parasitic effects. Moreover, it is best to use a FET compared to a bipolar device. Combining all these requirements, a pHEMT appears to be the best choice for the proposed application.

In the course of the project, two different GaAs pHEMT devices were used, the first being the MwT-4 transistor from Microwave Technologies, Inc., and the second device as the EC2612 FET from United Monolithic Semiconductors. The first device creates problems in preliminary designs, which is why the selection is finally narrowed down to the EC2612 as the device of choice for the entire receiver design in this Ph.D. thesis.

The MwT-4 transistor comes along with a relatively inaccurate model, which moreover ranges only until 27 GHz. The EC2612 is provided without any model, which brings us to the following design task of developing a nonlinear transistor model for the designated device.

1.4.6 Measurement

The measurements for transistor modeling are carried out at a probing station. The setup for this measurement is shown in Figure 3.23.

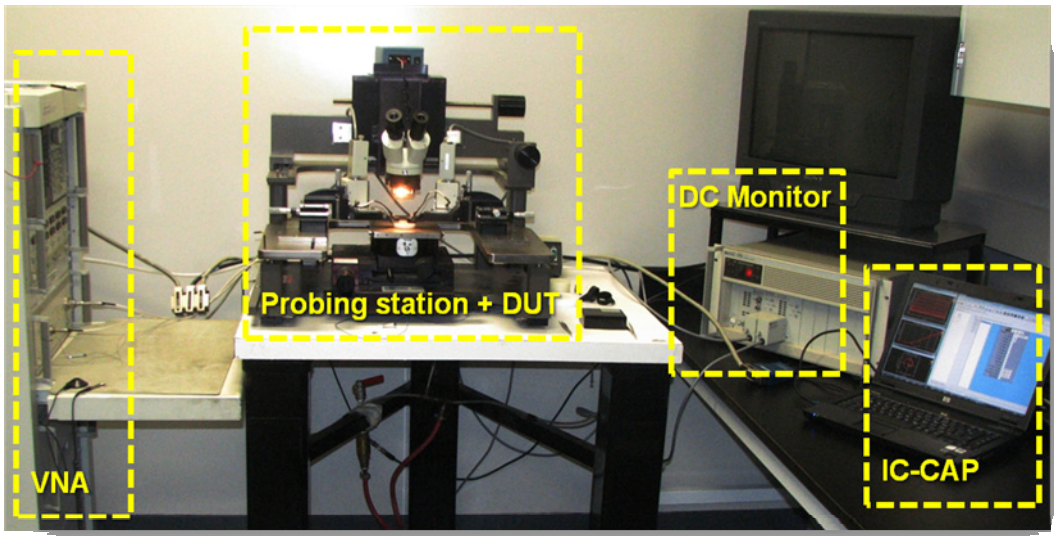

Figure 3.23 Test setup for the transistor model extraction.

The transistor is connected through a CPW transition to the probes as shown in Figure 3.24 and Figure 3.25. Specific software for transistor modeling software is used, which allows to control the measurement from the PC trough a GPIB interface. In this way, the software can control the DC bias varying the bias voltages through the DC monitor and measuring the respective currents. Simultaneously it can measure the *S*-parameters with the help of the network analyzer.

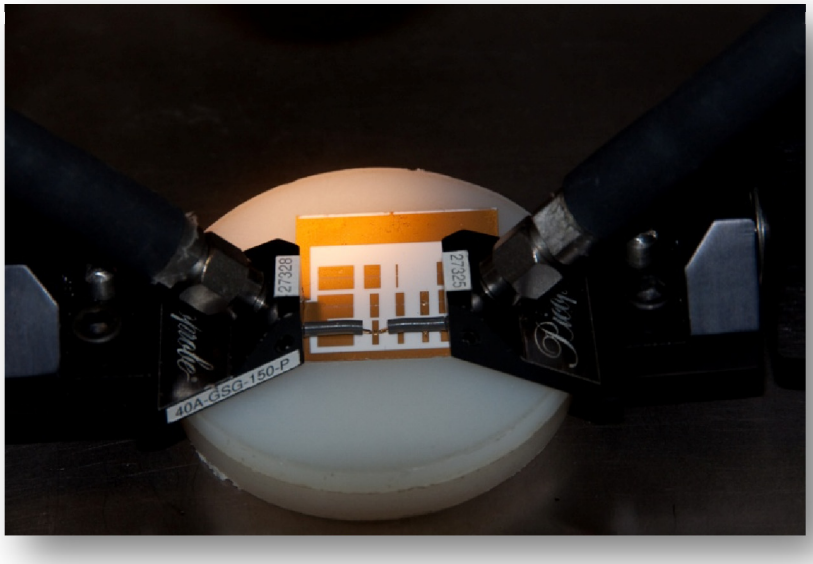

Figure 3.24 Transistor connected in the probing station.

Figure 3.25 Transistor under the microscope.

1.4.7 Model Selection

Especially in high-order transconductance mixing circuits it is important to pay attention to transistor modeling. The transconductance is given by the derivative of the I_d-V_{gs} waveform, and thus the description of this waveform in the transistor model is of ubiquitous importance for simulation accuracy. The higher the mixing order is selected, the higher the order of description of this curve must be. E.g. in a standard Curtice quadratic transistor model, the I_d-V_{gs} waveform is described by a quadratic term. Given the transconductance as the derivative of this waveform, we obtain only a linear term, which means that only first order mixing can be described, and moreover only without any saturation effects in LO pumping. The Curtice Cubic model includes a cubic term for the waveform, and thus limits the design to second order mixing (without LO saturation).

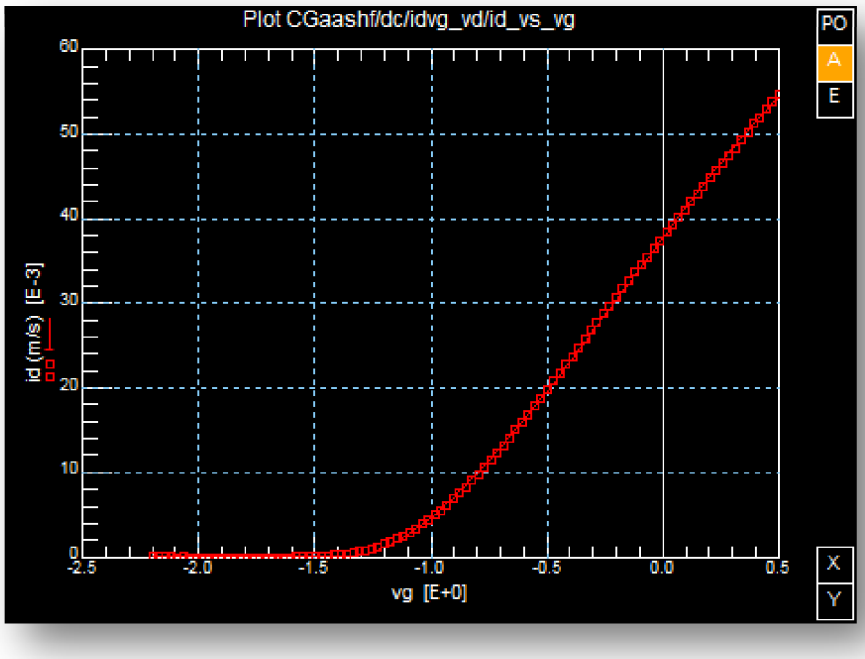

Figure 3.26 Transconductance curve plotted by Agilent IC-CAP.

Most transistor models describe the transconductance waveform with simple polynomials, which is somewhat limiting for high-order nonlinear applications as there is always a

maximum order above which the circuit cannot be correctly analyzed anymore. One suitable model for our purpose is the Angelov-Chalmers transistor model, which has been developed by Prof. Iltcho Angelov at the University of Chalmers, Sweden [58], [59]. This model is selected to be used in the modeling of the devices in this project and will be described briefly in the following sections.

1.4.8 Angelov-Chalmers Transistor Model

The equivalent circuit for the Angelov-Chalmers transistor model is shown in Figure 3.27. The main modeling equations are given in (3.9) to (3.10). From the relation for ψ_p it is obvious that the model exhibits free choice of polynomial order in harmonic designs, which represents an excellent choice for our high-order mixing application.

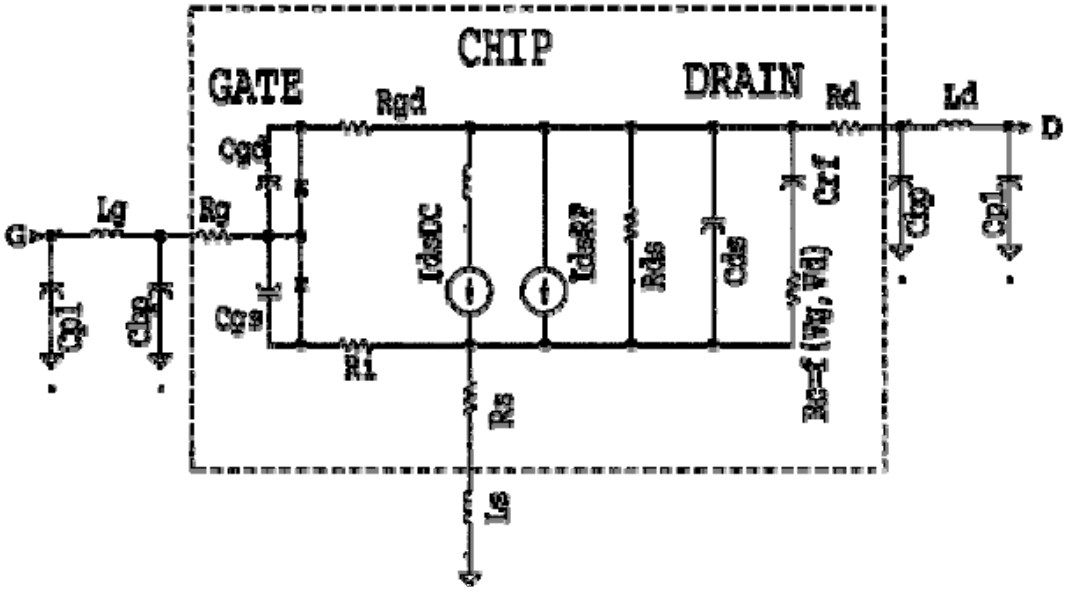

Figure 3.27 Equivalent circuit of the Angelov-Chalmers transistor model [58].

$$I_{ds} = I_{pks}\left(1 + \tanh\Psi_p\right)\tanh(\alpha V_{ds})\left(1 + \lambda V_{ds}\right) \tag{3.9}$$

$$\Psi_p = P_{1m}\left(V_{gs} - V_{pk0}\right) + P_2\left(V_{gs} - V_{pks}\right)^2 + P_3\left(V_{gs} - V_{pkm}\right)^3 \tag{3.10}$$

with the various modeling parameters as described in [58], [59].

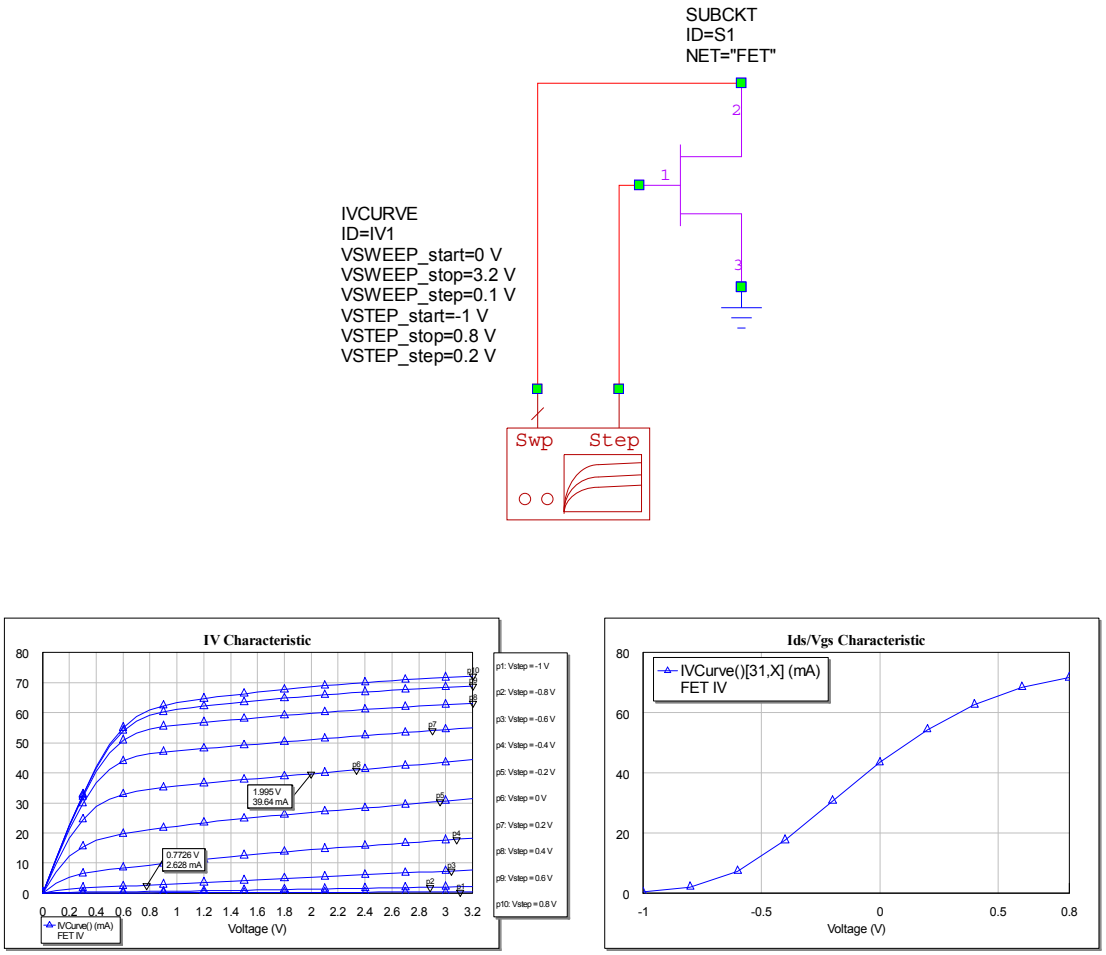

Figure 3.28 Extraction of DC characteristics.

1.4.9 Model extraction

The extraction of the model is carried out in three major steps. Each of these steps has been carried out aligning the results obtained using the model with the measured results by varying specific parameters in the Angelov transistor model. This procedure is described in detail in [58], [59] and will not be included in the description provided here. The first step is concerned with the identification of the DC characteristics of the transistor, i.e. the drain current vs. gate and bias drain voltages. Figure 3.28 shows the circuit schematic used for this purpose and the obtained I/V curve of the transistor.

The second step involves a comparison the *S*-parameters calculated from the model with the measurement.

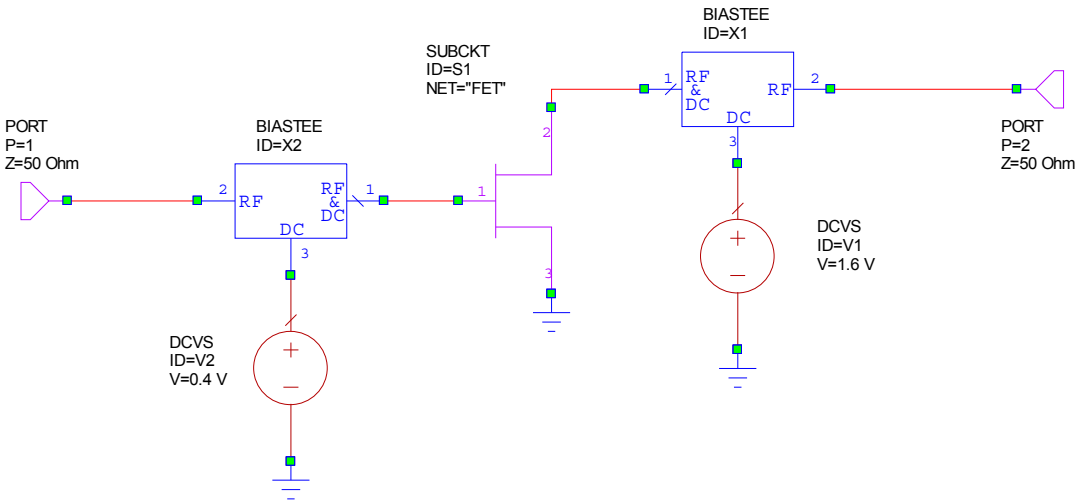

Figure 3.29 Extraction of RF characteristics.

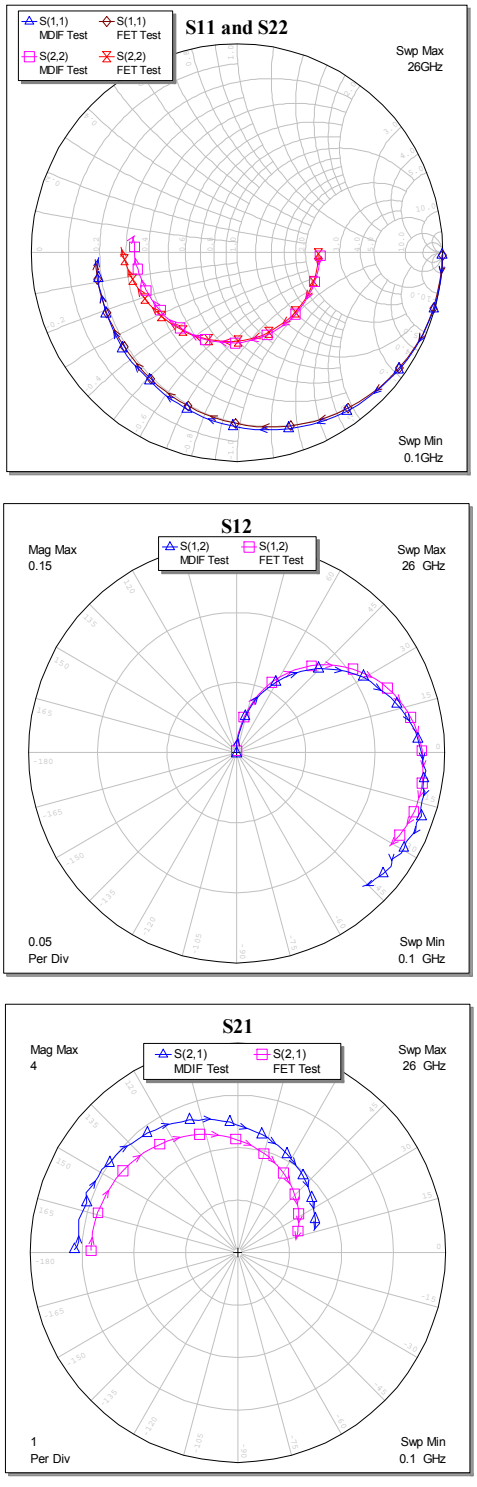

Figure 3.30 Extraction of RF characteristics.

In the third step, the capacitances in the model are identified. The Y-parameters are used for this step and plotted in Figure 3.31.

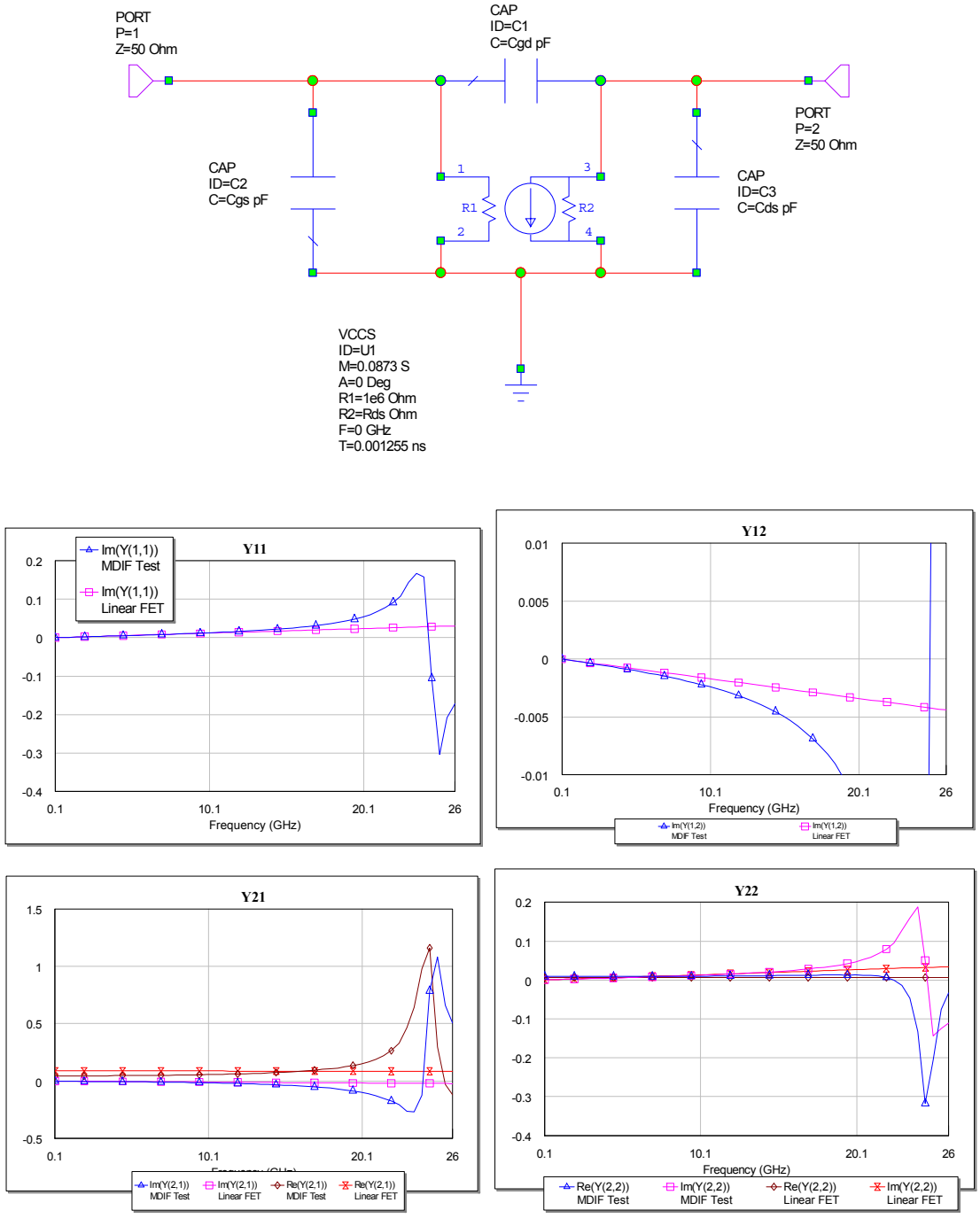

Figure 3.31 Extraction of capacitances.

The final model is then given by the following parameters:

Parameter	Value	Parameter	Value
Idsmod	0	**Rgd**	2 Ohm
Igmod	0	**Ls**	0.004 nH
Capmod	1	**Lg**	0.171 nH
Ipk0	30 mA	**Ld**	0.144 nH
Vpks	-0.1 V	**Tau**	0.0012 ns
Dvpks	0.25 V	**Rcmin**	125 Ohm
P1	2.3	**Rc**	1e6 Ohm
P2	0	**Crf**	1e3 pF
P3	0.8	**Rcin**	500000 Ohm
Alphar	0.3	**Crfin**	0.001 pF
Alphas	2	**Rth**	360 Ohm
Vkn	0.8 V	**Cth**	1e6 pF
Lambda	0.220	**Tcipk0**	-0.003
Lambda1	0	**Tcp1**	-0.003
Lvg	0	**Tccgs0**	0.003
B1	0.2	**Tccgd0**	0.003
B2	4	**Tclsb0**	0.001
Lsb0	0.1	**Tcrc**	0.001
Vtr	3 V	**Tccrf**	0.001
Vsb2	0	**Tnom**	25 DegC
Cds	0.183 pF	**TEMP**	25 DegC
Cgspi	0.1 pF	**Selft**	1
Cgs0	0.028 pF	**DTMAX**	300
Cgdpi	0.027 pF	**TMIN**	-263.15 DegC
Cgd0	0 pF	**Noimod**	0
Cgdpe	0 pF	**NoiseR**	0.5
P10	3.3	**NoiseP**	1
P11	5.9	**NoiseC**	0.9
P20	0	**Fnc**	0 GHz
P21	0	**Kf**	0

P30	0	**Af**	1
P31	0	**Ffe**	1e-9 GHz
P40	0	**Tg**	25 DegC
P41	0	**Td**	25 DegC
P111	0	**Tdl**	0.1
Ij	0.2 mA	**Tmn**	1
Pg	15	**Klf**	0
Ne		**Fgr**	0 GHz
Vjg	0.8	**Np**	1
Rg	2.5 Ohm	**Lw**	100 um
Rs	2.4 Ohm	**AFAC**	1
Rgd	2 Ohm	**NFING**	1

Table 3.1 Final values for the Angelov-Chalmers transistor model of the EC2612 FET.

3.6 IMPLEMENTATION OF A MILLIMETRE-WAVE SELF-OSCILLATING MIXER

The final SOM design step is the development of the device for an RF input frequency of 35 GHz. Two different designs have been considered, the first one being a third-harmonic SOM based on the same transmission-line circuit concept as presented in section 3.2 scaled to the millimeter-wave range, and the second circuit following a new topology employing an SIW cavity.

3.6.1 Transmission-line based SOM

The design proposed in this section follows the same concept as outlined previously at a different design frequency. The RF input is 35 GHz and downconverted using the third harmonic of the oscillation signal at 11 GHz. As in the previously proposed low-frequency circuit concept, the RF input is filtered by a coupled line filter and fed to the center of the transmission line, which is used to provide resonance between the two transistors. The outputs are combined with an IF balun and filtered by two stepped impedance filters.

The structure is simulated and optimized for conversion gain and fabricated in MHMIC technology on a 10 mil Alumina substrate with a dielectric constant of 9.9. The IF circuitry is realized on a Rogers RT5880 substrate with dielectric constant of 2.2 and connected to the MHMIC part through bond wires. Measurement is carried out through connection with *K*- and SMA connectors, respectively. Figure 3.32 shows a photograph of the implemented and fabricated mixer.

The performance of the presented circuit is only partly satisfactory. The oscillation behaviour of the circuit is very good, yielding a stable LO signal at the desired frequency of 11 GHz. However, the mixing performance is giving a weak result with a conversion gain of only -25 dB.

These problems have been examined carefully and attributed to the difficult circuit performance prediction for subharmonic operation. The transistor used in the design isan MwT-4 FET from Microwave Technologies, Inc., and its transistor model is found to be only specified to match well with measurements up to a frequency of 27 GHz, which represents an unusable modeling solution for our RF input frequency of 35 GHz. Moreover, especially when dealing with high harmonics, the quality of the nonlinearity description in is ubiquitous, which in the given model (Curtice model) was not the case.

The conversion gain of a mixer design is basically determined by the quality of termination of its ports at RF, LO, and IF frequency, their harmonics, and any of their combinations as in (3.1). Thus, if the model cannot predictably describe the transistors impedances at these frequencies, a design cannot be established and conversion gain performance suffers.

Considering these aspects, it becomes understandable, why it is essential to develop a high-quality transistor model for the proposed design, as outlined in section 3.5.

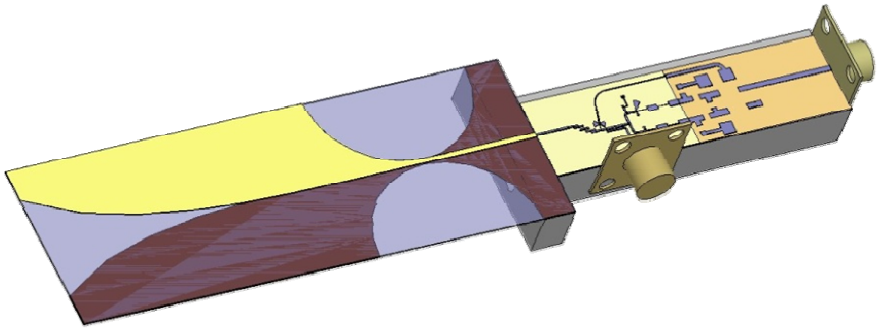

Figure 3.32 3D illustration of the proposed 35 GHz self-oscillating mixer.

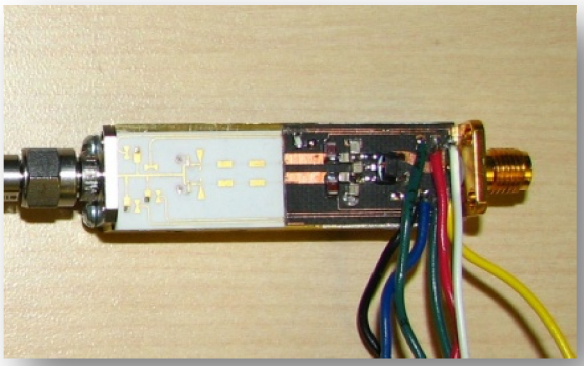

Figure 3.33 Photograph of the proposed 35 GHz self-oscillating mixer.

3.6.2 Substrate integrated waveguide based SOM

Based on the unsatisfactory results with the previous design, a novel concept has been established and is presented in this section.

The concept of the proposed circuit is shown in Figure 3.34. The main idea behind this structure is given by the use of a higher-order mode SIW cavity. It is designed to resonate in a TM_{201} mode, meaning that the two lines connected to the cavity as seen in Figure 3.34 are forced to a phase difference of 180 degrees. This exploits once again the basic concept we have already previously used in the transmission-line based circuit, namely the balancing of the circuit and hence the creation of an oscillation occurring out of phase between the gates of the transistors. This out-of phase relation creates a virtual ground

point for the LO frequency at the center of the structure, i.e. at the RF input and the IF output ports.

Regarding the harmonics of the LO frequency, this symmetry presents a virtual ground to the odd order harmonics (LO, 3 LO, 5 LO, etc.), as well as an open circuit to the even order harmonics (2 LO, 4 LO, 6 LO, etc.). In this way, designing the circuit as a second-order subharmonic self-oscillating mixer, we can extract the IF signal at the IF output simply by combining the two signals in phase.

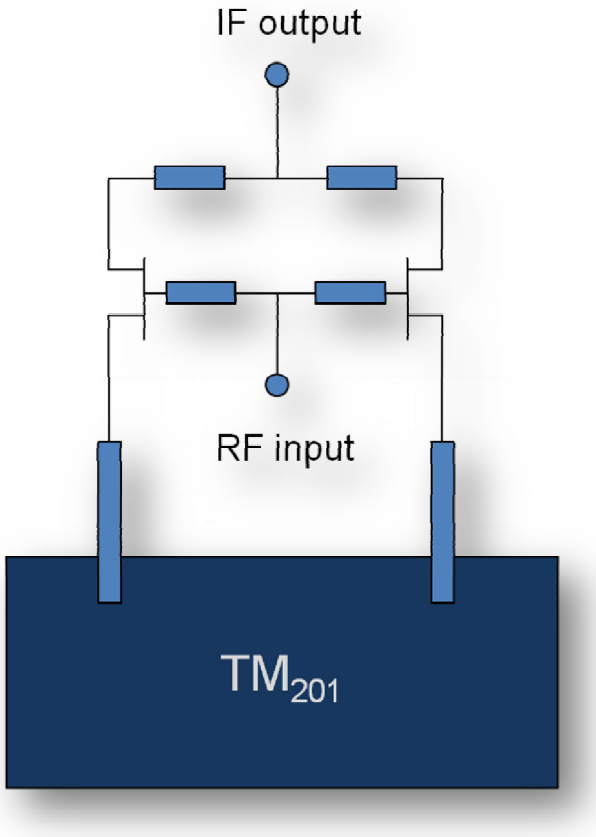

Figure 3.34 Circuit concept for the SIW-cavity based 35 GHz self-oscillating mixer.

The oscillator is designed in a common gate configuration with the sources connected to the resonator. The mixer function is then introduced using a straightforward gate transconductance mixer applying the RF input signal at the gates and extracting the IF output signal from the drain.

3.6.2.1 Substrate Integrated Waveguide Cavity

The cavity in the proposed circuit is realized in SIW technology. In recent years, SIW technology has experienced an enormous success as it offers a highly attractive method for the design of microwave and millimetre-wave waveguide-based integrated components and sub-systems in the form of planar circuits. SIW technology provides a low-cost and low-loss solution for system-on-substrate (SoS) designs allowing for a straightforward integration with other planar technologies such as microstrip and coplanar waveguide. Among the developed structures, SIW-based resonant cavities have been built exhibiting an excellent performance in terms of quality factor [91]. Therefore, an SIW cavity design represents an excellent choice for the use in oscillator circuits, where high quality factors are of importance.

In the presented application, an SIW will be used as the resonating element for the oscillator. However, we face one particular problem in the design of this architecture. The RF circuitry needs to be fabricated in MHMIC technology on an Alumina substrate with high dielectric constant of 9.9 in order to be able to bond the transistor dies to the microstrip circuitry. This, however, introduces a problem, as a cavity design on such a high dielectric substrate is prone to very high losses and unsatisfactory Q-factor performance.

One possible solution to this problem may be the adjacent locating of the SIW cavity and the MHMIC microstrip circuitry and connecting the two structures through wire bonds. However, it is very advisable to avoid bondwires and minimize their use and lengths, due to the inductive termination they introduce, creating problems especially for the design of less-predictable harmonic circuits.

Therefore, the presented design involves a multi-layer structure, in which the SIW cavity is fabricated on a Rogers RT5880 Duroid substrate with a dielectric permittivity of 2.2. It is located below the microstrip circuit layer, and the energy is coupled through a defected ground plane using either slot or via coupling. In this way, the compact-size high-Q structure desired for this application can be realized.

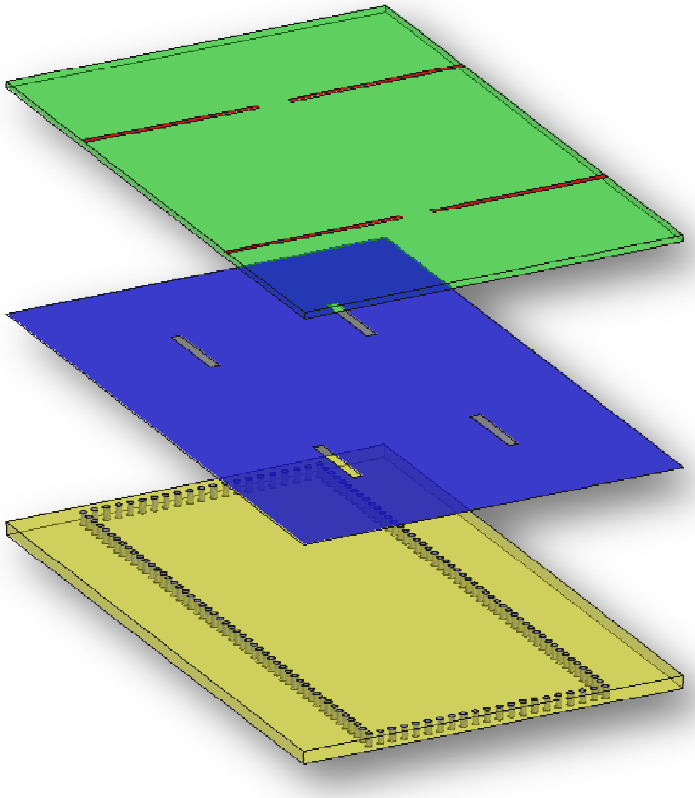

Figure 3.35 Multilayer concept used for the proposed SIW cavity based SOM.

Two different coupling methods have been studied, thereof the first being an aperture coupling structure as shown in Figure 3.35, corresponding to a standard type slotline-to-microstrip transition. Here, an additional requirement of the active circuit comes into consideration: the transistors require a DC return to ground for their biasing, which is why the aperture coupling needs to be realized with a short circuit stub instead of an open circuit stub. The second possibility involves the coupling of the energy through a via post (Figure 3.36and Figure 3.37), which inherently represents a DC return to ground. The method of choice is finally selected to the latter, as the aperture coupling realized with a short circuit stub introduces a second resonance into the frequency response, which interferes with our desired behaviour and is prone to introduce oscillation stability problems in the final oscillator design.

In the presented application we need to build an SIW cavity that resonates at an approximate frequency of 16.7 GHz providing the oscillation frequency, so that an RF input

of 35 GHz is downconverted using the second harmonic of the LO to an approximate IF frequency of 1.6 GHz.

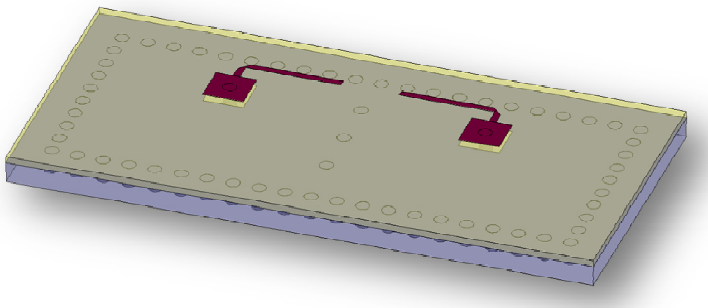

Figure 3.36 3D illustration of the proposed SIW cavity with via post coupling.

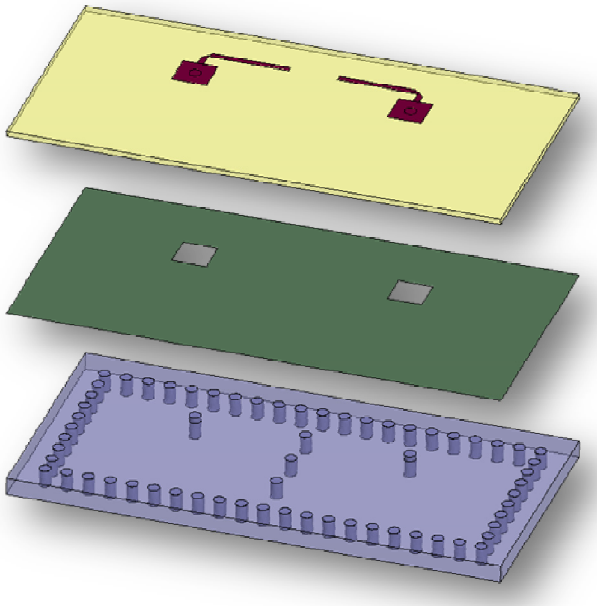

Figure 3.37 Exploded view of the proposed SIW cavity with via post coupling.

Considering these frequency requirements, the cavity has been implemented and simulated in Ansoft HFSS. As it is furthermore visible from Figure 3.36, three additional posts have been inserted in the center of the cavity. These posts are used to suppress

unwanted cavity modes, i.e. the fundamental TM_{101} and the third-order TM_{301} mode, by creating a short circuit to the *E*-field at the position of the post and therefore inhibiting these modes which would have a maximum at the that location. The simulation results are shown in Figure 3.41 and Figure 3.42, showing the *S*-parameters of the structure as well as the successfully implemented out-of-phase field distribution in the cavity.

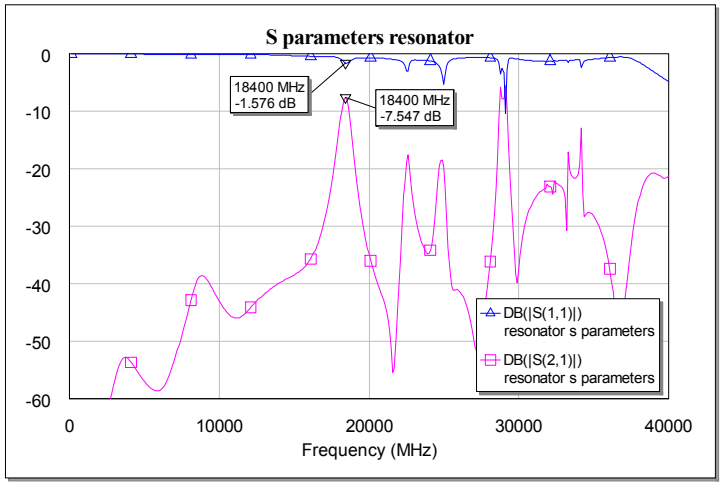

Figure 3.38 Simulated *S*-parameters for the second-order mode SIW cavity.

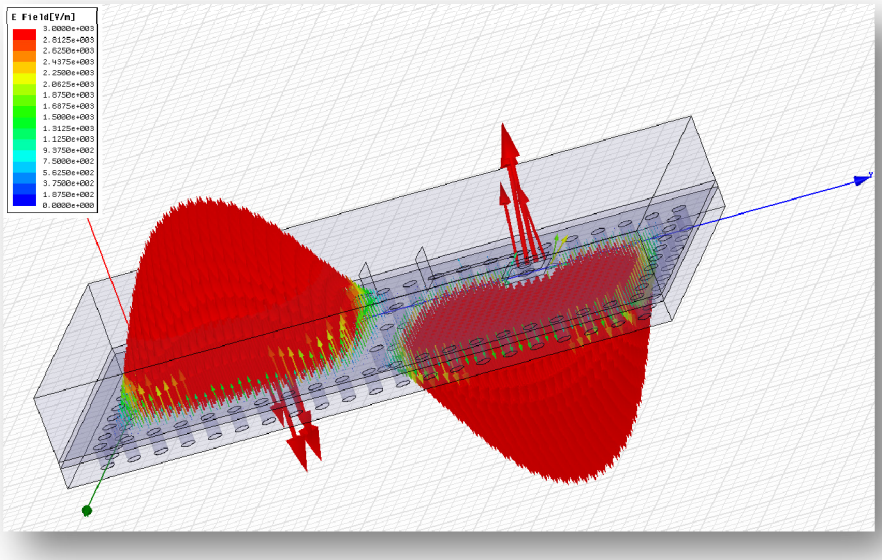

Figure 3.39 Simulated field distribution for the second-order mode SIW cavity.

3.6.2.2 Oscillator Design

Based on the designed cavity, an oscillator circuit has been designed as shown in Figure 3.40. The circuit is designed as a balanced common-gate oscillator architecture. The transmission lines between the gates, given the virtual ground in the center of the structure, are designed for introducing instability in order to enhance oscillation. Their length is determined from the behaviour of the load and source stability circles of the transistor. Then, with the SIW cavity connected to the sources, the drain interconnection can be determined with an appropriate length in order to guarantee oscillation.

The structure is simulated in AWR Microwave Office and results for the current spectrum and waveform are shown in Figure 3.41 and Figure 3.42, respectively.

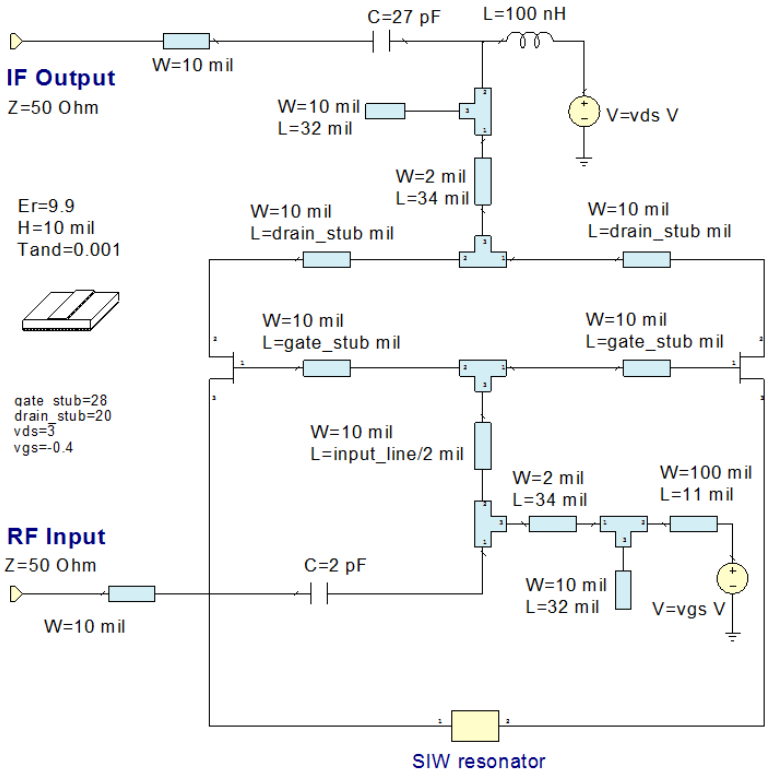

Figure 3.40 Schematic in Microwave Office for the 35 GHz oscillator.

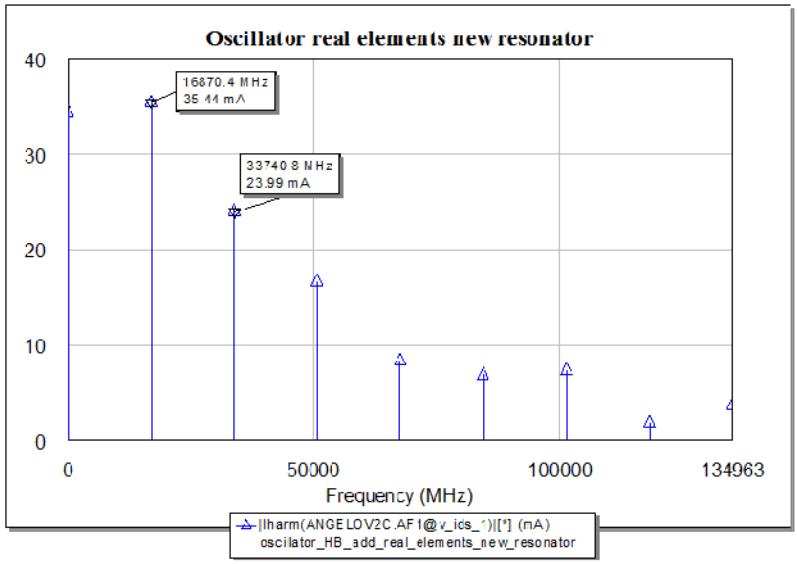

Figure 3.41 Simulated spectrum of the oscillation current.

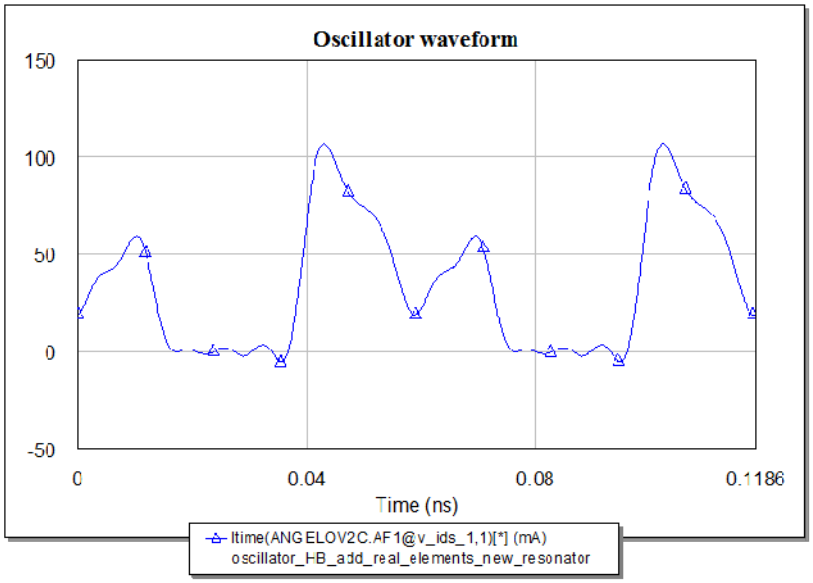

Figure 3.42 Simulated waveform of the oscillation current.

The presented simulation results exhibit a fundamental oscillation current of 35 mA at a frequency of 16.6 GHz at the internal drain node of the transistor. For a proper mixer design, it is essential to provide a large oscillation signal in order to provide a good large-signal pumping for creating the necessary harmonics.

3.6.2.3 Mixer Design

The mixer design is based on a straightforward gate transconductance mixer design. The RF signal is injected from the center of the structure and reaches the transistors in phase, where it is mixed with the out-of-phase oscillation signal. This allows for the generation of even-order mixing products in the case of an in-phase combination of the outputs. In the presented case, the second order is used for the mixing.

As it has already been described, for proper mixer performance it is important to short-circuit the drains at LO frequency, so that the transistor does not drop into the linear region during the LO pumping. This is realized by the virtual ground point at the center of the structure, and it is hence important to keep the lines connecting the drains as short as possible remaining within the requirements of the oscillator design.

Moreover, an open stub at RF frequency at the IF output proves important to be included. On the one hand, it serves as a stabilizing element of the circuit at RF frequency. The second-order harmonic of the LO signal being so close to the RF frequency, the circuit may easily exhibit an input coefficient greater than one at the gates at RF frequency. This would imply that no matching can be applied to the circuit, as it is inherently unstable at RF frequency. Moreover, it may start to oscillate at that frequency, which would entirely alter circuit function. Thus, this possibility needs to be eliminated. Moreover, the bandwidth is critical without this stub, as the output signal sees the IF line as a termination, whose electrical length varies in frequency, which results in a narrow band. An RF short circuit at the gates solves both of the described problems. In addition, a short-circuit stub at 2 LO is included in the design in form of a flag, i.e. a narrow high-impedance line of length $\lambda/4$ connected to a broad low-impedance line of $\lambda/4$. This flag is connected to the IF output line. A stepped-impedance output filter centered around a frequency of 2 LO is included at the IF output.

The simulation results for the mixing function of the presented SOM is shown in Figure 3.43. The RF input power is -10 dBm, thus yielding a simulated conversion gain of 2.4 dB. It is also visible that the remaining frequency components in the IF spectrum are low and thus easily eliminated by filtering.

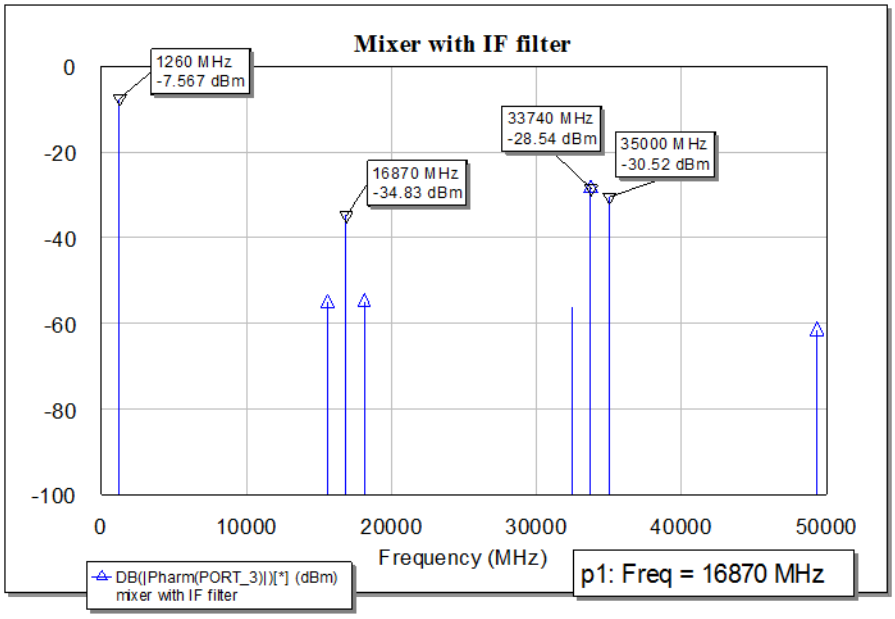

Figure 3.43 IF output spectrum for the 35 GHz self-oscillating mixer.

3.6.2.4 Assembly

Figure 3.44 and Figure 3.45 show a 3D illustration of the implemented 35 GHz self-oscillating mixer. The RF input is connected via a *K*-connector to the multilayer structure consisting of the SIW cavity on the bottom and the MHMIC active circuit containing the transistors on top. The bias connections cannot be soldered onto Alumina substrate and are mounted on the IF circuit on a Duroid substrate with dielectric permittivity 2.2 containing also the stepped impedance output filter.

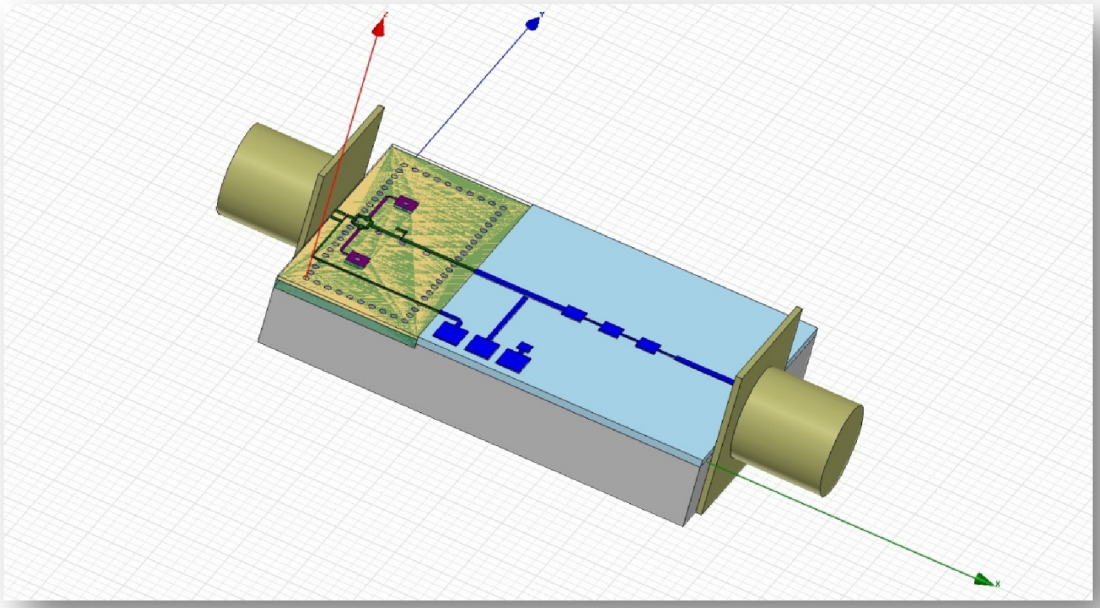

Figure 3.44 3D illustration for the 35 GHz self-oscillating mixer.

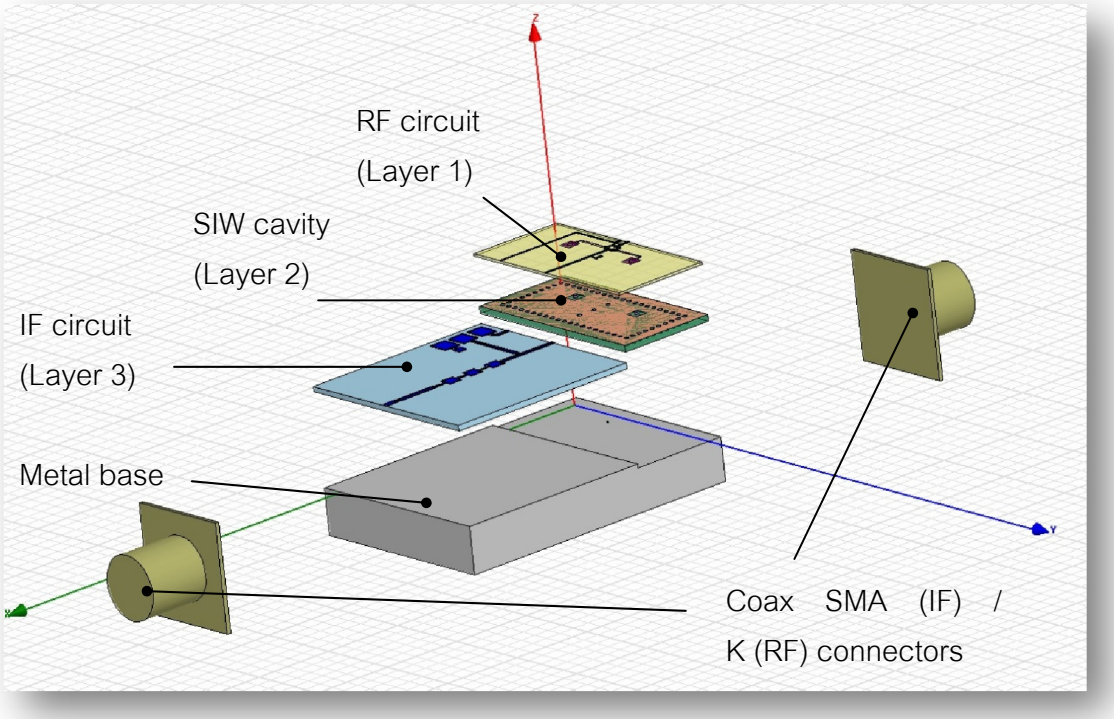

Figure 3.45 3D illustration in explosion view for the proposed SOM.

3.6.2.5 Experimental results

Figure 3.46 shows a photograph of the readily fabricated circuit. It is measured and characterized experimentally and a spectrum of the IF output signal is shown in Figure 3.47.

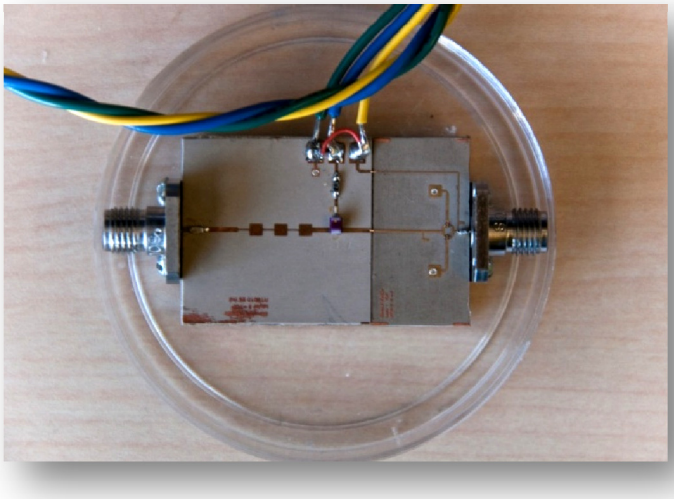

Figure 3.46 Photograph of the 35 GHz self-oscillating mixer.

The graph shows that oscillation at a frequency of 16.2 GHz can be achieved successfully. Applying an input power of -20 dBm to the circuit, an IF output power of -29.6 dBm is measured at an IF frequency of 1.404 GHz. Including cable losses, this yields a conversion gain of -8.7 dB, which is a good result for a subharmonically operating SOM at millimetre-wave frequencies. Figure 3.48 shows the measured conversion gain over bandwidth. A 5-dB bandwidth of 1.5 GHz or 4.2% is obtained, which is sufficient for the final system application requirements.

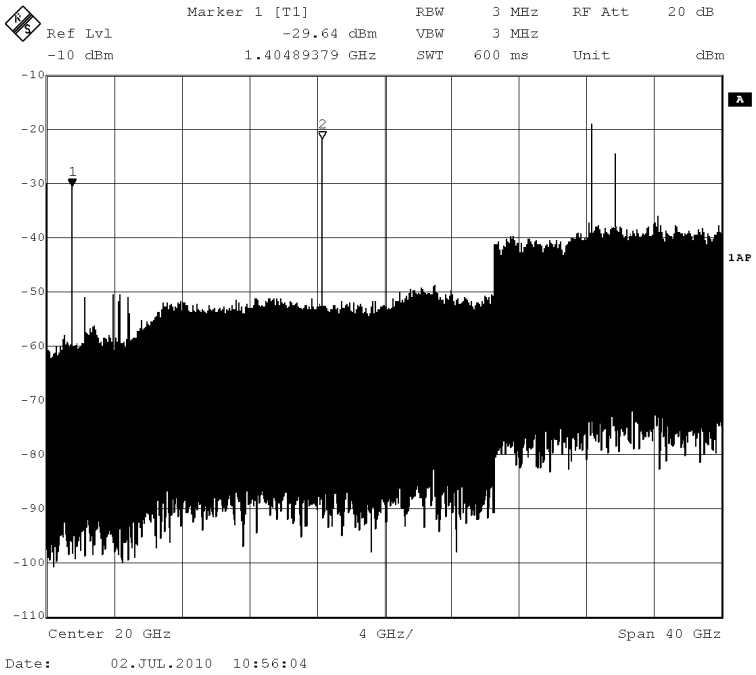

Figure 3.47 Measured IF output spectrum for the 35 GHz self-oscillating mixer.

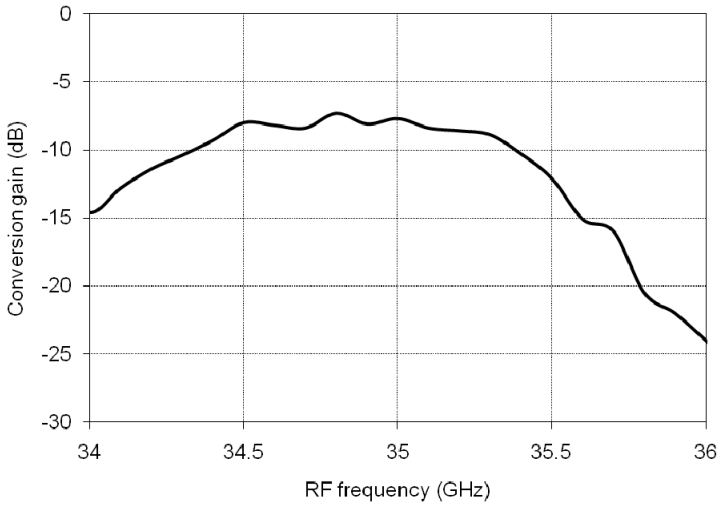

Figure 3.48 Measured bandwidth over RF input frequency.

3.7 THEORETICAL ANALYSIS OF SELF-OSCILLATING MIXERS

A very important part of SOM design consists in the use of adequate simulation and analysis tools in order to correctly predict their performance. Using standard HB methods, it is not straight-forward to analyze SOM circuits because of their autonomous operation nature. In general, standard RF circuit simulators must be adapted in order to be able to simulate these structures. Moreover, specific simulation algorithms may have to be developed, which adapt well to the special characteristics of SOM circuits.

This section deals with the development of a simulation code based on a Volterra series approach combined with a conversion matrix analysis in order to analyze subharmonic SOM behaviour.

The analysis and simulation of FET SOMs are critical due to the autonomous nature of the oscillation signal. There have been various approaches to solve this problem: A time domain method has been used, which has the disadvantage of long simulation times and additional constraints of time-step choice. Furthermore, an extension to the HB method with the help of an iterative optimization process is presented. This approach is interesting but requires an additional optimizing step over the already iterative HB algorithm, which yields a computationally intensive analysis procedure. Itoh applied the Volterra series approach to the problem of SOMs, which allows for an effective and rapid computation of harmonic components and shows very good accuracy for weakly nonlinear structures. Furthermore, it does not require any iterative procedure and is applicable to CAD solutions by using the nonlinear current method.

However, applying this procedure to subharmonic SOMs becomes very cumbersome: the analytical derivation of the Volterra kernels becomes increasingly laborious for higher orders and is therefore in most cases limited to a description up to the third order. In addition, higher-order coefficients derived from a transistor's DC *I-V* characteristics can significantly deviate from its RF behavior and thus can introduce large errors for higher order analyses.

In this research work, a novel hybrid solution to this problem is presented: the oscillating steady-state condition is derived from the Volterra series solution, whereas the mixing phenomena are analyzed by a conversion matrix method. The advantage of using a

conversion matrix description is its simple nature and the fact that computational effort does not increase with mixing order. Furthermore it is an easy single-step calculation after finding the oscillation steady-state condition and does not require any additional iteration, such as for example HB. The small-signal assumption of the mixing phenomena analysis holds true, since saturation effects shall not be considered. Moreover, this method provides a tool for future investigation on noise and intermodulation analysis.

3.7.1 Theory

The subharmonic SOM circuit investigated is shown in Figure 3.4. It combines a balanced oscillator structure with a singly-balanced gate mixer in order to form a third-order subharmonic SOM.

The proposed analysis is divided into two steps: at first the oscillating part of the circuit is analyzed by a Volterra series approach. A break is introduced into the circuit at an arbitrary point, as it is shown in Figure 3.49a. In this way, the circuit is converted into a one-port and the problem is reduced to the description by its input impedance Z_{IN}. Thus, the oscillation steady-state condition is reached for an input impedance Z_{IN} equal to zero at the break point. The analysis gives the oscillation frequency ω_0 and current I_0.

As a second step, the result for the oscillation can be applied as an input to the mixer analysis, which is described by a simple conversion matrix approach. The oscillation current I_0 can be converted to a voltage V_s at the mixer input, and a time-varying transfer admittance Y_{tran} of the circuit can be derived (shown in Figure 3.50b), which yields the conversion matrix and therefore the circuit's conversion gain. This approach includes losses due to mismatching.

3.7.1.1 Oscillator analysis

To determine oscillation behavior, an ideal current source I_0 is added at the artificial port created by the break-point (see Figure 3.49b). An ideal input impedance Z_0 presenting an open circuit at the fundamental oscillation frequency ω_0 and a short circuit at its harmonics is added to the port.

The input impedance Z_{IN} is a function of the oscillation frequency ω_0 and the current I_0. At small-signal condition, the observed input impedance is equal to the linear impedance. As

the oscillation builds up, the nonlinearity in the circuit influences the current level I_0 and therefore changes Z_{IN}. Thus, a nonlinear representation of the input impedance becomes necessary. Using the Volterra series expansion, Z_{IN} can be written in the following form:

$$Z_{IN}(\omega_0, I_0) = Z_1(\omega_0) + \tfrac{3}{4} Z_3(\omega_0, \omega_0, -\omega_0)|I_0|^2 + \tfrac{5}{16} Z_5(\omega_0, \omega_0, \omega_0, -\omega_0, -\omega_0)|I_0|^4 + \ldots \quad (3.11)$$

with Z_1, Z_3, and Z_5 as the first-, third-, and fifth-order Volterra kernels. The linear small-signal input-impedance is represented by $Z_1(\omega_0)$. Even-order components do not appear in (3.11) since only odd-order terms contribute to the fundamental oscillation frequency ω_0.

The Volterra kernels can be derived in an efficient manner by the nonlinear current method. For each nonlinear element, a port is added to the circuit as shown in Figure 3.49b: the first order voltages at these ports are found by the response of the linear circuit. Then, the second order response can be found by exciting the circuit with the first order currents. Subsequently, this method can be applied for the third order. A *Z*-Matrix relates the currents and voltages in between these ports.

The problem is now defined by the two unknowns ω_0 and I_0. Iterating the input impedance over the input frequency and the nonlinear current to find its zeros will give the oscillation steady-state solution.

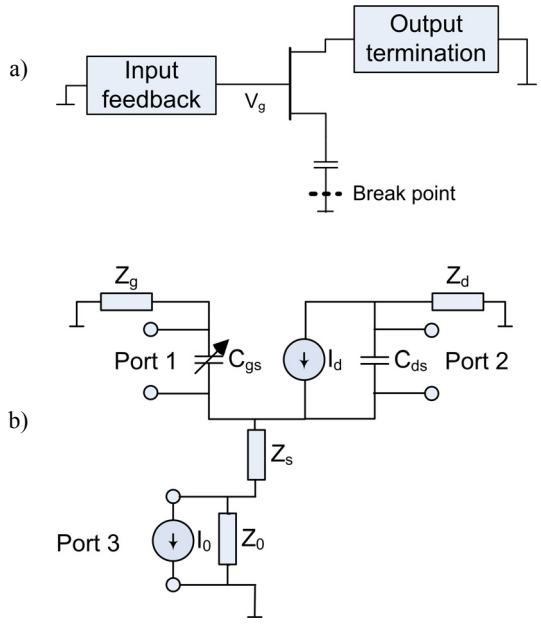

Figure 3.49 Schematic of the oscillator circuit: a) the circuit is converted into a one-port with an arbitrary break-point, b) the detailed oscillator circuit with the transistor model and an artificial current source $\mathbf{I_0}$.

3.7.1.2 Mixer simulation

Finally, the result of the oscillation analysis gives rise to the conversion matrix analysis. In this approach, the device of interest is described as a multiport network, each port representing a mixing frequency of interest. Conversion matrices for each circuit element relate current and voltage components at different mixing frequencies. The nonlinear elements are represented by matrices contain the Fourier coefficients for the oscillation frequency and its harmonics. Since linear circuit theory holds true for each matrix element, Kirchhoff's laws can be applied to connect the circuit elements. Finally, a conversion matrix can be developed for the entire circuit deriving its transfer impedance. This conversion matrix gives a result for the conversion gain between RF and IF frequencies.

After finding the transfer admittance matrix $\mathbf{Y_{tran}}$ for the entire circuit and extracting the components for the mixing frequencies of interest, a 2 x 2 matrix relating RF and IF currents is obtained:

$$\begin{bmatrix} I_{d,IF} \\ I_{d,RF} \end{bmatrix} = \begin{bmatrix} Y_{tran,11} & Y_{tran,12} \\ Y_{tran,21} & Y_{tran,22} \end{bmatrix} \begin{bmatrix} V_{s,IF} \\ V_{s,RF} \end{bmatrix} \tag{3.12}$$

where $I_{d,IF}$, $I_{d,RF}$, $V_{s,IF}$, and $V_{s,RF}$ represent the drain current and input voltage (as shown in Figure 3.49 and Figure 3.50) for IF and RF frequencies, respectively.

Subsequently, the final conversion gain considering matching with source and load impedances is given by

$$G_t = 4\left|Y_{tran,12}\right|^2 \mathrm{Re}(Z_{in})\mathrm{Re}(Z_{out}) \tag{3.13}$$

with Z_{in} and Z_{out} as the load and source impedances.

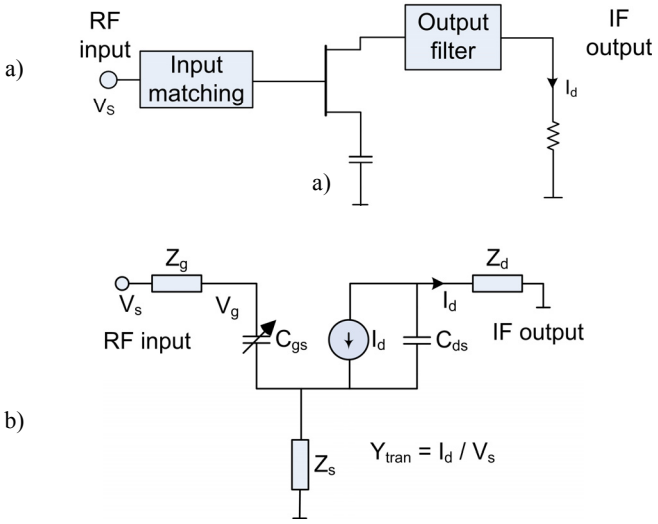

Figure 3.50 Schematic of the mixer circuit: a) the mixing circuit with input matching and output filter, b) the detailed mixer circuit with the transistor model described by the transfer admittance $\mathbf{Y_{tran}}$.

3.7.2 Numerical and Experimental Results

In order to verify the proposed method, the balanced third-harmonic SOM circuit in section 3.2 is considered. An input RF frequency of 5.8 GHz is applied and the measured oscillation frequency builds up to 1.88 GHz, which yields an IF frequency of 160 MHz. The device used is a NE34018 FET, which is described by a simplified nonlinear TriQuint TOM model as shown in Figure 3.51.

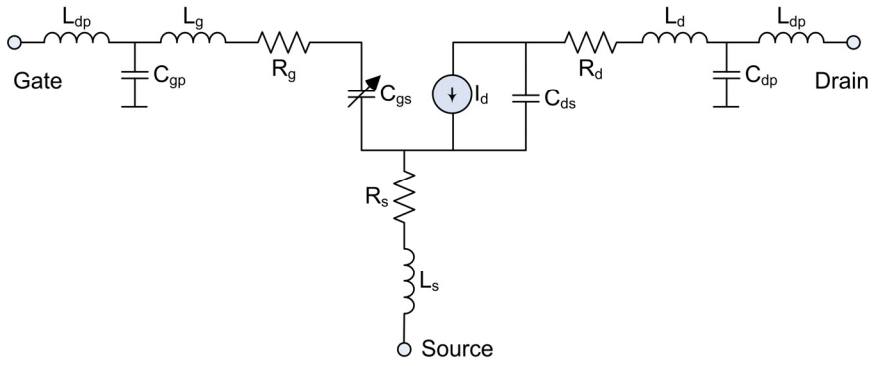

Figure 3.51 Simplified nonlinear model for the NE34018 FET used in this analysis including two nonlinear elements C_{gs} and I_d.

In this analysis, we include two nonlinear elements: the drain current source I_d and the gate-to-source capacitance C_{gs}. The gate-to-drain capacitance C_{gd} and the nonlinear effects of the drain-to-source voltage V_{ds} are neglected because their contribution is small but significantly complicates the analysis. For simplifying the calculation, the parasitic elements of the transistor are combined with the input- and output networks in simplified impedances Z_s, Z_g, and Z_d as shown in Figure 3.49 and Figure 3.50. Furthermore, only a single branch of the balanced circuit is analyzed since it can be easily extended to the full structure by doubling the conversion gain.

For the oscillation analysis, an iterative algorithm to search for zeros has been adapted. It searches for an oscillation frequency ω_0 by finding a zero of the imaginary part of the small-signal input impedance Z_{IN}, from which a guess for the current can be generated. As the oscillation current builds up, the input impedance is influenced, and a new ω_0 has to be determined. This process is repeated until the input impedance can be made to zero.

The proposed algorithm is independent of the initial guess and converges to the correct value, since the possibility of converging to local minima is eliminated.

Finally, the conversion matrix analysis can be adapted. The transfer admittance matrix $\mathbf{Y}_{\mathbf{tran}}$ is given by the inverse matrix of

$$\mathbf{Z}_{\mathbf{tran}} = -\mathbf{Z}_{\mathbf{S}} - \left[\left(\mathbf{Z}_{\mathbf{gs}} + \mathbf{Z}_{\mathbf{g}} + \mathbf{Z}_{\mathbf{S}}\right)\left(\mathbf{Z}_{\mathbf{cds}} + \mathbf{Z}_{\mathbf{d}}\right)\right]\left[\mathbf{Z}_{\mathbf{g}} + \mathbf{Z}_{\mathbf{gs}} + \mathbf{G}\mathbf{Z}_{\mathbf{gs}}\mathbf{Z}_{\mathbf{cds}}\right]^{-1} \tag{3.14}$$

with $\mathbf{Z}_{\mathbf{s}}$, $\mathbf{Z}_{\mathbf{g}}$, and $\mathbf{Z}_{\mathbf{d}}$ as the simplified impedance matrices for the source-, drain-, and gate circuit elements as shown in Figure 3.50 and $\mathbf{Z}_{\mathbf{gs}}$ and $\mathbf{Z}_{\mathbf{cds}}$ equal to the impedance matrices of the gate-to-source capacities C_{gs} and C_{ds}. From this equation, the conversion gain for a single branch of the circuit can be calculated with (3.13). Finally, the balanced nature of the design is considered by a 3-dB increase in conversion gain.

In order to verify the presented technique, the third harmonic SOM circuit in Figure 3.5 has been fabricated as shown in Figure 3.9.

With bias voltages of V_{gs} = −0.6 V and V_{ds} = 2 V and in- and output load impedances of 50 Ω, we measure a conversion gain of 9.2 dB, which compares very well with a simulated value of 9.06 dB.

A more detailed result of the proposed analysis is shown in Figure 3.52. The conversion gain over the gate bias voltages V_{gs}, for which the circuit is oscillating, is shown. A maximum conversion gain is obtained for V_{gs} = −0.6 V and V_{ds} = 2 V. This result agrees very well with the fact that for third-order harmonic mixing, the third-order Fourier coefficient must be maximized. The simulated and measured results agree very well.

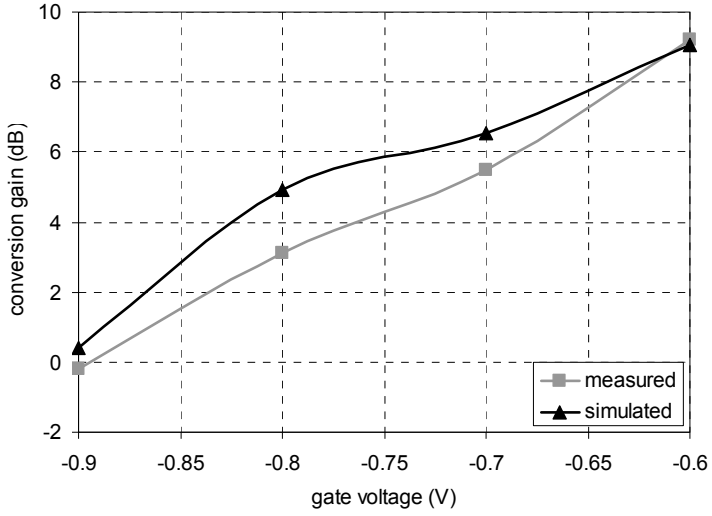

Figure 3.52 Comparison of the simulated and measured conversion gain over the gate bias voltage for a drain bias voltage of V_{ds} = 2 V.

In Figure 3.53, the oscillation frequency and its variation over the drain bias voltage V_{ds} are shown. The obtained values agree very well in simulation and measurement. The deviation in the slope is due to the neglected description of the nonlinearity for the circuit elements with the drain voltage V_{ds}. A further reason for the deviation is the neglected the gate-to-drain capacity C_{gd}.

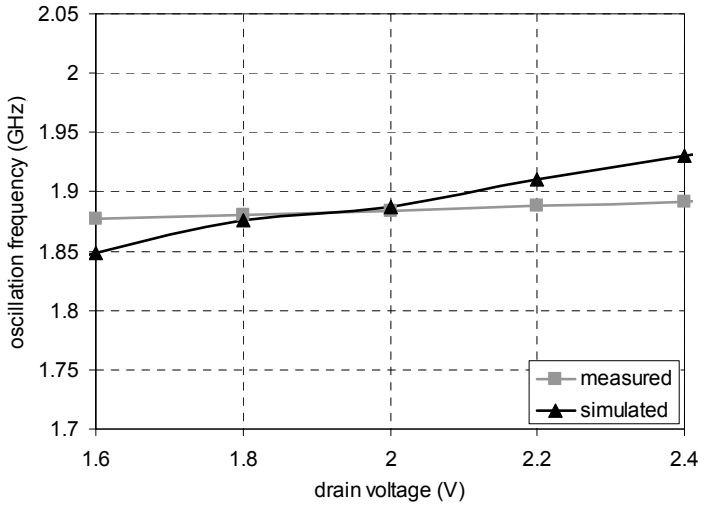

Figure 3.53 Comparison of the oscillation frequency over the drain bias voltage for a gate voltage V_{gs} = −0.6 V.

3.8 CONCLUSIONS

This chapter has introduced the main work of the presented Ph.D. thesis, which is concerned with the development of subharmonic SOMs. The chapter presents the basic nomenclature and functionality of SOMs and continues with the design of a low-frequency prototype in order to verify functionality before moving on to the millimetre-wave design. Circuit performance was excellent with a conversion gain of +11.1 dB. Subsequently, the circuit is designed at 35 GHz with a conversion gain of -9.7 dB using an SIW cavity. The chapter also includes theoretical analysis methods for SOMs and performance models that assess its practical applicability in system environments.

Chapter 4

ANTENNA DESIGN

This chapter presents the requirements for the presented radiometer antenna. The chapter outlines the design of two different feed types and their combination with a reflector that can be mechanically steered for image scanning. Theoretical analyses, simulation results, and measurements are presented. The work presented in this chapter has been completed in collaboration with a master student from the University of Pavia, Italy [86].

4.1 INTRODUCTION

As previously described, one of the various possibilities to obtain a passive millimetre-wave image is to perform an *x-y* scan across the scene of interest using a single-element receiver. The radiation is focused onto the receiver by means of a parabolic reflector that is mechanically rotated in order to progressively steer the beam direction toward the currently scanned image pixel. The purpose of the antenna is to collect the emitted energy from the target and present it to the radiometer input.

4.2 REFLECTOR ANTENNA BASICS

In this project the passive radiation emerging from the object of interest is focused on the receiver by a parabolic reflector antenna. According to the laws of optics and analytical geometry, for this type of reflector all the reflected rays are oriented parallelly to the axis of the paraboloid, which ideally gives a single reflected ray parallel to the main axis with no sidelobes [67].

Moreover, reflector antenna patterns yield very high boresight gain, and even if their beam directions are fixed at the time of antenna installation, pencil-beam reflectors may be fully steerable by mechanical means as it is carried out in this project.

The performance of these reflectors cannot be properly examined without knowledge of the feed configuration. In order to reduce aperture blocking effects, the best set-up is given by an offset feed configuration. In this way the feed can be directly connected to the radiometer, thus yielding the further advantage of decreasing the losses from long connections between the antenna and the rest of the receiver circuit.

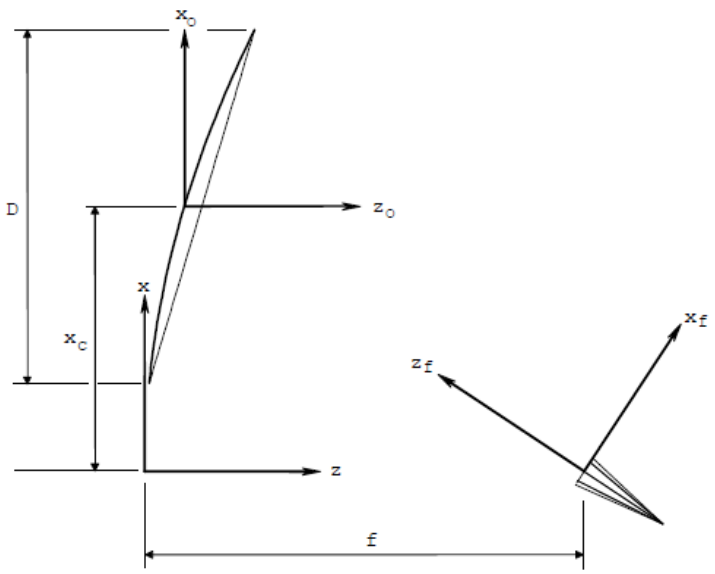

Figure 4.1 Reflector dish in offset configuration (D is the main reflector diameter, f is the main reflector focal length, and x_o is the distance between the main reflector axis and the axis of the parabola.)

Figure 4.1 shows a general sketch of an offset feed configuration with D as the main reflector diameter, f as the main reflector focal length, and x_o as the distance between the main reflector axis and the axis of the parabola.

4.2.1 Antenna Characteristics

The antenna is one of the most critical parts of the image system. In order to understand the design and realization of a reflector some of the key parameters that affect antenna behaviour are presented [67]. In the development of offset parabolic reflectors, design parameters such as the offset angle, illumination taper, location and orientation of the feed,

polarization, etc., are used to achieve the desired beamwidth, side lobe level, efficiency, and gain.

4.2.1.1 Antenna Gain

Gain is a measure of how much of the input power is concentrated in a particular direction. It is expressed with respect to a hypothetical isotropic antenna, which radiates equally in all directions. Thus in the direction (θ, φ), the gain is:

$$G(\theta, \varphi) = \frac{dP/d\Omega}{P_{in}/4\pi} \tag{4.1}$$

where P_{in} is the total input power and dP is the increment of radiated output power in solid angle $d\Omega$. The gain is maximum along the boresight direction. The input power is:

$$P_{in} = \frac{{E_a}^2}{\eta} \times \frac{A}{Z_0} \tag{4.2}$$

where E_a is the average electric field over the area A of the aperture, Z_0 is the impedance of free space, and η is the net antenna efficiency.

The output power over solid angle $d\Omega$ is:

$$dP = \frac{d\Omega}{Z_0} \times E^2 \times r^2 \tag{4.3}$$

where E is the electric field at distance r. But by the Fraunhofer theory of diffraction,

$$E = \frac{E_a}{r} \times \frac{A}{\lambda} \tag{4.4}$$

along the boresight direction, where λ is the wavelength. Thus the boresight gain is given in terms of the size of the antenna by the important relation:

$$G = \eta \times \frac{4\pi}{\lambda^2} \times A \tag{4.5}$$

This equation determines the required antenna area for the specified gain at a given wavelength. The net efficiency η is the product of the aperture taper efficiency η_a , which depends on the electric field distribution over the antenna aperture and the total radiation efficiency $\eta^* = P/P_{in}$ associated with various losses. These losses include spillover, ohmic heating, phase nonuniformity, blockage, surface roughness, and cross polarization. Thus:

$$\eta = \eta_a \times \eta_* \tag{4.6}$$

For a typical antenna, η = 0.7. For a reflector antenna, the area is simply the projected area. Thus for a circular reflector of diameter *D*, the area is $A = \frac{\pi D^2}{4}$ and the gain is:

$$G = \eta \times \left(\frac{\pi D}{\lambda}\right)^2 \tag{4.7}$$

which can also be written:

$$G = \eta \times \left(\frac{\pi D}{c} \times f\right)^2 \tag{4.8}$$

since $c = \lambda f$, where *c* is the speed of light (3 × 108 m/s), λ is the wavelength, and *f* is the frequency. Consequently, the gain increases as the wavelength decreases or the frequency increases.

4.2.1.2 Half-power beamwidth

The half power beamwidth (HPBW) is the angular separation between the half power points on the antenna radiation pattern, where the gain is one half the maximum value. For a reflector antenna it may be expressed:

$$HPBW = k \times \frac{\lambda}{D} \tag{4.9}$$

where k is a factor that depends on the shape of the reflector and the method of illumination. For a typical antenna, k =70° (1.22 if α is in radians). Thus the half power beamwidth decreases with decreasing wavelength and increasing diameter. The gain may be expressed directly in terms of the half power beamwidth by eliminating the factor D/λ. Thus:

$$G = \eta \times \left(\frac{\pi k}{HPBW}\right)^2 \tag{4.10}$$

where *HPBW* is expressed in degrees. This is a well known engineering approximation for the gain (expressed numerically). It shows directly how the size of the beam automatically determines the gain. The value of the numerator will be somewhat different in each case depending on the percentage of the power radiated flowing through the half-power beamwidth. Typical values are:

$$G = \frac{27000}{(HPBW)^2} \quad \text{, for 45\% of radiated power} \tag{4.11}$$

$$G = \frac{31000}{(HPBW)^2} \quad \text{, for 60\% of radiated power} \tag{4.12}$$

The horizontal spatial resolution for a microwave radiometer may be different from the HPBW of the antenna, and it is a function of the scan geometry of the instrument and the signal processing applied to the measurement. The spatial resolution as function of half power beamwidth is expressed as:

$$\Delta x = R\frac{HPBW\pi}{2 \times 180} \tag{4.13}$$

Since, as early explained, the HPBW depends on antenna gain, which is in turn a function of the antenna diameter, the dimensions of the reflector antenna become a key parameter to achieve the desired image resolution.

4.2.1.3 Antenna Directivity

Antenna directivity can be expressed as follows:

$$D(\theta, \varphi) = 4\pi \times \frac{power\ radiated\ per\ unit\ solid\ angle}{total\ power\ radiated\ by\ the\ antenna} \tag{4.14}$$

4.2.1.4 Antenna Efficiency

Antenna efficiency is defined as the ratio between gain and directivity in the wanted direction theta phi.

$$\xi = \frac{G(\theta, \varphi)}{D(\theta, \varphi)} \tag{4.15}$$

4.2.1.5 Antenna Pattern

A radiation pattern is a way of plotting the radiated energy from the antenna. This energy is measured at various angles at a constant distance from the antenna.

The main beam (or main lobe) is the region around the direction of maximum radiation, usually the region that is within 3 dB of the peak of the main lobe.

The sidelobes are smaller beams that are away from the main beam. These sidelobes are usually radiation in undesired directions which can never be completely eliminated. That's why the sidelobe level is an important parameter used to characterize radiation patterns.

4.2.1.6 Beam Width

It's the angular range of the antenna pattern in which at least half of the maximum power is still emitted. Bordering points of this major lobe are therefore the points at which the field strength has fallen in the room around 3 dB regarding the maximum field strength.

4.2.1.7 Aperture

Instead of an isotropic radiator, that disperses all energy at a surface of a sphere, a directive antenna concentrates the energy in a smaller area. This area is called effective aperture.

The effective aperture of an antenna A_e is the surface presented to the radiated (or received) signal. It's a key parameter, which governs the performance of the antenna. The gain antenna is related to the effective area by the following relationship:

$$G = 4\pi \times \frac{A_e}{\lambda^2} \tag{4.16}$$

The aperture efficiency depends on the distribution of the illumination across the aperture. If this is linear the effective collecting area of a reflector antenna can approach its projected geometric area:

$$A = \frac{\pi D^2}{4} \tag{4.17}$$

$$G = \eta \times \frac{4\pi \times A}{\lambda^2} \tag{4.18}$$

4.2.1.8 Polarization

The radiation field of an antenna is composed of electric and magnetic lines of forces. These lines are always at right angle to each other. The electric field determines the direction of polarization of the wave. The oscillations of the electric field may be oriented in a single direction (linear polarization), or the oscillation direction of the electric field may rotate as the wave travels (circular or elliptical polarization).

4.3 ANTENNA REQUIREMENTS FOR RADIOMETRY APPLICATIONS

The requirements for antennas in imaging systems are determined by its specifications in terms of spatial resolution but also its aperture distribution.

4.3.1 Spatial resolution

A highly important parameter for defining the performance of an imaging system is its spatial resolution. It is defined as the minimum separation of the object of interest from its surrounding that can be resolved by the imager, or in other words, for each object to be resolved, there should be at least one associated pixel in the final image. It mainly depends on the antenna gain and on the resolution of the mechanical stepping. For achieving a high resolution, a narrow beamwidth needs to be established, which corresponds to an antenna exhibiting high gain. In this project, as a first goal, we intend to achieve a spatial resolution of 2 cm for a target distance of 1 m. The spatial resolution can be calculated from the following relations:

$$HPBW = \frac{2\,\Delta x\,180}{\mathrm{R}\cdot\pi} \tag{4.19}$$

$$G = \frac{27000}{(HPBW)^2} \tag{4.20}$$

From (4.19) and (4.20) the required antenna gain is thus calculated to 37 dBi.

4.3.2 Aperture distribution

In many applications such as imaging radars tapering is used to transform the uniform antenna aperture distribution into a Gaussian distribution in order to reduce side lobes. Conversely, in radiometer design antennas with a uniform or even negatively tapered aperture distribution are used in order to attain the maximum spatial resolution available.

4.3.3 Losses

The minimization of losses in the antenna is a further very important design consideration, as the radiometric signal collected by the receiver is very weak in nature. The antenna input of the receiver is the weakest part of the receiver and any losses introduced at this point are highly critical. A high antenna loss reduces the measured radiometric brightness temperature and thus presents it to a receiver with proportionally higher system noise and therefore degrades receiver sensitivity.

4.3.4 Bandwidth

The antenna also needs to exhibit a certain bandwidth, so that a large portion of the noise spectrum can be collected, which increases measured power and therefore sensitivity.

4.4 REFLECTOR DIMENSIONING

As a matter of saving cost in the proposed project, we assess the possibility of using a commercially available satellite TV dish as a possible reflector antenna solution. Custom reflector antenna designs are very costly in manufacturing especially for the low number of prototypes used in this project, and the tight requirements on surface quality and shape make it difficult to fabricate it in our own laboratory.

Considering the requirements in terms of low weight and low size we are facing in the presented application, it may moreover prove a good idea to reduce the dimensions of the reflector to a size corresponding only to the area the feed actually illuminates, discarding the portion of the reflector remaining unused. This saves weight and hence power in the final motor movement, but also reduces reflector size and therefore production and material cost in a mass-producible final system solution.

4.4.1 Reflector with original dimensions

The original dimensions of the parabolic reflector are given as 51.5 cm in length and 48 cm in width. A first measurement of the reflector (Figure 4.2 and Figure 4.3) with an SGH as

feed antenna is carried out in the anechoic chamber. The SGH employed in this experiment is a broadband horn operating between 18 and 40 GHz with an aperture of 5 cm x 5 cm, a length of 11.2 cm, and an angle illumination of 53°. It exhibits a gain of 17 dBi with a beamwidth of 17° at -3dB. The measurement results in a maximum gain of 37 dBi compared to a calculated value of 38 dBi.

Even though the results in terms of gain are satisfactory for the proposed image acquisition task, reducing the reflector size is recommended in order to improve the overall system design.

Figure 4.2 Reflector antenna measurement.

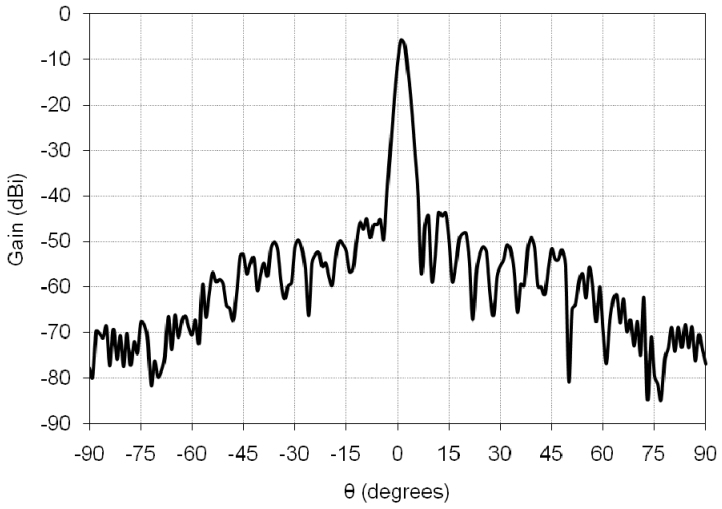

Figure 4.3 Radiation pattern of the reflector antenna on the vertical plane.

4.4.2 Reflector with reduced dimensions

Starting from the plot in Figure 4.3 and calculating the illuminated area on the reflector, it is noticed that not the entire reflector surface is illuminated by the feed. Calculations of the gain as a function of reflector diameter have been performed via simulation in Grasp with the input values given in Table 4.1.

Para-meter	Description	Value
θ_f	Offset angle	25°
θ_{ill}	Feed illumination angle at −10 dB	26+26° = 52°
F	Main reflector focal length	29.09 cm
Ψ_u	Angle between paraboloid axis and highest illumination ray	$\theta_f + \theta_{ill}/2$
H	Height relative to angle between paraboloid axis and lowest illumination ray	$F\tan(\theta_f + \theta_{ill}/2)$
D	Diameter of the illuminated surface	$2F\tan(\Psi_u/2) - H$
x_o	Distance between main reflector axis and parabola axis	$D/2 + H$

Table 4.1 Required parameters for the simulation of the reduced reflector dimensions in Grasp.

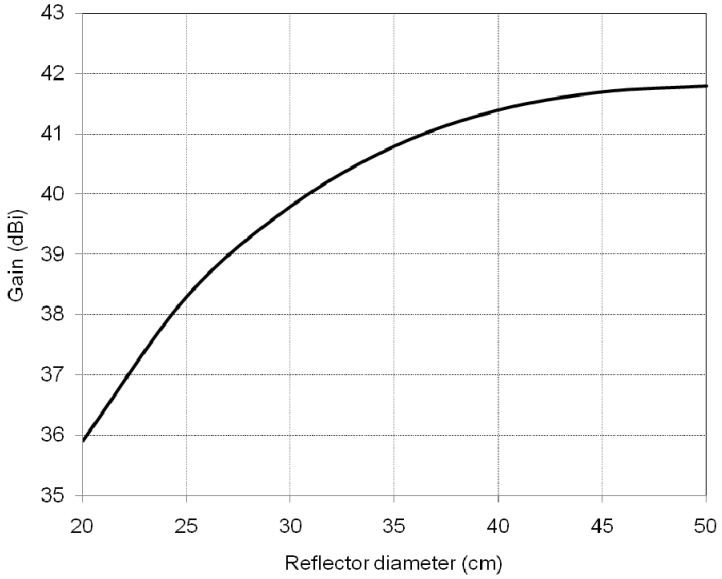

Figure 4.4 Reflector gain as a function of reflector diameter.

Figure 4.4 shows the simulated results for the antenna gain as a function of the reflector diameter. It is obvious that beyond a certain value, the gain remains more or less constant with only very low variation. For this reason, a diameter value of 30 cm has been selected as a good balance between slight gain loss (approximately 2dB at 30 cm) and the advantages outlined previously that may be achieved using reduced reflector dimensions. Table 4.2 shows the values obtained with the help of Grasp for optimum illumination. These values calculate to a diameter of 28.5 cm, very similar to the value of 30 cm selected in the final application.

Para-meter	**Value**
$\boldsymbol{\theta_f}$	25°
$\boldsymbol{\theta_{ill}}$	26+26°
$\boldsymbol{F}$	29.09 cm
$\boldsymbol{H}$	$F \tan(\theta_f + \theta_{ill}/2)$ = -0.5 cm

$\boldsymbol{D}$	$2F\tan(\Psi_u/2) - H = 28.25$cm
$\boldsymbol{x_o}$	$D/2 + H = 13.62$ cm

Table 4.2 Simulation results for the reduced reflector dimensions.

4.4.2.1 Measurements

The smaller reflector is then measured in the anechoic chamber together with the SGH antenna feed in order to compare performance. The maximum reflector gain is measured to 36.79 dBi, very close to the value measured with the original size reflector, which proves that the reflector dimension reduction was carried out correctly and successfully.

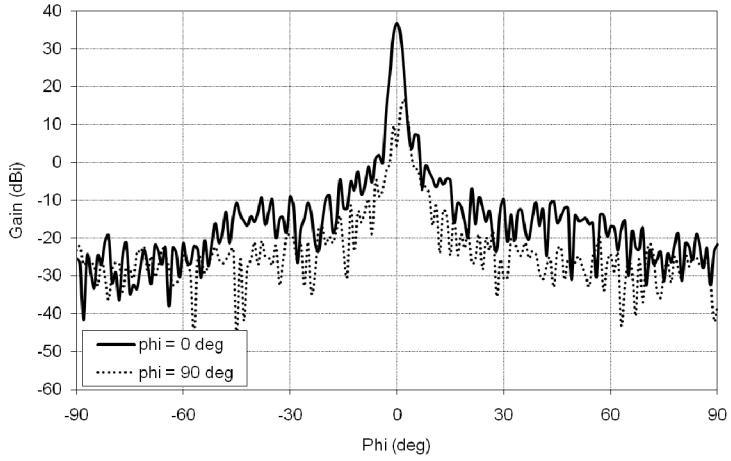

Figure 4.5 Gain radiation pattern of the reflector with a feed horn (theta plane)

4.5 REFLECTOR WITH VIVALDI FEED

An additional important consideration for the proposed antenna is concerned with the dimensions, weight, and performance of the feed antenna. A smaller and lighter feed with the same characteristics as the SGH employed in the previous section will, of course, represent a better choice for this project as it further reduces the weight and size of the system. One such design is given by the so-called Vivaldi antenna [40]. The unique characteristics of the Vivaldi antenna include a theoretically frequency-independent

structure, which in practice offers a very large bandwidth of around 50%. Moreover, due to its large size compared to the wavelength, it provides high gain and narrow beamwidth. It shows endfire characteristics and is used in numerous applications such as imaging radar and radiometer and UWB circuits.

4.5.1 Vivaldi feed design

The Vivaldi antenna is a slotline antenna with an exponential tapering to offer the broadband and high-gain capability described earlier. The tapering curve is shown in Figure 4.6.

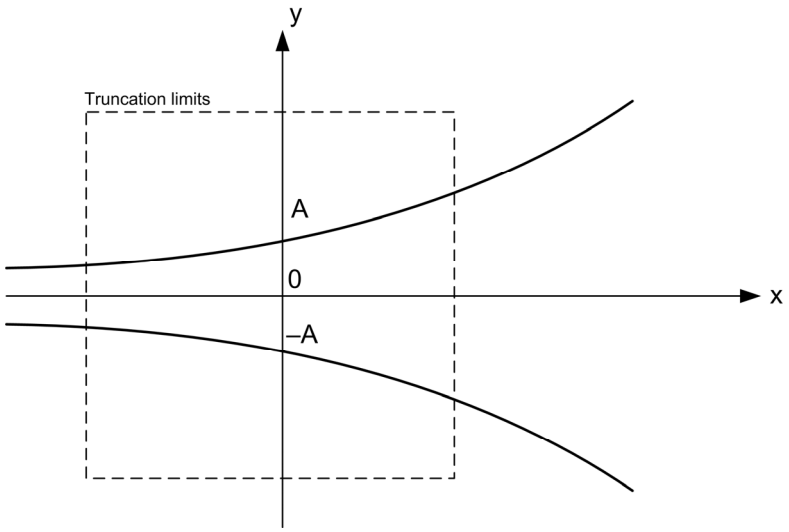

Figure 4.6 Geometrical dimensions of a Vivaldi antenna.

This antenna type uses a balanced slotline architecture, whereas the receiver circuit proposed for this project is designed in single-ended microstrip technology. Therefore, it is necessary to insert a transition in form of a balun between these two geometries into the antenna structure. Recently, this problem has been solved by using an antipodal antenna geometry with a balun as shown in Figure 4.7 [42].

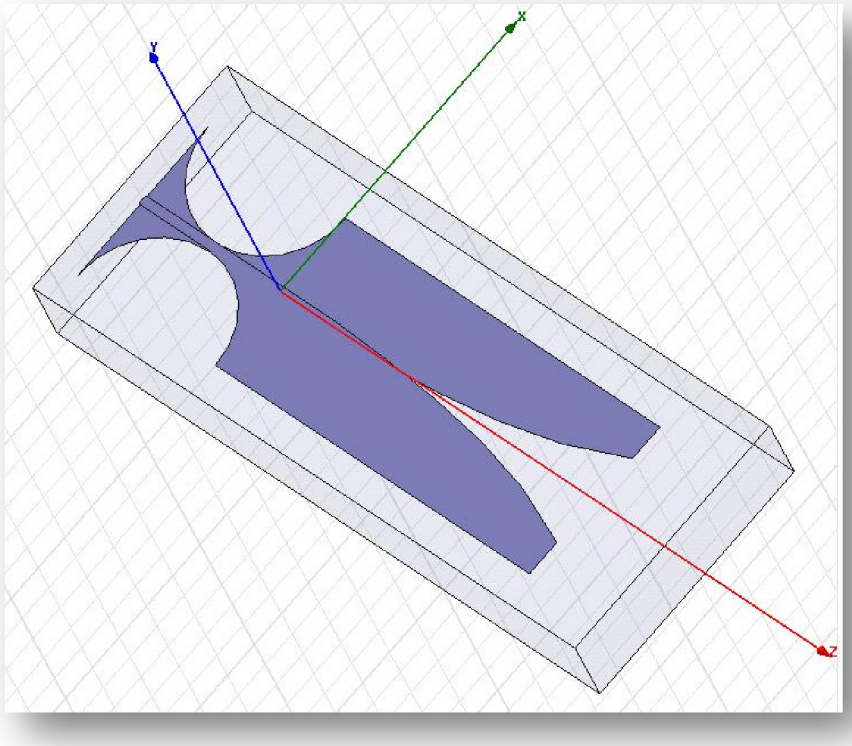

Figure 4.7 Schematic of the proposed Vivaldi antenna.

4.5.1.1 Results

The antenna geometry in Figure 4.7 has been analyzed in simulation in order to predict proper functionality. The antenna design is proposed using a Taconics TLY substrate with a dielectric permittivity of 2.17 and a thickness of 10 mil. We obtain a gain of approximately 13 dBi in the simulation, which is a very good result for such a planar design. Figure 4.8 shows a photograph of the fabricated Vivaldi antenna. It is connected via a standard *K* connector and tested for gain performance in the anechoic chamber.

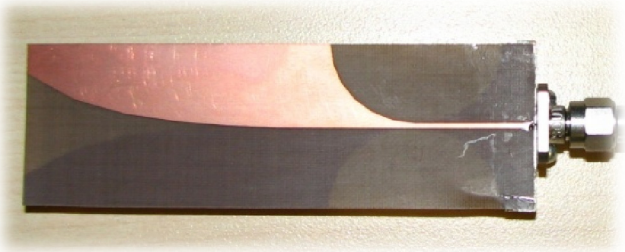

Figure 4.8 Photograph of the proposed Vivaldi antenna.

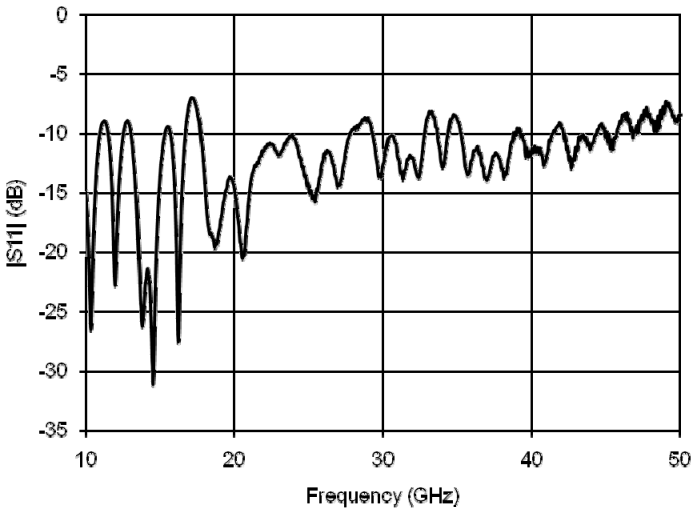

Figure 4.9 Measured matching results for the proposed Vivaldi antenna.

Measurements in the anechoic chamber give results close to simulations, with a co-polarization maximum gain of 9.27 dBi calculated on the vertical plane. Moreover, it can be seen how the beam width for the main lobe is approximately 30°.

Cross-polar radiation yields good results, and matching is below -9 dB for the entire frequency band from 10 to 40 GHz. For better illustration, in Figure 2.5 and Figure 2.6 the radiation pattern is shown in a 2D plot for *E*-plane and *H*-plane. The different gain curves as a function of θ for different fixed values of φ are shown.

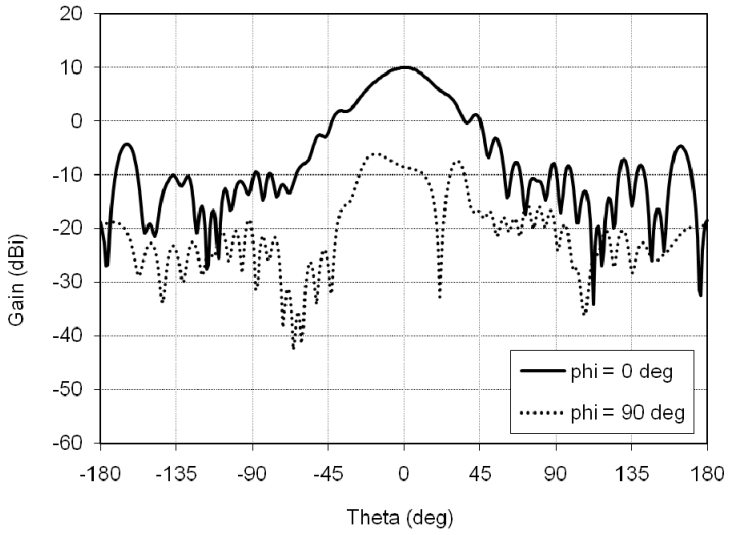

Figure 4.10 Magnitude on the *E*-plane for co- and cross-polarization.

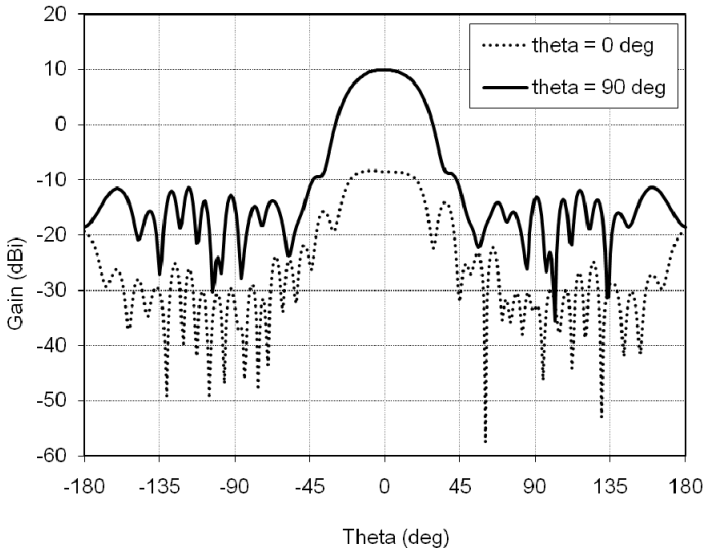

Figure 4.11 Magnitude on the *H*-plane for co- and cross-polarization.

Figure 4.12 shows the phase as a function of the illumination angle θ. It will be a key plot to understand the considerations in section 4.5.2 examining the overall gain.

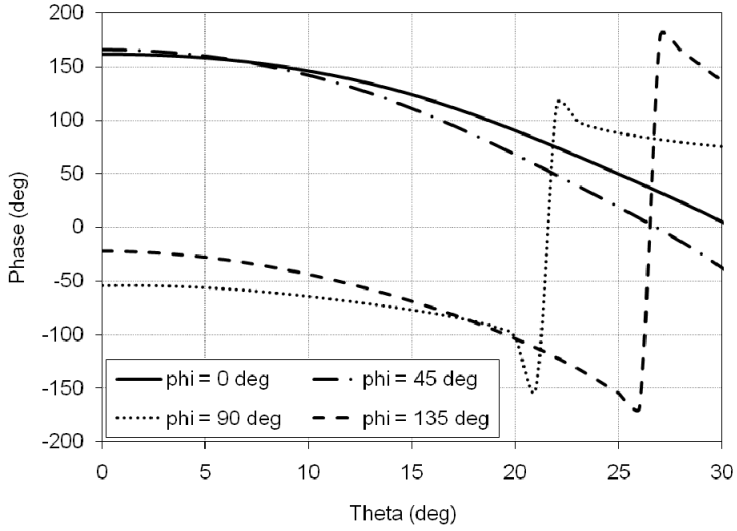

Figure 4.12 Vivaldi phase characteristics (*E*-plane).

4.5.2 Reflector with Vivaldi feed

This section is dedicated to the analysis of the reflector dish (reduced in dimensions) used in combination with the Vivaldi antenna feed.

4.5.2.1 Simulations

It is important to note that all the simulations carried out in section 4.4.2 utilize a Gaussian beam pattern feed. More accurate simulations importing the Vivaldi pattern data instead of the Gaussian waveform show an interesting result.

In this way, the simulation of the reflector shows a maximum gain of approximately 30 dBi, compared to a maximum gain of 45 dBi in the previous case of an ideal Gaussian beam pattern. This significant difference in performance can be attributed to two main causes. First, the paraboloid reflector intercepts only a fraction (approx. 85%) of the power generated by the feed. Second, the illumination in the view angle of ±30°, though not exhibiting a large variation in amplitude, shows a variation in phase of almost 180° as shown in Figure 4.12. This means that the power illuminating the paraboloid in the portions close to the edges is of almost opposite phase with respect to the inner portion, thus decreasing the achieved gain.

In fact a simulation of the same paraboloid using the Gaussian feed reducing the illumination to approximately 85% and applying a uniform phase distribution yields a maximum gain greater than 40 dBi. This shows that the main contribution to the loss in gain indeed comes, as expected, from the phase cancellation described earlier. Thus, interestingly, reducing the reflector size to 30 cm actually increases the gain by 2 dB, due to the fact that the opposite phase contributions are eliminated by removing the outer portion of the reflector as shown in Figure 4.13 and Figure 4.14.

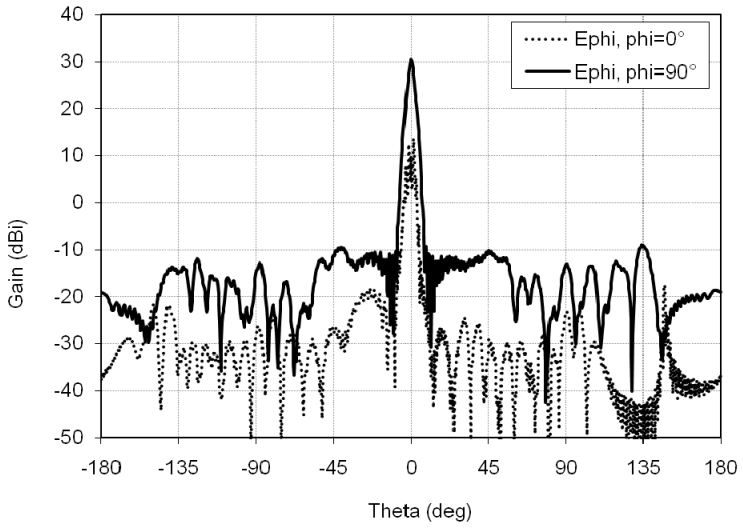

Figure 4.13 Reflector radiation pattern with Vivaldi feed and *D*=50cm.

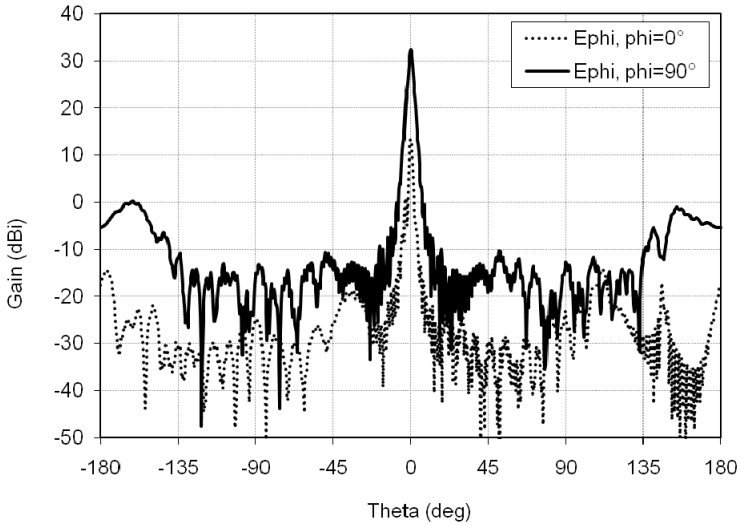

Figure 4.14 Reflector radiation pattern with Vivaldi feed and D=30 cm.

A final observation reveals that the reflector contains holes for mounting the supporting arm, which are positioned on the reflector making it impossible to perform the actual cut as previously simulated. Simply changing the offset angle to 34.15°, however, yields an illuminated area which can be safely cut out without introducing big changes to the gain performance. The results of a simulation performed with the new offset angle are shown in Figure 4.15.

Para-meter	**Value**
$\boldsymbol{\theta_f}$	34.15°
$\boldsymbol{\theta_{ill}}$	26+26°
$\boldsymbol{F}$	29.09 cm
$\boldsymbol{H}$	$F\tan(\theta_f + \theta_{ill}/2) = 4.16$ cm
$\boldsymbol{D}$	$2F\tan(\Psi_u/2) - H = 29.53$cm
$\boldsymbol{x_o}$	$D/2 + H = 18.92$ cm

Table 4.3 Simulation parameters for the reduced reflector dimensions with new offset angle.

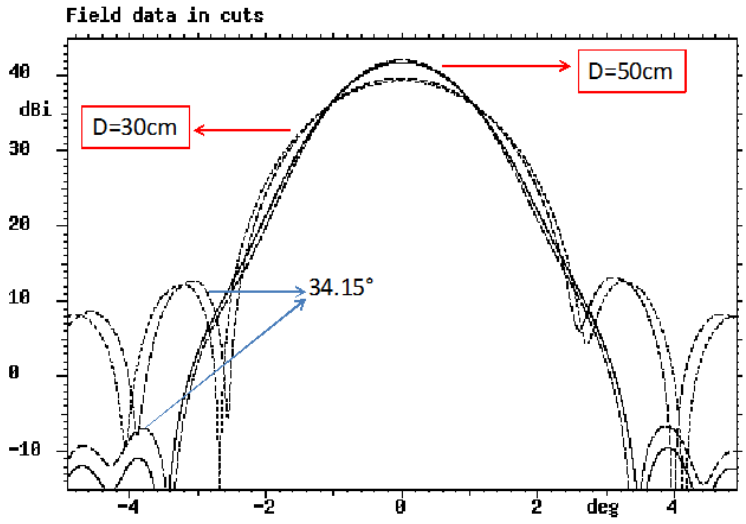

Figure 4.15 Reflector gain for a uniform illumination pattern at 25° and 34.15° offset angle.

4.5.2.2 Measurements

In order to test the behaviour of the simulated reflector together with the Vivaldi antenna feed, measurements in the anechoic chamber are presented.

Including cable loss of approximately 9 dB, we achieve a final gain of 28.64 dBi for the reflector dish together with the Vivaldi feed. Even if this value is close to the simulated result, the much smaller and lighter Vivaldi antenna yields unsatisfying gain performance caused by the non-uniformity in the illumination phase as described earlier.

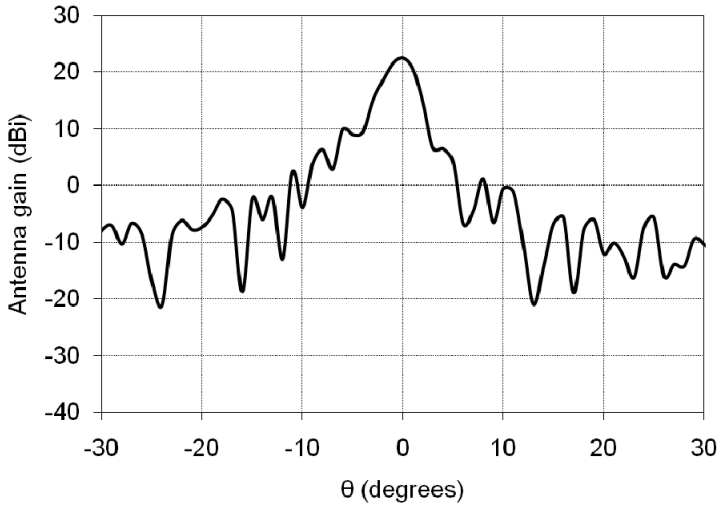

Figure 4.16 Reflector gain for a uniform illumination pattern at 25° and 34.15° offset angle.

4.6 REFLECTOR WITH CUSTOM HORN FEED

As the result for the Vivaldi feed presented in the previous section is unsatisfying, a new feed horn antenna is designed, which attempts to combine the advantages from both gain characteristics close to the already available SGH and the lightweight compact size properties of the Vivaldi feed.

The most widely used horn antenna is a pyramidal horn which is obtained flaring the dimensions of a rectangular waveguide in both *E*-field and *H*-field directions; its radiation characteristics are a combination of the *E*- and *H*-plane sectoral horns.

The design of such a pyramidal horn starts from the desired gain G_o and the dimensions a and b of the rectangular feed waveguide. The design objective for the proposed horn antenna is then to optimize the remaining dimensions (a_1, b_1, ρ_e, ρ_h, p_e, and p_h as shown in Figure 4.17) for optimum antenna gain.

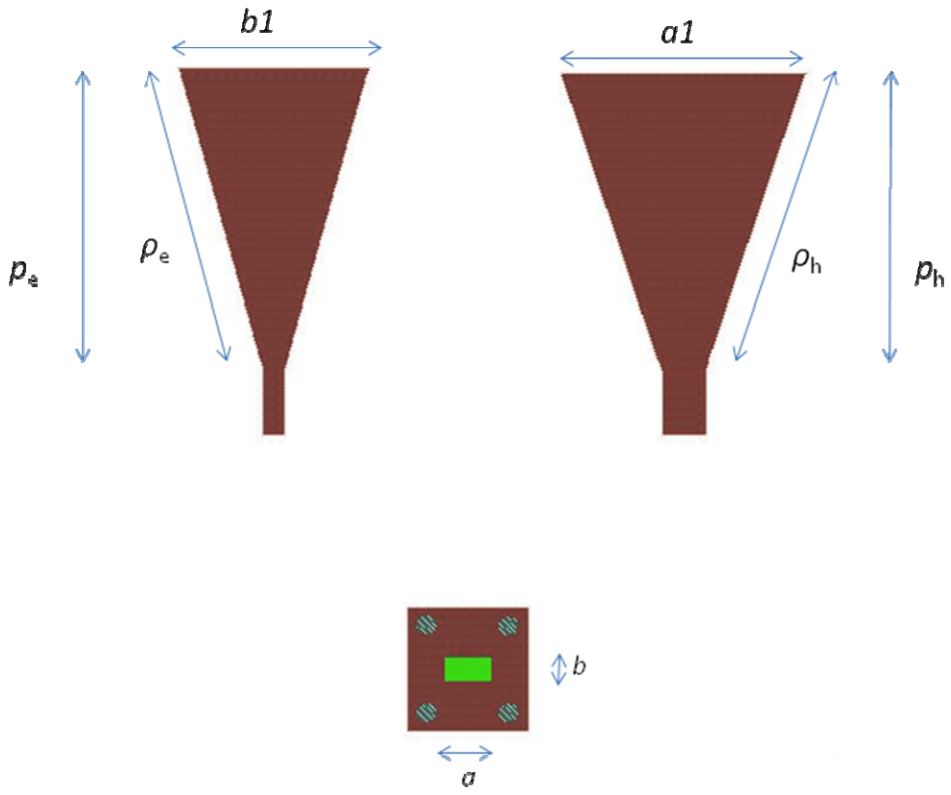

Figure 4.17 Pyramidal Horn and waveguide dimensions.

In the following, the design equations for the proposed horn structure are presented [67]. As a first step, values for b_1 and a_1 are selected, which lead to optimum directivities for the *E*- and *H*- plane sectoral horns, respectively:

$$b_1 \simeq \sqrt{(2\lambda\rho_1)} \tag{4.21}$$

$$a_1 \simeq \sqrt{(3\lambda\rho_2)} \tag{4.22}$$

As the overall efficiency (including both the antenna and aperture efficiencies) of a horn antenna is approximately 50%, the gain of the antenna can be related to its physical area. Thus, using:

$$G_0 = \in \frac{4\pi}{\lambda^2}\,(a_1 \times b_1) = \frac{2\pi}{\lambda^2}\sqrt{3\lambda\rho_2}\sqrt{2\lambda\rho_1} \simeq \frac{2\pi}{\lambda^2}\sqrt{3\lambda\rho_h}\sqrt{2\lambda\rho_e} \tag{4.23}$$

as for long horns $\rho_2 \sim \rho_h$ and $\rho_1 \sim \rho_e$ holds true. For a pyramidal horn to be physically realizable, p_e and p_h must be equal.

$$p_e = (b_1 - b)\left[\left(\frac{\rho_e}{b_1}\right) - \frac{1}{4}\right]^{1/2} \tag{4.24}$$

$$p_h = (a_1 - a)\left[\left(\frac{\rho_h}{a_1}\right) - \frac{1}{4}\right]^{1/2} \tag{4.25}$$

Expressing this equality, the following horn design pyramidal equation can be established:

$$\left(\sqrt{2\chi} - \frac{b}{\lambda}\right)^2 (2\chi - 1) = \left(\frac{G_0}{2\lambda}\sqrt{\frac{3}{2\pi}}\frac{1}{\sqrt{\chi}} - \frac{a}{\lambda}\right)^2 \left(\frac{G_0}{6\pi^3}\,\frac{1}{\chi} - 1\right) \tag{4.26}$$

The design procedure starts from the set of data in Table 4.4,

Parameter	Value
G	20 dBi
f	35 GHz
λ	8.57 mm
a	0.8296 λ
b	0.4154 λ

Table 4.4 Design parameters for the pyramidal horn.

and follows the procedure outlined below:

1. The first step is given by finding the value of χ, which satisfies the design horn equation for a desired gain G_0 (dimensionless), utilizing an iterative technique and starting from an initial value of

$$\chi = \frac{G_0}{2\pi\sqrt{2\pi}} \tag{4.27}$$

2. Once the correct value for χ has been found, the second step is to determine ρ_e and ρ_h, respectively:

   ρ_e = 5.19 cm

   ρ_h = 5.71 cm

3. At this point, it becomes possible to find the corresponding values of a_1 and b_1

   a_1 = 3.83 cm

   b_1 = 2.98 cm

4. Finally, the values of p_e and p_h are then calculated and:

   $p_h = p_e$ = 4.38 cm

4.6.1.1 Simulations

Before proceeding with the antenna fabrication, simulations of the antenna behaviour have been carried in FEKO in order to predict proper functionality. With the dimensions found in the previous section, a simulated maximum gain of 19.05 dBi is achieved compared to a theoretical value of 20 dBi. This result confirms that the horn is well designed and ready to be fabricated.

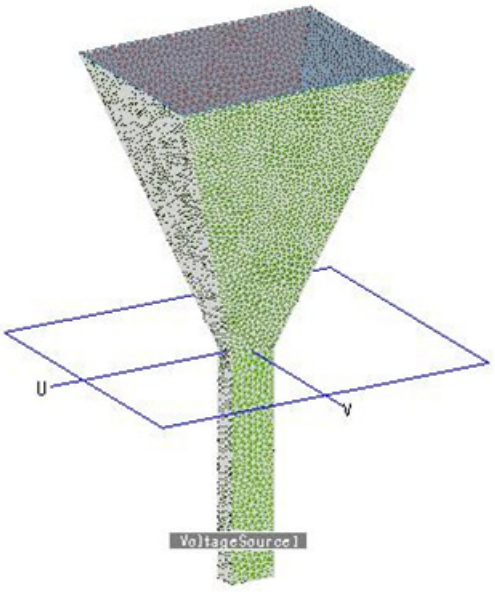

Figure 4.18 Simulated pyramidal horn in FEKO.

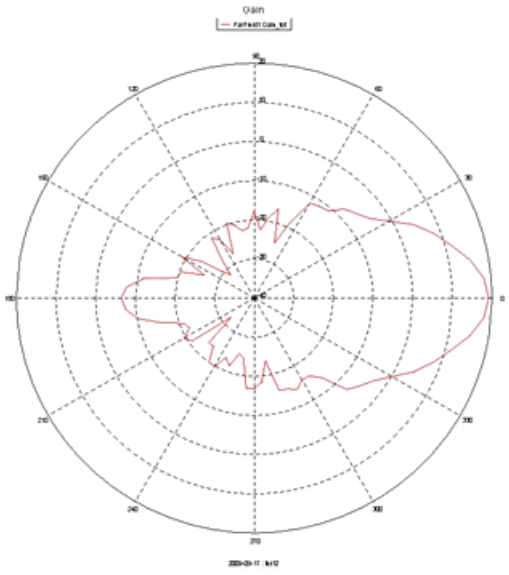

Figure 4.19 Polar plot of the simulated gain for the pyramidal horn antenna.

4.6.1.2 Measurements

The fabrication of the proposed pyramidal horn is realized in a very cost-effective and fast way using a foldable thin layer of brass for the four side walls of the horn, and a photograph of the final structure is shown in Figure 4.20. Measurements of the feed horn in the anechoic chamber confirm the presented simulation results. The maximum gain on the horizontal and vertical plane is equal to 19.02 dBi and 18.96 dBi, respectively, as shown in Figure 4.21.

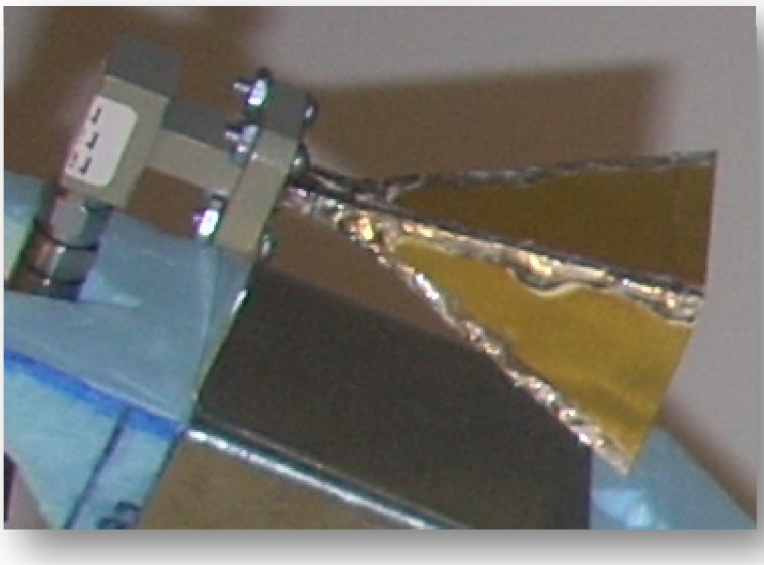

Figure 4.20 Photograph of the realized 20 dBi gain pyramidal horn.

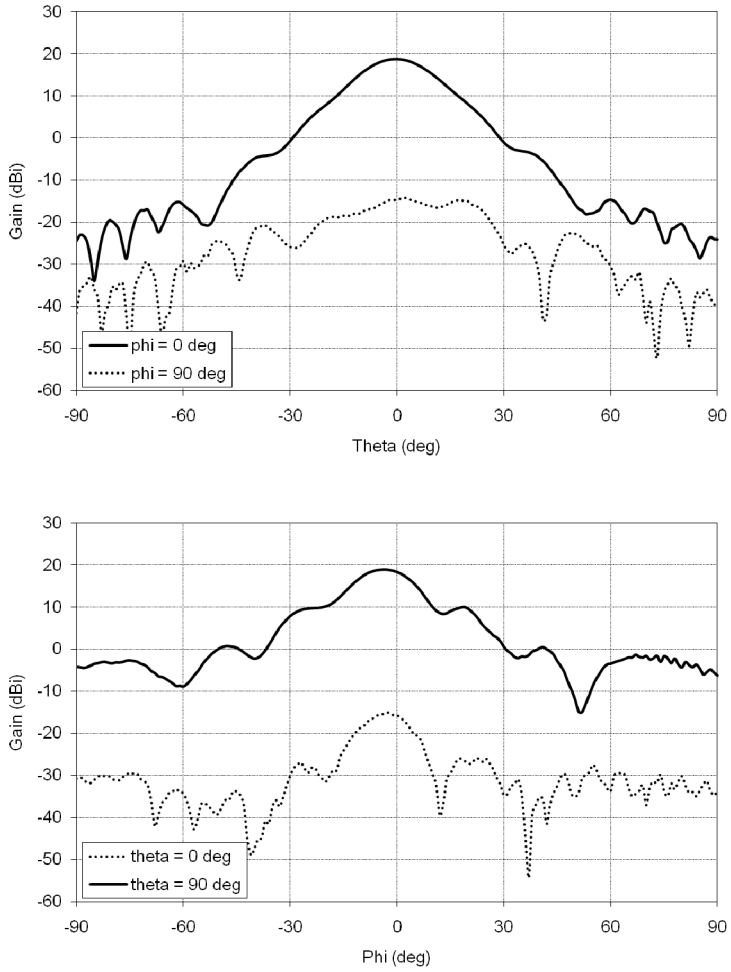

Figure 4.21 *H*- and *E*-plane radiation pattern of the simulated 20 dBi pyramidal horn.

4.6.2 Reflector with custom horn feed

The final step in the proposed reflector antenna design is to mount the designed horn on the reflector dish and measure the radiation pattern. A final maximum gain on the *E*-plane of approximately 34 dBi is measured at 35 GHz.

The beam width at –3dB is almost 1.5° as shown in Figure 4.22. Consequently, the new brass horn presents a strong improvement in terms of weight and size compared with the broadband 17 dBi SGH in section 4.4 and still yields a value of gain that gives the desired spatial resolution of 2 cm at 1 m from the target.

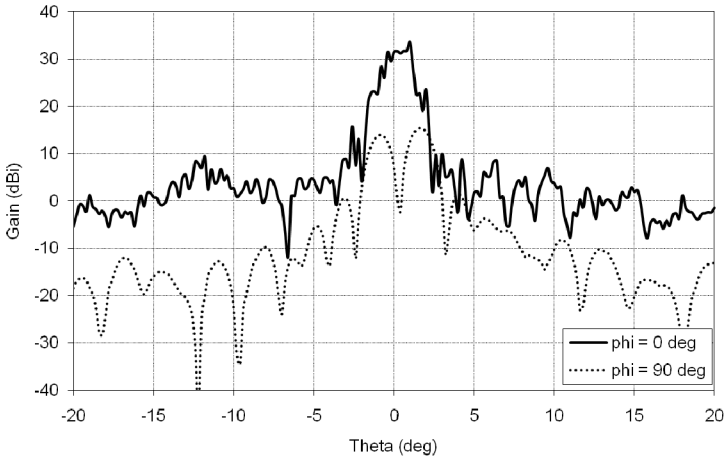

Figure 4.22 Gain measurement of the reflector dish together with the pyramidal feed horn.

4.7 CONCLUSIONS

In this chapter the design, simulation, and testing of a reflector antenna at 35 GHz has been discussed.

The antenna is the first component of the radiometer system. It collects the passive energy radiated by the target and presents it to the input receiver. Scanning of the image required for image acquisition is achieved by a mechanical movement of the reflector.

Two main parameters have been taken in to account in order to design an antenna suitable for this project: the antenna gain, which affects the spatial resolution of the image, and the size and weight of the overall antenna system (reflector, feed, and support mechanics), affecting the performance and requirements for the motors used for the mechanical steering.

Initial considerations concerning the illumination area of a low cost, commercially available reflector suggest that its initial diameter can be reduced by cutting the dish to a smaller diameter, which yields an excellent compromise between reduced dimensions and gain performance.

Subsequently, two different light-weight feed antennas have been tested: a Vivaldi feed and a broadband SGH antenna. The results obtained led to the design of a new light-weight 35 GHz horn feed, which allows for combining the performance advantages of both.

Measurements confirm that it offers the desired performance characteristics, exhibiting very small and light geometric dimensions together with a measured gain of 34 dBi, which yields the initially specified spatial resolution of 2 cm at a target range of 1 m.

Chapter 5

RADIOMETER RECEIVER DEVELOPMENT

This chapter presents the development of a single-element radiometer receiver based on the successfully implemented SOM design presented in Chapter 3. A general outlook on radiometer receiver architectures is shown, along with a performance model, and the proposed design including a feed antenna as designed in Chapter 4 is described and experimentally verified.

5.1 INTRODUCTION

As for the development of low cost and compact receiver imaging radiometer architectures, subharmonic SOMs provide excellent downconverting elements for such architectures. The purpose of this project is to integrate the described subharmonic SOM technique with imaging radiometry. SOMs are excellent choices for the design of a radiometer receiver, as no phase coherent detection is necessary.

A typical radiometer receiver, known as super-heterodyne total power radiometer, is shown in Figure 5.1. It consists of an antenna to receive the electromagnetic radiation, an LNA, a mixer to downconvert the high-frequency signal to an IF signal in order to make it processable by standard electronic equipment, a filter to select the desired bandwidth, an IF amplifier, a power detector and an integrator.

For high-frequency applications we can take advantage of the concept that has been introduced by the above described high-order subharmonic mixing, because transistors with lower frequency requirements can be used, which facilitates our design.

5.2 PERFORMANCE REQUIREMENTS

The goal of a radiometric measurement is to measure the power related to the brightness temperature *T* radiated by the object and convert it to a DC signal at the receiver output.

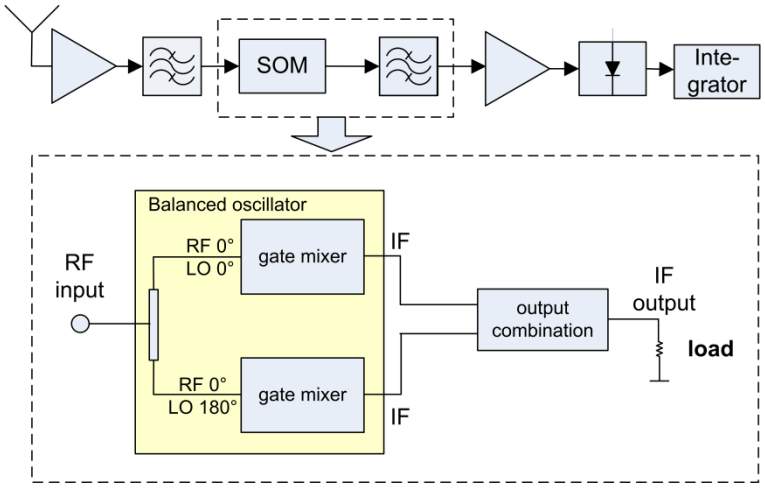

Figure 5.1 Circuit concept of the investigated superheterodyne total power radiometer receiver based on a subharmonic SOM.

In (2.6) the output power of a radiometer has been described. Including the amplification in the receiver, the noise power can be written as:

$$P = kBGT \tag{5.1}$$

with T as the measured noise temperature, B as the receiver bandwidth, and G as the overall system gain. In real life the noise temperature a radiometer measures is not only given by the noise temperature collected by the antenna but also includes the noise the receiver adds up to the input signal, i.e.

$$P = kBG\left(T_A + T_N\right) \tag{5.2}$$

with T_A as the noise temperature collected by the antenna and T_N as the receiver noise temperature.

In the development of radiometer receivers, it is very important to consider different factors that affect performance. A radiometer measures its incident radiation in the form of noise power, which adds up to the internal system noise of the receiver. Considering this aspect, it becomes clear that one of the key parameters in a radiometer receiver is its sensitivity ΔT, which is defined as the incident signal that is just equal to the effective value of the output fluctuations due to the internal system noise. This value is usually given in Kelvin:

$$\Delta T = \frac{T}{\sqrt{B\,\tau}} = \frac{G\left(T_N + T_A\right)}{\sqrt{B\,\tau}} \tag{5.3}$$

with τ as the integration time, and T as the system noise temperature denoting the sum of antenna and receiver noise amplified by the system gain G.

From (5.3) it becomes evident that sensitivity increases 1) with larger bandwidth due to the higher noise quantity collected; 2) with a lower receiver noise figure as it reduces the internal system noise; 3) with the system gain as the incident radiation is amplified more; and 4) the integration time as averaging over the collected noise power eliminates the system noise further. The theoretical sensitivity [30] only represents lower limits, which are further degraded by gain fluctuations, antenna efficiency, and other system losses. Thus, for our overall system design it is not only important to achieve a low noise, high gain, and broadband design but it is also essential to minimize losses as far as possible.

In order to achieve a high-performance radiometer design, it is necessary to identify the parameters in the circuit that influence these performance characteristics. In this section, a brief summary of this so-called radiometer performance model is presented.

5.2.1 System gain

The overall system gain in the proposed receiver is determined by the antenna losses, the LNA gain, the conversion gain of the SOM and the gain of the IF amplifier along with the insertion loss of other components in the receiver chain such as filters. IF amplification is easy to obtain and well-studied. Therefore, the main weight lies on the achievement of suitable RF gain using an LNA as well as minimizing the losses in the SOM.

5.2.2 Bandwidth

The bandwidth of the proposed receiver is determined by the smallest value among antenna, LNA, SOM, and IF filter bandwidth. The most critical element in terms of bandwidth is usually the SOM, as it is challenging to design such a device exhibiting high bandwidth, low noise, and high conversion gain at the same time. Furthermore, also the antenna needs to offer adequate bandwidth, which imposes restrictions to the antenna type selection.

5.2.3 Noise figure

The noise figure of the overall system is a very important factor as it is added to the collected radiometric noise in the receiver and degrades receiver sensitivity. Thus, we need to ensure a low-noise design of the entire receiver circuit. The most critical point in terms of noise performance is the first element in the receiver circuit, since its noise figure is multiplied by each of the subsequent components. Thus, as it is shown in (5.3) we must employ an LNA with good noise characteristics. Moreover, the SOM circuit should follow a low-noise design. This has been studied for the low-frequency SOM prototype in section 3.3.4, where noise reduction has mainly been achieved by introducing a balanced structure for the third-order SOM. Furthermore, as it is well-known for active mixer circuits, good matching of the input and output ports improves the noise behavior.

5.2.4 Integration time

From (5.3) it follows that a longer integration time increases sensitivity. Regarding the final imaging application, a few considerations have to be taken: very short integration times cause ambiguous image edges due to low sensitivity, whereas very long integration times are not compatible with real-time imaging requirements since they cause tailing of the image. Thus, a trade-off needs to be made in order to maintain an adequate radiometer performance in terms of real-time requirements of the radiometer application.

5.3 LOW FREQUENCY SELF-OSCILLATING MIXER RECEIVER

In this step, a first test circuit for a receiver architecture has been built up combining the SOM circuit described in section 3.2 with a patch antenna. This experiment is carried out to verify if the insertion of an antenna into the SOM circuit influences performance and if such a structure is fully functional.

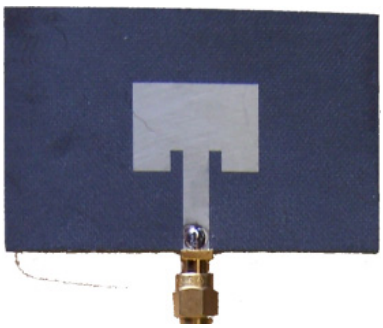

Figure 5.2 Photograph of the fabricated antenna used for the third harmonic SOM receiver circuit.

Due to the inherent RF-LO isolation of the presented SOM structure we do not need to take particular care of termination impedances at LO frequency for the antenna and a simple design can be used, which presents a further advantage of the proposed design.

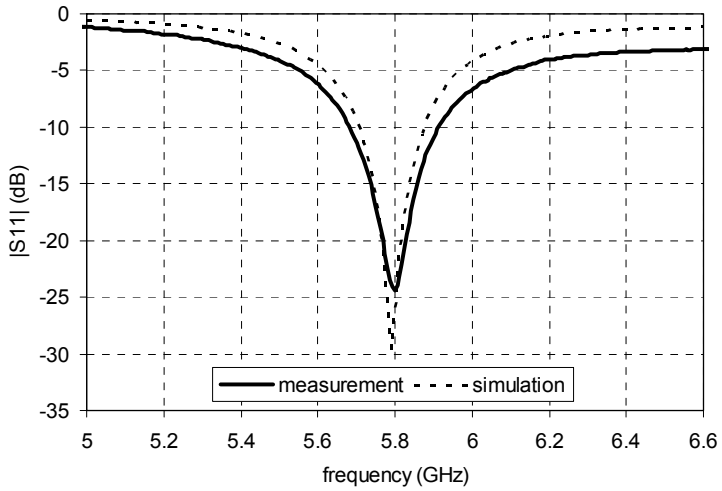

Figure 5.3 $|S_{11}|$ of the antenna used for building the complete receiver.

A patch antenna with rectangular shape shown in Figure 5.2 was simulated and measured separately in order to verify its functionality. The input matching is shown in Figure 5.3. Simulation and measurement agree very well and the slight deviation observed in the figure is attributed to the fact that losses were not included in the simulation. The antenna exhibits a gain of 7.25 dBi in the simulation and a 10-dB bandwidth of 4.3% in the measurement.

The receiver has been tested with a second transmitting patch antenna connected to a signal generator with an RF power of 5 dBm. The distance between the antennas was selected to 1 m.

Figure 5.4 shows the IF output spectrum for the measurement of the complete receiver circuit. With the above stated values for the antenna gain, Friis formula gives a theoretical power of –28.2 dBm at the receiver input. Referring this value to the IF power level at the receiver output, a theoretical conversion gain of 7.2 dB is achieved. This value is lower compared to the gain of the stand-alone SOM due to an antenna gain lower than the simulated value used in the Friis formula. The conversion gain of the presented receiver is shown in Figure 5.5.

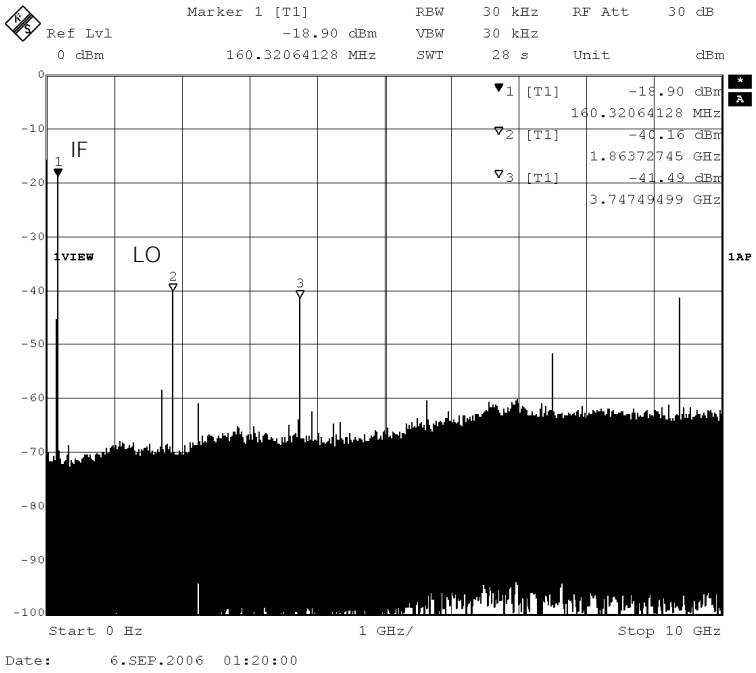

Figure 5.4 Output spectrum of the third-harmonic SOM at an RF input of 5.8 GHz and –30 dBm. The oscillation built up to 1.863 GHz, which yields an IF frequency of 160 MHz.

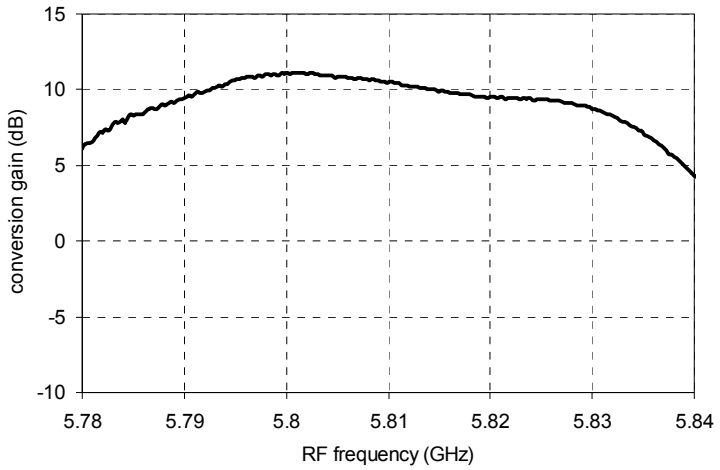

Figure 5.5 Conversion gain for the 5.8 GHz prototype (measured).

It is to be noted that the spectrum in Figure 5.4 compares very well to the stand-alone SOM result in Figure 3.8, which proves that the SOM performance is not affected by the added antenna and remains fully functional. The presented design therefore opens up a wide range of applications offering the possibility of a planar low-cost and low-power heterodyne receiver design.

5.4 LOW-FREQUENCY RADIOMETRY TEST BED

As a next important step, a number of first radiometric measurements are carried out using a spectrum analyzer substituting the receiver developed later. In this step, for the first time real radiometric noise power is measured and evaluated with the help of a simple and predictable receiver structure. The frequency of choice for this experiment is 5.8 GHz, and the radiation from different objects is measured. These experiments allow for a deeper understanding of the behaviour of radiometric radiation and the problems faced during its measurement and essential experience for further experimentation is gained. The experiment includes three steps as shown in Figure 5.6:

As a first object to be measured, a calibrated known noise source is connected to the receiver. Its noise power can be controlled by an attenuator for the experiment. This test can be used to obtain information about the system noise adding up to the noise diode source power.

Second, a standard known termination of 50 Ω is connected to the receiver circuit through a wired connection and is cooled and heated in a temperature chamber (Figure 5.7) from -10°C to 40°C (263.15 K to 313.15 K). The results for this experiment are shown in Figure 5.8. We obtain a measured noise power that agrees very well with the theoretical value obtained through (5.1). The applied temperature difference of 50 K results in a power difference of 7 nW, and a resolution of better than 5 K can be easily achieved, even considering the low bandwidth of only 10 MHz the spectrum analyzer based receiver emulation provides. This result also suggests that an improvement in temperature resolution and sensitivity can be easily achieved by increasing the bandwidth.

A third experiment involves the use of an antenna and the measurement real radiation in nature instead of directly connected noise sources. A high-gain horn antenna with 24 dBi

gain is connected to the receiver and pointed towards known radiation sources such as the sky, the earth, and the sun. The temperature of the earth is around 290 K according to the ambient temperature; the cold sky with scarce radiation sources has a cold radiometric temperature of around 3 K, and the sun 6000 K. These values are empirically verified and observed during an exterior experiment. Exact observations prove difficult to be obtained as clouds in the sky reflecting the warm ground falsify the result, and the antenna collects energy not only from its main lobe but also from all sidelobes, making the exact temperature difference a combination of the emission and reflection of different objects and therefore difficult to interpret. However, the experiment gives very good insight into the nature of radiometric measurements in order to continue the research plan on the intended path and is concluded successfully.

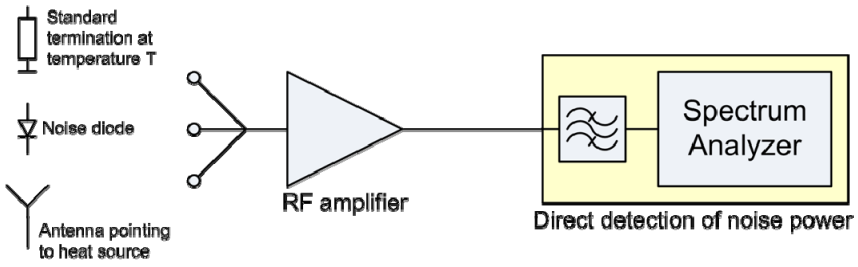

Figure 5.6 Illustration of the proposed radiometry testbed: a) a standard termination heated or cooled to a temperature *T* is used, b) a calibrated noise source is measured, and c) an antenna is pointing at an object of interest of temperature *T*.

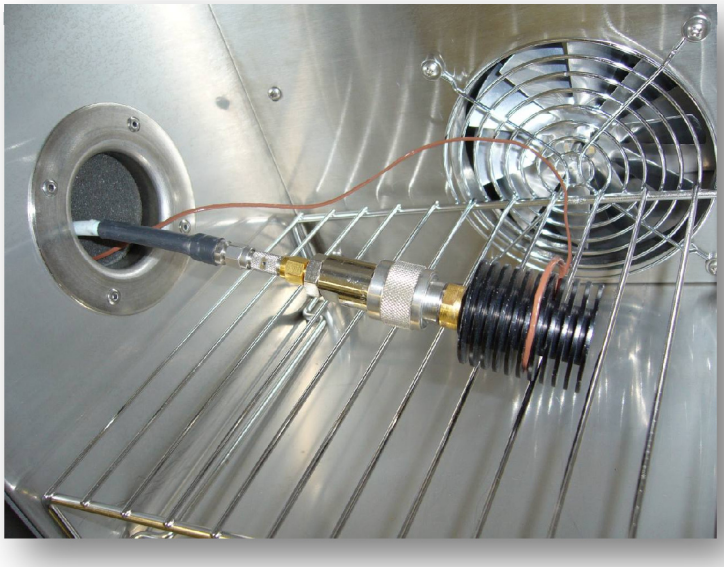

Figure 5.7 The standard termination used in the second part of the radiometer test-bed experiment.

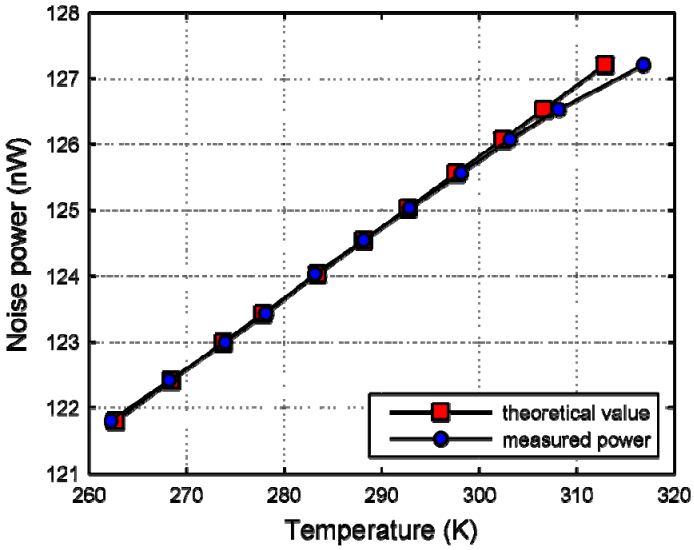

Figure 5.8 Experimental and theoretical results for the standard termination.

5.5 MILLIMETER-WAVE RADIOMETER RECEIVER DESIGN

The next design step involves the setup and testing of a 35 GHz radiometric receiver. In a first step, standard commercially available components are used in order to evaluate the system and eliminate possible sources of error. This setup has been built up by the members of the imaging group at the Poly-Grames Research Center. Figure 5.9 shows a block diagram of the receiver circuit. A Hittite HMC263 LNA and a standard mixer (Hittite HMC329) are used in the proposed receiver. An IF amplifier (Cernex CBL02045620-01) together with an IF filter form the IF circuit. The power output is initially evaluated with a power meter for easier understanding and evaluation of the results. In subsequent steps, the power meter is substituted by a power detector circuit, and the DC output voltages are communicated to the PC by a PIC microcontroller interface. A very important consideration proves to be the design of a suitable target and is described later in this chapter. Figure 5.10 shows a photograph of the implemented receiver test setup.

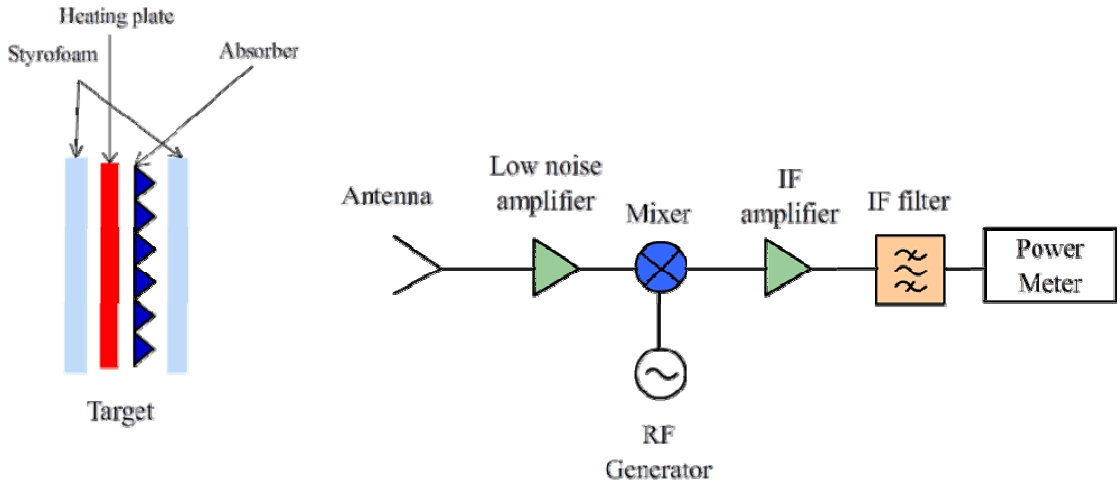

Figure 5.9 Block diagram of the proposed receiver design with target description.

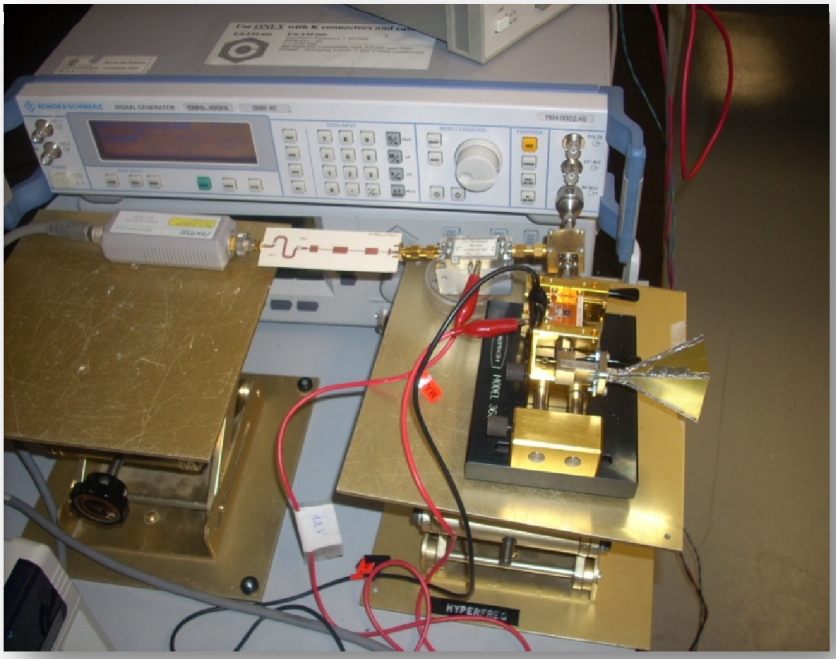

Figure 5.10 Photograph of the receiver in operation.

5.5.1 Low-Noise Amplifier

The signal to be measured is noise-like in nature and very weak, i.e. in the order of -80 dBm. For this reason it is necessary to include an LNA in order to be able to push the level of the incoming radiation to a level exceeding the noise floor of the subsequent receiver components and make the signal measurable by the detector diode. A photograph of the LNA along with its performance is shown in Figure 5.11 and Figure 5.12.

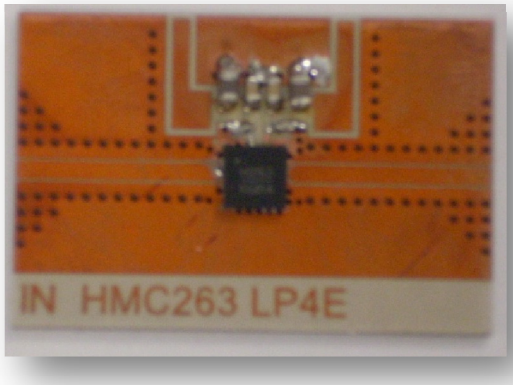

Figure 5.11 Photograph of the implemented LNA.

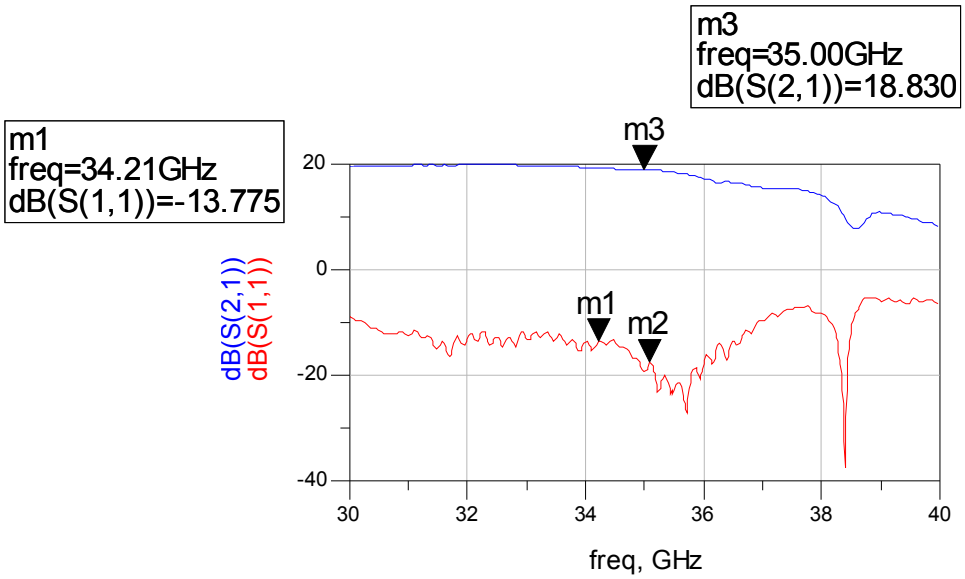

Figure 5.12 Gain characteristics of the LNA.

5.5.2 IF Circuitry

The IF circuitry includes an IF amplifier, which is used to elevate the signal level to the dynamic range of the detector circuit. Its characteristics are shown in Figure 5.13, and an IF gain of 65 dB is used in the receiver. Figure 5.14 shows the IF power detection board used for converting the IF power into a DC voltage. The detector circuit has an input range

from -52 dBm to +8 dBm and yields a DC voltage of 50 mV/dBm. Moreover, an IF filter with a center frequency of 1.5 GHz and a bandwidth of 1 GHz is designed and included in the receiver setup. A PIC microcontroller including an 8-bit ADC is used to digitize the measured voltage and transfers the measured data to the PC via an RS-232 interface.

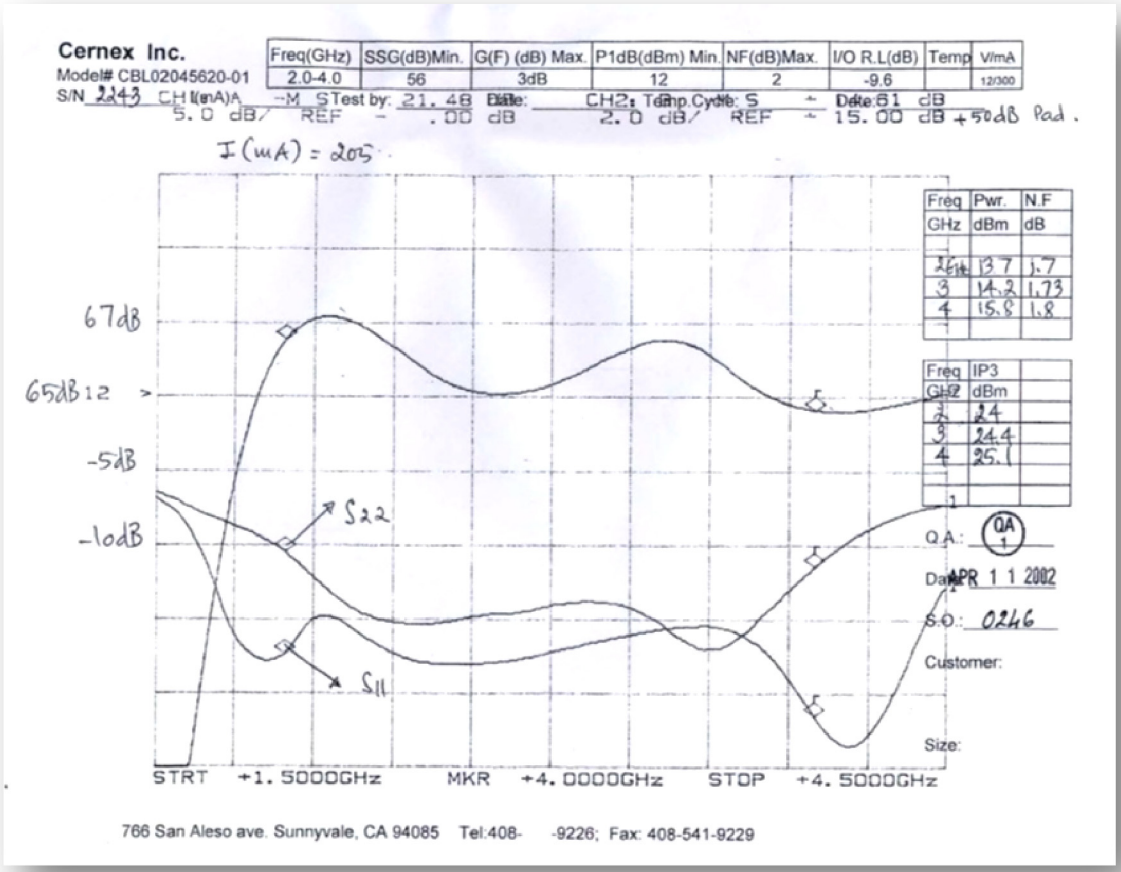

Figure 5.13 Gain characteristics of the IF amplifier.

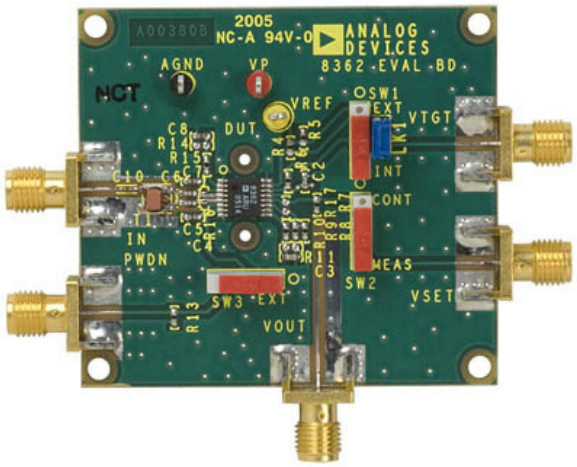

Figure 5.14 The power detector board used in the proposed project.

5.6 TARGET EMULATION

As a matter of fact, the measurement of radiometric signals represents a difficult task due to the low power levels observed. In many cases, it is hard to distinguish a measured radiometric noise power from the omnipresent system noise at all. Therefore, for first experimental purposes it is of high importance to have a known reference target available, which is fully controllable in temperature and therefore provides predictable results. In the case of the presented project, a target that may be heated to arbitrary temperatures is designed as shown in Figure 5.15. Most microwave remote sensing systems use a standard target a blackbody radiator for testing purposes. A millimetre-wave absorbing sheet has been used whose temperature can be varied with heating elements to a desired value. An aluminum plate spreads the heat evenly, and two Styrofoam side walls isolate the structure thermally. A photograph of the heatable target is shown in Figure 5.16.

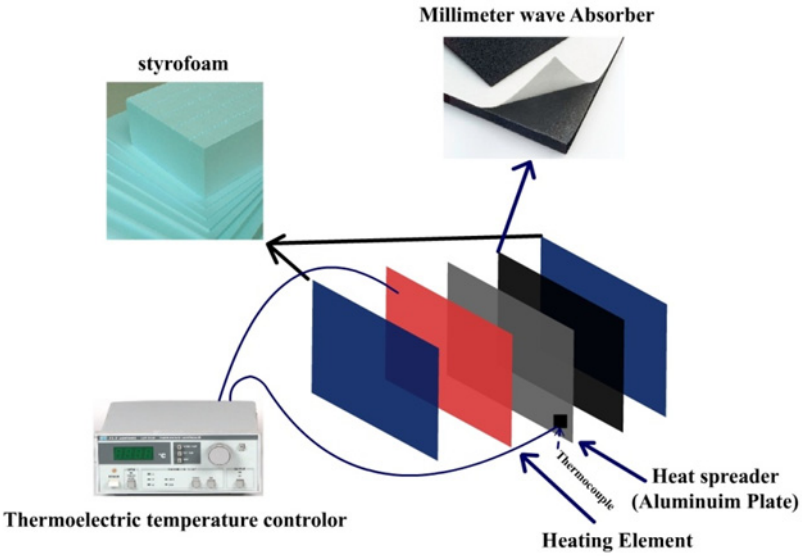

Figure 5.15 Illustration of the target composition.

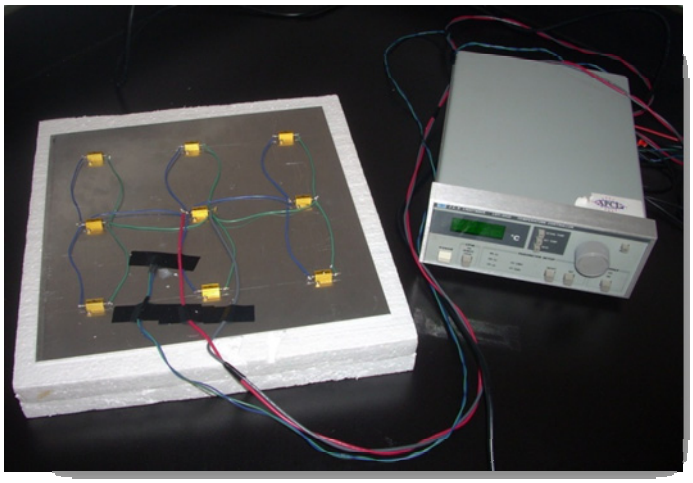

Figure 5.16 Photograph of the designed target.

5.7 MILLIMETER-WAVE RADIOMETRY EXPERIMENTS

Using the described receiver environment, a series of tests has been carried out by the members of the imaging group at the Poly-Grames Research Center and is included for reference. Figure 5.17 shows a photograph of the laboratory setup including the Styrofoam isolated target, the receiver circuit with horn antenna.

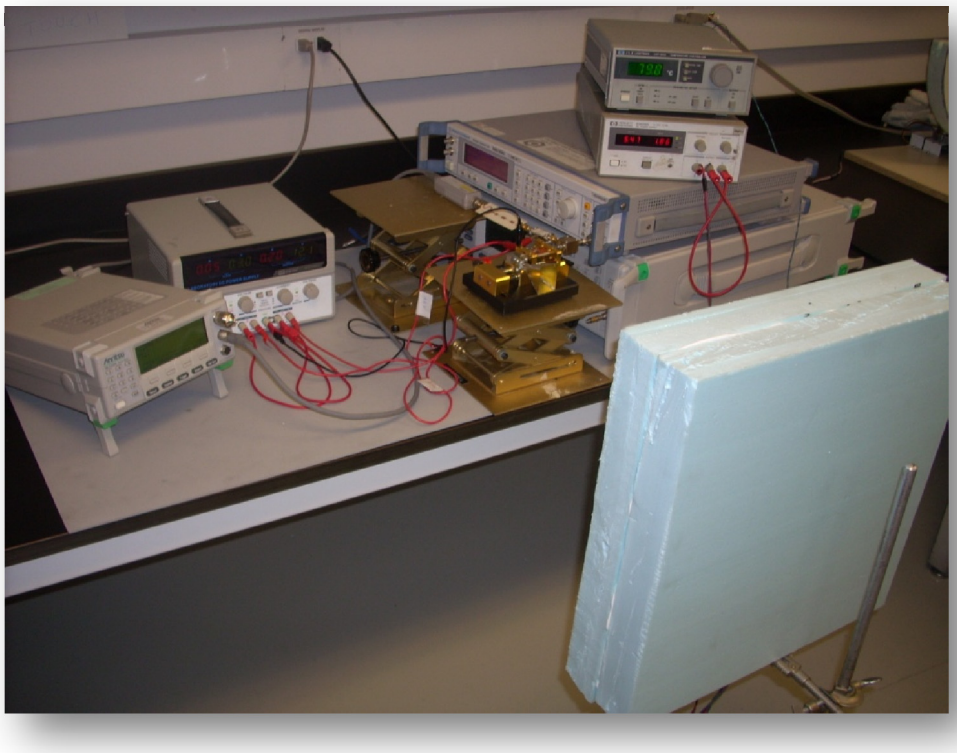

Figure 5.17 Test environment of the proposed millimetre-wave radiometer.

5.7.1 Temperature variation

A first test includes a measurement of a temperature sweep similar to the way it has been carried out in section 5.4 by varying the temperature of the heatable target located at a distance of 50 cm and measuring the output power of the radiometer receiver. The result in Figure 5.18 shows that a linear behaviour can be achieved that agrees well with theoretical assumptions. It also shows that the output power at the filter for this

temperature range lies around -9 dBm, which is a value easy to detect by commercially available components.

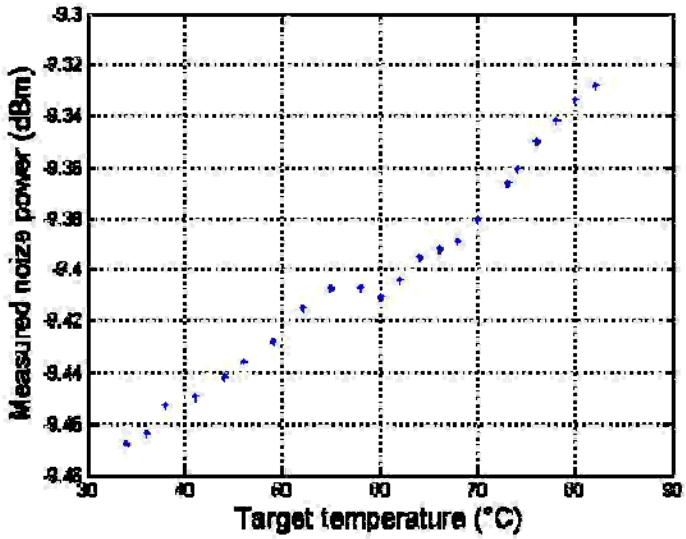

Figure 5.18 Verification of power measurement using the test setup.

5.7.2 Target distance variation

A second test included the examination of different target distances and their influence on the measurement result. From Figure 5.19 it is obvious that a target placed at different distances, i.e. 50 cm and 3 m results in a power difference, in the presented case of 0.2 dB and 0.01 dB, respectively.

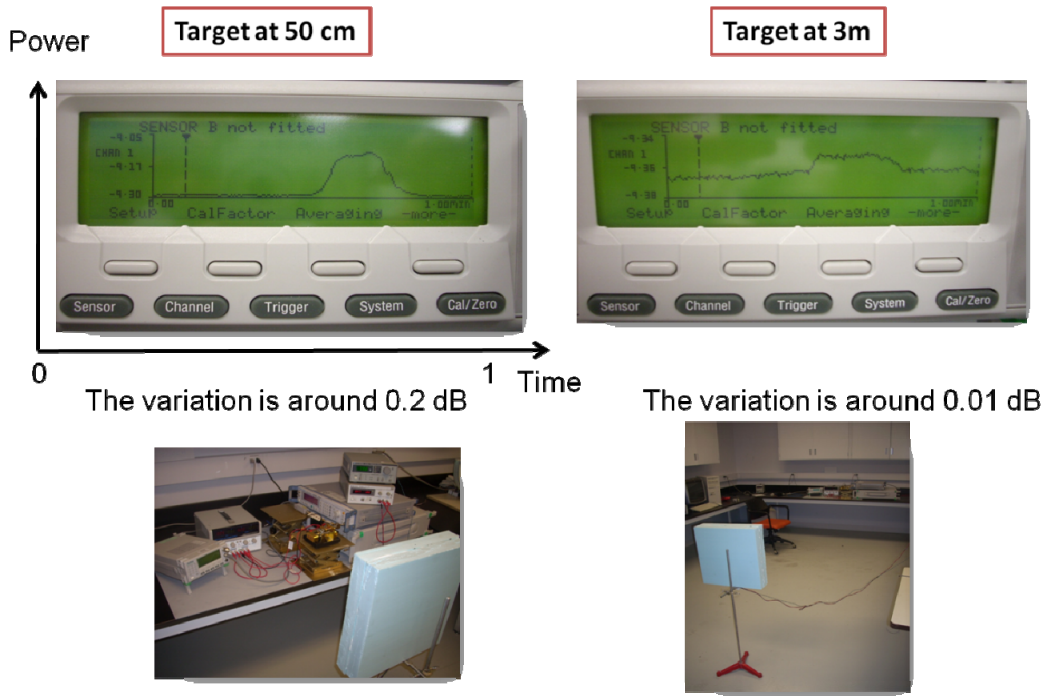

Figure 5.19 Difference in power levels for different target distances.

5.7.3 Target detection

The following test was carried out detecting the presence of a human body at a distance of 1.5 m, as shown in Figure 5.20, and a perfectly reflecting metal plate, as shown in Figure 5.21. Both results clearly show the presence of the respective object and therefore the presented system proves useful to be used for radiometric measurements.

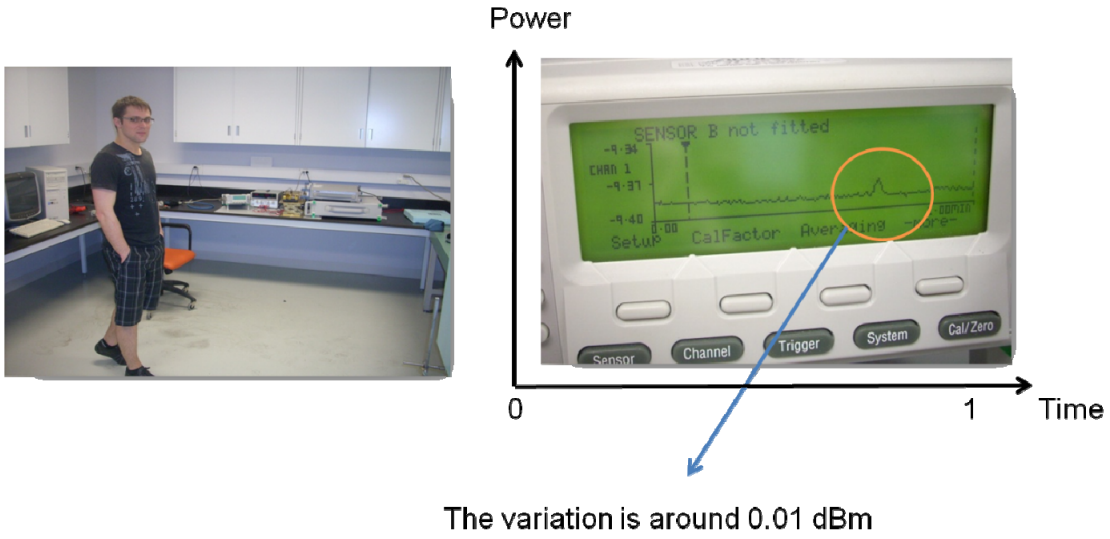

Figure 5.20 Interceptance of human body.

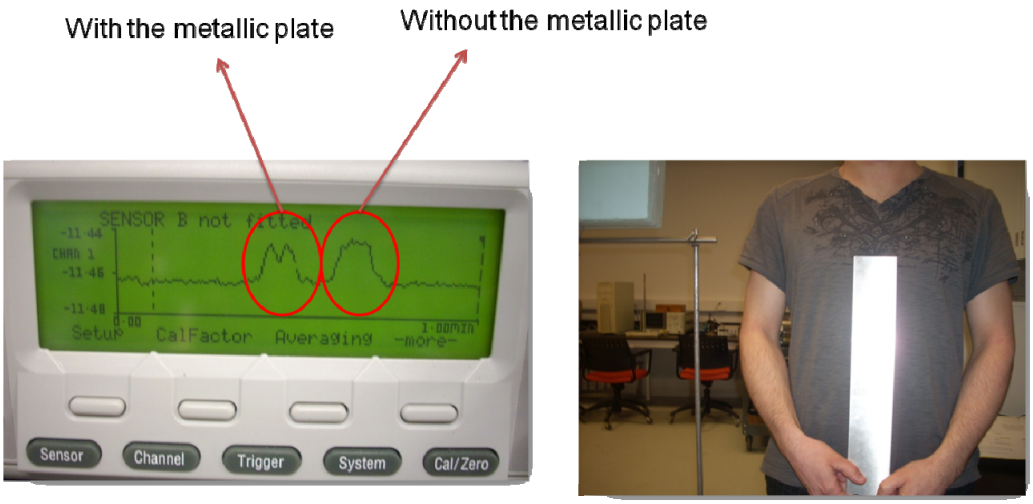

Figure 5.21 Measurement of a metal plate.

5.8 CONCLUSIONS

This chapter introduces the development of a radiometer receiver and outlines the required performance as well as the simulation of a system model. It shows the development of a low-frequency receiver and a low-frequency test-bed to assess radiometric measurement capabilities. Subsequently, the receiver is scaled to 35 GHz and tested with a specifically designed heat-controllable target. Preliminary experiments are carried out detecting the target temperature, and with other targets such as the detection of a human body and a metal plate.

Chapter 6

INTEGRATION INTO COMPLETE IMAGING SYSTEM

In this chapter, the entire imaging system is presented. The work is concerned with the setup of an imaging system environment based on standard components is the result of a cooperation of a group of students at the Poly-Grames Research Center including a co-directed master thesis at the University of Pavia, Italy [86] together with the author of the presented thesis and will be presented in detail. The proposed system is using a mechanical scanning technique using the reflector designed in previous chapters.

6.1 INTRODUCTION

One of the various possibilities to obtain a passive millimetre-wave image is to perform an *x-y* scan across the scene interest using a single-element receiver. The radiation is focused onto the receiver by means of a parabolic reflector that is mechanically rotated in order to progressively steer the beam direction toward the currently scanned image pixel.

The proposed scanning system is designed using a gimbal-mounted reflector dish as shown in Figure 6.1 containing the feed antenna and receiver circuitry mounted on its supporting mechanics. This allows for controlling the rotation of the reflector around two independent axes using two independent motors. In the proposed design, this task is carried out by two stepper motors due to their easy implementation, controllability, and cost-efficiency.

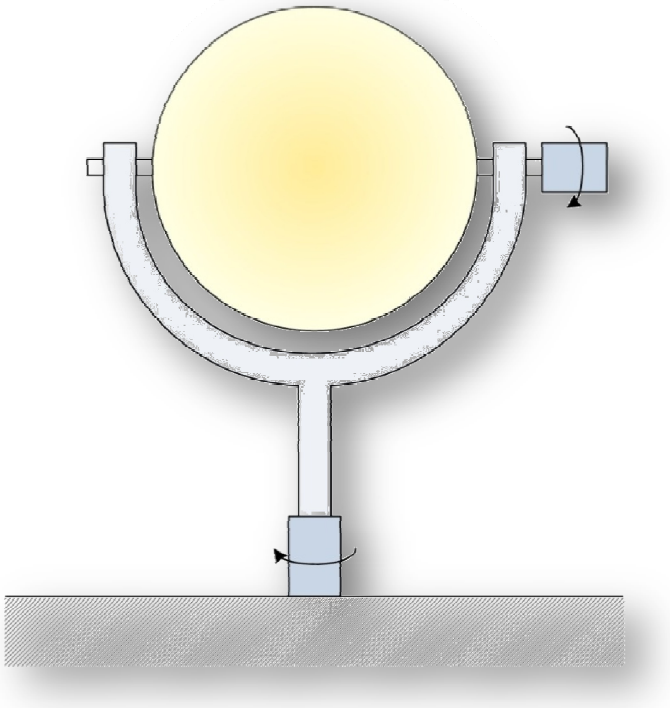

Figure 6.1 Illustration of the proposed mechanical scanning system with two stepper motors allowing for a scanning in two dimensions.

6.2 PERFORMANCE CONSIDERATIONS

In addition to the performance considerations taken for the receiver portion of the system in section 5.2, a few additional aspects are important considering the entire imaging system environment.

6.2.1 Scanning time

The overall scanning time is an important factor in the case of applications requiring fast imaging responses. Of course, a mechanical system as presented in this chapter, is one of the slowest possible methods to require an image. However, it is the simplest approach for realizing the desired test setup of the system as we do not require any real-time capability in this first experiment.

6.2.2 Spatial resolution

A highly important parameter for defining the performance of an imaging system is its spatial resolution. It is defined as the minimum separation of the object of interest from its surrounding that can be resolved by the imager, or in other words, for each object to be resolved, there should be at least one associated pixel in the final image. It mainly depends on the antenna gain and on the resolution of the mechanical stepping. For achieving a high resolution, a narrow beamwidth needs to be established, which corresponds to an antenna exhibiting high gain. The proposed reflector antenna in Chapter 4 is well suited for this purpose.

However, an important role is also played by the stepper motor control, as the minimum possible step size directly defines the maximum achievable imaging resolution.

6.3 STEPPER MOTOR IMPLEMENTATION

A stepper motor is an electromechanical device converting electrical pulses into discrete mechanical movements. As its name suggests, it moves one step at a time, unlike conventional motors that rotate continuously. Sending a command to a stepper motor results in the application of pulsed signals driving the rotation of the motor shaft and an incremental rotation of the exact desired number of steps with a subsequent stop.

One of the most significant advantages of a stepper motor is its ability to be accurately controlled in an open loop system. This means that no feedback information about the current position is required and consequently the need for expensive sensing and feedback devices such as optical encoders is eliminated. The current motor position is simply known by keeping track of the number of steps that have been completed.

Repeatability of the movement is easily achievable as good stepper motors exhibit a positioning accuracy of 3-5% for a single step, which moreover represents a non-cumulative error, with an excellent response to starting/stopping/reversing.

The two motors used in this project are Portescap geared motors of the 42M type 'Z' series. A photograph and the main characteristics are presented in Figure 6.2 and Table 6.1, respectively. The proposed motor is a bipolar motor having the advantage of the current

flowing through an entire winding at a time as opposed to unipolar motors, where current only flows through half of the winding. As a result bipolar motors produce more torque than unipolar motors of the same size.

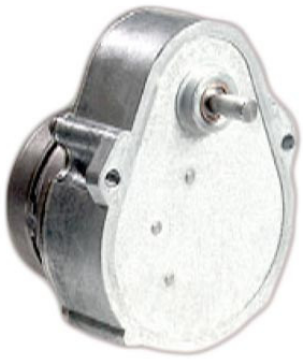

Figure 6.2 Stepper motor with gear ratio 50:1.

DC Operating Voltage	5
Resistance per Winding (ohms)	9.1
Inductance per Winding (mH)	16.7
Holding Torque* (mN•m/oz-in) (motor only)	84.0 / 11.9
Rotor Moment of Inertia ($g.m^2$)	12.5×10^{-4}
Step Angle* (motor only)	7.5°
Steps per Revolution* (motor only)	48
Gear Train Ratjng (N•m / oz-in)	
Static	2.12 / 300
Running*	1.41 / 200
Max. Operating Temperature	100°C
Ambient Temperature Range	
Operating	-20°C to 70°C
Storage	-40°C to 85°C
Bearing Type	Bronze sleeve
Insulation Resistance at 500Vdc	100 megohms
Weight (g/oz)	312 / 11.0
Leadwires	26 AWG

Table 6.1 Stepper motor specifications.

6.3.1 Motor control

In the proposed imaging system, the motors are controlled by a dedicated BS0710 driver board shown in Figure 6.3. It is a complete unipolar/bipolar dual stepper motor controller system, which can be controlled from a computer using a USB connection. It includes the capability of driving one or two stepper motors, each of which being either unipolar (4-pole) or bipolar (2 pole).

Figure 6.3 Stepper motor control board.

6.3.1.1 Current requirements

The motor control board offers different operation modes, which depend on the specified application. Depending on the use in more accurate applications requiring fine steps or its implementation into applications requiring larger weights to be carried, the controller mode can be selected to either microstep/half-step or full step mode, respectively. The proposed application with a resolution requirement of 2 cm does not need extremely fine steps but needs to support a bulky reflector dish and hence yield maximum torque output from the motor, which makes the full step double winding operation mode the best choice for the presented application. In this mode both windings are “on” at a time. The motor winding current can be calculated as follows:

$$I_1 = \frac{U}{R} = \frac{5\ \text{V}}{9.1\ \Omega} = 0.55\ \text{A} \tag{6.1}$$

In full-step mode, a corrective multiplication factor for the required current is introduced:

$$I_2 = I_1 \cdot 2.5 = 1.37 \text{ A} \tag{6.2}$$

The BS0710 motor control board can drive a maximum winding current equal to 1 A, which corresponds a total maximum current value for the two motor windings of 2 A. The current calculated in (6.2) can therefore be driven by the board and the reflector system can be built-up using this configuration.

6.3.1.2 Serial interface with PC

The presented motor control board features a USB interface based on a serial RS-232 protocol, which is used in the proposed project to communicate motor control commands from the PC. In order to facilitate data communication with the board, a simple Matlab interface for the motor movement is developed.

6.4 DATA ACQUISITION AND SIGNAL PROCESSING

The proposed Matlab interface is subsequently also used to perform the task of data acquisition and signal processing and is shown in Figure 6.4. The interface can be used to initialize the motors at a certain position and can be used to define scanning parameters such as the number of pixels and the overall scanning range in degrees.

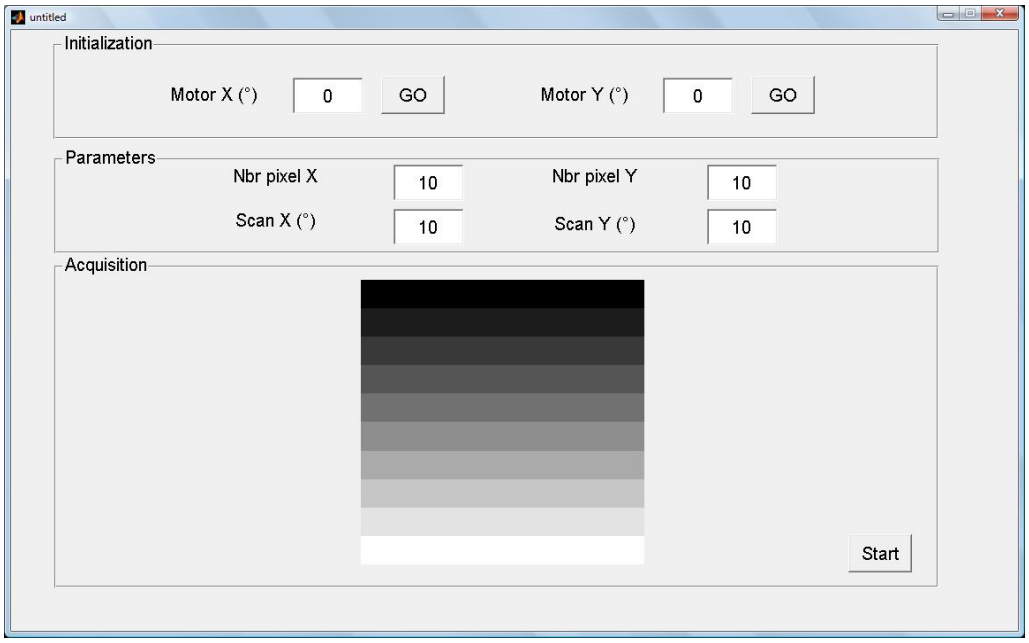

Figure 6.4 Matlab interface used for motor control, data acquisition, and signal processing.

As a first step, only very straightforward basic signal processing is applied, representing the maximum and minimum measured levels of DC voltage in black and white, respectively and divide the range in between by the 256 possible values delivered by the 8-bit ADC used in the project. Signal processing in imaging radiometry in fact can be compared to the processing of optical images due to their similar nature, and hence generally, standard imaging processing algorithms are applied in order to achieve enhanced image quality, contrast, resolution and noise reduction [45]. Especially for applications such as concealed weapon detection, these methods are applied in order to automatize the detection hidden objects.

6.5 EXPERIMENTAL RESULTS

This section presents the experimental results obtained with the proposed imaging system. As a first step, the spectrum analyzer is used together with the mechanical setup for a preliminary assessment of system functionality. The second step involves the combination

of the receiver structure presented in section 5.5 with the mechanical steering aspects presented in this chapter.

6.5.1 First experimental test

Figure 6.5 and Figure 6.6 show the first setup of the proposed imager using the reflector antenna with a lightweight Styrofoam arm for mounting the feed at its intended offset focal position as developed in Chapter 4. The setup is connected to the motor control board, and a first assessment is made with a three-stage cascaded 35 GHz amplifier and the spectrum analyzer.

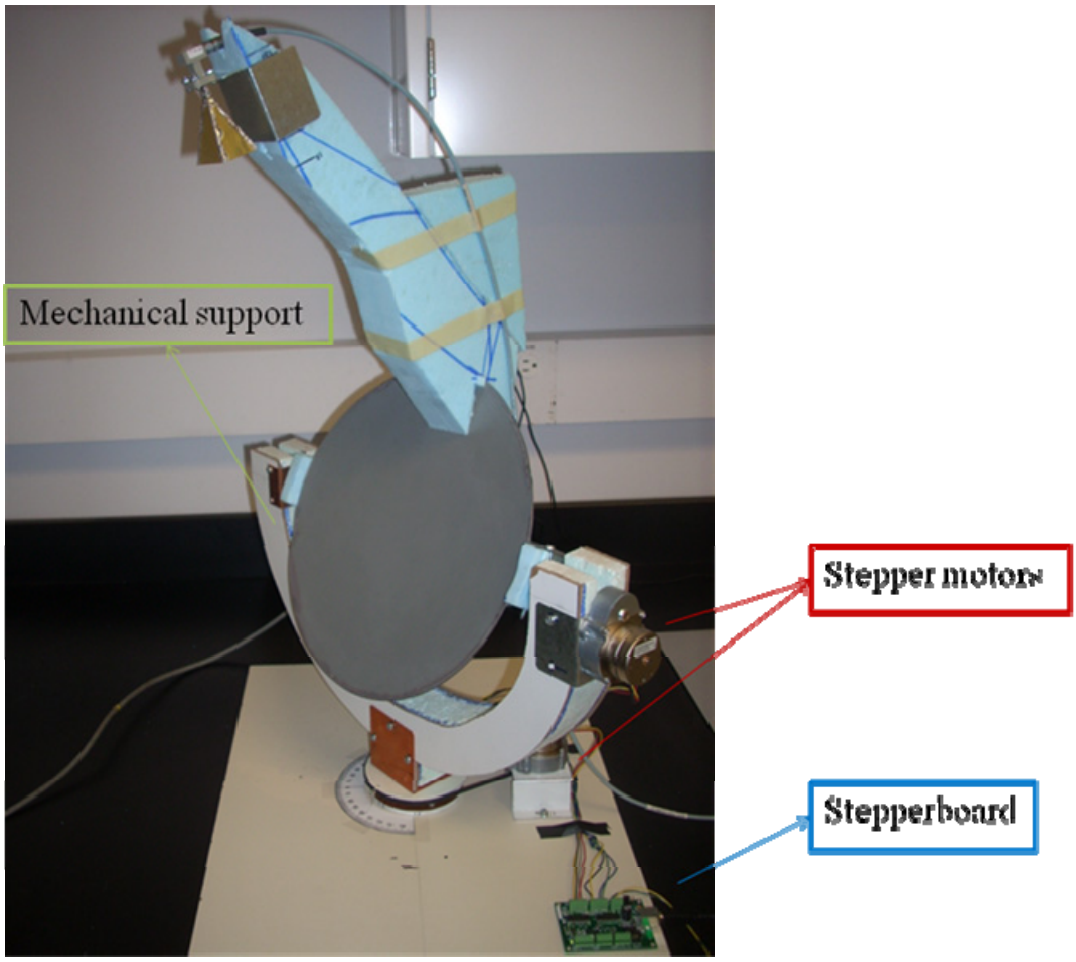

Figure 6.5 First test setup of the mechanical scanning environment.

The purpose of this first prototype is a preliminary test for assessing whether the system is able to detect radiometric temperature differences for distinct materials. As seen in the previous chapters, difference in thermal temperature between distinct objects is translated by the radiometer into a difference in signal powers.

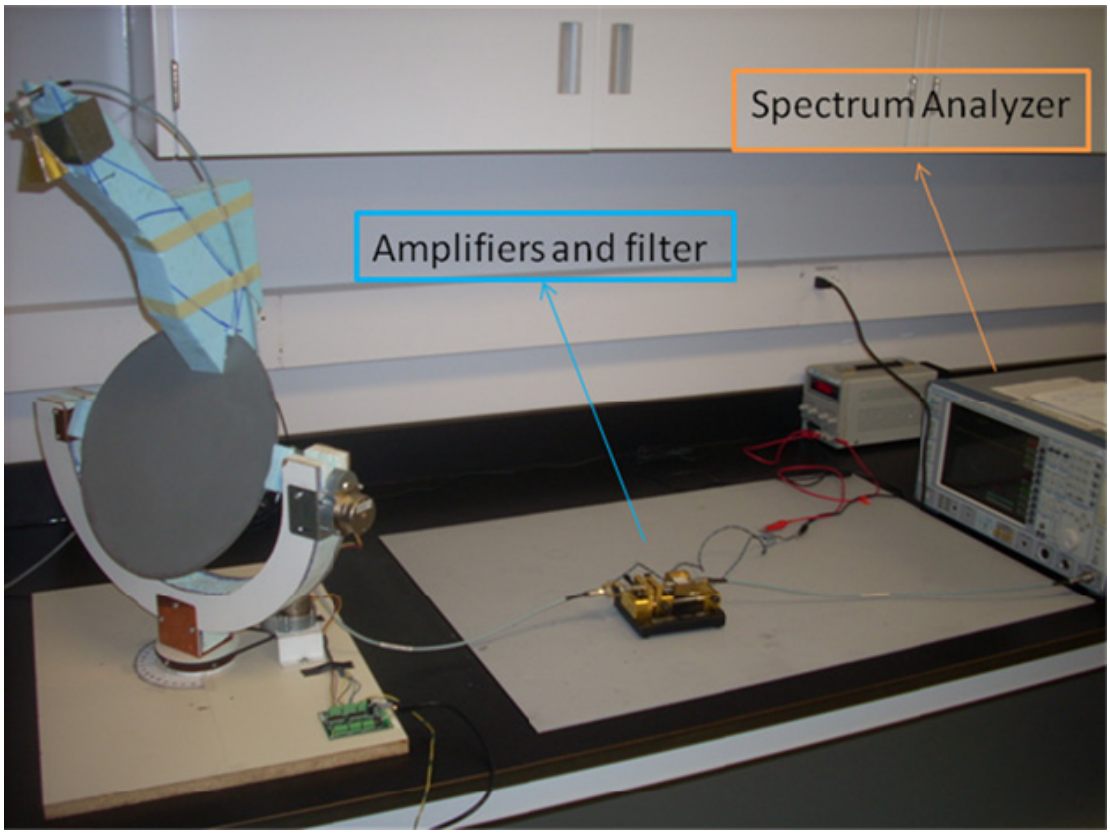

Figure 6.6 Test system: antenna, filter, amplifiers and Spectrum Analyzer

The measurement has been carried out comparing the signal levels shown by two different materials presenting very different emissivity values. One of the materials is represented by a microwave absorbing sheet as used in the anechoic chamber and ideally having an emissivity very close to 1. The second material is an aluminium foil, with a total normal emissivity of approximately 0.04.

The measurement uses an RF LNA with a gain of 62 dB and leads to a first observable result exhibiting a power level difference of about 10 dBm measured with the spectrum analyzer when inserting the aluminum foil.

A number of additional observations can be made, in the attempt to better understand the behaviour of the prototype system and possible future developments.

First, the measurement repeatability is critical: a change in signal level is observed during the scanning movements of the antenna. This is principally due to the consequent movement of the connecting cable between the antenna feed and the amplifier stage as the power levels are extremely low before reaching the amplifier. The input antenna therefore needs to be connected directly to the amplifier and filter stage, in order to reduce these cable losses.

Further observations are including factors observed with millimetre images in general. Tests show that signal level is affected by a variety of parameters, such as different viewing angles, surface orientation, and variations in the position of objects surrounding the aluminum foil as the latter represents a reflector directing the radiation of other objects towards the system.

These preliminary results give a starting point, from which further developments of the radiometer system can be attained as described in the next section.

6.5.2 Imaging system with heat-controlled target

Figure 6.7 shows an improved test setup environment with the newly designed heat-controllable target presented in section 5.6.

Figure 6.7 Laboratory test setup for the proposed system.

Mechanically scanning the region of interest with a 10 x 10 raster scan we obtain the image result in Figure 6.8, which corresponds well to the shape of the object. The differences in intensity in the presented images are attributed to stability issues in the receiver design. Even very small changes in gain or temperature cause a large variation compared to the measured power levels, which may result in different intensities measured for different pixels of the image. These issues are usually addressed with an adaptation of the receiver circuits using a Dicke switch [30] or can be solved with differential circuits as outlined among the many future tasks to work on in Chapter 8.

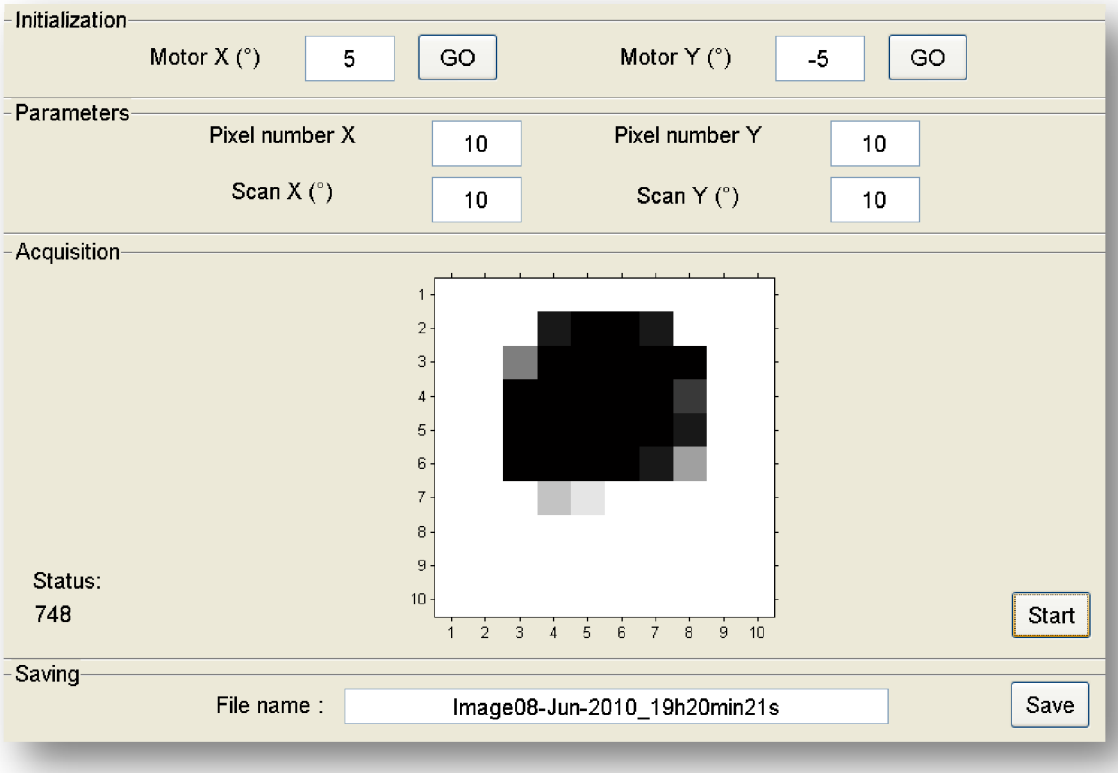

Figure 6.8 Imaging result for a target at 80 degrees C and a resolution of 10 x 10 pixels.

6.6 CONCLUSIONS

This chapter presents the first results obtained for the entire imaging system. A basic mechanical scanning setup is built up using the reflector antenna described previously, and stepper motors are responsible for the beam steering. A Matlab interface is designed to acquire the data and control the motor movement and is used to display the final image. Future work will include the detailed investigation of this system and its application to various application scenarios.

Chapter 7

MULTI-POLARIZATION SYSTEM

The presented chapter concentrates on the possible implementation of a multi-polarization system for the proposed imaging application. As a polarizing device, an FSS structure is examined, designed, and tested experimentally.

7.1 INTRODUCTION

One very interesting and innovative aspect in the development of millimetre-wave imaging systems lies in the development of a multi-polarization imager [43], [44]. The use of polarimetry adds an extra dimension to the acquisition of imaging data. Essentially, natural background MMW radiation is unpolarized, but refraction and reflection from media and objects introduces polarization, which can be exploited in order to distinguish between objects naturally emitting electromagnetic radiation by themselves and objects reflecting the radiation of other parts of the scene such as the cold sky. A means to characterize these polarization effects is given by the Stokes parameters [30]. Certainly, the envisioned imaging system needs to be adapted in order to function as a multi-polarization system. The proposed receiver architecture will use a Vivaldi antenna that is only capable of capturing radiation in one polarization. Using a crossed Vivaldi structure [41] with mirrored antipodal architecture [42] we will be able to extend our linearly-polarized FPA MMW imager towards a multi-polarization system. The dual-polarized Vivaldi antenna and its extension to a 2 D array is shown in Figure 1.4.

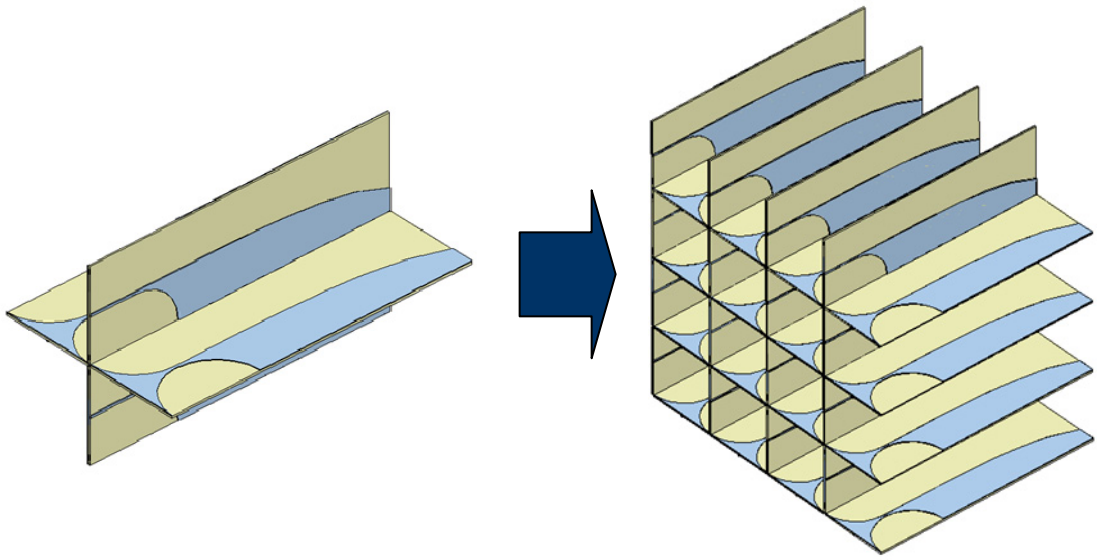

(a) (b)

Figure 7.1 Concept of dual-polarization Vivaldi antenna: a) 4-element Vivaldi antenna employing dual polarization; b) integration into a multibeam array.

Another possibility is the use of a polarizing FSS, as it may separate the incoming radiation into a horizontally and vertically polarized wave for reflected and transmitted energy. In the presented thesis, such a polarization rotating FSS is built and tested, and serves for a future dual-polarization test of the proposed imaging system.

7.2 FREQUENCY SELECTIVE SURFACE BASICS

FSS are planar periodic arrays of metal patches or slots that function as filtering elements for free-space radiation [88]–[90]. A large variety of element shapes including rectangles, crosses, and more complex geometries have been employed as periodic elements [88]. Their shape and dimensions as well as the substrate characteristics determine the performance of an FSS structure and they are selected and optimized according to different specifications.

FSS are widely used in the microwave, millimetre-wave, and sub-millimeter-wave frequency regions and find various applications, such as in the design of dichroic mirrors in deep-space antennas for radio-astronomy and the band or channel separation in quasi-optical systems. Furthermore, they are used as antenna radomes and as shielding elements in microwave ovens.

In this work, an FSS based on the SIW technology has been developed and demonstrated. In recent years, SIW technology has experienced an enormous success as it offers a highly attractive method for the design of microwave and millimeter-wave waveguide-based integrated components and sub-systems in the form of planar circuits. SIW technology provides a low-cost and low-loss solution for SoS designs allowing for a straightforward integration with other planar technologies such as microstrip and coplanar waveguide. Among the developed structures, SIW-based resonant cavities have been built exhibiting an excellent performance in terms of quality factor [91]. The combination of SIW resonant cavities with slotted FSS designs offers a combination of two different resonances and therefore provides a low-loss and low-cost architecture with a high quality factor and thus sharp roll-off at the passband edges [92].

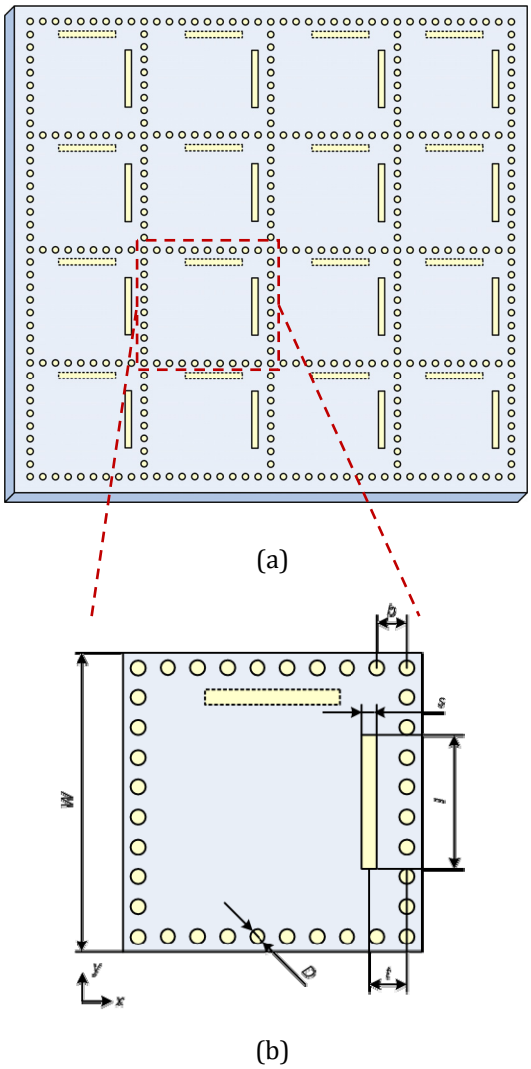

Figure 7.2 a) Structure of the proposed FSS architecture using a 2-D array of SIW cavities; b) a unit cell of the FSS structure with the coupling slots including the notation for the dimensions used in this paper.

In this paper, a novel concept has been introduced for SIW-based FSS architectures that allows for the selection of a linear polarization of the incident wave and its subsequent 90-degree polarization rotation. The proposed structure can be used in a variety of applications such as so-called filtennas combining an antenna with a filtering shield in a single unit [93]. Moreover, it can be employed in quasi-optical systems requiring a separation of polarization, such as it is the case e.g. in polarimetric imaging radars and/or

radiometers. Such systems are taking advantage of the concept inherent in the proposed structure where an incident wave is transmitted with a rotated polarization, while the reflected wave maintains the same polarization, thus allowing for a separation of the two polarizations and filtering of an incident wave in a single component.

Moreover, the proposed structure provides a number of advantages in terms of performance: the design is based on a dual-mode configuration, which offers a second-order resonance and therefore provides a low-loss and low-cost architecture with a broader bandwidth, as well as a high quality factor and thus a sharp roll-off at the passband edges. In addition, a very good decoupling of incident and outgoing waves is achieved using this dual-mode configuration.

For the design of the proposed structure, a code based on the method-of-moments boundary integral-resonant mode expansion (MoM/BI-RME) [94]-[95] has been adopted: this code provides a fast and accurate modeling of single-layer and multi-layered FSS with arbitrarily shaped elements, allowing for a considerable reduction in computation time over commercial full-wave electromagnetic software. In addition, the paper includes a detailed parametric performance study based on this method, providing a profound and computationally efficient insight into the performance optimization of SIW-based FSS.

Finally, a prototype operating at 35 GHz has been fabricated in order to verify the proposed concept. Its performance is investigated in detail, and measurements of different incidence angles are included in this paper in order to manifest the applicability of the proposed structure in practical high-end millimeter-wave applications.

The presented paper is organized as follows: section 7.3 describes the FSS architecture and design concept, section 0 outlines the simulation with particular emphasis on the analysis based on the MoM/BI-RME method. Section 7.5 introduces a performance model with a parametric analysis of the FSS, and in section 7.6 the experimental implementation and results are outlined and compared to the simulation results.

7.3 FSS ARCHITECTURE AND CONCEPT

7.3.1 Concept

The primary function of the FSS proposed in this work is the selection of a linear polarization of an incident wave and its subsequent rotation of 90 degrees while, at the same time, filtering the signal in a given bandwidth around the center frequency. The proposed structure is shown in Figure 7.2a. It consists of a 2-D array of SIW cavities with two orthogonal slots in each cavity on the front and back sides of the FSS, respectively. The SIW cavity is designed providing a resonance at the desired center frequency. Then, a vertical slot on the input (front) plane of the FSS is used for selecting the horizontal polarization from the incident radiation. The energy coupled from the slot is exciting a field in the cavity, and the outgoing wave is subsequently coupled through an orthogonal (horizontal) slot at the back side of the structure. In this way, it is possible to introduce the desired 90-degree rotation of the polarization of the incident wave.

7.3.1.1 SIW cavity design

The main element in the proposed design is the SIW cavity. Its resonance frequency $f_{R,C}$ for TM_{mn0} modes can be determined as follows [93]:

$$f_{R,C,TM_{mn0}} = \frac{c_0}{2\sqrt{\varepsilon_r}}\sqrt{\left(\frac{m}{W_{eff}}\right)^2 + \left(\frac{n}{L_{eff}}\right)^2} \tag{7.1}$$

with

$$W_{eff} = W - \frac{D^2}{0.95b} \qquad \text{and} \qquad L_{eff} = L - \frac{D^2}{0.95b}, \tag{7.2}$$

which is valid for

$$b < \frac{\lambda_0\sqrt{\varepsilon_r}}{2} \qquad \text{and} \qquad b < 4D. \tag{7.3}$$

D stands for the diameter of the SIW posts, *b* for their distance, *W* and *L* for the width and length of the cavity, respectively, and c_0 is the speed of light in vacuum. The dimensions W_{eff} and L_{eff} are effective measures relating the SIW cavity to a standard metallic rectangular cavity. Moreover, λ_0 represents the wavelength at the operation frequency, and ε_r is the relative dielectric permittivity of the substrate. Finally, *m* and *n* represent the modal indices with respect to the cavity resonances. In the case of the proposed structure, it is favorable to use a square cavity in order to maintain symmetry between the two polarization planes, i.e. $W = L$.

Mode	SIW cavity width *W*
TM_{110}	3.75 mm
TM_{120}, TM_{210}	6.13 mm
TM_{220}	7.84 mm
TM_{130}, TM_{310}	8.80 mm

Table 7.1 Cavity dimensions for different modes for a resonance frequency of 35 GHz.

7.3.1.2 Slot geometry

The second element required in the presented structure are the slots, which couple the incident energy into and out of the cavity. Their resonance frequency $f_{R,S}$ is related to the length of the slots, which should be selected approximately equal to half a wavelength, thus giving the following approximate equation for $f_{R,S}$:

$$f_{R,S} = \frac{c_0}{2l\sqrt{\varepsilon_{\text{eff}}}} \tag{7.4}$$

with *l* as the slot length, and ε_{eff} as the effective dielectric permittivity. This frequency needs to be selected close to the resonance frequency of the SIW cavity, so that a coupled incident wave can determine the excitation of the cavity mode. As a starting point, the

length of the slot is calculated according to (7.4) using the desired center operation frequency.

7.3.1.3 Selection of cavity mode

For the SIW resonator an appropriate cavity mode needs to be selected. In general, SIW cavity structures only support TM_{mn0} modes with $m = 1, 2, 3,\ldots$ and $n = 1, 2, 3,\ldots$ (considering the axis definitions used as a convention in resonators as shown in Figure 7.2b): first of all, SIW structures are usually very thin and therefore permit no field variation in *z*-direction; secondly, TE modes cannot exist in the structure, as the electric current density on the lateral side walls (for the case of resonators these are the *x*-*z*- and *y*-*z*-planes) can flow only in *z*-direction along the via holes.

Figure 7.3 shows an illustration of theoretically possible cavity modes for the use in our structure. In order to realize the desired polarization rotating behavior, we need to find a slot arrangement, in which, first of all, only horizontally polarized waves are coupled into the cavity, as well as only vertically polarized waves are emitted from the cavity. To this aim, the *E*-field-vectors need to be aligned orthogonally with respect to these slots in order to realize a proper coupling between the incident wave and the modal field in the cavity.

As shown in Figure 7.3a, e.g. the TM_{110} mode offers a field distribution suitable for such a configuration: the input coupling slot can be aligned vertically near the cavity edge, whereas the output slot is aligned horizontally so that for both input and output slots the *E*-field-vectors are aligned orthogonally with respect to the slot.

Another suitable configuration is given by a dual-mode configuration using TM_{120} and TM_{210} modes as shown in Figure 7.3c and Figure 7.3d, respectively. In this concept, the two modes coexist in the cavity, and the incident wave is coupled into the cavity through the vertical slot exciting a TM_{210} mode. Then, the TM_{210} input mode is coupled with the TM_{120} output mode in the cavity. Finally, the outgoing wave is coupled from a horizontal slot using the TM_{120} mode. The combination or coupling of these two modes in the cavity needs to be induced by a small perturbation, which, in the proposed structure, is given by the presence of the SIW via holes and the slots.

Additional solutions for realizing the desired functionality are given by any other dual-mode configuration combining TM_{1n0} and TM_{m10} modes with $m = n > 2$ (e.g., TM_{130} and TE_{310} modes, see Figure 7.3e and Figure 7.3f.).

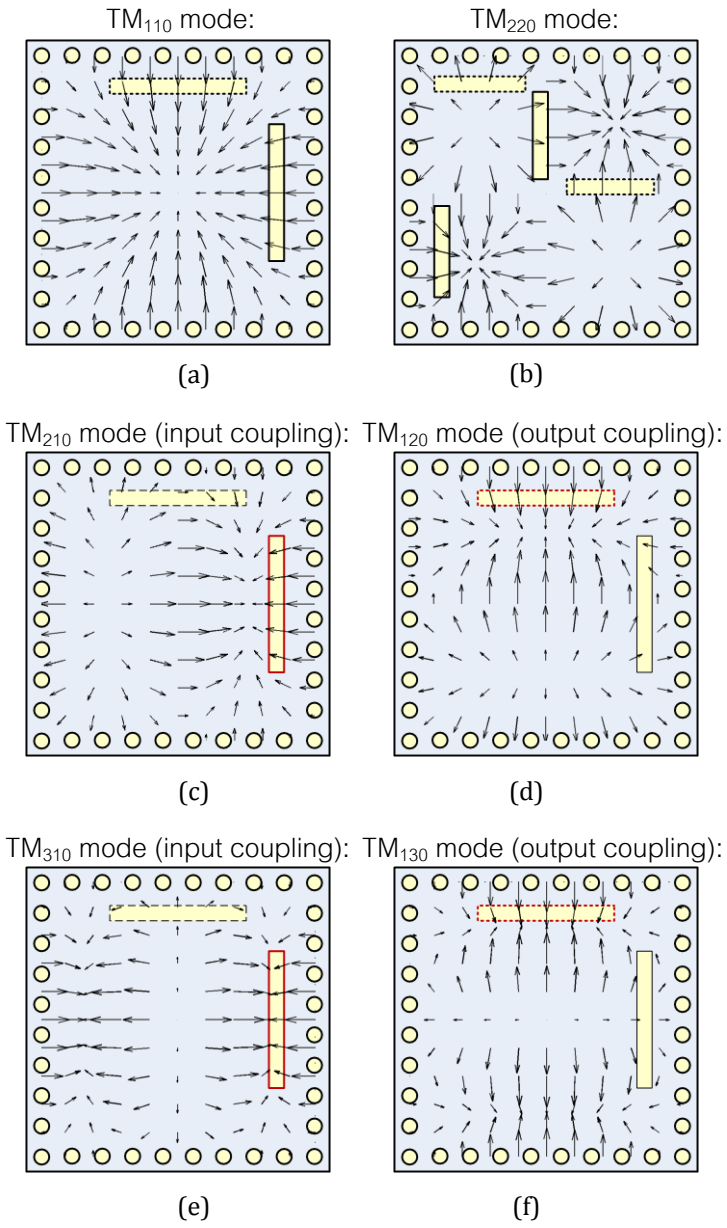

Figure 7.3 A unit cell of the FSS structure with the coupling slots and an overlaid vector plot of the respective mode (arrows: *E*-field vectors, solid lines: input slot, dashed lines: output slot): a) TM_{110} and b) TM_{220} mode suitable for both input and output coupling, c)–e) TM_{210}/TM_{120} and TM_{310}/TM_{130} dual-mode configurations suitable for input/output coupling (the bold red lines indicate the respective slot coupling with the mode shown in the figure).

Furthermore, in principle, TM_{mn0} modes with $m > 1$ and $n > 1$, such as the TM_{220} mode, also offer a proper mode configuration for the proposed structure when two separate slots are

used on either side of the cavity. However, as the slots need to be located at a distance corresponding to a value in the range of a wavelength, they bear the problem of creating transmission zeros under certain conditions due to field interference problems.

Thus, the possible implementations include the TM_{110} mode and the dual-mode configurations combining TM_{1n0} and TM_{m10} modes ($m = n > 1$). For the final selection of the mode, also geometrical restrictions and fabrication limitations posed by the structure need to be considered. In the following, a Rogers 5880 substrate with a dielectric constant $\varepsilon_r = 2.2$ and a thickness $h = 62$ mil (1.57 mm) is used. These substrate values are selected for their advantages in terms of bandwidth and of reasonably big geometric dimensions allowing for the use of a standard PCB fabrication process at an operation frequency of 35 GHz in this case study. The lower limit for the SIW hole diameter D for this substrate thickness is 0.5 mm. Table 7.1 shows the size of the SIW cavity for a resonance frequency of 35 GHz using $D = 0.5$ mm, and a spacing $b = 0.78$ mm. The slot length determined from (7.4) for the above denoted substrate using a first-order approximation for the effective permittivity [$\varepsilon_{eff}=(\varepsilon_r+1)/2$] yields a preliminary value $l = 3.4$ mm.

Comparing the slot length to the dimensions in Table 7.1, it is noted that, for the TM_{110} mode, the slot length is almost equal to the cavity width. Considering the diameter of the SIW posts, the required slot would be too long to fit into a cavity using the TM_{110} mode. One possibility consists in forming the slot in a *U*-shape or *H*-shape, but in that case, the suppression of the undesired polarization is limited.

Thus, the selection of one of the TM_{1n0} and TM_{m10} dual-mode configuration ($m = n > 1$) appears viable. When using a higher order mode configuration, the cavity size increases (see Table 7.1) and therefore the slot length is smaller than the cavity width. Among them, the TM_{120}/TM_{210} dual-mode configuration appears the most suitable solution, as the cavity size is still comparably small and easily allows forming a periodic structure with several cells. For higher modes, such as the TM_{130}/TM_{310} dual-mode configuration and higher, the coupling with the incident field is weaker, as the direction of the field vectors vary more and more, and thus, performance is degraded. In addition, compared to single-mode configurations such as the TM_{110}-based solution, the dual-mode configuration offers a number of additional advantages, as the two modes are inherently separated, and therefore a better decoupling of the incident and outgoing waves can be achieved.

In addition to the advantage of decoupling, with the dual-mode configuration we also achieve a broader bandwidth, as the two dual modes form a second-order resonance and thus two distinct poles in the frequency spectrum.

7.3.1.4 Slot position

Using the TM_{120}/TM_{210} configuration, different possibilities can be considered for the position of the slots as shown in Figure 7.4. For example, locating them in the center of the structure would lead to an intersection of the two slots and would therefore increase the leakage of the incoming wave towards the output. Locating the slots near the cavity edge represents therefore a better solution in terms of leakage performance. The finally adopted configuration is the concept shown in Figure 7.4a.

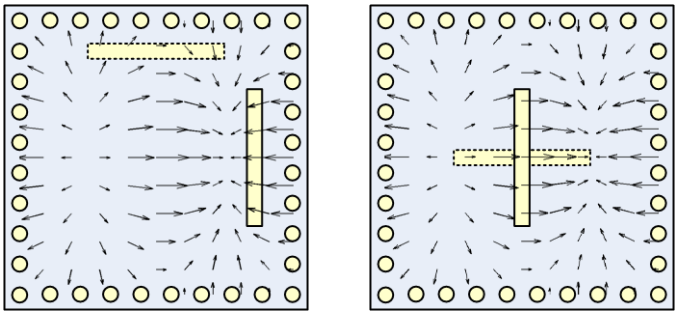

Figure 7.4 Different possible slot positions for the TM_{120}/TM_{210} dual-mode configuration: a) near the cavity edges; b) in the center of the unit cell.

7.3.1.4.1 Operation concept

For a better understanding of the operation principle of the proposed structure, all the different possible signal paths are illustrated in Figure 7.5. Four different scenarios are of interest using the structure in a realistic environment (note that in the following description an arrangement with vertical input slots and horizontal output slots as depicted in Figure 7.2 is considered):

1. The desired effect, i.e. transmission in cross-polarization, is given by an incident wave of horizontal polarization (orthogonal to the input slot), which is coupled to the output with a vertical polarization (orthogonal to the output slot).
2. Impedance matching, i.e. reflection in co-polarization, is described by an incoming wave of horizontal polarization with a reflected wave of the same polarization.
3. Transmission leakage (in our case corresponding to transmission in co-polarization) is defined by an incident wave of horizontal polarization, and its non-rotated outgoing wave of the same polarization.
4. Reflection leakage (here reflection in cross-polarization) describes the reflection with a polarization rotation, i.e. a wave incident with horizontal polarization and a reflected wave with vertical polarization.

Certainly, in an analogous manner, the same characteristics (with reversed polarization considerations) can be seen from the output side of the structure as the proposed structure is passive in nature.

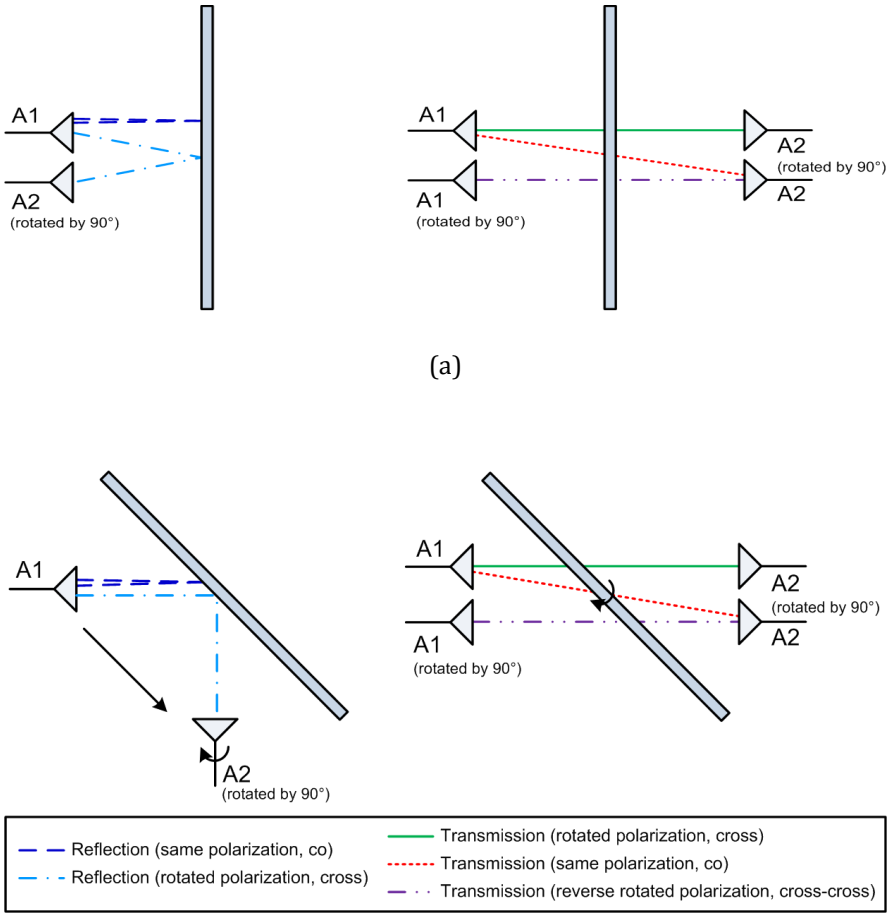

(a)

(b)

Figure 7.5 Measurement of different incident angles: Transmission and reflection paths for a) orthogonal and b) non-orthogonal incidence angles.

7.4 SIMULATION

The analysis of FSS can be carried out in different ways: One possible solution are algorithms based on the finite difference time domain (FDTD) technique or the finite element method (FEM), which apply to very general structures and can be used in the analysis of a very large variety of EM structures. However, these numerical methods are

usually quite slow in terms of computational time and require a large memory allocation. Recently, a novel algorithm has been proposed [94], [95], based on the use of the method of moments (MoM) with entire-domain basis functions defined on arbitrarily shaped domains. In the case of unconventional shapes, a proper set of basis functions is efficiently calculated by the boundary integral-resonant mode expansion (BI-RME) method. This algorithm is named the MoM/BI-RME method and was implemented in an efficient simulation code, which was used for the design of frequency selective surfaces [96], [97], of boxed microstrip circuits [98] and of electromagnetic band-gap structures [99]. Thanks to the use of entire-domain basis functions, the code based on the MoM/BI-RME method allows to perform wideband simulations in extremely short computational time, much shorter than commercial general purpose electromagnetic simulators.

The analysis and optimization of the proposed FSS structure has been performed with a specifically developed version of the code based on the MoM/BI-RME method. For reducing the simulation complexity and the computing time, the SIW cavity was modeled as a standard waveguide cavity using dimensions according to the basic equivalent waveguide concept for SIW structures.

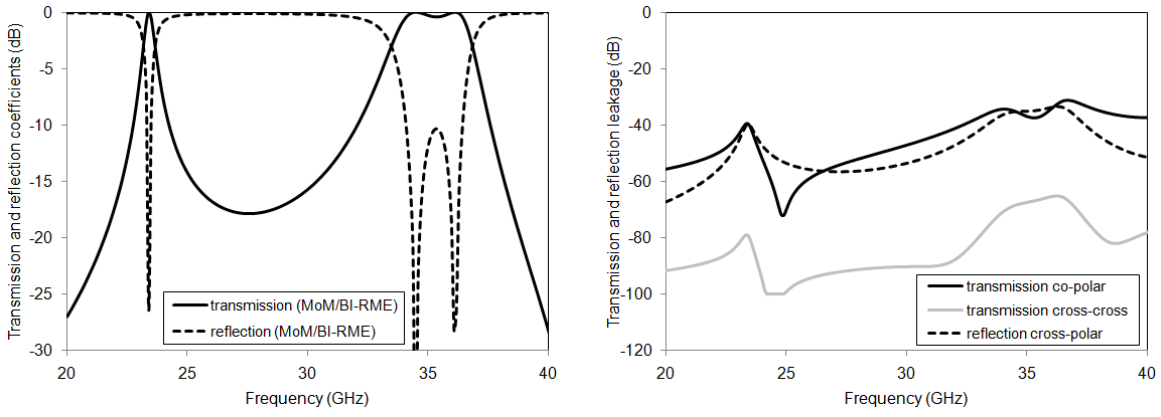

(a) (b)

Figure 7.6 Simulation results for the proposed FSS structure with optimized dimensions: a) transmission and reflection coefficients, b) simulation of leakage with the MoM/BI-RME method.

As a starting point, (7.1)–(7.4) are evaluated for a TM_{120}/TM_{210} dual-mode configuration at the desired operation frequency of 35 GHz, using a selected hole diameter D = 0.5 mm and a spacing b = 0.78 mm. This yields an SIW cavity width W = 6.13 mm (square cavity) and a slot length l = 3.4 mm. A preliminary simulation with these values is performed setting the initial slot width to $l/8$ and positioning the slot close to the cavity edge (t=1.55 mm).

A simulation of this preliminary structure gives a frequency shift compared to the originally calculated SIW cavity resonance in (7.1). This is an expected behavior, as the presence of the slots perturbs the field distribution in the cavity given the fact that the slot dimensions are comparable to the size of the cavity. Furthermore, for the final design, impedance matching needs to be adjusted and bandwidth maximized. Therefore, an optimization iteration is performed including the parameters W, l, s, and t as shown in Figure 7.2b yielding the final design dimensions given in Table 7.2.

Figure 7.6a shows a simulation of the wideband performance from 20 GHz to 40 GHz for the optimized design obtained with the MoM/BI-RME method. The desired pass-band is obtained at the center frequency of 35 GHz, with an impedance matching better than –10 dB over a relative bandwidth of 9.1%. The simulation also shows another resonance occurring at 23.4 GHz, which is attributed to the TM_{110} cavity mode. Comparing the two transmission peaks in Figure 7.6a, the performance advantages in terms of bandwidth and roll-off introduced by the dual-mode resonances in our structure are clearly visible and correspond to the design considerations that have been taken in section 7.3. Figure 7.6b also shows the results for transmission/reflection leakage (refer to Figure 7.5 for details in path definition). All values are below –30 dB. More detailed simulation results can be found in the parametric analysis in section 7.5 and in the comparison with measured results in section 7.6.

Parameter	Value
W	5.7 mm
D	0.5 mm
b	0.81 mm
l	3.58 mm
s	0.57 mm
t	1.55 mm
h	1.57 mm

Table 7.2 Final Dimensions for SIW Cavity FSS.

7.5 PERFORMANCE STUDY

In order to establish a generally applicable design procedure for structures such as the FSS proposed in this paper, a performance study based on a parametric analysis is developed. The analysis is carried out simulating different variations of the proposed structure with the help of the previously outlined MoM/BI-RME method, which has been proven to yield very accurate analysis results.

As explained earlier, in the proposed FSS design, we combine two resonances originating from the selected TM_{120}/TM_{210} dual-mode configuration in order to achieve the desired frequency response. In order to understand its working principle, it is important to note the following details: in the proposed structure, the cavity provides a resonance that occurs exactly at the same frequency for both the TM_{210} mode (input coupling) and the TM_{120} mode (output coupling), respectively. When a slot is inserted into the cavity, the field in the cavity is perturbed by the presence of the slot. Considering, for example, the input slot, its effect on the TM_{210} mode (input) is not the same as its effect on the TM_{120} mode (output), as the field distributions for the two modes are orthogonal to each other. Thus, for the two modes, the presence of the slot results in a different field perturbation. In an analogous manner, also the output slot gives a different effect on the two modes. In combination, this effect leads to the development of two different distinct poles with a certain frequency spacing as shown in the simulation result in Figure 7.6a.

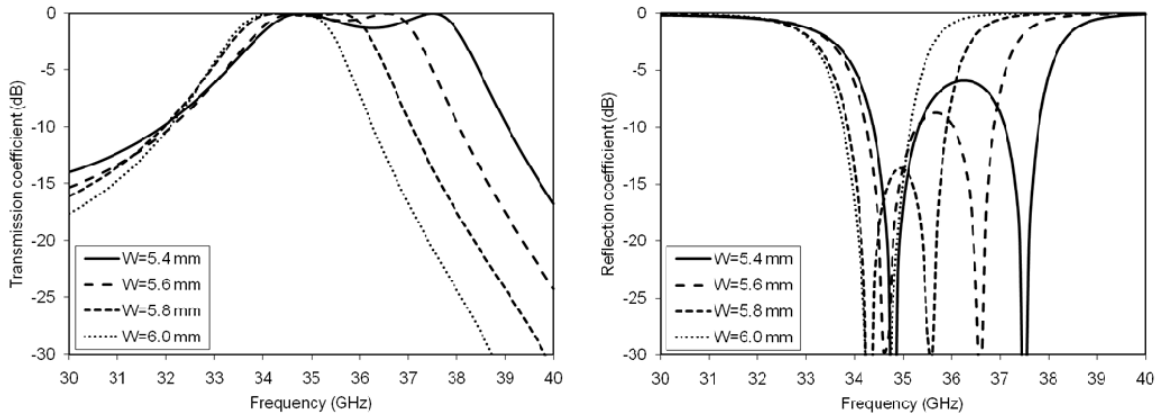

(a) (b)

Figure 7.7 Simulation results for different SIW cavity widths *W*: a) transmission coefficients, b) reflection coefficients.

7.5.1 Resonance frequency

For the determination of the desired resonance frequency, the two main design parameters are the SIW cavity width *W* and the slot length *l*. The cavity width directly defines the frequency of the resonant TM_{120}/TM_{210} modes. The slot length defines the frequency, at which an incident wave is coupled into the cavity, and therefore needs to be selected close to the cavity resonance. In both cases, smaller values lead to a higher resonance frequency. A plot for a parametric sweep of these two parameters is shown in Figure 7.7 and Figure 7.8, respectively. When increasing *W*, the center frequency of the passband moves to higher values. Varying the slot length *l* leads to a similar effect.

Optimizing the two parameters together in the proposed design, the dimensions *W* = 5.7 mm and *l* = 3.58 mm are selected, as they provide a center operation frequency of 35 GHz as desired.

7.5.2 Bandwidth

For bandwidth considerations, the design aim is to increase the frequency spacing between the two resonances. In principle, any variation, which changes the perturbation of the cavity field caused by the slot, leads to a change in frequency spacing and thus bandwidth.

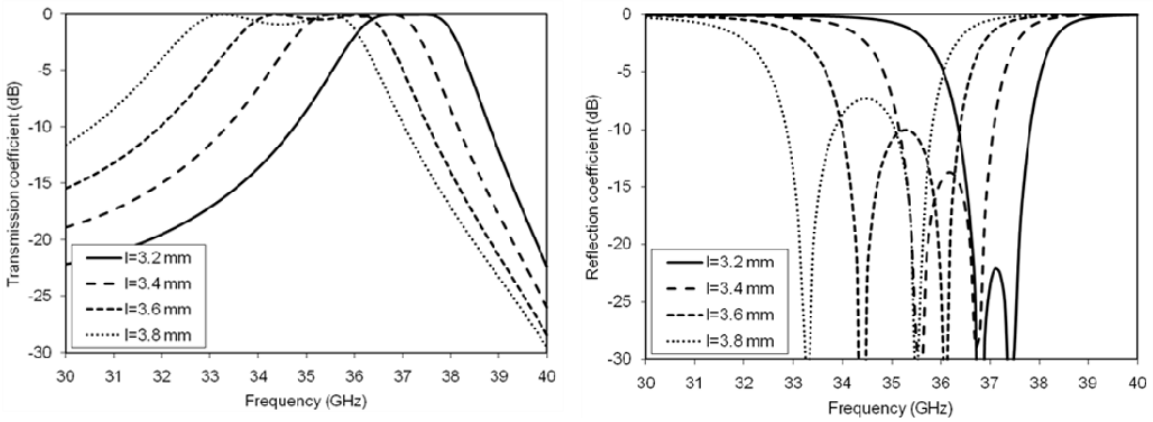

(a) (b)

Figure 7.8 Simulation results for different slot lengths *l*: a) transmission coefficients, b) reflection coefficients.

First of all, the selection of the substrate thickness represents an important design step: if this value is changed, the effective permittivity of the substrate varies, which plays a significant role for the field caused by the slot. With a thicker substrate, the effective permittivity increases, and thus the perturbation becomes more distinct, because the field is more confined within the substrate. This leads to a higher bandwidth as shown in Figure 7.9.

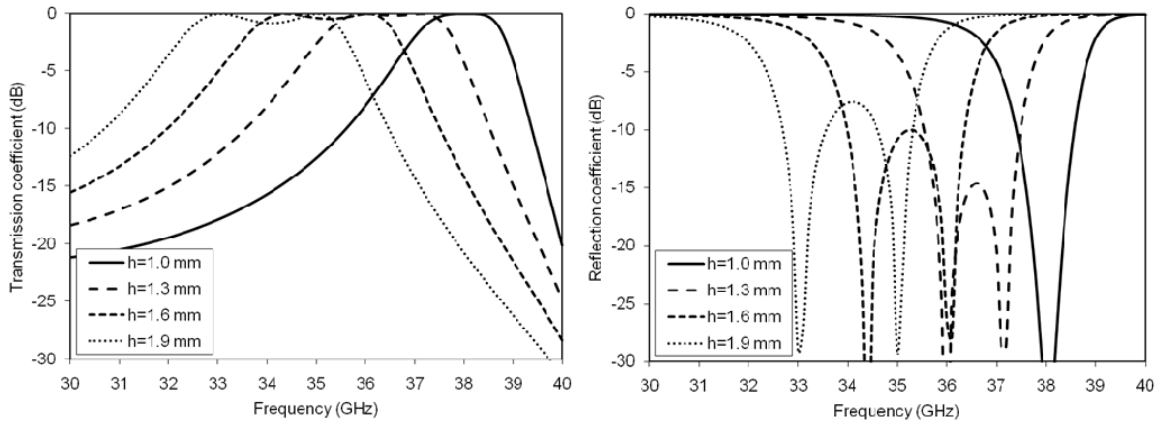

(a) (b)

Figure 7.9 Simulation results for different substrate heights *h*: a) transmission coefficients, b) reflection coefficients.

In the presented structure, we select a substrate with a thickness *h* = 62 mil (1.57 mm). Moreover, the relative values of *W* and *l*, respectively, largely influence bandwidth, as varying them indirectly also influences the field perturbation created by the slot. For instance, for higher values of *W*, the slot becomes shorter in comparison, and therefore perturbs the cavity field less resulting in a smaller bandwidth. On the other hand, when increasing the slot length *l*, the field perturbation is stronger, and so bandwidth increases.

7.5.3 Impedance matching

The above described approach for maximizing bandwidth performance always has to be carried out in accordance with impedance matching specifications. If the two resonances move away from each other, the level of the return loss becomes higher. Thus, all the parameters need to be optimized in order to find a suitable trade-off between bandwidth and matching specifications.

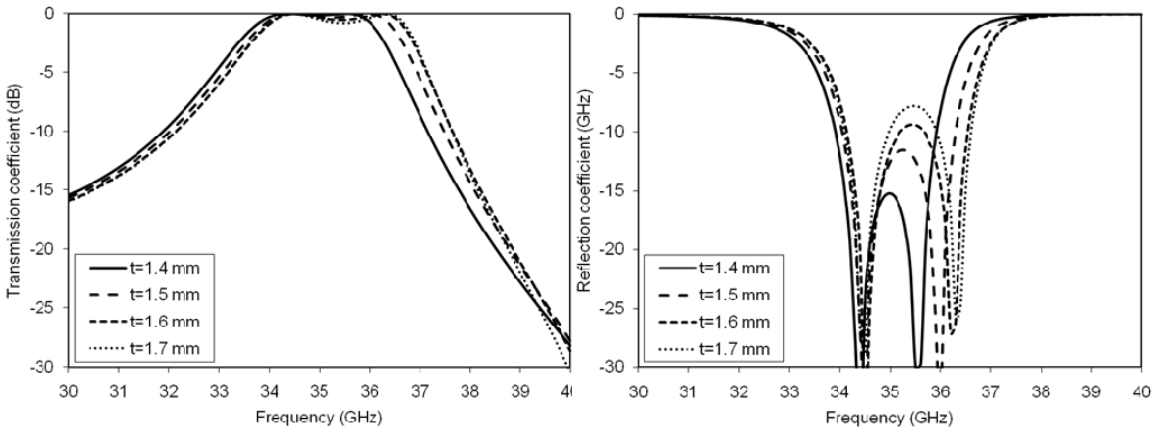

(a) (b)

Figure 7.10 Simulation results for different slot positions *t*: a) transmission coefficients, b) reflection coefficients.

In addition to these considerations, the slot position *t* is an important parameter: it has only a marginal influence on the slot resonance, but impedance matching is largely affected. Theoretically, the best performance in terms of impedance matching is achieved if the slot is positioned at the edges of the cavity, as the field distribution at that point is orthogonal to the slot for a metallic waveguide resonator. The effect is shown in Figure 7.10, where matching becomes better and better for higher values of *t*. However, in reality, the via holes of the SIW cavity perturb the ideal field distribution given by a metallic rectangular cavity, and so it is necessary to position the slot at a certain distance from the edge where the field is only negligibly influenced by the via posts. Note that in Figure 7.10, which shows an analysis using the MoM/BI-RME method, this effect is not visible, as the simulation is carried out with the equivalent cavity model as discussed in section 0. Thus, in an additional study using Ansoft HFSS [100], it has been found that the structure yields optimized performance when the slot is positioned at an approximate distance of $W/4$ from the SIW cavity edges.

Moreover, the variation of the slot width *s* enhances matching while maintaining a constant bandwidth as shown in Figure 7.11. For a wider slot, the coupling is higher while maintaining an almost constant bandwidth, and so impedance matching is increased.

Here, once more it becomes clear, why the selected TM_{120} mode is a good choice for the proposed structure: selecting a higher mode such as the TM_{130} mode, the available space for the slot decreases (see Figure 7.3), and so the maximum slot width that can be achieved is limited, which reduces coupling and thus impedance matching.

In our design, the slot position t is selected to 1.55 mm with a slot width s of 0.57 mm.

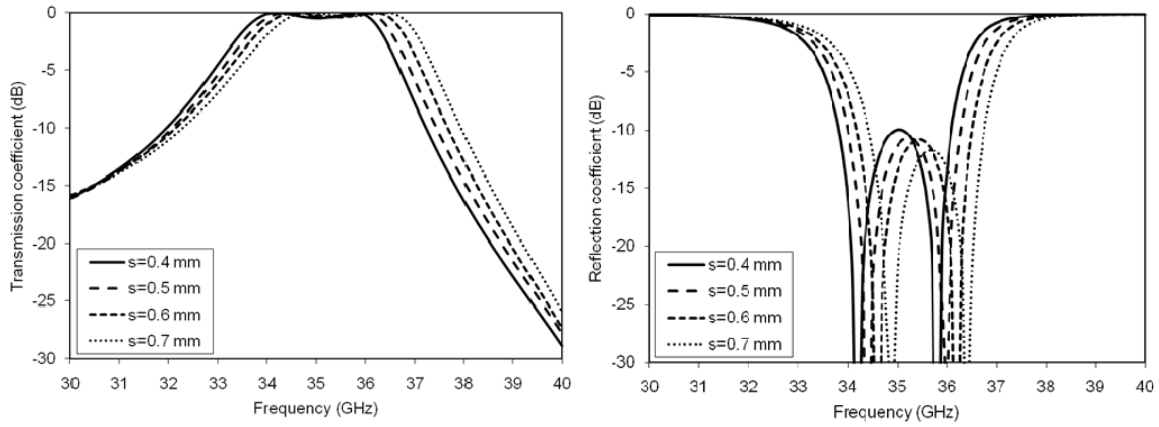

(a) (b)

Figure 7.11 Simulation results for different slot widths *s*: a) transmission coefficients, b) reflection coefficients.

7.6 EXPERIMENTAL RESULTS

To verify the functionality of the proposed architecture, the FSS has been fabricated with the optimized dimensions in Table 7.2 and measured. A photograph of the prototype is shown in Figure 7.12. It consists of a 30 x 30 array of SIW cavities with vertical and horizontal slots on the front and back sides, respectively.

The experimental setup used in the measurement of the proposed FSS is shown in Figure 7.13 using two standard gain K-band horn antennas and a vector network analyzer for measuring the S-parameters in order to determine the transmission/reflection characteristics. A number of important considerations need to be taken into account for achieving good measurement accuracy: first of all, the distance of the FSS with respect to

the antennas has to be selected in order to minimize the amount of radiation illuminating the edges of the FSS (< –15 dB). This distance can be determined from the radiation pattern of the horn antenna used in the measurement and yields a minimum distance of 50 cm between each antenna and the FSS in our case. Moreover, the size of the FSS has to be chosen sufficiently large in order to let this distance fall in the far field of the antennas. In addition, an arrangement of anechoic material in the form of absorbing cones is placed around the FSS as shown in Figure 7.13a–c in order to minimize the edge effects in the measurement.

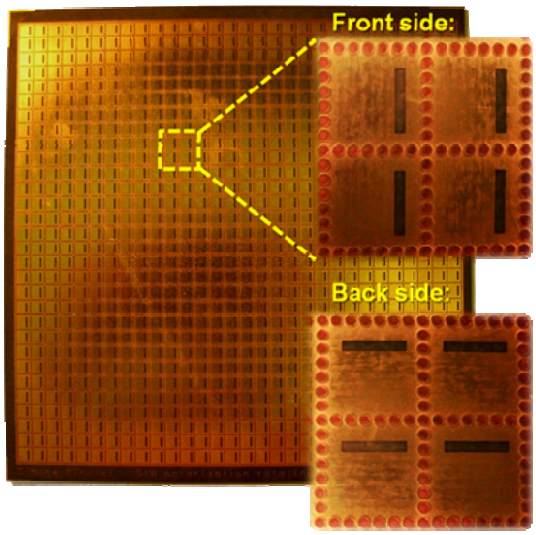

Figure 7.12 A photograph of the proposed 35 GHz polarization rotating FSS including a detailed view of front and back side unit cells.

7.6.1 Transmission and reflection measurement setup

All the important signal paths that have to be measured are shown in Figure 7.5 for both orthogonal and non-orthogonal incidence angles.

The measurement of transmission characteristics is carried out with two antennas on either side of the FSS as shown in Figure 7.13a. One antenna is facing the front side of the

FSS and the second antenna its back side. A reference measurement is taken without the FSS for normalization in order to exclude the effect of the free-space transmission and any possible interferences with surrounding objects. Both cross-polarization transmission (the desired function of the FSS) and co-polarization transmission (leakage) are measured. The former is obtained by orienting the polarizations of both antennas orthogonal to the input and output slots of the FSS, respectively, while the latter is measured with both antennas in the same orientation.

Figure 7.13b shows the measurement arrangement for a reflection measurement with two adjacent antennas. In theory, the parameter S_{11} of the transmission measurement is sufficient for characterizing reflection behavior. However, in practice, in most cases, the level of the reflected signal is lower than the return loss of the antenna, as it also includes losses introduced by the free-space transmission path between the antenna and the FSS, and thus a separate configuration for the reflection measurement with two adjacent antennas needs to be used. Once again, in this setup, a reference measurement is carried out for eliminating the effects of free-space radiation from the measurement. This measurement step is carried out using a reflecting metal plane of the size of the FSS. Moreover, the crosstalk between the two adjacent antennas has to be taken into account and is measured separately for reference, as the antennas are positioned very close to each other, especially in the case of a measurement of orthogonal incidence (Figure 7.13b). In addition, the antennas need to be aligned correctly with each other and with the FSS ensuring that the maximum of the antenna beam illumination lies at the center of the FSS, which is realized in practice using a laser beam together with a small mirror in order to align the signal paths as shown in Figure 7.13c. Finally, the reflection in both co- and cross-polarizations is measured with the two antennas in parallel and orthogonal polarization orientations, respectively.

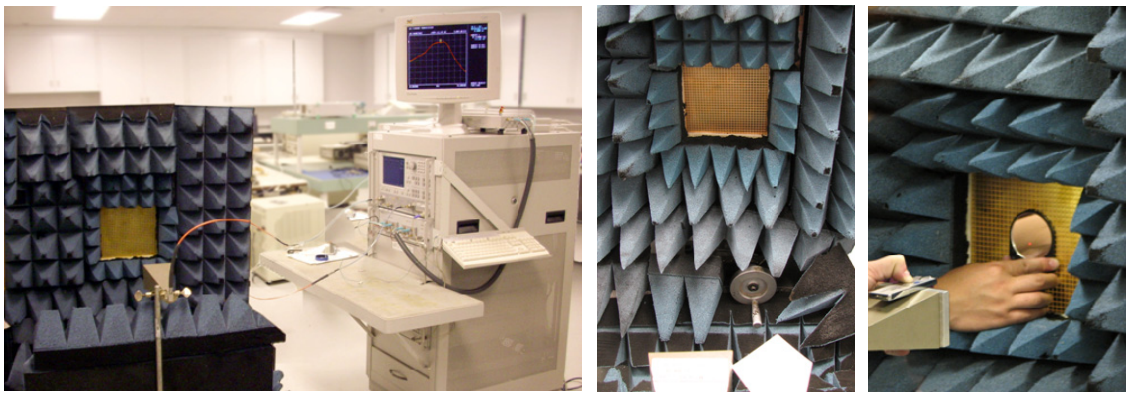

(a) (b) (c)

Figure 7.13 A photograph of the measurement setup for the proposed 35 GHz polarization rotating FSS: a) overall setup with network analyzer in transmission configuration; b) reflection measurement with two adjacent antennas and crank handle setup for non-orthogonal incidence angle measurements; c) alignment procedure with reflected laser beam.

7.6.2 Orthogonal incidence

Figure 7.14a shows the results for the case of an orthogonal incidence for transmission and reflection, respectively. We obtain a very good matching below –12 dB for a 3-dB-bandwidth of 3.2 GHz or 9.1% with a maximum insertion loss of 0.2 dB in the passband. The ripple on the measurement data can be attributed to the diffraction at the edges of the FSS: the maximum size of the FSS is limited by the PCB fabrication process, and therefore on one hand the illumination cannot be considered as locally planar, whereas on the other hand the antenna beam is scattered at the edge of the FSS surface. The measured data agree very well with the simulation using the M0M/BI-RME method, which proves once more its high accuracy and practical applicability. Considering also the immense reduction in terms of computational time, the proposed simulation method represents a highly interesting solution in the design of high-end passive microwave- and millimeter-wave structures.

Figure 7.15b shows the results for transmission and reflection leakages in comparison with the simulation results. All values are below –30 dB for the entire frequency band. The slight

deviation between simulations and measurements is due to the low level of the leakage measurement signals, as they partly fall below the return loss of the two antennas.

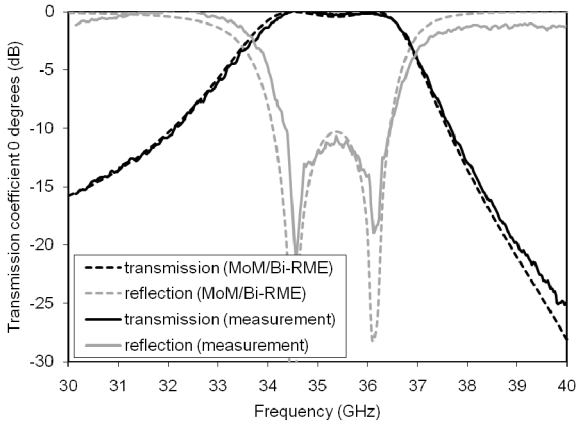

(a)

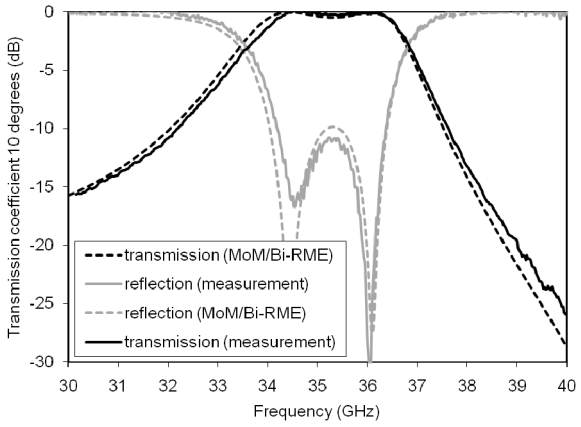

(b)

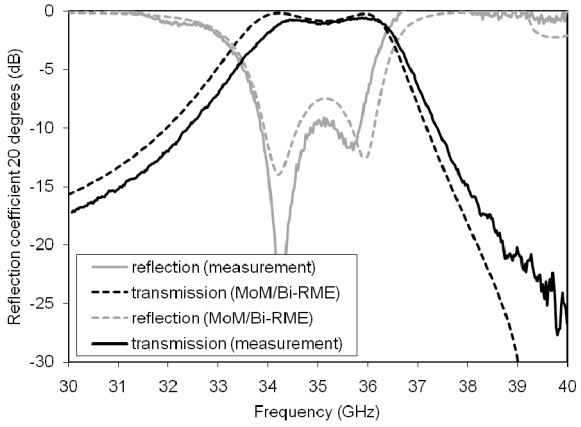

(c)

Figure 7.14 Transmission and reflection in simulation and measurement for incidence angles of a) 0 degrees, b) 10 degrees, c) 20 degrees.

7.6.3 Non-orthogonal incidence

A very important criterion for the performance of FSS structures is its behavior for the case of non-orthogonal incidence angles. Usually, inclining an FSS structure, the dimensions such as e.g. slot lengths an incident wave sees, appear shorter, and therefore frequency shifts may occur. In the proposed structure, for the case of the desired transmission in cross-polarization, a horizontally polarized wave is coupled through a vertical input slot into the cavity. Varying the incidence angle by rotating the FSS around its vertical axis, the transmission antenna always sees the same slot length as for an orthogonal incidence. However, the horizontal slot at the output plane seen from the receiving antenna appears shorter and thus its resonance appears shifted to a higher frequency. In addition, the slot width of the input slot appears narrower, and so input coupling is decreased. The combination of these two effects leads to a decrease in bandwidth on one hand, and to a worsened matching performance on the other hand. Considering this problem, it becomes clear why it is important to describe the FSS behavior for non-orthogonal incidence angles.

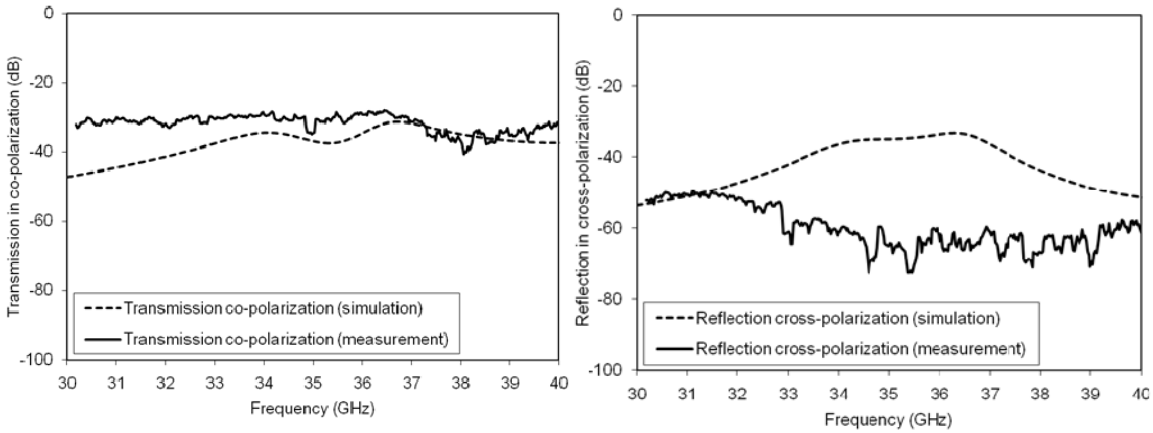

(a) (b)

Figure 7.15 Leakage in simulation and measurement for the proposed FSS polarization rotating architecture: a) leakage due to transmission in co-polarization; b) leakage due to reflection in cross-polarization.

The measurement of non-orthogonal incidence angles is carried out in the same way as the above described reflection and transmission measurements. The rotation of the FSS is achieved using a crank handle as shown in Figure 7.13b, on which the FSS support including its anechoic embedding is mounted. This setup allows for a precise rotation of the structure while maintaining the remaining setup unchanged. The measurement is carried out for incidence angles of 0 degrees, 10 degrees, and 20 degrees, respectively. Attention needs to be paid in the case of reflection measurements as the two antennas need to be positioned at the correct angles and positions relative to the FSS structure as shown in Figure 7.5. Their alignment is again achieved using a laser beam that is redirected with a small mirror positioned in the plane of the FSS. Again, for every angle, a reference measurement is taken as described for the measurement of orthogonal incidence.

Figure 7.14 shows the results for transmission and reflection. It is clearly visible that the FSS shows good performance for all the measured incidence angles.

As previously described, the measurement setup includes an arrangement of anechoic cones around the FSS in order to reduce the edge effects. At 30 degrees and higher, the measurement result is strongly influenced by the presence of these cones, as the shadow they drop on the FSS strongly absorbs the incident energy. For an accurate measurement, a different measurement setup using a thin layer of plane anechoic material should be used, which was not available at the time of writing.

Moreover, once again, the excellent prediction of the FSS performance by the MoM/BI-RME method is visible: simulations and measurements agree very well and prove the high quality of the proposed method.

7.7 CONCLUSIONS

This chapter describes an FSS structure based on a periodic SIW cavity architecture, which can be used in the proposed imaging system in order to separate horizontal and vertical polarizations from the incident radiation. Future work will include the use of this FSS in the system.

Chapter 8

FUTURE WORK

The presented Ph.D. thesis presents part of the work completed within a very big project governed by several students in the Poly-Grames Research Center. Thus, a large variety of future projects are possible and advisable in order to take the suggested system to a high-performance level that is practically applicable in commercial applications and involves new future-oriented design elements.

8.1 FOCAL PLANE ARRAY

Future work may include the parallelization of the proposed receiver elements to an FPA in order to allow for real-time processing capability.

Regarding the intention to create entirely monolithic integrated circuit architectures, a purely planar broadside radiating structure might be desirable for the proposed FPA system but poses space problems for complete IF circuitry integration and furthermore difficulties in thermal dissipation due to the high number of active devices within limited space. Thus, an endfire-based array geometry appears viable using a design with “circuit cards” as shown in Figure 8.1.

Furthermore, a number of important performance requirements for the feed elements, such as efficient antenna illumination in terms of sidelobes, low losses, effective coupling to active devices, high polarization purity, and low cost represent important factors in terms of antenna selection and design.

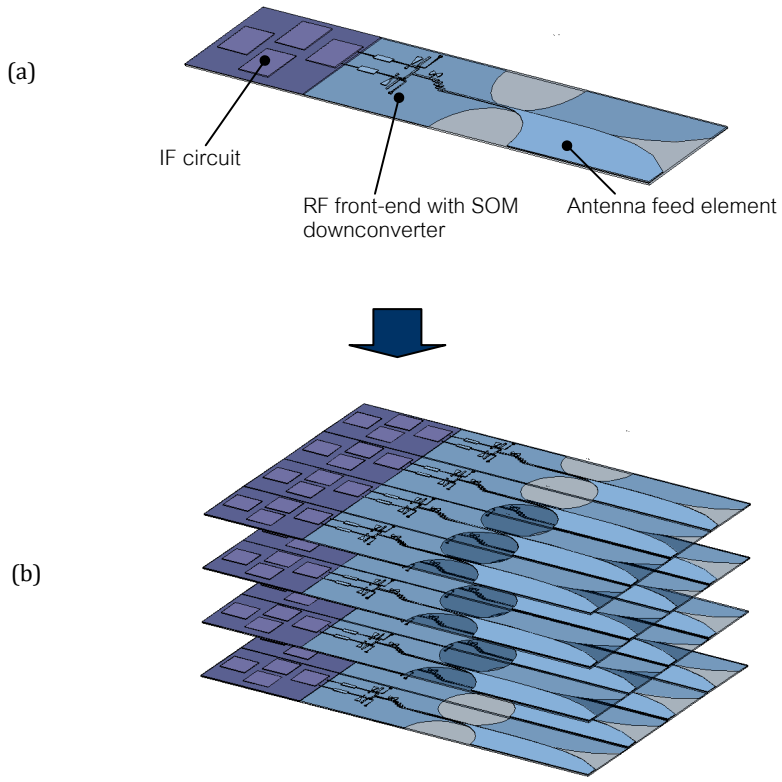

Figure 8.1 Architecture of the proposed multibeam FPA system: a) single receiver module employing feed element, RF front-end, and IF circuitry; b) integration of receiver module into a multibeam imaging array.

A highly important parameter for defining the performance of an imaging system is its spatial resolution. It is defined as the minimum separation of the object of interest from its surrounding that can be resolved by the imager, or in other words, for each object to be resolved, there should be at least one associated pixel in the final image. Employing an FPA multibeam imaging system, a high number of compact feed elements are located within a minimum of space and the achievable spatial resolution is an immediate consequence of the spacing of its feed elements in the focal plane of a lens or reflector. Minimum element spacing is therefore of high importance to achieve reasonably high-resolution images. Applying the Nyquist theorem for the case of imaging systems, the feeds must be placed at

an interval of $\lambda/2 * f/D$ [33]. In such a system, spatial resolution depends on the half-power beamwidth of the antenna, which for a distance R between receiver and target, a wavelength λ, and an antenna aperture D yields a spatial resolution of $d \sim R\,\lambda/D$.

However, it can be shown that it is not possible to design an imaging system with this resolution, which also has an aperture efficiency approaching that of a typical single-beam system [10]. For example, creating an imaging array of waveguide horn feeds with high efficiency yields a spatial resolution as high as four times the Nyquist interval. Thus, suitable feed types need to be considered for the realization of a high-efficiency high-resolution MMW imaging array and a trade-off between element spacing and aperture efficiency needs to be found. Theoretical and experimental investigations have been carried out on finding optimized feed elements for FPA imaging arrays. Suitable types include horns, tapered slot arrays (TSAs), such as the linear TSA or the Vivaldi antenna, double dipoles, Yagi antennas, and dielectric rod antennas [34]–[38]. In general, feed elements such as TSA antennas and dielectric rod antennas that derive their gain from length more than from their cross-section are preferred. Recent publications also introduce studies on the optimal dithering of FPAs in order to maximize spatial resolution in MMW imaging systems [39]. In the proposed project, we plan to implement a Vivaldi antenna based FPA imaging system offering adequate gain, high bandwidth, and moderate cross-section [40]–[42].

In addition, mutual coupling between the feed elements will become an important issue. Generally, the electric field distribution in such antennas is tapered in order to minimize sidelobes. However, this tapering broadens the main antenna beam and therefore causes interaction via fields or currents between the feed elements. This can cause undesired destructive and constructive interferences, which effectively reduces the system's spatial resolution.

Combining all these aspects, a certain feed element distribution has to be found in order to allow for a certain spatial resolution with required beam efficiency. Accurate numerical simulations and experimental verifications will allow for taking these effects into account and achieving an array design, which guarantees the required performance in terms of spatial resolution.

8.2 STABILITY IMPROVEMENT

As it has become clear in the course of the experiments carried out, stability of the radiometer is an important issue that needs to be carefully addressed, as any small changes in system temperature or gain largely affect the measured result. In a standard manner, Dicke radiometers [30] solve this problem by calibrating during every measurement with a known load, which is connected through a switch, the so-called Dicke switch.

Moreover, the imaging group at Poly-Grames is implementing a radiometer structure eliminating this expensive and lossy switch from the receiver circuit by using a differential structure entirely based on low-loss SIW architecture.

8.3 ELECTRONIC SCANNING

Given a satisfactory performance, an electronic scanning system would be the best choice for the proposed project. At the same time such a system would be real-time capable, compact and inexpensive. However, the design of electronic scanning antennas that provide satisfactory resolution and overall scan angle remains still very difficult.

The imaging group is currently working on the development of an electronic scanning antenna based on SIW beamforming networks.

8.4 IMAGE FUSION

A very interesting approach is also image fusion, which is used to unite both a visual and a millimetre-wave image with an optional infrared image in order to combine the complimentary advantageous aspects of each of these sensors [4].

8.5 BROADBAND SUBSTRATE INTEGRATED WAVEGUIDE

Requiring broadband receiver structures, the bandwidth capabilities may be examined. The authors have been working on the development of broadband SIW transmission lines, which would suit a possible implementation in a future imaging radiometer system [85].

8.6 MEASUREMENT TECHNIQUES

One important future aspect includes the development of accurate and high-quality measurement techniques for the proposed system. At this first level of the system, rather empirical methods have been employed that can be extended.

A single receiver element can be characterized in terms of coherent sensitivity for the application of a sinusoid input signal, from which the noise-equivalent bandwidth can be derived. Furthermore, it is important to determine the receiver's noise-equivalent temperature difference (NETD), which is carried out in two separate steps. First the voltage difference between two input temperatures (e.g. one at room-temperature (293 K) and one in a liquid nitrogen cooled environment (77 K) or a load in a freezer (248 K)) yields the temperature sensitivity, whereas the second measurement analyses the root mean square output noise voltage for a terminated input. In addition, stability measurements characterize gain and noise fluctuations over time and specify calibration requirements. A critical requirement in these measurements is the thermal equilibrium of the radiometer, which can be realized by using a temperature stabilized enclosure.

At imaging system level the same experiments can be performed by using a uniform illumination at two different ambient temperatures, which gives the temperature sensitivity for the overall system that is generally lower due to efficiency reductions and mutual coupling. In addition, a characterization of overall power consumption and heat dissipation is of interest.

For each of these measurements it must be kept in mind that radiometry receivers deal with extremely low signal levels in the range of –80 dBm, and therefore very accurate measurement techniques with stable, well-known, and well-calibrated sources and instruments are necessary. Each of these fabrication steps and experiments will be carried

out at the Poly-Grames Research Center offering nearly all the possibilities for this research. Finally, measurement results will be carefully compared to simulations in order to verify proposed design techniques and functionality.

8.7 MULTI-POLARIZATION SYSTEM ENHANCEMENT

The system may be characterized for its multi-polarization capability by adding the designed FSS in the setup. It may contain two receiver structures, whereof one measures the radiation transmitted through the FSS, while the second receiver collects the radiation reflected from the FSS. The FSS must be oriented at a certain angle to make this measurement possible, which is proven to be viable by the angular measurements taken in the FSS design.

For a characterization of the multi-polarization system, half and quarter wave plates are generally employed in front of the radiometer feed in order to measure the polarization in different orientations [42].

8.8 FREQUENCY SCALING FROM 35 GHZ TO 94 GHZ

An improvement in imaging resolution and system size is achieved by scaling the proposed system to a frequency of 94 GHz or higher. Such a future system can be designed on the basis of a multi-pixel FPA imager fabricated in MMIC technology.

8.9 SIGNAL PROCESSING ENHANCEMENT

A final aspect of future work includes the development of high-quality signal processing techniques. The IF circuitry in the presented radiometer receiver yields voltage signals proportional to the temperature measured at each pixel, which is either fed to a PC based data acquisition system or digitized by an analog-digital converter (ADC) and processed by

a DSP. A major part of image acquisition and quality lies in the subsequently adapted signal processing schemes, which are described in this section.

Due to the similar nature of radiometric images compared to optical images, generally, standard imaging processing algorithms can be applied in order to achieve enhanced image quality, contrast, resolution and noise reduction [45]. Especially for applications such as concealed weapon detection, these methods are applied in order to detect hidden objects. Wavelet transform algorithms are applied for denoising and enhancement, and morphological filters are used for clutter filtering. Finally, shape description techniques detect specific objects [4]. Additionally, superresolution techniques [46], [47] can be applied to enhance spatial resolution and therefore reduce required aperture size. A variety of such methods has been developed for the purpose of passive imaging enhancement, which can be classified into linear and nonlinear methods. The latter offer better sharpening but require an enormous computation complexity compared to their linear counterparts.

CONCLUSION

In this project, a complete passive millimetre-wave imager at 35 GHz based on the subharmonic SOM technique is proposed and studied. The research work in this Ph.D. thesis focuses in particular on the design, implementation, and experimental testing of subharmonic SOMs. The final 35 GHz SOM circuit is proposed to be implemented into a straight-forward mechanical raster scanning imaging system based on a single-element receiver in order to prove functionality of the SOM technique in the framework of millimetre-wave imaging systems.

Within the presented thesis, the physical background of radiometry, the peculiarities of millimetre-wave radiation and its propagation in atmosphere, as well as its usefulness for imaging systems. An outline of various possible application scenarios of high industrial and commercial importance was given.

The main work of the presented Ph.D. thesis is concerned with the development of subharmonic SOMs and design of a low-frequency prototype in order to verify functionality has been fabricated before moving on to the millimetre-wave design. Circuit performance proves to be excellent with a conversion gain of +11.1 dB. Subsequently, the circuit has been designed at 35 GHz with a conversion gain of -9.7 dB using an SIW cavity. Moreover, an overview of analysis methods including the development of a new algorithm for the simulation of SOMs are presented along with performance models that assess its practical applicability in system environments.

In terms of imaging system design, the development, simulation, and testing of a reflector antenna at 35 GHz is discussed. Two main parameters are taken in to account in order to design an antenna suitable for this project: the antenna gain, which affects the spatial resolution of the image, and the size and weight of the overall antenna system (reflector, feed, and support mechanics), affecting the performance and requirements for the motors used for the mechanical steering.

The development of a radiometer receiver is described following the design of a low-frequency receiver and a low-frequency test-bed to assess preliminary radiometric measurement capabilities. Subsequently, the receiver is scaled to 35 GHz and tested with a

specifically designed heat-controllable target. Preliminary experiments are carried out detecting the target temperature, and with other targets such as the detection of a human body and a metal plate.

As a consequence of these results, the first measurements were obtained for the entire imaging system. A basic mechanical scanning setup is built up using the reflector antenna described previously with stepper motors responsible for the beam steering. A Matlab interface is designed to acquire the data and control the motor movement and is used to display the final image.

An FSS structure based on a periodic SIW cavity architecture, which can be used in the proposed imaging system in order to separate horizontal and vertical polarizations from the incident radiation. Future work will include the use of this FSS in the system.

This first millimetre-wave imaging test-bed serves as the base for future research in the field. Future work includes the parallelization of these receivers in the form of an FPA system, and also the task of pushing the design toward higher frequencies, in particular 94 GHz, for achieving higher image resolutions and more compact-sized imagers. More possible extensions for the future include the integration into a fully automatized multi-polarization system. Also, the mechanical scanning may be substituted by an electronic scanning system, which permits the beam steering to be carried out without any bulky mechanic movement. In terms of signal processing and algorithmic enhancements, specific techniques may be applied to enhance resolution and automatically detect objects in images. Also, image fusion can be investigated in order to combine the advantages of different frequency ranges for the desired end applications. Finally, the presented topic represents a large field of research and a highly interesting domain for present and future industrial applications and can be extended in a large number of ways to achieve the desired outcome and performance for a given specific application scenario.

BIBLIOGRAPHIE

[1] R. Appleby and A. H. Lettington, "Passive millimetre wave imaging," *Communication Engineering Journal*, vol. 3, pp. 13-16, Feb. 1991.

[2] A. H. Lettington, D. Dunn, M. Attia, and I. M. Blankson, "Passive millimetre-wave imaging architectures," *Journal of Optics A: Pure and Applied Optics*, vol. 5, pp. 103-110, Jul. 2003.

[3] E. Detlefsen, A. Dallinger, and S. Schelkshorn, "Approaches to millimeter-wave imaging of humans," *Proc. 1st European Radar Conference,* Amsterdam, pp. 279-282, Oct. 2004.

[4] H.-M. Chen, S. Lee, R. M. Rao, M.-A. Slamani, and P. K. Varshney, "Imaging for concealed weapon detection: a tutorial overview of development in imaging sensors and processing," *IEEE Signal Processing Magazine*, vol. 22, pp. 52-61, Mar. 2005.

[5] A. H. Lettington, D. Dunn, N. E. Alexander, A. Wabby, B. N. Lyons, R. Doyle, J. Walshe, M. F. Attia, and I. Blankson, "Design and development of a high-performance passive millimeter-wave imager for aeronautical applications," *Optical Engineering*, vol. 44, pp. 093202-1-093202-6, Sep. 2005.

[6] R. Doyle, B. Lyons, J. Walshe, P. Curtin, A. H. Lettington, T. McEnroe, and J. McNaboe, "Low cost millimetre wave camera imaging up to 140GHz," *Proc. 34th European Microwave Conference,* Amsterdam, pp. 1285-1288, Oct. 2004.

[7] D. R. Vizard and R. Doyle, "Invited paper: Advances in millimeter wave imaging and radar systems for civil applications," *IEEE MTT-S Int. Symp.,* San Francisco, CA, pp. 94-97, June 2006.

[8] T. Luthi and C. Matzler, "Stereoscopic passive millimeter-wave imaging and ranging," *IEEE Transactions on Microwave Theory and Techniques*, vol. 53, pp. 2594-2599, Aug. 2005.

[9] G. S. Dow, T. N. Ton, H. Wang, D. C. W. Lo, W. Lam , B. Allen, K. Tan, J. Berenz, L. Yujiri, M. Mussetto, and P. Lee, "W-band MMIC direct detection receiver for passive imaging system," *Proc. IEEE MTT-S Int. Symp. Dig.,* Atlanta, GA, pp. 163-166, June 1993.

[10] P. F. Goldsmith, C.-T. Hsieh, G. R. Huguenin, J. Kapitzky, and E. L. Moore, "Focal plane imaging systems for millimeter wavelengths," *IEEE Transactions on Microwave Theory and Techniques*, vol. 41, pp. 1664-1675, Oct. 1993.

[11] H. Kim, S. Duffy, J. Herd, and C. Sodini, "SiGe IC-based mm-wave imager," *IEEE International Symposium on Circuits and Systems,* New Orleans, LA, pp. 1975-1978, May 2007.

[12] G. S. Dow, D. C. W. Lo, Y. Guo, E. W. Lin, T. T. Chung, M. D. Biedenbender, O. Miromontes, A. Marashi, L. Yujiri, P. S. C. Lee, M. M. Shoucri, and B. R. Allen, "Large scale W-band focal plane array for passive radiometric imaging," *Proc. IEEE MTT-S Int. Symp. Dig.,* San Francisco, CA, pp. 369-372, June 1996.

[13] R. Kuroda, G. S. Dow, Y. R. Guo, R. Johnson, M. Biedenbender, A. Marashi, L. Yujiri, and M. Shoucri, "Direct-detection MMIC FPAs for MMW imaging," *Proc. SPIE Conf. Passive Millimeter-Wave Imaging Technology,* Orlando, FL, pp. 90-97, Apr. 1997.

[14] J. Richter, D. Notel, F. Kloppel, J. Huck, H. Essen, and L.-P. Schmidt, "A multi-channel radiometer with focal plane array antenna for W-band passive millimeter wave imaging," *Proc. IEEE MTT-S Int. Symp. Dig.,* San Francisco, CA, pp. 1592-1595, June 2006.

[15] R. Appleby, R. N. Anderton, S. Price, N. A. Salmon, G. N. Sinclair, J. R. Borrill, P. R. Coward, P. Papakosta, A. H. Lettington, and D. A. Robertson, "Compact real-time (video rate) passive millimeter-wave imager," *Proc. SPIE Conf. Passive Millimeter-Wave Imaging Technology III,* Orlando, FL, pp. 13-19, Apr. 1999.

[16] R. Appleby, R. N. Anderton, S. Price, N. A. Salmon, G. N. Sinclair, P. R. Coward, A. R. Barnes, P. D. Munday, M. Moore, A. H. Lettington, and D. A. Robertson, "Mechanically scanned real-time passive millimeter wave imaging at 94 GHz," *Proc. SPIE Conf. Conf. Passive Millimeter-Wave Imaging Technology VI and Radar Sensor Technology VII,* Orlando, FL, pp. 1-6, Apr. 2003.

[17] C. Martin, S. Clark, J. Galliano, and J. Lovberg, "Advances in millimeter-wave imaging technology for enhanced vision systems," *Proc. 21st Digital Avionics Systems Conf.,* Irvine, CA, pp. 11-14, Oct. 2002.

[18] R. Wanner, "Low Phase Noise SiGe Push-Push Oscillators for Millimeter Wave Frequencies," PhD. dissertation, Technische Universität München, Germany, 2006.

[19] I. D. Higgins, "Performance of self-oscillating GaAs MESFET mixers at X-band," *Electron. Lett.*, vol. 12, no. 23, pp. 605–606, Nov. 1976.

[20] J. Xu and K.Wu, "A subharmonic self-oscillating mixer using substrate integrated waveguide cavity for millimeter-wave application," in *IEEE MTT-S Int. Microw. Symp. Dig.*, Jun. 2005, pp. 2019–2022.

[21] Y. Chen and Z. Chen, "A dual-gate FET subharmonic injection-locked self-oscillating active integrated antenna for RF transmission," *IEEE Microw.Wireless Compon. Lett.*, vol. 13, no. 6, pp. 199–201, Jun. 2003.

[22] D. H. Evans, "A millimetre-wave self-oscillating mixer using a GaAs FET harmonic-mode oscillator," in *IEEE MTT-S Int. Microw. Symp. Dig.*, Jun. 1986, pp. 601–604.

[23] S. A. Winkler, K. Wu, and A. Stelzer, "Integrated Receiver Based on a High-Order Subharmonic Self-Oscillating Mixer," *IEEE Transactions on Microwave Theory and Techniques*, vol. 55, pp. 1398-1404, Jun. 2007.

[24] M. Sironen, Y. Qian, and T. Itoh, "A subharmonic self-oscillating mixer with integrated antenna for 60-GHz wireless applications," *IEEE Trans. Microw. Theory Tech.*, vol. 49, no. 3, pp. 442–450, Mar. 2001.

[25] N. Siripon, K. S. Ang, M. Chongcheawchamnan, and I. D. Robertson, "Design and performance of a novel balanced self-oscillating mixer," in *Proc. 30th Eur. Microw. Conf.*, Paris, France, Oct. 2000, pp. 16–19.

[26] N. Bourhill, S. Iezekiel, and D. P. Steenson, "A balanced self-oscillating mixer," *IEEE Microw. Guided Wave Lett.*, vol. 10, no. 11, pp. 481–483, Nov. 2000.

[27] T.-C. Huang and S.-J. Chung, "A new balanced self-oscillating mixer (SOM) with integrated antenna," in *IEEE Int. AP-S Symp.*, Columbus, OH, USA, Jun. 2003, pp. 89–92.

[28] S. A. Maas*, Microwave Mixers*, 2nd ed. Norwood, MA: Artech House, 1993.

[29] K. S. Ang, M. J. Underhill, and I. D. Robertson, "Balanced monolithic oscillators at K- and Ka-band," *IEEE Trans. Microw. Theory Tech.*, vol. 48, no. 2, pp. 187–193, Feb. 2000.

[30] N. Skou and D. Le Vine, *Microwave Radiometer Systems, 2nd ed.* Norwood, MA: Artech House, 2006.

[31] N. A. Salmon, S. Hayward, R. L. Walke, and R. Appleby, "Electronic scanning for passive millimeter-wave imaging," *Proc. SPIE Passive Millimeter-Wave Imaging Technology VI and Radar Sensor Technology VII,* Orlando, FL, pp. 71-76, Apr. 2003.

[32] A. R. Harvey, R. Appleby, P. Coward, R. Anderton, and G. Hawkins, "Electronic beam-steering for passive millimeter-wave imaging," *Proc. SPIE Conf. Millimeter and Submillimeter Waves IV,* San Diego, CA, pp. 415-424, July 1998.

[33] J.W. Goodman, *Introduction to Fourier Optics*. New York: McGraw-Hill, 1968.

[34] M. Sato, T. Hirose, H. Sato, K. Sawaya, and K. Mizuno, "A novel small tapered slot antenna for passive imaging sensors," *IEEE MTT-S Int. Symp.,* Long Beach, CA, pp. 147-150, June 2005.

[35] S. Sugawara, Y. Maita, K. Adachi, K. Mori, and K. Mizuno, "A mm-wave tapered slot antenna with improved radiation pattern," *IEEE MTT-S Int. Symp.,* Denver, CO, pp. 959-962, June 1997.

[36] K. A. S. Qassim and N. J. McEwan, "Printed Yagi antennas as a focal plane array in an imaging system," *Proc. 7th Int. Conf. on Antennas and Propagation,* York, pp. 193-196, Apr. 1991.

[37] K. S. Yngvesson, T. L. Korzeniowski, Y.-S. Kim, E. L. Kollberg, and J. F. Johansson, "The tapered slot antenna-a new integrated element for millimeter-wave applications," *IEEE Transactions on Microwave Theory and Techniques*, vol. 37, pp. 365-374, Feb. 1989.

[38] J. Richter and L.-P. Schmidt, "Dielectric rod antennas as optimized feed elements for focal plane arrays," *Proc. IEEE Antennas and Propagation Society Int. Symp.,*pp. 667-670, July 2005.

[39] Y. Gao and S. J. Reeves, "Optimal dithering of focal plane arrays in passive millimeter-wave imaging," *Optical Engineering*, vol. 40, pp. 2179-2187, Oct. 2001.

[40] P. J. Gibson , "The Vivaldi aerial," *Proceedings of the 9th European Microwave Conference,*pp. 101-105, Sept. 1979.

[41] H. Loui, J. P. Weem, and Z. Popovic, "A dual-band dual-polarized nested Vivaldi slot array with multilevel ground plane," *IEEE Transactions on Antennas and Propagation*, vol. 51, pp. 2168-2175, Sep. 2003.

[42] S.-G. Kim and K. Chang, "A low cross-polarized antipodal Vivaldi antenna array for wideband operation," *IEEE Antennas and Propagation Society Symposium, 20-25 June 2004,*pp. 2269-2272, June 2004.

[43] N. A. Salmon, R. Appleby, and P. Coward, "Polarimetric passive millimetre wave imaging," *Proc. 3rd Int. Conf. on Microwave and Millimeter Wave Technology,* Beijing, pp. 540-543, Aug. 2002.

[44] H. A. Zebker and J. J. Van Zyl, "Imaging radar polarimetry: a review," *Proceedings of the IEEE*,

vol. 79, pp. 1583-1606, Nov. 1991.

[45] R.C. Gonzalez and R.E. Woods, *Digital Image Processing, 2nd ed.* Upper Saddle River, NY: Prentice-Hall, 2002.

[46] J.S. Son, G. Thomas, and B.C. Flores, *Range-Doppler Radar Imaging and Motion Compensation*. Norwood, MA: Artech House, 2001.

[47] A. H. Lettington, M. R. Yallop, and D. Dunn, "Review of super-resolution techniques for passive millimeter-wave imaging," *Proc. SPIE Conf. Infrared and Passive Millimeter-wave Imaging Systems: Design, Analysis, Modeling, and Testing,* Orlando, FL, pp. 230-239, Apr. 2002.

[48] J. Preissner, "The influence of the atmosphere on passive radiometric measurements," *Symp. Millimeter Submillimeter Wave Propag. Circuits*: AGARD Conf. Proc., no. 245, pp. 48/1-48/13.

[49] L. Yujiri, M. Shoucri, P. Moffa, "Passive millimeter-wave imaging," *IEEE Microwave Magazine*, vol. 4, Iss. 3, Sep. 2003, pp. 39-50.

[50] J. Zhang, Y. Wang, and Z. Chen, "Integration of a self-oscillating mixer and an active antenna," *IEEE Microwave and Guided Wave Letters*, vol. 9, Mar. 1999, pp. 117-119.

[51] S. A. Winkler, K. Wu, A. Stelzer, "A Novel Balanced Third and Fourth Harmonic Self-Oscillating Mixer with High Conversion Gain", *Proc. 36th European Microwave Conf.*, Manchester, UK, pp. 1663-1666, Sep. 2006.

[52] R. W. Rhea, Oscillator Design & Computer Simulation, 2nd ed. New York: McGraw-Hill, 1997.

[53] A. Mortazawi and B. C. De Loach, Jr., "Multiple element oscillators utilizing a new power combining technique," *IEEE Trans. on Microwave Theory Tech.*, vol. 40, pp. 2397-2402, Dec. 1992.

[54] S. ver Hoeye, L. Zurdo, and A. Suarez, "New nonlinear design tools for self-oscillating mixers," *IEEE Microwave and Wireless Components Letters*, vol. 11, pp. 337-339, Aug. 2001.

[55] J. Morales, A. Suarez, E. Artal, and R. Quere, "Global stability analysis of self-oscillating mixers," *Proc. 25th European Microwave Conf.*, Bologna, Italy, pp. 1216-1219, Sep. 1995.

[56] K. Schmidt von Behren, D. Pienkowski, T. Mueller, M. Tempel, G. Boeck**,** "77 GHz harmonic mixer with flip-chip Si-Schottky diode**,"** Microwaves, Radar and Wireless Communications, 2002. MIKON-2002. 14th International Conference on, vol. 3, pp. 743 - 746.

[57] S. A. Maas, *Noise in Linear and Nonlinear Circuits*, 1st ed. Norwood, MA: Artech House, 2005.

[58] I. Angelov, H. Zirath, N. Rorsman, "A New Empirical Nonlinear Model for HEMT and MESFET Devices," *IEEE Trans. on Microwave Theory Tech.*, vol. 40, pp. 2258-2266, Dec. 1992.

[59] I. Angelov, L. Bengtsson, M. Garcia, "Extensions of the Chalmers Nonlinear HEMT and MESFET Model," *IEEE Trans. on Microwave Theory Tech.*, vol. 44, pp. 1664-1674, Oct. 1996.

[60] I. Kipnis and A. S. Khanna, "Large-signal computer-aided analysis and design of silicon bipolar MMIC oscillators and self-oscillating mixers, " *IEEE Trans. on Microwave Theory Tech.*, vol. 37, pp. 558-564, Mar. 1989.

[61] S. T. Chew and T. Itoh, "Application of Volterra Series to the Problem of Self-Oscillating Mixer," *IEEE Trans. on Microwave Theory Tech.*, vol. 44, pp. 269-274, Feb. 1996.

[62] S. A. Maas, Nonlinear Microwave and RF Circuits, 2nd ed. Boston, MA: Artech House, 2003.

[63] S. A. Maas, A. Crosmun, "Modeling the gate I/V characteristic of a GaAs MESFET for Volterra-Series analysis, " *IEEE Trans. on Microwave Theory Tech.*, vol. 37, pp. 1134-1136, Jul. 1989.

[64] T. K. Johansen, J. Vidkjaer, and V. Krozer, "Analysis and Design of Wide-Band SiGe HBT Active Mixers," *IEEE Trans. on Microwave Theory Tech.*, vol. 53, pp. 2389-2397, Jul. 2005.

[65] S. A. Winkler, K. Wu, and A. Stelzer, "Design of a novel balanced high-order subharmonic self-oscillating mixer," *Electronics Letters*, vol. 42, pp. 1405-1406, Nov. 2006.

[66] K. K. M. Cheng and J. K. A. Everard, "A new and efficient approach to the analysis and design of GaAs MESFET microwave oscillators," in *IEEE MTT-S Int. Microwave Symp. Dig.*, pp 1283-1286, June 1990.

[67] C. A. Balanis, Antenna Theory, Analysis and Design, Hoboken, NJ: Wiley-Interscience, 2005.

[68] Z. Liu, R. M. Weikle II, "High-order subharmonically pumped mixers using phased local oscillators," *IEEE Trans. Microwave Theory & Tech.*, vol. 54, no. 7, pp. 2977-2982, July 2006.

[69] D. N. Held, A. R. Kerr, "Conversion loss and noise of microwave and millimeter-wave mixers: Part I–Theory," *IEEE Trans. Microwave Theory & Tech.*, vol. MTT-26, no. 2, pp. 49-55, Feb. 1978.

[70] U. Hiroshi, T. Takeshi, and M. Fujii, "Development of a 'laminated waveguide'," *IEEE Trans. on Microwave Theory and Techniques*, Vol. 46, No. 12, pp. 2438-2443, Dec. 1998.

[71] Y. Cassivi, L. Perregrini, P. Arcioni, M. Bressan, K. Wu, and G. Conciauro, "Dispersion Characteristics of Substrate integrated rectangular waveguide," IEEE *Microwave and Wireless Components Letters*, Vol. 12, No. 9, pp. 333–335, Sept. 2002.

[72] D. Deslandes and K. Wu, "Single-Substrate Integration Technique of Planar Circuits and Waveguide Filters," *IEEE Trans. on Microwave Theory and Techniques*, Vol. 51, No. 2, pp. 593-596, Feb. 2003.

[73] F. Xu and K. Wu, "Guided-Wave and Leakage Characteristics of Substrate Integrated Waveguide," *IEEE Trans. on Microwave Theory and Techniques*, Vol. 53, No. 1, pp. 66-73, Jan. 2005.

[74] D. Deslandes and K. Wu, "Accurate Modeling, Wave Mechanisms, and Design Considerations of a Substrate Integrated Waveguide," *IEEE Trans. on Microwave Theory and Techniques*, Vol. 54, No. 6, pp. 2516–2526, June 2006.

[75] K. Wu, "Towards System-on-Substrate Approach For Future. Millimeter-Wave and Photonic Wireless Applications," *Proc. of Asia-Pacific Microwave Conference*, pp. 1895–1900, 2006.

[76] Z. Li and K. Wu, "24-GHz Frequency-Modulation Continuous-Wave Radar Front-End System-on-Substrate," *IEEE Trans. on Microwave Theory and Techniques*, Vol. 56, No. 2, pp. 278-285, Feb. 2008.

[77] N. Grigoropoulos, B. S. Izquierdo, and P. R. Young, "Substrate integrated folded waveguides

(SIFW) and filters," *IEEE Microwave Wireless Component Letters*, Vol. 15, No. 12, pp. 829–831, Dec. 2005.

[78] W. Hong, Y. Wang, Q. H. Lai, and B. Liu, "Half mode substrate integrated waveguide: A new guided wave structure for microwave and millimeter wave application," *Proc. Joint 31st Int. Conf. Infrared Millimeter Waves 14th Int. Conf. Terahertz Electronics*, p. 219, Shanghai, China, Sep. 18–22, 2006.

[79] G. H. Zhai, W. Hong, K. Wu, J. X. Chen, P. Chen, J. Wei, and H. J. Tang, "Folded Half Mode Substrate Integrated Waveguide 3 dB Coupler," *IEEE Microwave and Wireless Components Letters*, Vol. 18, No. 8, pp. 512-514, Aug. 2008.

[80] M. Bozzi, D. Deslandes, P. Arcioni, L. Perregrini, K. Wu, and G. Conciauro, "Efficient Analysis and Experimental Verification of Substrate Integrated Slab Waveguides for Wideband Microwave Applications" *International Journal of RF and Microwave Computer–Aided Engineering*, Vol. 15, No. 3, pp. 296-306, May 2005.

[81] W. Che, C. Li, P. Russer and Y. L. Chow, "Propagation and Band Broadening Effect of Planar Integrated Ridged Waveguide in Multilayer Dielectric Substrates," *IEEE MTT-S Inter. Microwave Symposium Digest 2008*, pp. 217-220, Atlanta, GA, June 15-20, 2008.

[82] S. B. Cohn, "Properties of ridge waveguide, " *Proc. IRE*, Vol. 35, pp. 783-788, Aug. 1947.

[83] S. Hopfer, "The Design of Ridged Waveguides," *IRE Trans. on Microwave Theory and Techniques*, Vol. 3, No. 5, pp. 20-29, Oct. 1955.

[84] T.-S. Chen, "Calculation of the Parameters of Ridge Waveguides," *IRE Trans. on Microwave Theory and Techniques*, Vol. 5, No. 1, 12-17, Jan. 1957.

[85] M. Bozzi, S.A. Winkler, and K. Wu, "Novel Compact and Broadband Interconnects based on Ridge Substrate Integrated Waveguide," *2009 IEEE MTT-S Intern. Microwave Symp.*, Boston, USA, June 7-12, 2009.

[86] M. Cametti, "Design and Testing of a Radiometer System at 35 GHz", *master thesis*, University of Pavia, Italy.

[87] M.D. Janezic, J.A. Jargon, "Complex permittivity determination from propagation constant measurements," *IEEE Microwave and Guided Wave Letters*, Vol. 9, No. 2, pp. 76–78, Feb. 1999.

[88] T. K. Wu, *Frequency Selective Surface and Grid Array*. New York: Wiley, 1995.

[89] J. C. Vardaxoglou, *Frequency Selective Surfaces*. New York: Wiley, 1997.

[90] B. A. Munk, *Frequency Selective Surfaces*: Theory and Design. New York: Wiley Interscience, 2000.

[91] Y. Cassivi, L. Perregrini, K. Wu, G. Conciauro, "Low-cost high-Q millimeter-wave resonator using substrate integrated waveguide technique," *Proc. European Microw. Conf.*, Oct. 2002, pp. 1-4.

[92] G. Q. Luo, W. Hong, Z.-C. Hao, B. Liu, W. D. Li, J. X. Chen, H. X. Zhou, K. Wu, "Theory and experiment of novel frequency selective surface based on substrate integrated waveguide technology," *IEEE Trans. Microwave Theory Tech.*, vol. 53, no. 12, Dec. 2005, pp. 4035-4043.

[93] G. Q. Luo, W. Hong, J. X. Chen, X. X. Yin, Z. Q. Kuai, K. Wu, "Filtenna Consisting of Horn Antenna and Substrate Integrated Waveguide Cavity FSS," *IEEE Trans. Antennas Propag.*, vol. 55, no. 1, Jan. 2007, pp. 92-98.

[94] M. Bozzi, L. Perregrini, J. Weinzierl, C. Winnewisser, "Efficient Analysis of Quasi-Optical Filters by a Hybrid MoM/BI-RME Method," *IEEE Trans. Antennas Propag.*, vol. 49, no. 7, Jul. 2001, pp. 1054-1064.

[95] M. Bozzi and L. Perregrini, "Analysis of Multilayered Printed Frequency Selective Surfaces by the MoM/BI-RME Method," *IEEE Trans. Antennas Propag.*, vol. 51, no. 10, Oct. 2003, pp. 2830-2836.

[96] P. Besso, M. Bozzi, L. Perregrini, L. Salghetti Drioli, and W. Nickerson, "Deep Space Antenna for Rosetta Mission: Design and Testing of the S/X-Band Dichroic Mirror," *IEEE Trans. Antennas Propag.*, vol. 51, no. 3, pp. 388-394, March 2003.

[97] S. Biber, M. Bozzi, O. Guenther, L. Perregrini, and L.-P. Schmidt, "Design and Testing of Frequency Selective Surfaces on Silicon Substrates for Sub-mm Wave Applications," *IEEE Trans. Antennas Propag.*, vol. 54, no. 9, pp. 2638-2645, Sept. 2006.

[98] M. Bozzi, L. Perregrini, A. Alvarez Melcon, M. Guglielmi, G. Conciauro, "MoM/BI-RME Analysis of Boxed MMICs with Arbitrarily Shaped Metallizations," *IEEE Trans. Microwave Theory Tech.*, vol. 49, no. 12, pp. 2227-2234, Dec. 2001.

[99] M. Bozzi, S. Germani, L. Minelli, L. Perregrini, and P. de Maagt, "Efficient Calculation of the Dispersion Diagram of Planar Electromagnetic Band-Gap Structures by the MoM/BI-RME Method," *IEEE Trans. Antennas Propag.*, vol. 53, no. 1, pp. 29-35, Jan. 2005.

[100] Ansoft HFSS EM simulator.